

ECSC COAL RTD PROGRAMME

Project N°: *LL/NNN*
Contract N°: 7220-PR-125

**Capture of CO₂ in Coal Combustion
(CCCC)**

Final Report

Authors:

*Chalmers University of Technology,
"Chalmers" (Co-ordinator)*

**Consejo Superior de Investigaciones
Científicas, "CSIC".**

**Vienna University of Technology,
"TU-Vienna"**

Cranfield University, "Cranfield"

**Technical Research Centre of Finland,
"VTT"**

Version: *Final*

Date: 25/10/2005

ECSC COAL RTD PROGRAMME**Report data sheet**

Document title: 12-month report		Contract N°: 7220-PR-125
Language: E	N° of pages:	Project N0.: (LL/NNN)
Project title:		
Capture of CO₂ in Coal Combustion (CCCC)		
Authors:		Sponsors:
T. Mattisson, JC. Abanades , A. Lyngfelt		
A. Abad, M. Johansson, J. Adanez,		
F. Garcia-Labiano, LF. de Diego, P. Gayan		
B. Kronberger, H. Hofbauer, M. Luisser		
JM. Palacios, D. Alvares, G. Grasa		
J. Oakey, B. Arias, M. Orjala		
V-P Heiskanen		
Abstract:		
<p>The aim of the project is to develop processes for carbon dioxide capture from coal-fired power plants with small energy penalties. Two novel processes are studied: chemical-looping combustion (CLC) and the lime carbonation/calcination cycle (LCCC). Both parts of the project have been highly successful. With respect to CLC the process was a paper concept when the project started, never tested in actual operation. In this project a large number of oxygen carriers have been produced and tested and many were found to have suitable properties for the process. A small reactor system for chemical-looping combustion was developed, tested and found to be working well with three different oxygen carriers. Furthermore cold-flow models indicate the realism of the process in full scale. The kinetics of a limited number of particles has been studied in detail, and modelling shows that the solids inventories needed will be small. With respect to the LCCC part, some of the options investigated can be potentially competitive to capture CO₂ in coal-based power generation and cement plants. The observed decay in capture capacity of the sorbent can be compensated with a large make up flow of fresh limestone due to its low price. The key reactor systems (carbonator and calciner) have shown no major barriers for continuous operation. All the options studied have the inherent advantage of low efficiency penalties. For some options, no major technical barriers have been identified and confidence has been built on the operation and understanding of individual units. Some of the options are ready to be demonstrated at large pilot level in a continuous power plant.</p>		
Key words:		
CO ₂ capture, chemical-looping combustion, lime carbonation calcination cycles		
Additional information from:		EC approval:
<i>Anders Lyngfelt, CLC-part</i> <i>Carlos Abanades, LCCC-part</i>		<i>(For Commission use)</i>
Confidentiality: <i>(Public, restricted, etc.)</i>		Date:

ECSC COAL RESEARCH PROGRAMME**Project N°.:****Contract N°.:** 7220-PR-125**Contact persons**

Financial matters	Technical matters
<u>Co-ordinator:</u> Chalmers University of Technology Anders Lyngfelt Prof. Department of Energy Conversion Chalmers University of Technology S 412 96 Göteborg, Sweden Phone: + 46 31 772 1427 Fax: + 46 31 772 3592 E-mail: anly@entek.chalmers.se	<u>Co-ordinator:</u> Chalmers University of Technology Anders Lyngfelt Prof. Department of Energy Conversion Chalmers University of Technology S 412 96 Göteborg, Sweden Phone: + 46 31 772 1427 Fax: + 46 31 772 3592 E-mail: anly@entek.chalmers.se
Consejo Superior de Investigaciones Científicas, "CSIC". J Carlos Abanades Instituto de Carboquímica Miguel Luesma Castan 12 50015 Zaragoza, Spain Phone: + 34976733977 Fax: + 34976733318 E-mail: jcabanad@carbon.icb.csic.es	Consejo Superior de Investigaciones Científicas, "CSIC". J Carlos Abanades Instituto de Carboquímica Miguel Luesma Castan 12 50015 Zaragoza, Spain Phone: + 34976733977 Fax: + 34976733318 E-mail: jcabanad@carbon.icb.csic.es
Vienna University of Technology Hermann Hofbauer Prof. Institute of Chemical Engineering, Fuel Technology and Environmental Technology Getreidemarkt 9/159 A- 1060 Vienna, Austria Phone: + 43-1-58801-159-70 Fax: + 43-1-58801-159-99 E-mail: hhofba@mail.zserv.tuwien.ac.at	Vienna University of Technology Hermann Hofbauer Prof. Institute of Chemical Engineering, Fuel Technology and Environmental Technology Getreidemarkt 9/159 A- 1060 Vienna, Austria Phone: + 43-1-58801-159-70 Fax: + 43-1-58801-159-99 E-mail: hhofba@mail.zserv.tuwien.ac.at
Cranfield University John E Oakey Cranfield University Cranfield Bedfordshire MK43 0AL UK Phone: + 44-1234-754253 Fax: + 44-1234-752473 E-mail: j.e.oakey@cranfield.ac.uk	Cranfield University John E Oakey Cranfield University Cranfield Bedfordshire MK43 0AL UK Phone: + 44-1234-754253 Fax: + 44-1234-752473 E-mail: j.e.oakey@cranfield.ac.uk

Technical Research Centre of Finland, "VTT" Markku Orjala VTT Energy P.O. Box 1603 FIN-40101 Jyväskylä Finland Phone: + 35814672534 Fax: + 35814672597 E-mail: +Markku.Orjala@vtt.fi	Technical Research Centre of Finland, "VTT" Markku Orjala VTT Energy P.O. Box 1603 FIN-40101 Jyväskylä Finland Phone: + 35814672534 Fax: + 35814672597 E-mail: +Markku.Orjala@vtt.fi
--	--

Table of Contents

1. INTRODUCTION	7
2. SUMMARY	9
2.1 CHEMICAL-LOOPING COMBUSTION (CLC)	9
2.2 LIME CARBONATION-CALCINATION CYCLE (LCCC)	10
3. RESEARCH DESCRIPTION	12
3.1 CHEMICAL-LOOPING COMBUSTION (CLC)	12
3.1.1 <i>Introduction</i>	12
3.1.2 <i>Chemical-looping combustion</i>	12
3.1.3 <i>Methodology</i>	14
3.1.4 <i>Results</i>	16
3.2 LIME CARBONATION CALCINATION CYCLES (LCCC)	24
3.2.1 <i>Introduction</i>	24
3.2.2 <i>Experimental systems and procedures</i>	26
3.2.3 <i>Discussion</i>	27
4. CONCLUSIONS	32
4.1 CHEMICAL-LOOPING COMBUSTION (CLC)	32
4.2 LIME CARBONATION-CALCINATION CYCLES (LCCC)	33
5. RECOMMENDATIONS	34
5.1 CHEMICAL-LOOPING COMBUSTION (CLC)	34
5.2 LIME CARBONATION-CALCINATION CYCLES (LCCC)	34
ANNEX A. TECHNICAL ANNEXES	35
A.1 TASK 1. DEVELOPMENT OF OXYGEN CARRIER PARTICLES	35
A.1.1 <i>Work performed at CSIC</i>	35
A.1.2 <i>Work performed at Chalmers</i>	44
A.1.3 <i>Selected particles for further testing</i>	56
A.2 TASK 2. COMPREHENSIVE TESTING OF OXYGEN CARRIER PARTICLES	57
A.2.1 <i>Work performed at CSIC</i>	57
A.2.2 <i>Work performed at Chalmers</i>	71
A.3 TASK 3. FLUIDISATION CONDITIONS.	78
A.3.1 <i>Work performed at VUT</i>	78
<i>Effect of gas density on CFB fluid dynamics</i>	92
A.4 TASK 4. CONSTRUCTION AND OPERATION OF A LABORATORY CHEMICAL-LOOPING COMBUSTOR.	95
A.4.1 <i>Work performed at Chalmers</i>	95
A.5 TASK 5. CHARACTERISATION OF SORBENT (CAO) PERFORMANCE IN THE LCCC	108

<i>A.5.1 Work carried out at CSIC</i>	110
<i>A.5.2 Work performed at VTT</i>	120
A.6 TASK 6. PILOT PLANT EVALUATION OF THE CO ₂ SEPARATION CONCEPT.	146
<i>A.6.1 Work performed at VTT</i>	146
<i>A.6.2. Work performed at Cranfield. In duct testing.</i>	155
A.7 TASK 7. PILOT TESTING AND DESIGN SPECIFICATION OF THE CALCINER.	170
<i>A.7.1 Work performed at CSIC</i>	170
<i>A.7.2 Work performed at Cranfield. Calcination in flame.</i>	175
A.8 TASK 8. THE DEVELOPMENT OF BASIC REACTOR SIMULATION TOOLS.	183
<i>A.8.1 Work performed at CSIC. Fluidized bed carbonator model.</i>	183
<i>A.8.2. Work performed at Cranfield. In-duct sorbent injection modelling.</i>	188
A.9 TASK 9. INTEGRATION OF COMPONENTS (CSIC AND CRANFIELD)	195
A.10 TASK 10. ECONOMICAL ASSESSMENT.	204
ANNEX B. PUBLICATIONS AND REPORTS MADE WITHIN PROJECT	208
B.1. CHEMICAL-LOOPING COMBUSTION	208
B.2. LIME CARBONATION CALCINATION CYCLES (LCCC)	210
ANNEX C. NOTATION	212
ANNEX D. REFERENCES	217

CAPTURE OF CO₂ IN COAL COMBUSTION

Final Report

1. INTRODUCTION

Carbon dioxide is a greenhouse gas, and about 75% of the anthropogenic release of carbon dioxide comes from combustion of fossil fuels. (IPCC, 2001) It is generally accepted that greenhouse gases contribute to the increased global temperature. In order to stabilize the atmospheric concentration of CO₂, substantial measures are necessary quickly. One possibility to decrease the CO₂ emissions is to capture and dispose of the carbon dioxide from the combustion of fossil fuels. As coal is the most abundant fossil fuel resource, it is important to find combustion techniques where CO₂ can be captured from coal combustion. The problem with many of the more conventional techniques for carbon dioxide capture is the high energy demand necessary for the capture and sequestration. Thus, the aim of the project is to develop processes for carbon dioxide capture from coal-fired power plants with small energy penalties. Two novel processes are studied: chemical-looping combustion (CLC) and the lime carbonation/calcination cycle (LCCC).

Chemical-looping combustion (CLC) is a combustion technology where an oxygen carrier is used to transfer oxygen from the combustion air to the fuel, thus avoiding direct contact between air and fuel. The fuel is syngas from coal gasification, although both natural gas or refinery gas could be used. The overall reactions in the fuel and air reactor are:



Here MeO is a metal oxide and Me the metal or reduced metal oxide. The total amount of heat evolved from reaction (1.1) plus (1.2) is the same as for normal combustion where the oxygen is in direct contact with the fuel. However, the advantage with this system compared to normal combustion is that the CO₂ and H₂O are inherently separated from the rest of the flue gases, and no major energy is expended for this separation. The project has involved three research teams from Sweden, Spain and Austria, with focus on i) the development of oxygen carrier particles, ii) establishing a reactor design and feasible operating conditions and iii) construction and operation of a continuously working hot prototype reactor.

The LCCC process is based on separation of CO₂ from combustion gases with the use of lime as an effective high temperature CO₂ sorbent to form CaCO₃. The reverse calcination reaction can produce a gas stream rich in CO₂ and supply sorbent (CaO) for subsequent cycles of carbonation:



The separation of CO₂ at the high temperatures at which carbonation takes place is intrinsically associated with lower energy penalties in the separation step, because the heat required to regenerate the sorbent (at temperatures close to 900°C) is recovered at around 650°C (at atmospheric pressure) during the carbonation reaction.

The background for the basic separation process goes back to 1867 and was proven in the Acceptor Gasification Process (Curran et al, 1967) in successful pilot tests involving interconnected fluidized beds at high pressure and temperature. However, the application to combustion systems with a need to obtain a purified stream of CO₂ for geological storage, is new. In this project a number of processes that would be suitable for integration of the lime carbonation calcination cycle (LCCC) in a coal combustion system with CO₂ capture were investigated. The results from the work to characterise sorbent performance in the capture-regeneration loop, to test individual reactor components in small pilots, simulate overall systems and identify possible economic barriers, are presented in this Report.

2. SUMMARY

2.1 Chemical-looping combustion (CLC)

One part of the project has focused on developing chemical-looping combustion (CLC) for synthesis gas from coal gasification. The CLC part of the project involves work in several interconnected areas: i) the development of oxygen carrier particles, ii) establishing a reactor design and feasible operating conditions and iii) construction and operation of a continuously working hot prototype reactor. Below a more detailed summary of the results can be found.

Oxygen carriers: The objective of this part of the project was to develop an oxygen carrier which can be used in a CLC system of interconnected fluidized beds. The oxygen carriers should have a high reduction and oxidation rate under both reducing and oxidizing conditions, be resistant to attrition and agglomeration and have a high durability, maintaining the chemical, structural and mechanical properties in a high number of reduction-oxidation cycles. The oxygen carriers investigated are composed of an active metal oxide to transport the oxygen, and an inert to enhance the reactivity, and in certain cases provide added mechanical strength. A large number of oxygen carriers (~300 samples) based on the transition metals Fe, Ni, Cu and Mn have been prepared and tested under alternating oxidizing and reducing conditions using both TGA and fluidized bed reactors. The particles have been manufactured using three types of production methods, using a large number of inert materials, for example Al₂O₃, TiO₂ and ZrO₂. Many of the particles could be discounted in the initial testing phase of the project due to low reactivity, deactivation, de-fluidization or insufficient mechanical strength. However, several particles were found to have a combination of good properties which made them feasible as oxygen carriers. Detailed reactivity investigations in TGA and fluidized bed of the most promising particles based on Ni, Cu, Fe and Mn found high initial reactivity with both H₂ and CO for all carriers. The solid inventory needed in the CLC system was found to be very low for three of the selected carriers based on Ni, Fe and Cu, i.e. between 25-88 kg/MW of syngas. A comparison of the reactivity of particles in syngas with natural gas showed that Fe₂O₃ and Mn₃O₄ have considerably better reactivity with syngas, whereas NiO had a high initial reactivity with both syngas and natural gas. Because materials based on manganese and iron are much cheaper and less toxic in comparison to nickel, Fe₂O₃ and Mn₃O₄ may be more suitable for a CLC process using gasified coal in comparison to NiO, which has received most of the attention in other studies where natural gas is the fuel.

Reactor design and fluidization conditions: In a CLC system of interconnected fluidized beds it is important that i) the recirculation rate of particles is high enough to transport the oxygen from the air to the fuel, ii) the solid inventory sufficient to react with the fuel and iii) the gas leakage between the reactors minimized. Thus, the determination of the effects of reactor design, solid properties and fluidization conditions on the fluid dynamics of CLC reactor designs was established. Three reactor concepts, differing in scale and operating conditions, were designed and tested experimentally by means of scale models operated at ambient temperatures. The purpose of the first unit was to develop a small, simple CLC laboratory reactor to be used for i) the study of the process, and ii) testing of different oxygen carriers. Experiments with different flow model designs showed that it is possible to achieve sufficient circulation of particles for the oxygen transfer in a model operated between 100-300 W. Also the gas leakage was low enough for a laboratory reactor. A final design,

optimized in terms of solids flow and gas mixing, was constructed and put into operation, see below.

Two additional models were constructed: a CLC pre-demonstration unit and a pressurized CLC demonstration plant.

The hot prototype reactor: From the results of the fluidization investigations carried out in the first cold model, a hot laboratory size continuously operated chemical-looping combustor was designed, built and operated. This system was designed for an input power between 100 and 300 W, using syngas as the fuel. The relatively low inventory of oxygen carrier needed in this unit made it suitable for testing of different types of oxygen-carrier. Three particles based on Ni, Fe and Mn, selected from the screening phase of the project were tested in the unit. All oxygen carriers achieved a high conversion of the fuel with small amounts of unburnt from the fuel reactor. For many of the tests with NiO, equilibrium is reached and combustion efficiency was 0.994 at 850 °C. For Mn₃O₄, the CO and H₂ concentrations were below the detection level of the gas analyzer. The Fe-based oxygen carrier also showed high conversion of the fuel with a combustion efficiency of 0.988 at 850 °C. The investigated particles have been fluidized with recirculation in hot conditions for approximately 150 h for the Ni particles, 130 h for the Mn and 60 h for the Fe based particles without any signs of deactivation and very little attrition.

2.2 Lime carbonation-calcination cycle (LCCC)

The second part of the project concerns the investigation of high temperature separation of CO₂ using a carbonation-calcination cycle. Several options were considered in the project proposal that have been further refined and expanded in the course of this project. The options have been developed in different extent in the specific tasks (sorbent performance studies, pilot plant studies of individual units, simulation and integration work, and economic studies).

One option has considered CO₂ capture in existing boilers using entrained mode contact of sorbent with the flue gas. The aim would be to inject a flow of CaO fine powder into a suitable point of the power plant gas path. Gas-solid contact in these conditions is limited to a few (2-10) seconds and maximum carbonation rates are required. Experimental work on the carbonation design was carried out at Cranfield in two different rigs (coiled entrained tube reactor and cooling chamber of an existing coal PF burner). Experimental results were in line with what was anticipated, with CO₂ capture efficiencies in the order of 30-40% when using contact times as low as 2-4 seconds and fresh calcines. Data from VTT CFB test rig operated with no sorbent circulation offered similar qualitative information. Fast calcination test confirmed that the concept is technically feasible if these short of low CO₂ capture efficiencies were acceptable and realised at very low cost.

The main options investigated in the project involved fluidised bed systems at atmospheric and high pressure, where CO₂ capture efficiencies can be over 90%. Experimental pilot data in a fluidized bed carbonator has been generated mainly by the collaboration of CSIC with the CANMET Energy Technology Center in Canada, showing that a dense fluidised bed of CaO is an effective sink of the CO₂ contained in a typical coal combustion flue gas. Results in this pilot could be interpreted with a fluid-bed reactor model, using sorbent performance data obtained at laboratory scale (the sorbent capture capacity, and its decay along cycling, is the critical parameter to understand the behaviour fluidised beds using CaO). Extensive experimental work has been conducted in lab scale equipment to investigate the (rapid) decay

in sorbent capacity along cycling and modelling work has aided the interpretation and extrapolation of results.

Simulation work on the different fluidised bed options to integrate carbonation-combustion and calciner reactors in a single system have identified several high efficiency systems (with negligible efficiency penalties beyond the penalties for compression of CO₂ and calcination of the make up flow of limestone). Some of these options involve the calcination of the sorbent by transferring heat from the combustor chamber to the calciner. Cold model investigations at CSIC have obtained fundamental design data for fluidised bed calciners. High temperature calcinations tests at Cranfield have shown viability for entrained bed calciners. A bubbling fluidised bed systems involving high pressure and high temperature carbonation-combustion-calcination system has also been simulated using basic data on sorbent performance from laboratory tests.

An economic analysis was carried out to assess the implications of the large make up flows of sorbent in this system, as this is always considered a weak point of any LCCC process. This exercise showed that despite the very large mass flows of sorbent make up required (in the same order as the coal) the cost is comparable to the make up cost of other existing and emerging CO₂ capture system (because the low price of crushed limestone compared to any other synthetic sorbent or precursor).

In general, this project has been instrumental to reduce the gap of knowledge on a wide range of fundamental aspects of the system. All the project results have been widely disseminated in CO₂NET workshops and meetings, international conferences, two patents, and scientific and technical international journals (11 papers in ISI referred journals). Plausible design data and design tools are now available, and some options have been defined as ready for demonstration in a pilot of sufficient scale to proof the concepts. Some of these systems are already the subject of other projects at national, European and international level.

3. RESEARCH DESCRIPTION

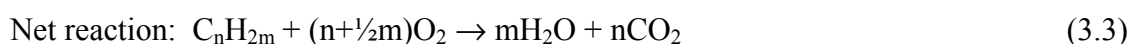
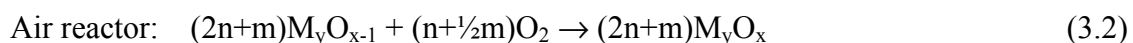
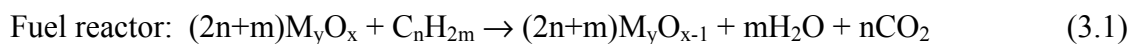
3.1 Chemical-looping combustion (CLC)

3.1.1 Introduction

Increasing amounts of CO₂ released to the atmosphere can promote the natural greenhouse effect, and as a result affect the global climate. Although the effects of increased levels of greenhouse gases are difficult to quantify, it is generally accepted that a reduction in emissions of gases that contribute to global warming is necessary. The increase of efficiency of energy conversion as well as increasing the use of renewable sources (biofuel, wind power, etc.) will not be enough to cover the increasing energy demand, and fossil fuels will be the dominant energy source worldwide in the short and medium term (Takematsu, 1991). Of the fossil fuels, there are considerably larger resources of coal available in comparison to natural gas and oil. Furthermore, coal releases larger amounts of CO₂ per energy unit than the other fossil fuels. A strategy to decrease emissions of greenhouse gases and still use fossil fuels in combustion processes is CO₂ capture and sequestration. Several different techniques exist today that can be used to obtain CO₂ in a pure stream from a combustion unit. The three most mentioned are posttreatment, O₂/CO₂ firing (oxyfuel) and CO-shift. Chemical-looping combustion is another technique for combustion which could be used for CO₂ separation with potentially much lower energy penalties than the above mentioned techniques. This is due to the inherent separation of CO₂ from the rest of the flue gases.

3.1.2 Chemical-looping combustion

Chemical-looping combustion (CLC) is a two-step gas combustion process that produces a pure CO₂ stream, ready for compression and sequestration. The process is composed of two reactors, a fuel and an air reactor, see Figure 3.1. In the fuel reactor the fuel in gaseous form reacts with the metal oxide according to reaction 3.1. The reduced metal oxide, M_yO_{x-1} is transferred to the air reactor where it is oxidized back to M_yO_x with air, reaction (3.2). The metal oxide is then returned to the fuel reactor and begins a new cycle of reactions. The flue gas leaving the air reactor will contain N₂ and any unreacted O₂. The exit gases from the fuel reactor contain CO₂ and H₂O, which are kept separate from the rest of the flue gas. After condensation of the water almost pure CO₂ is obtained, without any energy lost for separation. The total amount of heat evolved from reactions in the two reactors is the same as for normal combustion, where the oxygen is in direct contact with fuel, reaction (3.3).



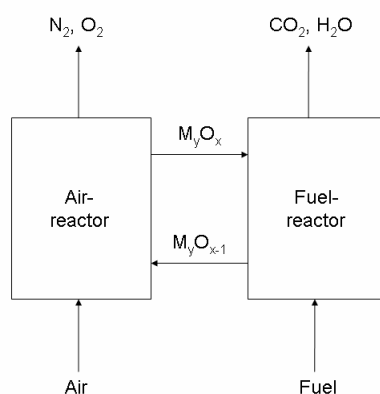


Figure 3.1.1 Chemical-looping combustion

In the current project the fuel in reaction (3.1) is syngas produced from coal gasification. Coal gasification is a well established technology for the production of synthesis gas. It is likely that the reactors shown in Figure 3.1 will be designed using interconnected fluidized beds, although alternative designs are possible. (Lyngfelt et al., 2001)

3.1.2.1 Oxygen carriers

One crucial issue for a CLC system of interconnected fluidized beds is finding suitable oxygen carrier particles. It is important that an oxygen carrier has a combination of good thermal properties, high rates of reaction under alternating reducing and oxidizing conditions and high mechanical and chemical stability for thousands of cycles in a fluidized bed system. It is of key importance that oxygen carriers are found that fulfill these criteria. In the end, the production cost in combination with the lifetime of the oxygen carriers will be an important factor when comparing costs of chemical-looping combustion to that of other separation techniques.

Prior to this project, most of the investigations of oxygen carriers have been carried out using CH₄ or H₂ as the fuel with focus on oxides of the metals Fe, Ni and Co. (e.g. Ishida and Jin, 1994; Jin et al., 1998; Mattisson et al. 2000). Only Copeland et al. had investigated some iron and nickel based oxides using syngas. (Copeland et al., 2001, 2002) Since inception of the project there have been a considerable amount of papers published on the performance of oxygen carriers, see Cho, 2004 and Johansson, 2005a for a review of these investigations.

3.1.2.2 Reactor design

For chemical-looping combustion two inter-connected reactors are needed. Various systems of interconnected fluidized beds are in actual use for various applications or have been proposed in the literature. (Johansson, 2005b) When this project started the CLC process had never been demonstrated in actual practice, it was entirely a paper concept. However, during this project, two CLC combustors have been constructed and operated in addition to the one presented here. A 10 kW chemical-looping combustor was built and tested at Chalmers University of Technology, (Lyngfelt et al. 2004; Lyngfelt and Thunman 2005). The design was similar to that of a circulating fluidized bed boiler, with the important difference that the

fluidized bed heat exchanger in the CFB is exchanged for a fuel reactor and that an additional particle seal is added. Further, a 50 kW CLC unit was demonstrated at Korea Institute of Energy Research (Ryu et al. 2004). In the 10 kW combustor at Chalmers, an oxygen-carrier based on nickel oxide was operated for 100 h with natural gas as fuel. A fuel conversion efficiency of 99.5% was achieved, and no carbon dioxide escaped to the air reactor. Only small losses of fines were observed. The 50 kW combustor was operated with methane as fuel, and two types of oxygen-carriers. A nickel oxide oxygen-carrier was tested during 3.5 h and a cobalt oxide was tested during 25 h. For the nickel oxide oxygen-carrier, the concentration based on dry flue gases of CO₂ leaving the fuel reactor was 98% and for cobalt oxide 97%. No combustion of syngas in CLC prototypes has been reported in the literature.

3.1.3 Methodology

3.1.3.1 Development of oxygen carrier particles

In the CLC system an oxygen carrier is used to transport the oxygen and the heat from the oxidation reactor to the fuel reactor. The objective of this task was to develop an oxygen carrier with enough reduction and oxidation rates, resistant to the attrition and with high durability, maintaining the chemical, structural and mechanical properties in a high number of reduction-oxidation cycles.

Thermal aspects of oxygen carriers

It is paramount to the success of the process that the oxygen carrier can fully convert the fuel gas, i.e. CO and H₂ to CO₂ and H₂O respectively. Table 3.1.1 shows the equilibrium degree of gas yield, γ , for CO, H₂ and CH₄ for 800 and 1000°C. A gas yield lower than 1 would mean that some combustible gases would remain in the outlet from the fuel reactor. Also included in the table is the yield with respect to the heating value of the incoming fuel. Clearly, there are systems based on Fe, Cu and Mn which have complete conversion, although Fe and Mn both have some metal oxides which have low conversions of the gas. NiO has a rather high gas yield at both temperatures, although some H₂ and CO would always remain at the outlet.

Table 3.1.1 Gas yield of different fuels for different oxygen carriers. Taken from Jerndal et al., 2005.

	γ_{heat}		γ_{CH4}		γ_{CO}		γ_{H2}	
	800°C	1000°C	800°C	1000°C	800°C	1000°C	800°C	1000°C
NiO/Ni	0.9949	0.9917	0.9949	0.9883	0.9949	0.9883	0.9946	0.9931
CuO/Cu	1.0000	1.0000	1.0000	1.0000	1.0000	1.0000	1.0000	1.0000
Cu ₂ O/Cu	1.0000	0.9999	1.0000	0.9999	1.0000	0.9999	1.0000	0.9999
Fe ₂ O ₃ /Fe ₃ O ₄	1.0000	1.0000	1.0000	1.0000	1.0000	1.0000	1.0000	1.0000
Fe ₃ O ₄ /Fe _{0.945} O	0.5529	0.7579	0.5406	0.6820	0.5408	0.6820	0.5264	0.7841
Mn ₂ O ₃ /Mn ₃ O ₄	1.0000	1.0000	1.0000	1.0000	1.0000	1.0000	1.0000	1.0000
Mn ₃ O ₄ /MnO	1.0000	0.9999	1.0000	0.9999	1.0000	0.9999	1.0000	0.9999
MnO/Mn	0.0020	0.0206	0.0000	0.0000	0.0000	0.0000	0.0000	0.0000
Co ₃ O ₄ /CoO	1.0000	1.0000	1.0000	1.0000	1.0000	1.0000	1.0000	1.0000
CoO/Co	0.9695	0.9496	0.9691	0.9299	0.9691	0.9299	0.9674	0.9574

Oxygen carrier preparation

As shown above, the metals Cu, Ni, Fe and Mn have oxide systems which could be used for oxygen transport. Usually the active oxygen carrier needs to be combined with an inert to supply a convenient mechanical strength to the samples and to improve the reactivity of the materials. For the preliminary selection of the suitable materials to be used in a CLC process, CSIC and Chalmers prepared approximately 300 different types of oxygen carriers using three different types of preparation method: extrudation, impregnation and freeze granulation.

At CSIC particles were prepared by mechanical mixing and extrusion of a large number of oxygen carriers (~240 samples), corresponding to all possible combinations of metal oxides (CuO, Fe₂O₃, MnO₂, and NiO) and inerts (Al₂O₃, sepiolite, SiO₂, TiO₂, and ZrO₂), in three different MeO/inert weight ratios (80/20, 60/40, and 40/60), and calcined at four temperatures from 950 to 1300 °C. The particles produced are summarized in the annex, see Table A.1.1.1. Moreover, several Cu-based oxygen carriers were prepared by impregnation to analyze, and finally avoid, the agglomeration problems detected in the copper containing materials.

At Chalmers oxygen carriers based on Fe, Ni and Mn were produced by freeze granulation, and the procedure is described in detail in the Annex. The formulations were based on the more promising carriers found during screening at CSIC. The particles produced are summarized in the annex, see Table A.1.2.1.

Reactivity testing of oxygen carriers

In the screening phase of the project tests were carried out in a TGA (CSIC) and a fluidized bed reactor (Chalmers, CSIC). Both methods are suitable and complementary for obtaining reactivity data for gas-solid reactions. Whereas the reactivity is obtained under well defined gaseous concentrations in the TGA, fluidized bed test simulate a CLC system better. With the latter method it is also possible to measure the gaseous products and see possible side reactions. In addition to determining the rates of reaction of the oxygen carrier, physical characterization was also performed with respect to crushing strength, porosity, phase composition and morphology. Please see the annex for a detailed description of the experimental procedure and data evaluation.

3.1.3.2 Reactor design and fluidizing conditions

The design of the reactor system is important for a CLC system. At the Institute of Chemical Engineering at Vienna University of Technology, the effects of reactor design, solid properties and fluidisation conditions on the fluid dynamics (solids circulation rate, gas leakage) of CLC reactor designs were investigated. To this end, three reactor concepts, differing in scale and operating conditions, were designed and tested experimentally by means of scale models operated at ambient temperatures. One of the units was then optimized and constructed as a hot prototype CLC reactor at Chalmers.

The relationships of the operating parameters obtained from experimental work were integrated into mathematical models. Thus, the reactor system characteristics could be made independent of size and reliable scale-up tools for future chemical-looping combustion plants are available.

3.1.3.3 Hot chemical-looping combustor prototype

From the results of the fluidization investigations carried out in the first cold model, a hot laboratory size continuously operated reactor system was designed, built and operated, see Figure 3.1.2. This system was designed for an input power between 100 and 300 W, using syngas as the fuel. The relatively low inventory of oxygen carrier needed in this unit made it feasible for testing of different types of oxygen-carrier. The actual total solids inventory depends upon the density of the oxygen carrier, but was approximately 300 g for particles investigated in this work. Three particles based on Ni, Fe and Mn, selected from the screening phase of the project were tested as oxygen carriers.

3.1.4 Results

3.1.4.1 Oxygen carrier selection

In the screening phase of the project CSIC and Chalmers tested approximately 300 types of oxygen carriers in with respect to parameters which are important for CLC, most importantly reactivity under alternating oxidizing and reducing conditions and mechanical strength. Some oxygen carriers were found to be unsuitable even before testing, due to low melting points, formation of irreversible phases and inability to obtain granules from the powders. Below follows a brief summary of the results with the extrudated particles prepared and tested at CSIC and the freeze granulated sample prepared and tested at Chalmers.

Particles based on extrusion and impregnation (CSIC)

Table A.1.1.5 shows the selection of the best candidates produced by mechanical mixing and extrusion (about 77 samples). For the most promising material, tests with 100 reduction/oxidation cycles were carried out in the TGA with the 10 most promising candidates produced by extrusion and Cu-based materials produced by impregnation. With respect to the Cu impregnated oxygen carriers, these materials exhibited high reactivity, excellent chemical stability, small attrition rates, and it is possible to avoid the agglomeration during fluidized bed operation, which is the main reason adduced in the literature to reject this type of oxygen carriers. Moreover, the operation temperature is limited to 900 °C due to the low melting point of the Cu. The reactivity tests consider the problems arising from the structural changes produced in the particles because of the successive reduction and oxidation reactions of the metal oxide present in the carrier. To finally improve the screening it was necessary to know the behaviour of the carriers during successive reduction/oxidation cycles in a fluidized bed, which considers both the structural changes because of the chemical reaction, and the attrition phenomena existing in a fluidized bed, as well as the possible agglomeration of the solids. This was done in the installation showed in Figure A.1.1.6 of the annex. The attrition rates were high in the first 5 cycles due to the rounding effects on the particles and to the fines stuck to the particles during preparation and crushing/sieving. Later, the attrition rates due to the internal changes produced in the particles by the successive reduction and oxidation processes, decreased. It must be remarked that the particles prepared by impregnation exhibited very low attrition rates with values about 0.01%/cycle (< 0.02%/h in our tests) or even lower for some oxygen carriers. Assuming this value as a measure of the steady-state attrition of the carrier particles, this led to a lifetime of the particles of 10000 cycles (5000 h in CSIC tests).

Particles based on freeze granulation (Chalmers)

When comparing all oxygen carriers which were produced by freeze granulation it becomes clear that the nickel oxides are by far the most reactive ones. This can be seen in A.1.2.6 where all investigated particles are displayed in one graph as rate index vs. crushing strength. The rate index is an average normalized rate of reaction which gives a simple way of comparing the reactivity of oxygen carriers. The iron oxides are in general the hardest but not very reactive, whereas the manganese based carriers seem to be somewhere in-between nickel and iron in strength and reactivity. In general, de-fluidization mainly seems to concern manganese based oxygen carriers. It was possible to find freeze granulated particles based on Fe, Ni and Mn which could be suitable as oxygen carriers in a real CLC process. These showed a combination of high reactivity, good fluidization, high strength and limited or no particle breakage during reaction.

Selected particles for further testing

A vast number of oxygen carriers were tested at CSIC and Chalmers using three different type of preparation methods. Particles of all investigated transition state metals Fe, Cu, Ni and Mn were found which could feasible be used as oxygen carriers. More specifically the following particles were selected and tested further:

1. 10 wt% CuO on Al₂O₃ prepared by impregnation (C1A-I)
2. 60% Fe₂O₃ with Al₂O₃ prepared by freeze granulation (F6A-FG)
3. 40% NiO with Al₂O₃ prepared by freeze granulation (N4A-FG)
4. 60% NiO with MgAl₂O₄ prepared by freeze granulation (N6AM-FG)
5. 40% Mn₃O₄ with ZrO₂ (doped with Mg) (M4MZ-FG)

3.1.4.2 Detailed reactivity of selected oxygen carrier particles

After the selection of the most feasible oxygen carriers, a detailed reactivity of these materials was carried out to determine their behaviour during the reduction with CO and H₂, and oxidation reactions at different operating conditions. All of the above selected carriers were tested in the TGA at CSIC, and kinetic parameters necessary for the design of a CLC system was determined for some of these particles.

Kinetic parameters from TGA experiments

The kinetics of the reduction and oxidation reactions of the three oxygen carriers based on Ni, Cu and Fe (Particles 1-3 above) were determined by thermogravimetric analysis at atmospheric pressure in a thermobalance (CI Electronics Ltd.) at temperatures from 723 K to 1223 K. The composition of the gas during metal oxide reduction was varied to cover the majority of the gas concentrations present in the fluidized-bed fuel reactor of a CLC system (fuel, 5-70 vol %; H₂O, 0-48 vol %; CO₂, 0-40 vol %). For the oxidation reaction, oxygen concentrations from 5 to 21 vol % were used.

It was found that the three oxygen carriers exhibited high reactivities in the majority of the conditions and could be used in a CLC plant.

The use of the changing grain size model (CGSM) (see Table A.2.1.2 for equations) together with the experimental data allowed us to obtain the kinetic parameters corresponding to the different reactions for the several oxygen carriers (see Table A.2.1.3). The reaction rates were normally fitted assuming kinetic control, with the only exception of the NiO reduction with H₂, where an additional diffusion resistance was used. The effect of temperature was low in all cases, with the activation energies values varying from 14 to 33 kJ mol⁻¹ for the reduction, and from 7 to 15 kJ mol⁻¹ for the oxidation. The reaction order depended on the reaction and oxygen carrier considered, and values from 0.25 to 1 were found. No effect of the gas products (H₂O or CO₂) on the reduction reaction rates was detected.

The reactivity of the two additional samples which showed good behavior at Chalmers was performed. These corresponds to the samples N6AM-FG, i.e. 60 wt% NiO and MgAl₂O₄ (sintered at 1300, 1400, and 1500 °C), and M4MZ-FG, i.e. 60 wt% Mn₃O₄ and Mg-ZrO₂ (sintered at 1100, 1150, and 1200 °C), and for several particle sizes (0.09-0.125, 0.125-0.18, 0.18-0.25 mm). Figures A.2.1.14 and A.2.1.15 shows the conversion versus time curves obtained during the reduction and oxidation in the TG. The reduction was carried out with H₂ (40 vol%) or CO/CO₂ (40/10 vol%), and the oxidation was carried out with air. The reactivity of the oxygen carrier NiO/MgAl₂O₄ depended on the sintering temperature and on the gas used for the reduction. A higher sintering temperature produced a lower reduction and oxidation reaction rate, decreasing a lot for the highest sintering temperature (1500 °C). On the other hand, the reaction rate of the reduction with H₂ was higher than the reduction with CO. The particle size did not affect the reactions.

The reaction rate of the Mn-based oxygen carrier was very high and it was not affected by the particle size or by the sintering temperature.

Investigation of selected samples in a fluidized bed reactor

Three types of carriers based on Fe, Ni and Mn (selected particles 2,4 and 5 above) were also tested in the fluidized bed at Chalmers using syngas, and for comparison methane. The reactivity with syngas was investigated for different temperatures in the range 650-950°C. All of the particles were highly reactive. Fig. A.2.2.7 shows the gas yield of CO to CO₂, γ_{CO} , for the three investigated oxygen carriers. Manganese showed no difference in reactivity as a function of temperature, for iron small differences were found, but still a high gas yield was achieved independent of the temperature. For Ni however, there was a clear decrease in reactivity at lower degrees of conversion, see Figure. A.2.2.7c. Thus one implication of these results are that when using syngas as fuel it is likely that the cheaper, more environmentally sound Mn and Fe likely are much better candidates compared to Ni. On the other hand, when using natural gas, Ni seems to have much higher reactivity.

Effect of total pressure

To analyse the effect of total pressure on the behaviour of the oxygen carriers, some experimental work was carried out in a pressurised Cahn TG-2151 thermobalance (see Figure A.2.1.7) at 1073 K and pressures up to 30 atm. Figure A.2.1.9 shows, as an example, the results obtained during the reduction of the Cu-based oxygen carrier. Both the experiments carried out with a constant molar fraction (10 vol %) of reducing gas, CO or H₂, and the carried out with a constant partial pressure (P_p=1 atm) showed a decrease of the reaction rate

with the increasing pressure. This negative effect of pressure has been also observed by other authors in several gas-solid reactions (Agnihotri et al., 1999; Qiu et al., 2001; Adánez et al., 2004a; García-Labiano et al., 2004b).

Therefore, the use of CGSM and the kinetic parameters obtained at atmospheric pressure together were unable to predict the experimental results obtained at higher pressures. The most probably reason of the pressure effect was the changes suffered by the oxygen carriers in their internal structure during pressure operation (Chauk et al., 2000). To know the magnitude of the effect of total pressure on the decrease of the reaction rates, an empirical fit was done (see Figure A2.1.11). The value of the preexponential factor at pressurized conditions, $k_{0,p}$, which best fit the experimental data considering the gas dispersion was obtained for each oxygen carrier and reaction. In the majority of the cases, a sharp decrease in the value of $k_{0,p}$ was observed when the pressure changed from 1 to 5 atm, with a smoother decrease for increasing pressures. For some reactions the decrease was softer, although in any case the values of $k_{0,p}$ at 30 atm were between 5 and 95 times lower than at atmospheric pressure.

Table A.2.1.3 shows the values of the parameter "d" obtained for the different oxygen carriers and reacting gas. In this way it was possible to predict the experimental results, showed as continuous lines in Figure A.2.1.10, within the range of total pressures used and when the molar fraction or the partial pressure of the reacting gas was maintained constant.

Application of reactivity to design criteria.

The kinetic data obtained at atmospheric pressure were used to calculate some design parameters of a CLC system, as the recirculation rate and the total solid inventory (García-Labiano et al., 2004b). The recirculation rate of oxygen carrier can be calculated from a mass balance in the fuel reactor, and it mainly depends on the conversion variation obtained in the oxygen carrier in the fuel and air reactors. The recirculation flow when $\Delta X_s=0.3$ were ~12 kg/sMW, ~15 kg/sMW, and ~3 kg/sMW for the oxygen carriers C1A-I, F6A-FG, and N4A-FG, respectively. See Annex 2.1 for details of these calculations.

The solids inventory for a given oxygen carrier depends on the recirculation rate and on the solid conversion at the inlet to each reactor, as well as on their metal oxide content and reactivity. Considering as reference 1 MW_f, and that the reactions between the gas fuel and air with the oxygen carrier take place in a bubbling fluidized beds (fuel reactor) or in the dense zone at the bottom of the riser (air reactor). Further, perfect mixing of the solids, gas plug flow in the beds, no resistance to the gas exchange between the bubble and emulsion phases, and complete conversion of the gas fuel were assumed. The solid inventories using syngas as fuel varied from 25 kg to 88 kg of oxygen carrier. The lowest solid inventories of oxygen carrier corresponded to the N4A-FG because the NiO presents a high oxygen transport capacity and the oxygen carrier has a high NiO content (40 wt%). The F6A-FG presents higher values due to the lower oxygen transport capacity of the Fe₂O₃ (to Fe₃O₄). The higher inventories corresponds to the C1A-I because, although the CuO can transport a lot of oxygen, the oxygen carrier present a low active metal oxide content (10 wt%). However, the values of solids inventories are low and the three oxygen carriers could be used in a CLC system. It must be remembered however that these values correspond to preliminary data, where the resistance to the gas exchange between the bubble and emulsion phases, which can be important in a fluidized bed, has been ignored.

3.1.4.3 Reactor design and fluidizing conditions

From previous research arose a need to study different oxygen carrier particles in continuous operation. The purpose of the first CLC reactor design at laboratory scale was therefore to develop a small CLC laboratory reactor to be used for i) the study of the process, and ii) testing of different oxygen carriers. The unit is characterised by a simple design and a small bed inventory. The design chosen for this CLC system is a two-compartment fluidised bed having a thermal power range of 100 – 300W_{th} for the original reactor. The reactor (Figure 3.1.2) consists of two adjacent fluidised beds divided by a vertical wall with two orifices. At one side the air reactor, (AR), has a higher velocity causing particles to be transported upwards, and some of them fall into the downcomer, (D), that has a bottom opening leading to the fuel reactor, (FR). The slot in the bottom of the wall between the two reactors allows particles to move through this slot from the fuel reactor to the air reactor. The solids separation from the flue gas streams is realised by an increase of the cross section at the top of the reactors.

Four different design variations were designed, constructed, and tested with respect to the solids flow and the gas leakage. A final design, optimized in terms of solids flow and gas mixing, was constructed and put into hot operation and tested with different oxygen carrier particles, see below.

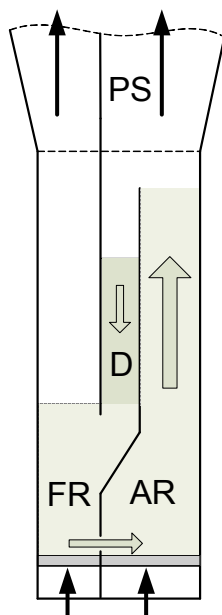


Figure 3.1.2. Laboratory CLC reactor (D) downcomer, (PS) particle separators

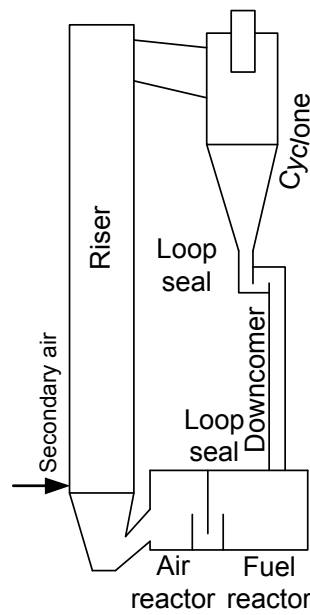


Figure 3.1.3. CLC Atmospheric demonstrator

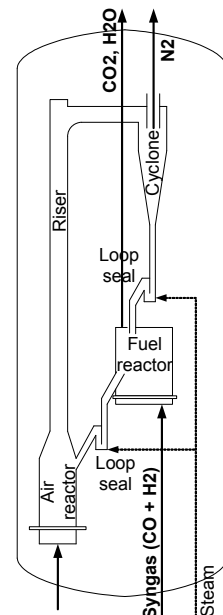


Figure 3.1.4. PCLC combustor

The second unit models a CLC pre-demonstration unit, following a “close to real system” approach, it was developed and downscaled by applying common scaling criteria for fluidized

bed reactors. Aspects of interest of this work were effects of design particularities and operating parameters in view of reaction engineering aspects that are critical for chemical-looping combustion performance at large scale. The design includes features specific for a large scale CFB unit and required for optimum performance of the CLC process like air staging for better control of the solids circulation rate and advanced loop seal designs for prevention of gas mixing between the two reactors (Figure 3.1.3).

In an extensive experimental programme it could be seen that solids circulation is sufficient and can be controlled efficiently and the gas leakage is very low.

A mathematical model of the riser and each CFB component was set up. Analysis showed that the model is suitable for prediction of operational behaviour of the unit. The operational stability of the system also in off- design operation could be demonstrated. The mathematical model of the fluid dynamics is an excellent scale-up tool for assistance of design of a future demonstration plant.

The third CLC reactor design forms the basis for future employment of CLC for coal combustion power plants featuring combined cycle power processes. This shall allow a significant increase of the energy efficiency but numerous aspects need to be studied before this can be realised. The present study focused on the fluid dynamics and the basic design of a pressurized CLC demonstration plant.

To this end, a flow model, based on a pressurized CLC of interconnected fluidized beds was designed and tested. The unit represents a 60kW_{th} bench scale reactor and experimental tests correspond to three different pressure levels, i.e. 1bar, 4.1bar, and 10 bar. In addition the



Figure 3.1.5. The CLC prototype reactor.

experimental work allowed a mathematical description of the effects of pressurised conditions on the fluid dynamics of CFB CLC systems. It was shown that the proposed design (Figure 3.1.4) is suitable for PCLC, which can be realised in a future CLC development project.

3.1.4.4 Hot prototype CLC reactor

From the results of the fluidization investigations carried out in the first cold model, i.e. Figure 3.1.2, a hot laboratory size continuously operated reactor system was designed, built and operated, see Figure 3.1.5. This system was designed for an input power between 100

and 300 W, using syngas as the fuel. The relatively low inventory of oxygen carrier needed in this unit made it feasible for testing of different types of oxygen-carrier. From the extensive work devoted to screening for oxygen carriers at CSIC and Chalmers, three particles based on Ni, Fe and Mn, were selected and tested in the the unit: i) 60% Fe₂O₃ with Al₂O₃ (F6A-FG), ii) 60% NiO with MgAl₂O₄ (N6AM-FG) and 40% Mn₃O₄ with ZrO₂ (doped with Mg) (M4MZ-FG). All oxygen carriers had a high conversion of the fuel with small amounts of unburnt from the fuel reactor. This can be seen in Figure 3.1.6 where the outlet gas fractions are shown as a function of the velocity in the air and fuel reactor. Clearly there is almost only carbon dioxide from the outlet of the reactor for all of the oxygen carriers. For many of the tests with NiO, equilibrium is reached and combustion efficiency was 0.994 at 850 °C. For Mn₃O₄, the CO and H₂ concentrations were below the detection level of the gas analyzer. The Fe-based oxygen carrier also showed high conversion of the fuel with a combustion efficiency

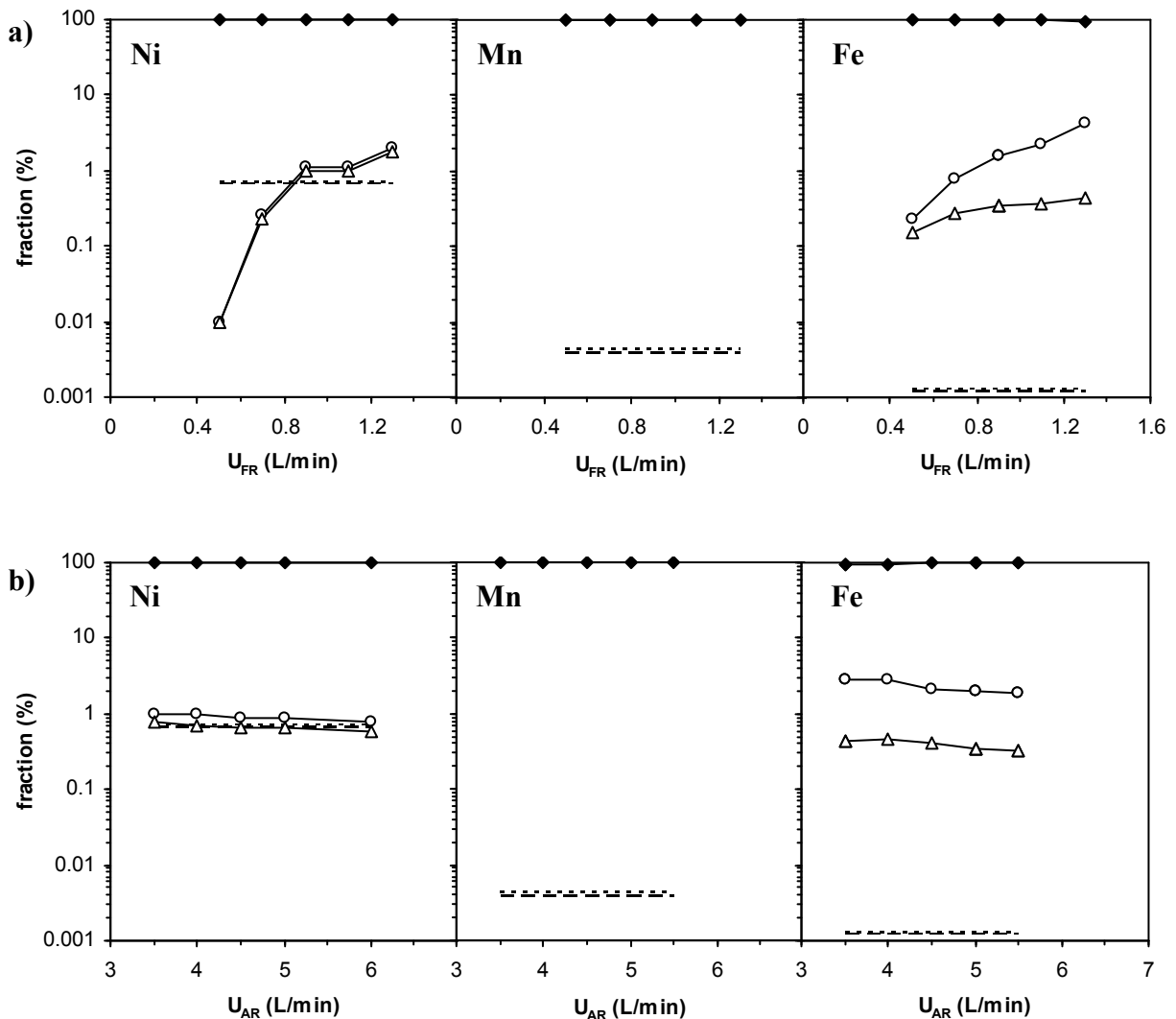


Figure 3.1.6. The fraction of CH₄, CO, H₂ and CO₂ in the combustion products of syngas as a function of a) the flow in the fuel reactor, b) the flow in the air reactor. Symbols: —○— CO; —△— H₂; —◆— CO₂; CO at equilibrium; — — H₂ at equilibrium.

of 0.988 at 850 °C. The investigated particles have been fluidized with recirculation in hot conditions for approximately 150 h for the Ni particles, 130 h for the Mn and 60 h for the Fe based particles without any signs of deactivation and very little attrition.

3.2 Lime Carbonation Calcination Cycles (LCCC)

The following pages include the description of the research conducted in the part of the project concerned with the Lime Carbonation Calcination Cycles (LCCC). As with the CLC part, the discussion is closely link to the Technical Annexes A, that provides a more detail presentation of the work of each partner in the different nine Tasks in which the Technical Annex of the project was divided. Here, a more integrated description of the work is carried out, with continuous references to the Annexes. First and introduction provides an overview of what was the state of the art and the key issues to be solved when the project started. Second, the experimental facilities used in the project, the experimental methodology and significance in the context of the different tasks is presented. Finally, the main results from this project are summarised (details in the Annex A). We have organised this part of the Report as an overview paper of the systems investigated, and not as a task by task description of the work (that is followed in previous Progress Reports and in Annex A). The Annexes are therefore an essential part of this part of the Final Report, but we provide in the following pages a sufficiently detail description of the key issues and results.

3.2.1 Introduction

The separation of a CO₂ pure stream, combined with a well managed geological storage site is already gaining momentum as a major mitigation option for climate change using existing technologies. It is generally accepted that the cost associated with the separation of CO₂ from flue gases introduces the largest economic penalty in carbon capture and storage. If the target in the capture system is the separation of CO₂ from a flue gas (post combustion), the main commercially available technology to separate CO₂ is based on amine-based absorption systems. This technology, however, introduces severe efficiency penalties (because the large energy demand for regeneration, that cannot be effectively recovered) and added costs. This justifies the investigation of emerging approaches that seek to be more energy efficient and cost-effective than low-temperature absorption-based systems.

Of the different approaches to separate gases from a gas stream several are based on the use of regenerable solid sorbents. The basic separation principle is depicted in Figure 3.2.1.

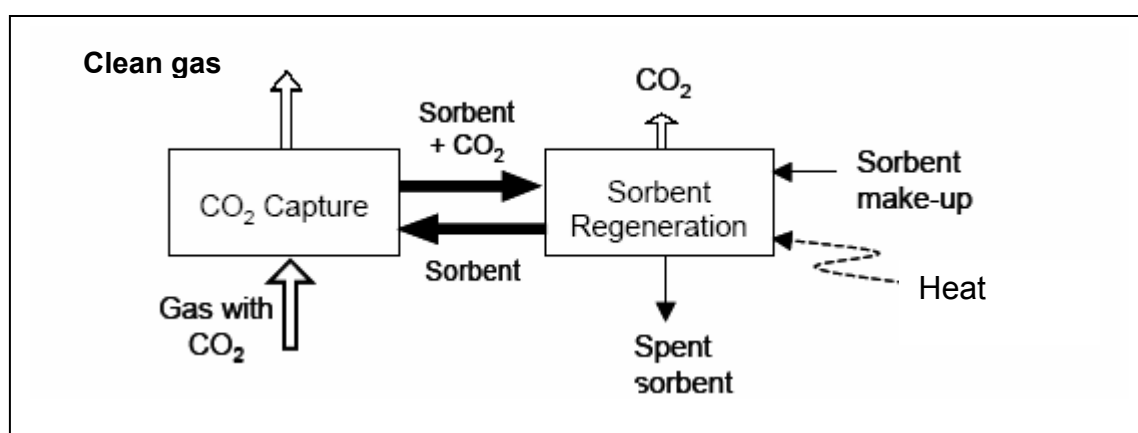


Figure 3.2.1. Scheme of a sorption-desorption CO₂ capture system.

The separation in these systems is achieved by putting in intimate contact the gas containing the CO₂ with a solid sorbent that is capable of capturing the CO₂. The sorbent with the captured CO₂ is transported to a different vessel, where it releases the CO₂ (regeneration). The sorbent resulting after the regeneration step is sent back to capture more CO₂ in a cyclic process. One common characteristic for all these CO₂ capture systems is that the flow of sorbent between the vessels of Figure 3.2.1 is of very large scale, because it has to match the huge flow of CO₂ being processed in a large power plant. When the sorbent is a solid, fluidised beds are therefore ideal contacting devices for these systems, that require large circulation rates of solids. Another common characteristic of these systems is that the energy required for sorbent regeneration can be high (depending on the nature of the bond sorbent-CO₂) and may translate into an important efficiency penalty (specially if regeneration is conducted at moderate temperatures, at which energy cannot be efficiently recovered). Finally, good sorbent performance under high CO₂ loading in repetitive cycles is obviously a necessary condition in these CO₂ capture systems. A makeup flow of fresh sorbent is always required to compensate for the natural decay of activity and/or sorbent losses. In systems using expensive sorbent materials there is always a danger of escalating cost related to the purchase of the sorbent and the disposal of sorbent residues.

There have been many works, tracing back to the XIX century (see references at Annex A, Task 5), exploring the use of CaO as regenerable sorbent in Figure 3.2.1. But all these works were concerned with gasification atmospheres (aiming at improving the heat content of the gasification gas) and released a flue gas on regeneration diluted again in CO₂ (therefore, not suitable for permanent storage). For combustion based systems, and for CO₂ capture purposes, this project has been a key piece of pioneering work to put the lime carbonation calcination cycles in the portfolio of emerging concepts for CO₂ capture. There are now several groups in the world, inside and outside Europe, including some major companies, pursuing a range of concepts for CO₂ capture in pre and postcombustion systems using the CaO/CaCO₃ system. Some of the options being considered have been developed in this project for the first time (those avoiding the use of oxyfiring to provide heat for regeneration, those where a reduction in the calcination temperature is achieved using steam and/or low pressure in the calciner and those aiming at in-duct sorbent injection).

Our approach in this project was to focus on combustion systems only. We structured the project in several tasks to fill what was regarded as key gaps in knowledge when the project was written in year 2000:

Task 5: Sorbent behaviour in multicycle operation, at the characteristic conditions expected in the different system units (combustor, carbonator and calciner/regenerator).

Task 6: Pilot plant evaluation of the CO₂ separation concept, investigating individual units (circulating fluidised bed vs entrained bed carbonator).

Task 7. Pilot testing and design specifications of the calciner. This includes the investigation of entrained bed calcination (in flame) and the fundamental aspects of new fluidised bed calciner designs (indirect heat transfer)

Task 8. Development of basic reactor simulation tools for the main units (in particular for the CO₂ absorber).

Task 9. Integration of components and estimation of overall power generation efficiencies in the different options.

Task 10 Economical assessment of the proposed CO₂ separation technologies, comparing their critical new features with existing and emerging alternatives for CO₂ capture.

The gaps in knowledge to carry out with confidence the last three tasks, were filled with an experimental programme, that made use of a range of facilities in the different institutions involved in the LCCC part of the project (CSIC, Cranfield, VTT and later CANMET of Canada, thanks to a close and ongoing scientific collaboration with CSIC on this subject). These experimental facilities and procedures are reviewed first in the next section.

3.2.2 Experimental systems and procedures

3.2.2.1 Multicycle test termobalance and fixed bed apparatus

Two laboratory test rigs for sorbent multicycle testing were built to adapt well known techniques (thermogravimetric analysis and small fixed bed reactor) to the special characteristics of the tests to be conducted in the project: rapid change in temperature around the sample (moving two ovens around the sample with a pneumatic system), long duration experiments (up to 500 cycles with 40 minute duration each cycle), changing atmospheres (CO₂, SO₂ and steam in air). As detailed in Annex A-Task5, the fixed bed apparatus was also used to allow detail textural studies (by SEM and Hg porosimetry) of the evolution of selected samples along cycling. The data obtained in these rigs was shown to be consistent with sorbent performance results measured in large pilot test carried out for the Acceptor Gasification Process (see A-Task 5) and also with pilot results described in A-Task 7. Therefore, the main information used in subsequent tasks to anticipate the performance of the sorbent (capture capacity along cycling and reactivity) in the full system was obtained from these two pieces of equipment.

3.2.2.2 In duct test rig

A laboratory scale entrained flow reactor was designed and constructed in order to study the carbonation process in the entrained mode. The reaction zone consists of a coiled tube of 6 m which gives reasonable flexibility in terms of gas/solid contact time. This tube is immersed in a fluidized bed in order to control the temperature. Lime is injected with particle sizes less than 100 µm. Different mixtures of air and CO₂ can be used in this reactor to modify particle residence time and CO₂ partial pressure. The reacted gas/solid stream is cooled down to stop the carbonation reaction using a coiled pipe immersed in a water bath. This system is equipped with two sampling ports to measure CO₂ concentrations, and with two filters to take particle samples. This device was used in this project to study the effect of the temperature, particle residence time and the CaO/CO₂ ratio in the entrained carbonation process.

3.2.2.3 Pilot carbonator

An existing pilot scale combustion facility located at the Cranfield University was modified to allow the in-duct injection of sorbent particles. This device is composed of two combustion units, a bubbling fluidized bed combustor and a pulverized coal combustor. This plant has a total combined output of 150 kW (see Annex-Task 6). During the test developed for this project anthracite was burned in the fluidized bed and the pulverized combustor unit was used a carbonator. The aim of this test was to study the viability of CO₂ capture using lime in a real combustion environment.

3.2.2.4 VTT's Circulating Fluidised Bed (CFB) as a pilot carbonator

VTT has a CFB reactor that consists of an air/water-cooled ceramic chamber enclosing a fluidised bed (See A-Task 6.1). The reactor is used to study combustion behaviour of different fuels, deposit formation, formation of pollutants and ash behaviour under CFB conditions. Desired temperature in the reactor can be maintained with electrical heaters, cooling system and by staging air feed. The amount of primary- and secondary air fed from three levels is controlled and measured by thermal mass flow meters. Riser height of the reactor is eight meters, ensuring a sufficient residence time for combustion also at high flue gas velocities. Sampling ports at different locations enable the determination of combustion profile as a function of residence time. Samples of solid material can be taken for analysing their quality and particle size. Particulate matter is separated from flue gases in the primary and secondary cyclones and in a fabric filter. Main characteristics of the reactor are:

- fuel input 50 kW on an energy basis
- riser height 8 m, diameter 167 mm
- option for fuel feed with two separate feeding lines
- fuel additive feed through a separate feeding line
- gas and solids sampling at different locations along the riser
- fly ash sampling after both cyclones

3.2.2.5 Calcination in flame

An entrained calciner was designed and built at Cranfield University (see Annex-Task 7). This reactor has a reaction chamber with a length of 0.50 m and a diameter of 0.10 m. Fresh limestone with different particle sizes can be fed to the reactor. Particles are heated by means of a CH₄/O₂ flame. Gases and particles are cooled down using a gas flow of N₂ at the end of the reaction zone. Particles are removed using a cyclone. Lime produce under these experimental conditions is expected to develop an higher surface area and reactivity. Different temperatures and CO₂ partial pressures can be adjusted in this rig in order to study its effect on calcination process.

3.2.2.6 Lateral mixing in adjacent fluidized bed calciner-combustor

A test rig was built to obtain fundamental design parameters of fluidised bed systems arranged to transfer heat from the combustion chamber to the calciner and drive the calcination reaction of the sorbent (see Figure A.7.1.1 and Annex-Task7). This was a fluidised bed cold model resembling the geometry of two narrow fluidised beds (the calciner and the combustor). The bed was contained between a front-facing transparent window and a metallic back-plate, and was 1.5 m long, 2 m tall. The bed material was limestone particles coated with a phosphor material that allowed the tracking of the solids in mixing experiments and the determination of the key transport properties to estimate heat transfer in the combustor-calciner system (see Annex A-Task 7).

3.2.3 Discussion

3.2.3.1 Sorbent performance in the LCCC system

The discussion of sorbent performance must be linked to the specific requirements for the sorbent in the different system options investigated in this project. There are two main

categories of contact devices considered for the carbonator and calciner reactor: fluidised beds and entrained bed reactors. We focus the discussion that follows in the carbonation reaction only. From the perspective of the sorbent, these two reactors have quite different requirements for sorbent performance: in the case of entrained bed reactors (like the carbonator for “in-duct” sorbent injection) the gas solid contact times are expected to be very short (several seconds) and solids are highly diluted in a gas stream. In these conditions, highly reactive solids are required. In the case of dense fluidised beds, the rate of reaction is also important, but not so critical from a point of sufficiently high rate. The particles of sorbent are usually allowed to convert to their maximum conversion capacity (residence time of several minutes, are possible, see Figure A.5.1.12). Unfortunately, this maximum conversion is not 100% in the carbonation reaction. This decays with the number of cycles and can reach very low values (< 5%) in highly sintered and or highly cycled samples. This maximum conversion achievable by the sorbent under normal reaction conditions (flue gas composition and temperatures) and times (a few minutes) in the fluidized bed carbonators, has been the main subject of investigation in this project, because it determines all the key design parameters of the system: solid flows, reactor volumes, CO₂ capture efficiencies, make up and purge flows etc.

We have investigated in detail the evolution of the maximum carbonation of the sorbents along cycling, in a wide range of experimental conditions (see Table A.5.1.1 in Annex A). The experimental work has generated a database of several thousand of thermograms, several hundred fixed bed cycles of carbonation-calcination and associated samples for textural studies. The emerging picture from all these studies is that there is an striking similarity in the decay curves along cycling despite the large differences in sorbent characteristics, particle sizes, reactor characteristics, reaction conditions and calcination and carbonation times in the original experiments (see Table A.5.1.2). In fresh calcines, the CaO is arranged in small (~100 nm breadth, variable length) parallel rods, which leave in between a network of quasi-cylindrical pores. When this material is submitted to recarbonation conditions, the microgranular structure of the grains is lost in an apparently dense groundmass (see Figure A.5.1.3). The voids of the calcines become wider as the number of cycles increase. In the large voids, the limiting factor for further reaction is not the lack of void space but the rapid increase in the resistance to gas diffusion through the product layer. Figure A.5.1.4 summarizes the mechanism of recarbonation discussed in the previous paragraphs. Other second order effects and deactivation mechanism (pore size and shape effects, including pore plugging, particle shrinking and irreversible loss of void space in the calcines) are also present under some conditions (see Figure A.5.1.6 in the Annex). However, the prevailing mechanism and semiempirical model to account for it (see text around A.5.1.1) has been useful to estimate what is the sorbent performance in the LCCC combustion based systems studied in this project (see Annex A Task 9).

The effect of SO₂ on the deactivation of the sorbent has also been experimentally investigated (see Figure A.5.1.9) and has shown a strong detrimental effect on sorbent performance, reducing both the reactivity and the maximum capture capacities of CO₂. This has been taken into account when estimating additional fresh sorbent requirements (see section A9) to maintain the sorbent activity in the system with respect to CO₂ capture.

Finally, experimental and modeling work has also been conducted to elaborate on the reactivity of sorbent particles in the carbonation reaction, for both the conditions in in-duct sorbent injection (see section Annex Task 5.2 and Task 7) and for fluidized bed reactor modeling purposes. In general, standard modeling tools for gas-solid reactions have been

implemented to interpret the results from laboratory equipment and discuss their extrapolation to larger rigs (see section A5.2 and A6).

3.2.3.2 Performance of individual reactor units

The type of work conducted to understand the performance of the individual units in the LCCC system is presented in the following paragraphs, with references to the sections to the Annex A where the specific activities are described in more detail. Two types of CO₂ carbonators have been studied: fluidised bed carbonator and entrained bed (in duct) carbonator.

Running a fluidised bed of CaO to capture CO₂ from a combustion flue gas had never been attempted before. Early experiments conducted in the circulating fluidized bed described in section 3.2.2.4 gave conflicting results and very modest capture capacity of CO₂ (see Annex A6.2), due to a lack of sufficient bed material circulating in the system. In contrast, experimental work conducted jointly with CANMET, in a fluidised bed test facility operated in batch mode for the solids (ie, with a starting point of freshly calcined bed material) showed a sharp uptake of the CO₂ by the solids. Results show that CO₂ capture efficiencies are very high while there is a sufficient fraction of CaO in the bed reacting in the fast reaction regime (breakthrough starts with about 5%w unreacted bed material). The total capture capacity of the bed decays with the number of carbonation-calcination cycles. The experimental CO₂ concentration profiles measured inside the bed during the fast reaction period were interpreted with a well established fluid bed model (see section Annex A8.1), by supplying information on sorbent deactivation from laboratory tests (from Annex A5). It was concluded that a fluidized bed of CaO can be a suitable reactor to achieve very effective CO₂ capture efficiencies from a combustion flue gas.

Carbonation experiments were also carried out in two laboratory scale entrained flow reactors to test the “in duct” concept. The experiments consistently showed reductions in the CO₂ content of the gas stream between 20-40 %. The carbonation reaction took place even when other species (SO₂) competed with CO₂ to react with lime. The concept is therefore attractive if these low capture efficiencies were allowed and the cost savings respect to full capture system were realized. (see Annex A.8.2)

In what respect to fluidized bed calciners, the experimental work and associated modelling, to derive effective heat conductivity in narrow fluidised bed has been completed (see Figure A.7.1.1). The results show that this option is technically feasible for relatively small and medium scale combustor chambers (providing material issues are solved) but becomes unpractical for large scale combustors, where the limited lateral heat transfer capacity of the fluidised bed heat exchangers makes the use of elongated geometries (“fluidized fins”) less efficient. The use of solid heat carriers (see next section) has not been tested experimentally as it requires the integration of combustor, carbonator and calciner (out of scope of this project).

3.2.3.3 Simulation of main system options

The simulation of the full systems considered in this project to generate electricity by burning coal is presented in Annex A9 and summarised here. Only options involving fluidized bed technology are considered. A summary of the key features of each option is outlined below (see Annex A9 and Figures A.9.1.3, A.9.1.4, A.9.1.5). The choice of operating conditions and solid circulation rates comes from the experimental information on sorbent performance studies (Annex A5) integrated with the models for reactor performance and mass balances in

the carbonation-regeneration loop with make up of fresh sorbent and purge of solids from the calciner. The systems studies were:

Case A. Coal-based power plant of any type incorporating a CaO-based CO₂ absorber in the form of a circulating fluidized bed carbonator (Figure A.9.1.3). Regeneration of CaCO₃ with O₂/CO₂ mixture occurs in a fluidized bed. The generation efficiency is predicted to be 38.8%(LHV). The main sources of efficiency penalty are compression of CO₂ and the necessary power for O₂ generation (about 1/3 of the fuel is burned with O₂ in the calciner).

Case B and C. Fluidized bed coal-based power plant following the scheme of figure A.7.1.1 and A.9.1.4. These options involve a high temperature circulating fluidized bed combustor (T = 1050°C) transferring heat to a fluidized bed calciner (T = 850°C) operating at a CO₂ partial pressure of 0.4 bar obtained in the calciner by injecting steam or reducing the total pressure in the calciner. The carbonator operates at 650°C after cooling the gases coming from the combustor. These systems offer the highest generation efficiency (higher than 40%LHV, see A.9.1.2) but involve bed configurations requiring special metallic materials or circulating systems. It is therefore not clear if these systems will be more feasible (economic) than the system of Case A, despite their higher efficiency and the lack of air separation unit.

Case D. In situ capture of CO₂ with CaO in a low temperature fluidized bed combustor. According to the CaO/CaCO₃ equilibrium, if a fuel could be burned at sufficiently low temperature (about 700°C) it would be possible to capture, in situ, the CO₂ generated in the combustion. Highly reactive lignites and biomass are possible fuels. Biomass is a potentially attractive fuel for this application because the synergies with coal can make it competitive in large scale (coprocessing). In the cases examined, the combustor-carbonator is assumed to be of relatively modest scale and close to an existing coal power plant. The flue gas, with a reduced amount of CO₂, and which might also contain CO, tar and unburned C, is fed to the existing power plant in a manner that these compounds are fully oxidized and the heat is recovered in the equipment of the existing boiler. An interesting point of this Case is that it can be used as a retrofitting option to existing plants, to reduce CO₂ emissions while increasing the energy output of the plant.

Case E. In situ capture of CO₂ at high pressures and temperatures. This is similar scheme to Case D above, but applied to high-pressure (10 bar) and high-temperature (850°C) fluidized bed combustor and calciner. As in Case D, the key benefit is high level of system integration, since combustion, CO₂ capture and SO₂ capture are all achieved in a single pressurized fluidized bed reactor. The high sulphur content in the fuel makes necessary a large supply of fresh sorbent to maintain the activity of the CO₂ capture loop (see Annex A5), in accordance with Equation A9.1.4. This has reduced the power generation efficiency respect to other cases (37.7%LHV), but the energy and carbon credits associated with the large flow of deactivated sorbent leaving the plant (mainly CaO) should also be considered.

3.2.3.4 Economic considerations. The consequence of modest sorbent performance

As indicated earlier, the prime candidates to apply CO₂ capture for final storage as a mitigation option for climate change are large scale power plants. Like the carbonation calcination cycle of CaO/CaCO₃, many other CO₂ capture concepts make use of a sorption-desorption cycle to separate CO₂ from a flue gas. These include commercial absorption processes, adsorption, and other high-temperature sorbents for CO₂. This particle mass balances in the loop are also valid for the O₂ chemical looping concepts. It is a common practice to represent the performance of different sorbents as a function of the number of

sorption-desorption cycles and the CaO-CaCO₃ system is usually pointed as an example of poor sorbent performance, as the decay is sharp in the first few cycles (see Annex A and section 3.2.1 above). However, it is also clear that crushed limestone is perhaps the cheapest possible material available in many places around the world, and therefore, large quantities of fresh material can be continuously fed to the systems to maintain a certain activity in the sorption-desorption loop. Since the governing mass balances (in terms of number of cycles that a particle has stayed in the system before leaving in the purge) are identical for all sorption-desorption systems, a parameter that highlights the minimum sorbent performance required to keep sorbent makeup costs at an acceptable level (around 2€/tonne of CO₂ separated) has been defined (see Annex 10). In addition, a well-established reference system for which reliable commercial data exist (absorption with monoethanolamine) was used as a technoeconomic baseline (see Annex 10). It is then demonstrated that sorbent make up cost are not going to be a critical cost barrier for lime carbonation calcination cycles, despite their modest cycle performance, because the low cost of limestone (as low as 5€/tonne) and the possible use of the deactivated sorbent as a cement feedstock (gaining further credits on CO₂ capture and energy efficiency if it substitutes CaCO₃).

4. CONCLUSIONS

4.1 Chemical-looping combustion (CLC)

Chemical-looping combustion for the combustion of syngas has been developed successfully. Different oxygen carriers based on Cu, Fe, Mn, and Ni can be prepared and used in a CLC process using syngas (CO, H₂). Suitable systems based on all of the above mentioned transition state metals were found and five types of particles were selected for detailed study: i) 10 wt% CuO on Al₂O₃ prepared by impregnation (C1A-I), ii) 60% Fe₂O₃ with Al₂O₃ prepared by freeze granulation (F6A-FG), iii) 40% NiO with Al₂O₃ prepared by freeze granulation (N4A-FG), iv) 60% NiO with MgAl₂O₄ prepared by freeze granulation (N6AM-FG) and v) 40% Mn₃O₄ with ZrO₂ (doped with Mg) (M4MZ-FG). All of these showed extremely high reactivity with syngas, good fluidizing behaviour and limited or no particle breakage during fluidization. It should be mentioned that with respect to the Cu- based oxygen carriers, the only method valid for the preparation of Cu-based oxygen carriers is the impregnation. The detailed kinetic data of particles i, ii, and iii was determined both under atmospheric and pressurized conditions. From this data the solids inventory was calculated, which showed that the process could be operated with relatively low solids inventory for all tested carriers.

Three different CLC scale-model reactor types based on interconnected fluidized beds have been designed, constructed and operated successfully, whereof one was constructed as a hot prototype reactor. There was important know-how gained on the fluid dynamic scale-up of CFB CLC reactors and mathematical models developed which can be used as scale-up tools for future design of large scale CLC power plants.

From the extensive work devoted to screening for oxygen carriers at CSIC and Chalmers, three particles based on Fe, Ni and Mn, i.e particles F6A-FG, N6AM-FG and M4MZ-FG, were selected and tested in the hot prototype 300 W CLC unit. All oxygen carriers had a high conversion of the fuel with small amounts of unburnt from the fuel reactor. For many of the tests with NiO, equilibrium is reached and combustion efficiency was 0.994 at 850 °C. For Mn₃O₄, the CO and H₂ concentrations were below the detection level of the gas analyzer. The Fe-based oxygen carrier also showed high conversion of the fuel with a combustion efficiency of 0.988 at 850 °C. The investigated particles have been fluidized with recirculation in hot conditions for approximately 150 h for the Ni particles, 130 h for the Mn and 60 h for the Fe based particles without any signs of deactivation and very little attrition.

In summary it can be concluded that the research on chemical-looping combustion has been highly successful. When the project started the process was a paper concept, never tested in actual operation, and a limited number of oxygen carriers had been tested in few cycles in laboratory. In this project a large number of particles have been produced and tested and many were found to have suitable properties for the process. A small reactor system for chemical-looping combustion was developed, tested and found to be working well. Furthermore cold-flow models indicate the realism of the process in full scale. The kinetics of a limited number of particles has been studied in detail, and modelling shows that the solids inventories needed will be small. Lastly, three oxygen carriers based on nickel, manganese and iron oxides has been tested for longer periods in the chemical-looping combustor with excellent results.

4.2 Lime carbonation-calcination cycles (LCCC)

The main conclusion obtained from the part of the studies on carbonation calcinations cycles is that some of the options investigated can be potentially competitive to capture CO₂ in coal-based power generation and cement plants.

Sorbent performance from the point of view CO₂ capture capacity of the sorbent is not going to be critical for the operation of the system if further decays in activity (respect to what is intrinsic in the carbonation calcinations loop) are avoided. Sorbent deactivation by sulphur must be compensated with a higher flow of fresh sorbent (make up). The sorbent reactivity is largely insensitive to limestone type (except for dolomites), gas composition and temperatures during carbonation and calcinations below 950 C. Carbonation reaction rates are sufficiently high in normal carbonation calcinations conditions to ensure a good utilisation of the sorbent in fluidized bed carbonators (up to the maximum conversion allowed for a given cycle number). In entrained bed carbonators, the conversions of the sorbent are much lower, limited by the gas solid contact time and the intrinsic reactivity of the calcined particles.

The operation of the full integrated system has not been demonstrated in this project, but the key reactor systems (carbonator and calciner) have shown no major barriers for continuous operation. In some of the cases, the individual units are commercially proven and/or there exist similar large-scale commercial processes operating in similar conditions. In the least developed and most efficient cases studied, the challenge is to demonstrate novel reactor concepts that offer substantial gains in efficiency and/or avoid the air separation unit for the calcination. The application of the lime carbonation to existing boilers (in duct) seems technically feasible if low capture efficiencies are allowed and the system proves to be truly cost saving respect to a new plant with capture.

All the options studied have the inherent advantage of low efficiency penalties, since the large flow of heat required for the calcination of the sorbent is recovered at the high temperatures of the carbonator. No major technical barriers have been identified and confidence has been built on the operation and understanding of individual units. Therefore, some of the options are ready to be demonstrated at large pilot level in a continuous plant, delivering a pure stream of CO₂, a flue gas depleted of CO₂ and a purge of deactivated sorbent (mainly CaO).

5. RECOMMENDATIONS

5.1 Chemical-looping combustion (CLC)

The process has high potential for achieving 100% CO₂ capture at low cost and with high efficiency. In view of the encouraging results it is strongly recommended that the development of this process is continued. The reactor system as such has large similarities to well-known, commercially available, systems used in circulating fluidized-bed combustion of solid fuels. The key difference is the role played by the oxygen carrier particles. It is very important that the research on the development of these materials is continued, both on the level of expanding the basis of tested materials, i.e. investigation of new materials and improving available materials, as well as looking at commercialization and scaling-up of production methods.

5.2 Lime carbonation-calcination cycles (LCCC)

This project has been a key step to put in the portfolio of emerging systems for CO₂ capture, the separation of the CO₂ at high temperatures using CaO as a regenerable sorbent. Large gaps in knowledge at fundamental and general level have been closed, but many areas of work have been open, some of which were not fully appreciated at the project started. Some clear priorities for future work are underlined in the following paragraphs:

Sorbent performance. Cheap and practical methods for sorbent preactivation and reactivation need to be investigated. Improving the fundamental understanding of the decay process (sintering) and the barriers to full conversion (product layer development, textural changes along reaction etc) may lead to sorbent performance improvements. Attrition resistance sorbents, and the evolution of the particle mechanical properties along cycling, needs investigation.

Reactors for carbonation. Fluidised bed carbonator reactors test at higher velocities are required. Also, further research on the practicalities of a large flow of sorbent injection for “in duct” CO₂ capture in existing plants. Validation, refinement of existing reactor simulation tools.

Regenerators or calciners. Devices for a very fast calcinations of sorbent are required to reduce sintering and maximise sorbent reactivity. Several options need to be investigated in practice: calcination with O₂/CO₂ flames, indirect heat transfer by solid heat carriers. Development of suitable reactor simulation tools.

Demonstration of a continuous full pilot system, interconnecting a carbonator, combustor and calciner. Generating a flue gas depleted of CO₂ and a pure stream of CO₂ from the calciner.

ANNEX A. TECHNICAL ANNEXES

A.1 Task 1. Development of oxygen carrier particles

One of the most important aspects of a CLC system based on interconnected fluidized beds is the properties of the oxygen carrier, which needs to transport the oxygen and the heat from the oxidation reactor to the fuel reactor. The objective of this task was to develop an oxygen carrier with enough reduction and oxidation rates, resistant to the attrition and with high durability, maintaining the chemical, structural and mechanical properties in a high number of oxidation-reduction cycles.

CSIC has manufactured oxygen carriers by two different preparation methods: extrusion and impregnation. Further, reactivity tests have been mainly carried out in a thermogravimetric analyzer (TGA) where the atmosphere an oxygen carrier would be exposed to was simulated.. Chalmers has prepared oxygen carriers by freeze granulation and tested these in a fluidized bed reactor under alternating oxidizing and reducing conditions.

A large number of oxygen carriers (~300 samples), including all possible combinations of metal oxides and inerts, were prepared and characterized at CSIC and Chalmers to do a preliminary selection of the most promising candidates to be used in a CLC process. A selection of about 10 samples showed highly promising results and were analyzed in-depth. Finally, at the end of the task, five samples were chosen for detailed reactivity testing and three of these were then manufactured and used in the hot CLC prototype reactor.

A.1.1. Work performed at CSIC

A.1.1.1. Task 1.1. Selection of possible carriers

The oxygen carrier is composed of a metal oxide to transport the oxygen, and an inert to supply a higher mechanical strength to the samples. The materials selected to produce the oxygen carriers are the following:

Metal oxides: CuO, Fe₂O₃, MnO₂, NiO

Inerts: Al₂O₃, sepiolite, SiO₂, TiO₂, ZrO₂

A.1.1.2. Task 1. 2. Preparation of oxygen carrier particles for screening

CSIC prepared all the possible combinations metal oxide-inert with the weight percentages corresponding to 40 %, 60% and 80% of metal oxide to carry out a preliminary screening of the oxygen carriers. The oxygen carriers, prepared by mechanical mixing and extrusion, were calcined at four different temperatures from 950 °C to 1300 °C.

A.1.1.3. Task 1.3. Characterisation of oxygen carriers for screening

The characterisation of the physical properties of the oxygen carriers prepared by mechanical mixing and extrusion, as apparent densities and mechanical strength, was first carried out. The mechanical strength of the oxygen carriers was determined by using the ASTM-4179 method.

This method allows the measurement of the minimum normal force required to crush a cylindrical extrudate placed between two plates in horizontal position. The crushing strength was obtained dividing the force applied by the extrudate length. The final measure was obtained from the average of at least 15 different measurements undertaken on different extrudates randomly chosen. Table A.1.1.1 shows the values obtained for all the oxygen carriers prepared by mechanical mixing and extrusion.

The crushing strength was highly dependent on the type of active metal oxide and its concentration, the inert used as a binder, and the sintering temperature. In general terms, a higher sintering temperature increased the crushing strength of the oxygen carriers. However, high sintering temperatures for some carriers was limited by decomposition or melting of the involved compounds. This effect was especially important in the Cu and Mn oxygen carriers, and in those using sepiolite as inert. On the other hand, there was not a clear correlation between crushing strength and active metal oxide content. For example, the oxygen carriers CuO/TiO₂ and Fe₂O₃/TiO₂ showed opposite dependency on the active metal oxide content.

In general, it can be concluded, that Cu-based oxygen carriers only showed a measurable crushing strength when using SiO₂ and TiO₂ as inerts. Fe-based oxygen carriers showed high crushing strength values, especially those prepared with Al₂O₃, TiO₂ and ZrO₂ and sintered at temperatures above 1100 °C. Mn-based oxygen carriers only had high crushing strengths when using SiO₂ or TiO₂ sintered at 1100 °C, and ZrO₂ sintered at temperatures higher than 1100 °C. Ni-based oxygen carriers showed in general terms a low crushing strength excepting when using SiO₂ or TiO₂ as inerts.

Table A.1.1.1. Crushing strength (N/mm) of the extrudates.

		Metal-based oxygen carriers															
		Cu				Fe				Mn				Ni			
T _{sint}		950	1100	1200	1300	950	1100	1200	1300	950	1100	1200	1300	950	1100	1200	1300
Inert	MeO																
Al ₂ O ₃	80	3	5			0	13	105	61	0	0	0		0	0	0	0
	60	0	0			0	12	17	57	0	0	0		0	0	0	0
	40	0	0			0	12	22	65	0	3	12		0	2	3	4
Sepi	80	4				9	48			1	23*			0	1	4	120
	60	0				7	20			1	12*			1	6	14*	
	40	0				1	14			0	27*			0	3	53	
SiO ₂	80	22				12	60			10	37			0	1	11*	25*
	60	20				15	85			16	28			6	16	32	45
	40	17				10	52			16	22			11	29	35	
TiO ₂	80	66				12	71	111	17	2	57			1	16	42	50
	60	59				21	45	36	11	8	77			4	17	32	48
	40	43				40	94	81	30	13	84			14	23	33	65
ZrO ₂	80	6				3	25	33	76	0	11	37	29	0	2	1	3
	60	2				12	20	29	54	1	16	33	25	0	0	3	5
	40	1				13	19	19	56	2	11	36	27	0	3	13*	11*



Melt or decompose



Soft (Values lower than 10 N/mm)

*

Broken after 5 cycles

On the other hand, reactivity tests of the oxygen carriers with respect to the reduction and oxidation reactions were carried out for the selection of the most promising candidates. Thermogravimetric (TG) experiments allowed us to analyse the reactivity of the oxygen carriers under well defined conditions, and in the absence of complex fluidising factors such as particle attrition and interphase mass transfer processes.

Experimental set-up. Oxygen carriers' reactivity has been carried out in a CI thermogravimetric analyser (TGA). The Figure A.1.1.1 shows the experimental set-up used. The reactor consists of a quartz tube (24 mm id) placed in an oven that can be operated at temperatures up to 1000 °C. The sample-holder is a wire mesh platinum basket (14 mm diameter and 8 mm height) to reduce mass transfer resistance around the sorbent sample. The temperature and sample weight are continuously collected and recorded in a computer. N₂ (9 NL/h) flowed through the microbalance head to kept the electronic parts free of reactant gas. The reacting gas mixture (30 NL/h), is measured and controlled by electronic mass flow controllers.

In the fuel reactor of a CLC system, water is always produced as a result of the reaction. To work under realistic conditions, water was introduced together with the reacting gases, CO and H₂. The water normally acts as an inert gas, the exception being some oxygen carriers based on Fe and Ni, where the presence of H₂O prevents carbon formation during the reaction. The reacting gas (CO+H₂) was saturated in water bubbling through a vessel containing water at the selected temperature necessary to reach the desired water concentration.

Procedure: For the reactivity experiments of the preliminary screening, about 50 mg of oxygen carriers with a particle size of about 1 mm (between 10 and 20 particles depending on the sample density) was loaded in the platinum basket. After the set temperature was reached, the experiment started by exposing the oxygen carrier to alternating oxidising and reducing conditions. To avoid the mixing of fuel gas and air, nitrogen was introduced for two minutes after each oxidising and reducing period. An experiment without sample was initially carried out to detect the buoyant effects due to the change of the reacting gases.

The composition of the syngas selected for the reducing experiments was normally 45 % CO, 25 % H₂ and 30% H₂O, and the gas used for oxidation was 100 % air. The experiments were carried out at 950 °C for the oxygen carriers based on Fe, Mn and Ni, and 800 °C for the oxygen carriers based on Cu. The reason for this lower temperature was to avoid the decomposition of CuO to Cu₂O, with the subsequent loss of transport capacity of the sorbent.

For the screening purposes, five cycles of reduction and oxidation were made. The sample normally stabilised after the first cycle, which was normally slower than the others. This was due to the changes produced in the internal structure of the oxygen carriers during their first reduction period. The oxygen carrier reactivity corresponding to cycle number 5 was used for comparison purposes.

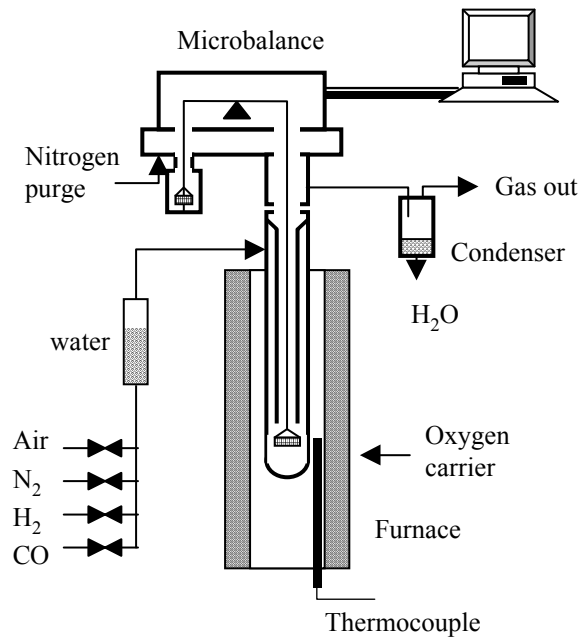


Figure A.1.1.1. Experimental set-up for reactivity data.

Data handling: To establish if all the metal oxide has been effective for reaction, it was necessary to know the reactants and products of the reactions and the metal oxide content of the oxygen carrier used. The transport capacity of the oxygen carriers can be known through the oxygen ratio between the reduced and oxidized metal, which can be defined as;

$$R_0 = \frac{m_{ox} - m_{red}}{m_{ox}} \quad (\text{A.1.1.1})$$

This equation compares the metal oxide in its oxidized, m_{ox} , and reduced, m_{red} , form and gives the fraction of oxygen which can be carried between the reactors for a given mass flow of metal oxide. Table A.1.1.2 shows values of the oxygen ratio for the metal oxide systems considered in this work. On the other hand, the oxygen carrier is always composed by a metal oxide and inert. Obviously, the presence of the inert decreases the transport capacity of the carrier. Table A.1.1.3 shows the transport capacity of the oxygen carriers depending on both the metal oxide content and the reduced/oxidised pairs considered. The Mn-based oxygen carriers were prepared using MnO₂ as starting material. However, this decomposes to Mn₂O₃ at about 500 °C, and to Mn₃O₄ at about 950 °C. The values showed in the Table A.1.1.3 correspond to initial mass% of MnO₂.

On the other hand, it was observed that sepiolite losses weight during calcination at high temperatures (23.8 wt%). Then, the initial metal oxide content was recalculated, and also the transport capacity of the oxygen carriers, as shown in Table A.1.1.4.

Table A.1.1.2 Oxygen ratio for different oxygen carriers.

M_vO_x/M_vO_{x-1}	R_0
CuO/Cu	0.201
Fe ₂ O ₃ /Fe ₃ O ₄	0.033
Fe ₂ O ₃ /FeO	0.100
Mn ₃ O ₄ /MnO	0.070
NiO/Ni	0.214

Table A.1.1.3. Maximum variation in weight percentage (%) for the different oxygen carriers

Mass % MeO	CuO / Cu	Fe ₂ O ₃ / Fe ₃ O ₄	Fe ₂ O ₃ / FeO	Mn ₃ O ₄ / MnO*	NiO / Ni
80	16.08	2.64	8.00	5.45	17.12
60	12.06	1.98	6.00	3.98	12.84
40	8.04	1.32	4.00	2.58	8.56
20	4.02	0.66	2.00	1.26	4.28

* The percentage values are referred to the initially used MnO₂.

Table A.1.1.4. Maximum variation in weight percentage for the different oxygen carriers when using sepiolite as inert.

Mass % MeO	CuO / Cu	Fe ₂ O ₃ / Fe ₃ O ₄	Fe ₂ O ₃ / FeO	NiO / Ni	Mass % MeO	Mn ₃ O ₄ / MnO*
84.0	16.88	2.77	8.40	17.98	82.17	5.75
66.3	13.33	2.19	6.63	14.19	63.33	4.43
46.7	9.38	1.54	4.67	9.99	43.43	3.04
24.7	4.96	0.81	2.47	5.28	22.35	1.56

* The percentage values are referred to the initially used MnO₂.

The figures showing the reactivity of all the oxygen carriers can be found in the previous reports of the project. However, since the number of samples used in this work (~240) was very high, it was difficult to compare all available reactivity data. So, Table A.1.1.5 gives a summary of the reactivity data for all the oxygen carriers prepared, and for a better understanding, Figure A.1.1.2 shows an example of the notation used in the table.

The main comments about the specific oxygen carriers behaviour are the following. Cu-based oxygen carriers sintered at 950 °C exhibited a high reactivity with reaction times for complete reduction lower than 1 minute. The oxidation conversions at 1 minute of reaction varied from 80 to 100%. In some cases, the final oxidation rate was substantially lower, probably due to diffusion effects inside the extrudates.

Fe-based oxygen carriers exhibited a high reactivity during reduction, although the conversion to FeO was not complete in most of the cases. The oxidation rate was high, the exception being some carriers prepared using TiO₂ as inert.

The Mn-based oxygen carriers showed a different behavior depending on the active metal oxide content, the type of inert, and the sintering temperature. For example, the reactivity of the carrier Mn40Ti, with a low concentration of manganese oxide, was very low due to the

Table A.1.1.5. Reactivity of different oxygen carriers and selection of the most promising carriers.

		Metal-based oxygen carriers															
		Cu				Fe				Mn				Ni			
T _{sint}		950	1100	1200	1300	950	1100	1200	1300	950	1100	1200	1300	950	1100	1200	1300
Inert MeO																	
Al ₂ O ₃	80	a-a	e-e			a-a	a-a	b-b	b-b	a-a	b-b	e-e		a-a	a-b*	a-b*	b-c*
	60	a-a	e-e			a-a	b-b	b-b	b-b	b-b	c-c	e-e		a-a	a-b*	b-c*	e-e
	40	a-a	e-e			a-a	a-a	b-b	b-b	c-c	e-e	e-e		a-a	b-c	c-c	e-e
Sepi	80	a-a				a-a	a-a			a-a	a-a			a-a	a-a	a-a	e-e
	60	a-a				a-a	a-a			a-a	a-a			a-a	a-a	b-b	
	40	a-a				a-a	a-a			a-a	c-e			a-a	b*-a	e-e	
SiO ₂	80	a-a				b-b	b-b			a-a	b-b			a-c*	a-c*	a-c*	a-b*
	60	a-a				a-a	b-b			a-a	e-e			a-c*	a-d	a-d	a-c
	40	a-a				a-a	a-a			a-a	e-e			a-c*	b-d	c-d	
TiO ₂	80	a-a				a-a	b-b	b-c*	b-c*	b-b	b-b			a-b*	a-b*	a-b*	b*-
	60	a-a				a-a	b-b	b-c*	c-c	e-e	e-e			a-a	a-a	a-a	a-b*
	40	a-a				a-a	b-c*	b-c*	b-d	e-e	e-e			a-a	a-a	a-a	a-b*
ZrO ₂	80	a-a				a-a	a-a	a-a	b-b	a-a	a-a	a-a	a-b*	a-c*	a-c*	a-d	a-d
	60	a-a				a-a	a-a	a-a	b-b	a-a	a-a	a-a	a-b*	a-b*	a-b*	a-b*	a-b*
	40	a-a				a-a	a-a	a-a	b-b	a-a	a-a	a-a	b*-	a-b*	a-b*	a-b*	a-b*

a = High reactivity and high conversion (X > 0.8 in 1 min)  Melt or decompose
 b = Conversion between 0.5-0.8 in 1 min.  Low reactivity and crushing strength
 c = Conversion between 0.3-0.5 in 1 min.
 d = Conversion lower than 0.3 in 1min but higher than 0.3 in 20 min.
 e = Low reactivity or low conversion (X < 0.3 in 20 min).  Selected particles by mechanical strength and reactivity
 * = Reach high conversion at long time

formation of titanates during sintering, however, when the MnO₂ content increased up to 80% the reactivity and conversion was higher. In general, the best performance with complete utilization of the manganese used and reaction times less than 1 minute was obtained when ZrO₂ was used as inert.

Most of the Ni-based oxygen carriers exhibited a very high reactivity during reduction with reaction times lower than 30 seconds for complete conversion. The behavior in the oxidation process was highly dependent on the oxygen carrier considered. In some cases, the oxidation rate was low from the beginning (Ni40Si), and in some others was fast up to a conversion and then suddenly decreased (Ni80Al). The best performance was obtained with NiO/TiO₂ carriers, which exhibited high reactivity both in the reduction and the oxidation processes for all conditions used in this work.

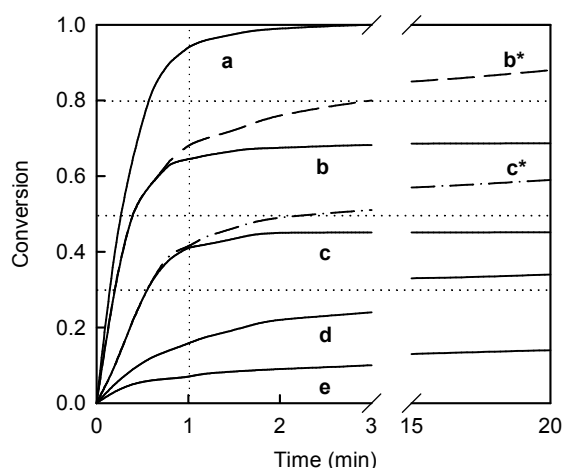


Figure A.1.1.2. Typical conversion curves obtained during reactivity testing, and used for notation in Table A.1.1.5.

A.1.1.4. Task 1.4. Selection of the most promising candidates

The first criterion for carrier rejection was an unacceptable low melting point of some one of the compounds either reduced or oxidized forms. The second one was the crushing strength of the fresh carriers and the third the reactivity obtained in TGA tests during both the reduction and the oxidation reactions. A preliminary screening to select the best carriers for further use in a CLC system was done.

Fresh extrudates with crushing strengths below 10 N/mm were considered exceedingly soft and then rejected. In some cases, the crushing strength of the extrudates was observed to substantially decrease during successive reduction/oxidation cycles in TGA tests (MnXSe1100 with X=40, 60, and 80; Ni60Se1200, Ni40Zr1200, etc.). This effect was also considered for the screening.

Reactivity was the criterion to reject oxygen carriers exhibiting low values due to the formation of inactive compounds by a solid/solid reaction (Mn40Ti) or excessive thermal sintering (Ni80Se1300), due to the use of high sintering temperatures. Considering the above criteria, Table A.1.1.5 shows the best oxygen carriers to be further used in CLC systems. That includes carriers prepared with SiO₂ or TiO₂ as inert and sintered at 950°C as the best Cu-based oxygen carriers. Fe-based oxygen carriers prepared with all inerts can be considered potentially suitable for CLC systems although some of them must be prepared at some specific conditions. Those prepared with Al₂O₃ and ZrO₂ as inerts showed the best behaviour. ZrO₂ was the best inert for preparing Mn-based oxygen carriers, and TiO₂ for preparing Ni-based oxygen carriers.

Other carriers, as Fe₂O₃/TiO₂ sintered at 1200 and 1300 °C, and NiO/SiO₂, exhibited an acceptable crushing strength but they did not have a very high reactivity. Taking into account that reactions as fast as possible are always desirable, since the time of reaction determines the necessary residence time in reactors and, therefore, the reactor size and pressure drop, the use of these carriers in a CLC system will depend on the needs of the system.

Based on reactivity tests in TGA and crushing strength measurements, a preliminary selection of the most promising carriers to be used in a CLC system was done. These oxygen carriers were later subjected to multi-cycle testing (100 cycles) in TGA to analyze the effect of the cyclic structural changes inside the oxygen carrier during the oxidation and reduction reactions. These correspond to the following oxygen carriers:

C4SE950, C4TE950, F4AE1300, F4ZE1300, M4ZE1200, N4TE1300.

The only oxygen carriers prepared by mechanical mixing and extrusion that maintained their integrity after the multicycle testing were F4AE1300 and F4ZE1300. Figure A.1.1.3 shows an example of the reactivity of the F4AE1300 oxygen carrier along the multicycle tests.

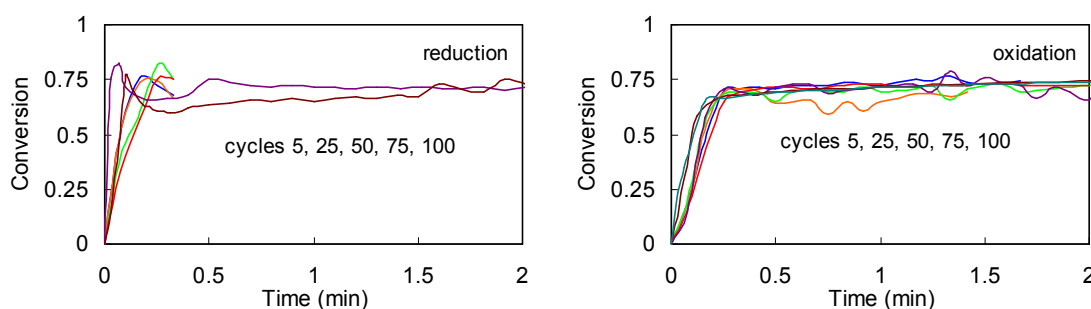


Figure A.1.1.3 Reactivity of the F4AE1300 oxygen carrier after multicycle testing.

Impregnated oxygen carriers. Due to the great effect of the cyclic reduction and oxidation reactions on the structure of the oxygen carriers, other preparation methods besides the mechanical mixing and extrusion were tested by CSIC (de Diego et al., 2004), especially for the development of Cu-based oxygen carriers. The conclusion was that the oxygen carriers prepared by impregnation fulfilled all the conditions needed to be used in a CLC process because these particles exhibited excellent chemical stability without any decay of the mechanical strength during multicycle testing. In this sense, the preparation conditions to produce CuO/Al₂O₃ oxygen carriers with high reactivities, and small attrition rates were found. Two different methods of impregnation, wet or dry, were compared (de Diego et al., 2005). Moreover, the agglomeration of these oxygen carriers, which is the main reason given in the literature to reject the Cu-based oxygen carriers, was avoided. In addition, a commercial catalyst supported on alumina (Aldrich Chemical Co., Inc.; catalogue no. 417971) with a 13 wt% of CuO was also analyzed for comparison purposes.

Attrition testing. To finally improve the screening it is necessary to know the behaviour of the carriers during successive reduction/oxidation cycles in a fluidized bed, which considers both the structural changes because of the chemical reaction, and the attrition phenomena existing in a fluidized bed, as well as the possible agglomeration of the solids.

Figure A.1.1.4 shows the experimental set-up located at CSIC for the oxygen carrier testing. It consists of a system for gas feeding, a fluidized bed reactor, a two ways system to recover the solids elutriated from the fluidized bed, and a gas analysis system. The gas feeding system has different mass flow controllers connected to an automatic three-way valve. This valve always introduces N₂ (inert) between the reducing gas and the oxidation gas to avoid explosions. The fluidized bed reactor is 54 mm I.D. and 500 mm height, with a 300 mm of preheating zone just under the distributor. At the exit, there is a double pipe with hot filters to recover the solids elutriated from the bed at different times. Finally, different gas analyzers continuously

determine the gas composition at each time. The concentrations of H₂O, CO, CO₂ and CH₄ are determined in an infrared analyzer (FTIR), O₂ in a paramagnetic analyzer, and H₂ by gas conductivity.

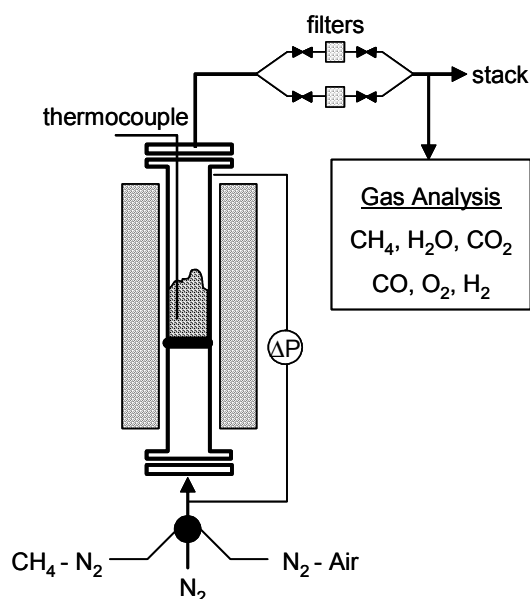


Figure A.1.1.4. Experimental set-up for attrition testing.

Operating procedure: For the preliminary screening tests, the fluidized bed was composed of sand of size 0.2-0.3 mm, and batches of about 50 g of oxygen carriers with a particle size 0.1-0.2 mm were used. For the selected oxygen carriers, the attrition rate was determined with batches of about 400 g of oxygen carrier, without any sand. The composition of the reducing gas was selected to avoid exceed the terminal velocity of the particles. On the other hand, a gas with an 8% of O₂ in Ar was used to avoid the over heating of the samples during the oxidation reaction.

Figures A.1.1.5 and A.1.1.6 shows the attrition rate obtained with some of the selected oxygen carriers prepared by mixing/extrusion and impregnation. The attrition rates are high in the first 5 cycles due to the rounding effects on the particles and to the fines stuck to the particles during preparation and crushing/sieving. Later, the attrition rates due to the internal changes produced in the particles by the successive reduction and oxidation processes, decreased. However, it can be observed that the particles prepared by impregnation exhibited very low attrition rates. An important fact was that the attrition rates did not change appreciably between cycle 50 to 100, with a mean attrition rate of 0.01%/cycle (< 0.02%/h in our tests) or even lower for some oxygen carriers (Cu10Al-DI-950, Cu15Al-DI-850). Assuming this value as a measure of the steady-state attrition of the carrier particles, this leads to a lifetime of the particles of 10000 cycles (5000 h in our tests).

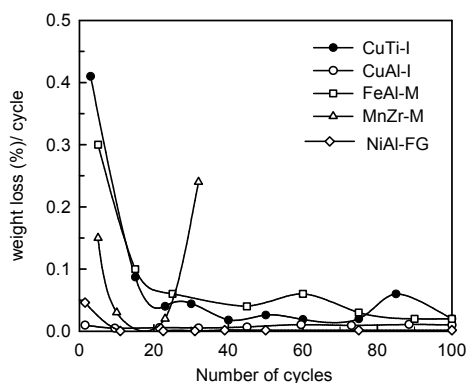


Figure A.1.1.5. Attrition rates of oxygen carriers produced by mechanical mixing+extrusion(M), impregnation (I), and freeze-granulation (FG) during multicycle fluidised bed testing.

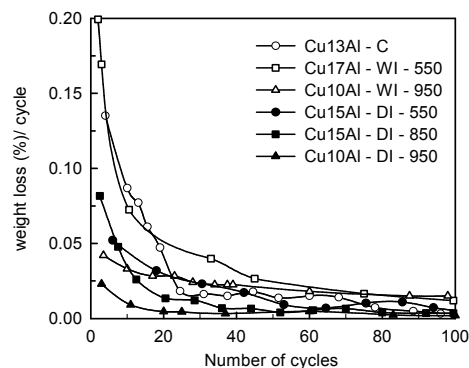


Figure A.1.1.6. Attrition rates of the impregnated particles during multicycle fluidised bed testing.

The attrition of the Ni40Ti prepared by extrusion was a little high. In general, all the Ni-based carriers prepared by extrusion showed low crushing strength. However, their excellent behaviour with respect to reactivity (the highest of all carriers tested) made us test the possibility of produce stronger Ni-based particles. In this sense, Chalmers University of Technology (CUT) produced particles by freeze-granulation (FG) with high crushing strength and reactivity, Ni_{CUT}-FG. This particles were also tested in the fluidized bed and exhibited very low attrition rates (see Figure A.1.1.5).

A.1.2. Work performed at Chalmers

Oxygen carriers

It is important that the metal oxide which is used as an oxygen carrier can convert the fuel gas to carbon dioxide and water to a high extent. In a thermodynamic analysis carried out prior to the start of the project, Mattisson and Lyngfelt found that some metal oxides of the transition state metals Fe, Mn, Cu and Ni were among the feasible candidates to be used as oxygen carriers in CLC using methane. (Mattisson and Lyngfelt, 2001). For oxygen carriers based on Fe and Mn there are some transformations which do not have an acceptable degree of gas conversion, such as Fe₃O₄/FeO and MnO/Mn. Further investigations by Jerndal et al. found that the systems which had a high gas yield for methane also had a high gas yield for CO and H₂. (Jerndal et al., 2005) The chosen metal oxides are preferably supported by an inert material which is believed to increase the reactivity and help to maintain the internal structure of the particles throughout the redox reactions. Prior to the current project there was some experimental investigations of different oxygen carriers for CLC. For instance, see the works by Mattisson and co-workers and Ishida et al., e.g. (Mattisson et al., 2000; Ishida et al., 1994).

At Chalmers oxygen carriers based on the metal oxides Fe₂O₃, NiO and Mn₃O₄ were prepared and tested in Task 1 of the project. The selection of the materials was chosen from the results of the screening selection at CSIC as well as previous work.

A.1.2.1 Experimental

Preparation of oxygen carriers. All the particles were produced by freeze-granulation. The selection of active metal oxide and inert were based on the results of the investigations at CSIC, see section A.1.1 above. However, in order to improve mechanical stability of some of the systems, in some instances the chemical composition in addition to the heat treatment temperature was changed somewhat. For instance, for the Ni-Al system, Mg, Ca and bentonite was used with the aim of increasing mechanical strength. Also the sintering temperature was increased.

The particles were prepared as followed: A water-based slurry of the composite material, in the form of chemical powders with a size less than 10 μm, and a small amount of polyacrylic acid as dispersant were prepared by ball milling for 24 h. After milling, some polyvinyl alcohol was added to the slurry as a binder to keep the particles intact during later stages in the production process, i.e. freeze-drying and sintering. Spherical particles were produced by freeze-granulation, i.e. the slurry is pumped to a spray nozzle where passing atomising-air produce drops, which are sprayed into liquid nitrogen where they freeze instantaneously. The frozen water in the resulting particles is then removed by sublimation in a freeze-drier operating at a pressure that corresponds to the vapour pressure over ice at -10°C. After drying, the particles were sintered at temperatures between 950°C and 1600°C for 6 h using a heating rate of 5°C/min. Finally they were sieved to obtain particles of well-defined sizes.

In Table A.1.2.1 the 51 oxygen carriers investigated in this section are presented. For these carriers, parameters such as ratio of metal oxide/inert, sintering temperature and type of inert are varied. The nomenclature used here for the different oxygen carriers is given in column 2 in Table A.1.2.1, and in the text these abbreviations will be followed by the sintering temperature, i.e. F4S950 corresponds to 40% Fe₂O₃/60% SiO₂ sintered at 950°C.

Characterization of oxygen carriers. The fresh and reacted particles were characterized prior to and after the reactivity experiments in the fluidized bed reactor. The physical appearance of the surface was characterized by scanning electron microscopy in addition to an optical microscope. The crystalline phases in the particles were identified using a powder diffractometer. The hardness of the fresh particles was also determined by measuring the force needed to fracture the particles using a Shimpo FGN-5 crushing strength apparatus. The crushing strength was measured on particles in the size range 0.180-0.250 mm and taken as the average value of 30 results.

Reactivity investigation in the fluidized bed reactor. Methane was chosen as reacting gas for the particle comparison, because it facilitates the experimental procedure. The results can be expected to give a measure for the ranking of particle reactivity, highly relevant also for other fuel gases like CO and H₂. The best particles are further tested using syngas, see section A.2.2.

The experiments were conducted in a laboratory fluidised-bed reactor of quartz. The reactor had a length of 820 mm with a porous quartz plate of 30 mm in diameter placed 370 mm from

the bottom. The inner diameters of the bottom and top sections were 19 and 30 mm. The temperature was measured 5 mm under, and 38 mm above the porous quartz plate, using 10% Pt/Rh thermocouples enclosed in quartz shells. A sample of 10 or 15 grams of oxygen carrier particles, in the size range of 125-180 μm , was initially heated in an inert atmosphere to 950°C. The metal oxides investigated in this work had a large difference in apparent density (800-4500 kg/m³), and thus the bed heights also varied in a wide range, between 4-33 mm. Because of the heat produced during the oxidation period, a gas mixture with 5% O₂ in N₂ was used instead of air. Thus, large temperature increases were avoided. The particles were then exposed alternatively to 5% O₂ and 50% CH₄/50% H₂O, thus simulating the cyclic conditions of a CLC system. To avoid air and methane mixing during the shifts between reduction and oxidation, nitrogen gas was introduced during 180 s after each period. The

Table A.1.2.1 Particles investigated in the project at Chalmers

Oxygen carrier composition.	Abbr.	Sintering temperature (°C)									
		950	1100	1125	1150	1175	1200	1300	1400	1500	1600
40% Fe ₂ O ₃ /60% SiO ₂	F4S	1	2					3			
40% Fe ₂ O ₃ /60% ZrO ₂	F4Z							4			
60% Fe ₂ O ₃ /40% Al ₂ O ₃								5			
60% Fe ₂ O ₃ /32% Al ₂ O ₃ + 8% Bentonite	F6AB		5				6	7			
40% Fe ₂ O ₃ /60% MgAl ₂ O ₄	F4AM		8				9	10			
60% Fe ₂ O ₃ /40% MgAl ₂ O ₄	F6AM		11	12	13	14	15				
80% Fe ₂ O ₃ /20% MgAl ₂ O ₄	F8AM		16				17	18			
40% Mn ₃ O ₄ /60% SiO ₂	M4S	19									
40% Mn ₃ O ₄ /60% ZrO ₂	M4Z	20	21					22			
40% Mn ₃ O ₄ /60% Ca-ZrO ₂	M4CZ	23	24				25	26			
40% Mn ₃ O ₄ /60% Mg-ZrO ₂	M4MZ	27	28		29		30	31			
40% Mn ₃ O ₄ /60% Ce-ZrO ₂	M4CeZ	32	33					34			
40% NiO/60% NiAl ₂ O ₄	N4AN							35			
40% NiO/60% NiAl ₂ O ₄	N4AN										36
40% NiO/48% Al ₂ O ₃ + 12% CaO	N4AC								37		
40% NiO/48% Al ₂ O ₃ + 12% Bentonite	N4AB							38			
60% NiO/40% MgAl ₂ O ₄	N6AM								39	40	41
40% NiO/60% MgO	N6M										

1. Horizontal lines indicate too soft particles. 2. Vertical lines shows particle with almost no reactivity. 3. Crossed lines sintered to cake at heat treatment. 4. Black fields with number indicate particles investigated further.

particles were tested in this manner for 4-17 cycles. The gas from the reactor was led to an electric cooler, where the water was removed, and then to a gas analyser where the concentrations of CO₂, CO, CH₄, and O₂ were measured in addition to the gas flow. The

experiments with a ten gram bed were conducted with an inlet gas flow of 600 mL_n/min for the reducing gas, while for the 15 gram bed the gas flow was 900 mL_n/min. Hence the ratio of gas flow/bed mass was held constant which makes the experiments comparable. For the oxidising gas, the gas flow was either 600 or 1000 mL_n/min. This corresponds to 2-12 u_{mf} and 4-15 u_{mf} for the incoming reducing and oxidising gases respectively, where u_{mf} is the minimum fluidisation velocity. However, as three moles of product gas are formed for every mole of reacted CH₄, the velocity may be as high as 4-24 u_{mf} .

Data evaluation. The degree of solid conversion is defined as,

$$X = \frac{m - m_{red}}{m_{ox} - m_{red}} \quad (\text{A.2.1.1})$$

where m is the actual mass of sample, m_{ox} is the mass of the sample when fully oxidized, i.e. Fe₂O₃, and m_{red} the mass of the sample in the reduced metallic form, i.e. Fe. The degree of conversion can be calculated as a function of time for the reducing period through reaction (A.2.1.2) when methane was used as fuel and through (A.2.1.3) when syngas was used.

$$X_i = X_{i-1} - \int_{t_0}^{t_1} \frac{1}{M_o P_{tot}} \dot{n}_{out} (4p_{CO_2,out} + 3p_{CO,out} - p_{H_2,out}) dt \quad (\text{methane}) \quad (\text{A.2.1.2})$$

$$X_i = X_{i-1} - \int_{t_0}^{t_1} \frac{1}{M_o P_{tot}} \dot{n}_{out} (2p_{CO_2,out} + p_{CO,out} - p_{H_2,out}) dt \quad (\text{syngas}) \quad (\text{A.2.1.3})$$

and for the oxidizing period from:

$$X_i = X_{i-1} + \int_{t_0}^{t_1} \frac{1}{M_o P_{tot}} (\dot{n}_{in} p_{O_2,in} - \dot{n}_{out} p_{O_2,out}) dt \quad (\text{A.2.1.4})$$

X_i is the conversion as a function of time for period i , X_{i-1} is the conversion after the preceding period, t_0 and t_1 are the times for the start and finish of the period respectively, M_o is the moles of active oxygen in the unreacted oxygen carrier, \dot{n}_{in} and \dot{n}_{out} are the molar flows of the gas going into and leaving the reactor after the water has been removed, P_{tot} is the total pressure, and $p_{O_2,in}$, $p_{O_2,out}$, $p_{CO_2,out}$, $p_{H_2,out}$ and $p_{CO,out}$ are the partial pressures of incoming and outlet O₂, and outlet partial pressures of CO₂, H₂ and CO after the removal of H₂O. $p_{H_2,out}$ was not measured on line but assumed to be related to the outlet partial pressure of CO and CO₂ through an empirical relation used in an earlier study. The calculated concentration of H₂ agreed relatively well with the concentration as calculated from the difference $1 - p_{CO_2,out} - p_{CO,out} - p_{CH_4,out}$ in the part of the reduction period where there is little or no back-mixing. The rate of reduction of the metal oxide was based on the conversion of the incoming methane or syngas and calculated for methane as

$$\frac{dX}{dt} = \frac{1}{M_o P_{tot}} \dot{n}_{in,CH_4} (4p_{CO_2} + 3p_{CO} - p_{H_2,out}) \quad (A.2.1.5)$$

and for syngas,

$$\frac{dX}{dt} = \frac{1}{2M_o P_{tot} (p_{CO_2} + p_{CO})} \dot{n}_{in} (2p_{CO_2} + p_{CO} - p_{H_2,out}) \quad (A.2.1.6)$$

where \dot{n}_{in,CH_4} is the incoming molar flow rate of methane to the reactor. A comparison of equation (A.2.1.2/A.2.1.3) and (A.2.1.5/A.2.1.6) shows that the important difference in calculation of the solid conversion and the rate of solid conversion is that the conversion uses the outgoing molar flow rate of gas, as measured in the gas analyzer, whereas the rate is calculated using the inlet molar flow rate of methane to the reactor.

In order to facilitate a comparison between the different oxygen carriers which contain varying amounts of oxygen depending upon the fraction of inert, a mass-based conversion was defined as:

$$\omega = \frac{m}{m_{ox}} = 1 + R_o (X - 1) \quad (A.2.1.7)$$

where R_o is the oxygen ratio, defined as:

$$R_o = (m_{ox} - m_{red}) / m_{ox} \quad (A.2.1.8)$$

The oxygen ratio is the theoretical maximum of mass fraction of oxygen that can be used in the oxygen transfer, and is dependent on the metal oxide used as oxygen carrier as well as the amount of inert in the particles. The mass-based reduction rate was calculated as,

$$\frac{d\omega}{dt} = R_o \frac{dX}{dt} \quad (A.2.1.9)$$

To compare the reactivity of the many different oxygen carriers tested, a rate index was calculated for each tested oxygen carrier. The methodology and assumptions for such a rate index follows here. If the mass transfer resistance between the bubbles and emulsion phases in the fluidized bed reactor is small, and assuming that the reaction between the methane and solid is first order with respect to methane, the exposure of particles to methane can be represented by a log-mean partial pressure of methane, p_m , which can be defined in terms of the inlet and outlet partial pressure:

$$p_m = \frac{p_{in} - p_{out}}{\ln\left(\frac{p_{in}}{p_{out}}\right)} \quad (A.2.1.10)$$

An effective first order reaction rate constant, k_{eff} , was defined as

$$k_{eff} = \frac{1}{p_m} \frac{d\omega}{dt} \quad (A.2.1.11)$$

A reaction rate normalized to a reference partial pressure of methane was calculated as

$$\left(\frac{d\omega}{dt}\right)_{norm} = k_{eff} \cdot p_{ref} \quad (\text{A.2.1.12})$$

where p_{ref} is a reference partial pressure of methane. Assuming an inlet partial pressure of methane of 1 and an outlet partial pressure of 0.001 the log-mean partial pressure would be 0.145, cf eq. A.2.1.10. Below, p_{ref} is chosen to be 0.15, which corresponds to a very high methane conversion. The fact that all of the oxygen was consumed in the initial part of the oxidation period suggests that there was good contact between all reacting gas and the particles in the reactor. Nevertheless, it should be noted that k_{eff} will include any mass-transfer between the bubble phase and emulsion phase. By utilizing the effective rate constant, a better comparison of reactivity data obtained under different methane concentrations in the reactor can be made. Although the effective reaction rate constant does not measure detailed kinetics, it facilitates an assessment of the reactivity to evaluate the feasibility of use of oxygen carriers, as well as a gives a basis for comparison.

A.1.2.2 Results and discussion

Analysis of fresh oxygen carriers. As seen in Table A.1.2.1 some of the prepared oxygen carriers were too soft and did not become spherical granulates after the sintering process. These are represented with horizontal lines in Table A.1.2.1, and are all three samples of Fe₂O₃/SiO₂, Mn₃O₄/SiO₂ sintered at 950°C and NiO/MgO sintered at 1100 and 1200°C. For

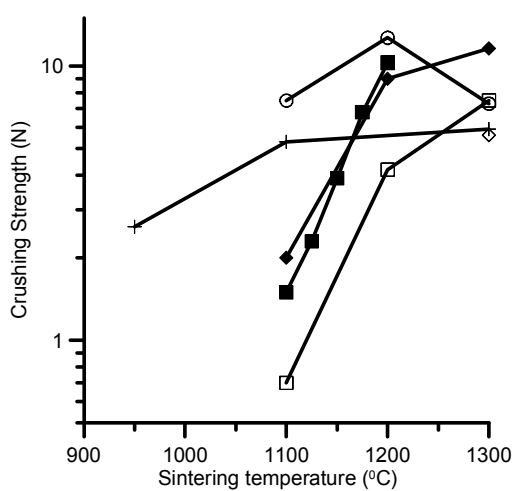


Figure A.1.2.1. Crushing strength as a function of the sintering temperature for iron based particles. + F4Z, ◆F6AB, □ F4AM, ■ F6AM and ○ F8AM

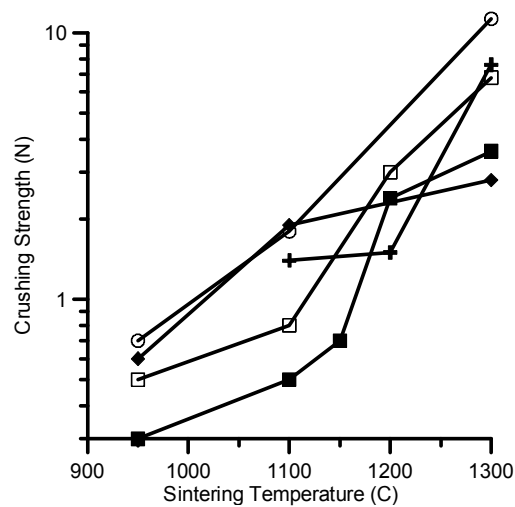


Figure A.1.2.2. Crushing strength as a function of the sintering temperature for manganese based particles. + M4S, ◇ M8T, ◆ M4Z, □ M4CaZ, ■ M4MgZ, ○ M4CeZ and ● M6AM.

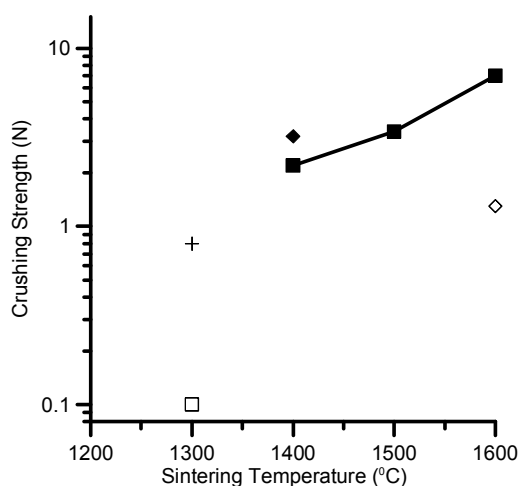


Figure A.1.2.3. Crushing strength as a function of the sintering temperature for nickel based particles. + N4AN1300, ◇ N4AN1600, ◆ N4AC, □ N4AB, ◆ N4AC and ■ N6AM

NiO/Ca-Al₂O₃ sintered at 1600°C, a single hard agglomerate was formed. For obvious reasons these mentioned particles were unsuitable for further testing for chemical-looping combustion. For almost all particles an increase in strength is observed when the sintering temperature is increased. This can be seen for all particles Figure A.1.2.1-A.1.2.3. As was found for extrudated particles at CSIC, also the freeze granulated particles based on Ni generally showed lower crushing strengths in comparison to Mn and Fe based carriers. All of the prepared samples were analyzed using x-ray powder diffraction before and after the experiments in the fluidized bed. In this way it is possible to identify crystalline phases in the solid samples and thus see possible interactions between the active metal oxide and the inert phase. The results are presented in Table A.1.2.2. As noted in the table, for some samples it was not possible to make conclusive judgements about the phases present. However, it is clear that for many of the systems there are chemical interactions between the inert and active phase even during heat treatment of the particles. However, from a technical point of view some systems which showed a high degree of interaction of inert and active material, for instance Fe₂O₃/MgAl₂O₄, showed high reactivity and limited deactivation during reactivity testing. This could mean that the new phases are not irreversible but can be reduced or oxidized or that only a small amount of the active material has reacted with the inert, and the rest is active.

Reactivity. Figure A.1.2.4a-d shows the outlet concentration of gaseous components for one reduction and one oxidation period conducted with an iron- and a nickel particle. During the reduction in Fig. A.1.2.4a and 4c, the incoming methane initially reacts completely to form mainly CO₂ and H₂O for both particles. For nickel oxides there is however a thermodynamic limitation, and hence some CO and H₂ are at all times present during the reduction. As the reaction proceeds and the degree of conversion is lower, the two particles behave differently. For iron, a large proportion of the methane pass unreacted through the bed and there is formation of some minor amounts of CO and H₂. H₂ is not measured on-line, but is rather assumed to be related to the outlet partial pressure of CO and CO₂ through an empirical relation based on the equilibrium of the gas-shift reaction. Since it was not measured on-line, it is not presented in the figures. For nickel, CH₄ does not pass through the reactor unreacted, but is catalyzed to CO and H₂, most likely through methane pyrolysis or steam reforming. Formed carbon can also be detected for some nickel oxides when the reduction is allowed to proceed to a low degree, i.e. when there is only a small amount of NiO in the particles. As for the oxidations in Figures A.1.2.4b and 4d, full conversion of the incoming oxygen occurs

initially. This means that the oxidation is limited by the supply of oxygen in these experiments, and all of the oxygen which is added to the bed reacts with the reduced particles. In order to gauge an oxidation reactivity which is not limited by addition of oxygen, smaller amounts of bed material would be needed. This is not feasible in these fluidized bed experiments, since enough material is needed to obtain proper fluidizing conditions as well as obtain an accurate measurement of the reduction rate. Thus, the major focus will therefore be on the reduction of the particles in this section. The concentration profiles in Figures A.1.2.4a-d are typical for iron and nickel oxides. For manganese based oxygen carriers the profiles are similar to iron, although in general slightly more reactive.

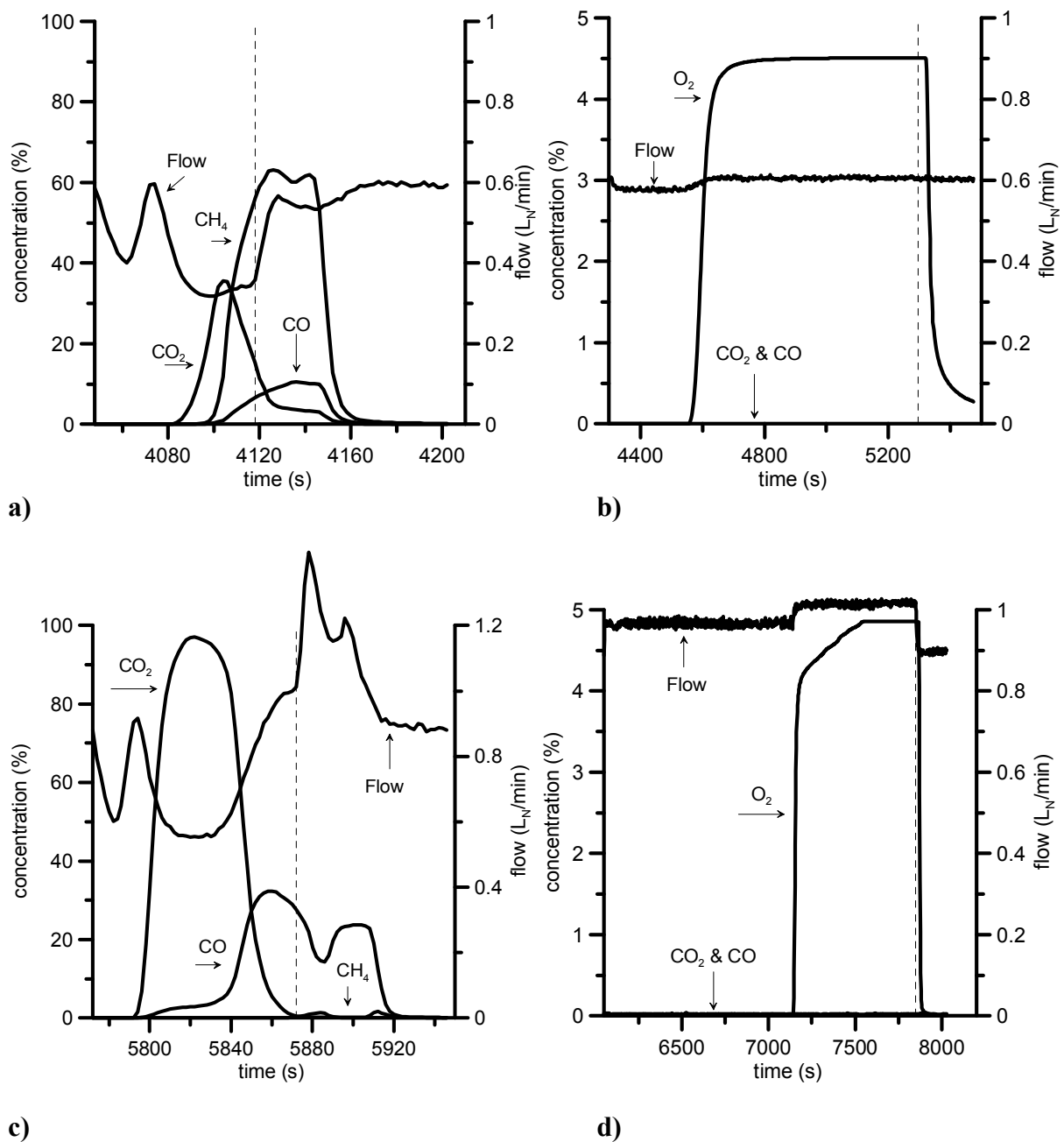


Figure A.1.2.4. Concentration profiles of a) reduction b) oxidation of F4AM950 and c) reduction d) oxidation of N6AM1400. Vertical dashed lines indicate transition to inert gas.

Table A.1.2.2. XRD results of freeze granulated particles before and after reactivity experiments.

	Fresh	After red.	After ox.	Comment
F4S950	Fe ₂ O ₃ , SiO ₂	-	-	
F4S1100	Fe ₂ O ₃ , SiO ₂	-	-	
F4S1300	Fe ₂ O ₃ , SiO ₂ (2)	-	-	
F4Z950	Fe ₂ O ₃ , ZrO ₂	Fe ₃ O ₄ , ZrO ₂	-	
F4Z1100	Fe ₂ O ₃ , ZrO ₂	Fe ₃ O ₄ , ZrO ₂	-	
F4Z1300	Fe ₂ O ₃ , ZrO ₂ , ZrSiO ₄	Fe ₃ O ₄ , ZrO ₂ , ZrSiO ₄	-	
F6A1300	Fe ₂ O ₃ , Al ₂ O ₃	Fe ₃ O ₄ , Al ₂ O ₃	Fe ₂ O ₃ , Al ₂ O ₃	
F6AB1100	Fe ₂ O ₃ , Al ₂ O ₃ (2)	Fe ₂ O ₃ , Fe ₃ O ₄ , Al ₂ O ₃	Fe ₂ O ₃ , Al ₂ O ₃ (2)	
F6AB1200	Fe ₂ O ₃ , Al ₂ O ₃ (2)	Fe ₃ O ₄ , Al ₂ O ₃	-	
F6AB1300	Fe ₂ O ₃ , Al ₂ O ₃ (2)	Fe ₃ O ₄ , Al ₂ O ₃	-	
F4AM1100	Fe ₂ O ₃ , Mg(Al,Fe) ₂ O ₄	Mg(Al,Fe) ₂ O ₄	-	Uncertain
F4AM1200	Mg(Al,Fe) ₂ O ₄	Mg(Al,Fe) ₂ O ₄	-	Uncertain
F4AM1300	Mg(Al,Fe) ₂ O ₄	Mg(Al,Fe) ₂ O ₄	-	Uncertain
F6AM1100	Fe ₂ O ₃ , Mg(Al,Fe) ₂ O ₄	MgFeAlO ₄ , Mg(Al,Fe) ₂ O ₄	-	Uncertain
F6AM1125	Fe ₂ O ₃ , Mg(Al,Fe) ₂ O ₄	MgFeAlO ₄ , Mg(Al,Fe) ₂ O ₄	-	Uncertain
F6AM1150	Fe ₂ O ₃ , Mg(Al,Fe) ₂ O ₄	MgFeAlO ₄ , Mg(Al,Fe) ₂ O ₄	-	Uncertain
F6AM1175	Fe ₂ O ₃ , Mg(Al,Fe) ₂ O ₄	MgFeAlO ₄ , Mg(Al,Fe) ₂ O ₄	-	Uncertain
F6AM1200	Fe ₂ O ₃ , Mg(Al,Fe) ₂ O ₄	MgFeAlO ₄ , Mg(Al,Fe) ₂ O ₄	-	Uncertain
F8AM1100	Fe ₂ O ₃ , Mg(Al,Fe) ₂ O ₄	MgFe ₃ O ₄ , MgFeAlO ₄	-	Uncertain
F8AM1200	Fe ₂ O ₃ , Mg(Al,Fe) ₂ O ₄	MgFe ₃ O ₄ , MgFeAlO ₄	-	Uncertain
F8AM1300	Fe ₂ O ₃ , Mg(Al,Fe) ₂ O ₄	MgFe ₃ O ₄ , MgFeAlO ₄	-	Uncertain
M4S950	Mn ₇ SiO ₁₂ , SiO ₂	-	-	Uncertain
M4S1100	Mn ₇ SiO ₁₂ , SiO ₂ etc.	Mn ₂ SiO ₄ , SiO ₂ etc.	-	Uncertain
M4S1200	MnSiO ₃ , SiO ₂ (3)	MnSiO ₃ , SiO ₂ (3)	-	Uncertain
M4S1300	Mn ₇ SiO ₁₂ , MnSiO ₃ , SiO ₂ etc.	Mn ₂ SiO ₄ , MnSiO ₃ , SiO ₂ etc.	-	Uncertain
M4Z950	Mn ₃ O ₄ , ZrO ₂ , C	MnO, ZrO ₂	-	
M4Z1100	Mn ₃ O ₄ , ZrO ₂ , C	MnO, ZrO ₂	-	

M4Z1300	Mn ₃ O ₄ , ZrO ₂ (2)	MnO, ZrO ₂ (2)	-	
M4CZ950	Mn ₃ O ₄ , ZrO ₂ , Ca _{0.15} Zr _{0.85} O _{1.85}	MnO, ZrO ₂ , Ca _{0.15} Zr _{0.85} O _{1.85}	-	
M4CZ1100	Mn ₃ O ₄ , ZrO ₂ , Ca _{0.15} Zr _{0.85} O _{1.85}	MnO, ZrO ₂ , Ca _{0.15} Zr _{0.85} O _{1.85}	-	
M4CZ1200	Mn ₃ O ₄ , ZrO ₂ , Ca _{0.15} Zr _{0.85} O _{1.85}	MnO, ZrO ₂ , Ca _{0.15} Zr _{0.85} O _{1.85}	-	
M4CZ1300	Mn ₃ O ₄ , ZrO ₂	MnO, ZrO ₂	-	
M4MZ950	Mn ₃ O ₄ , ZrO ₂	MnO, ZrO ₂	-	
M4MZ1100	Mn ₃ O ₄ , ZrO ₂	MnO, ZrO ₂	-	
M4MZ1150	Mn ₃ O ₄ , ZrO ₂	MnO, ZrO ₂	-	
M4MZ1200	Mn ₃ O ₄ , ZrO ₂	MnO, ZrO ₂	-	
M4MZ1300	Mn ₃ O ₄ , ZrO ₂	MnO, ZrO ₂	-	
M4CeZ950	Mn ₃ O ₄ , ZrO ₂ , Zr _{0.84} Ce _{0.16} O ₂	MnO, ZrO ₂ , Zr _{0.84} Ce _{0.16} O ₂	-	
M4CeZ1100	Mn ₃ O ₄ , ZrO ₂ , Zr _{0.84} Ce _{0.16} O ₂	MnO, ZrO ₂ , Zr _{0.84} Ce _{0.16} O ₂	-	
M4CeZ1300	Mn ₃ O ₄ , ZrO ₂ , Zr _{0.84} Ce _{0.16} O ₂	MnO, ZrO ₂ , Zr _{0.84} Ce _{0.16} O ₂	-	
N4AN1300	NiO, NiAl ₂ O ₄	Ni, NiAl ₂ O ₄	NiO, NiAl ₂ O ₄	
N4AN1600	NiO, NiAl ₂ O ₄	Ni, NiAl ₂ O ₄	-	
N4AC1400	NiO, NiAl ₂ O ₄ , CaSiO ₃	Ni, NiAl ₂ O ₄ , CaSiO ₃	-	
N4AC1600	-	-	-	
N4AB1300	NiO, NiAl ₂ O ₄	Ni, NiAl ₂ O ₄	-	
N6AM1400	NiO, MgAl ₂ O ₄ , NiAl ₂ O ₄	Ni, MgAl ₂ O ₄ , NiAl ₂ O ₄	NiO, MgAl ₂ O ₄ , NiAl ₂ O ₄	
N6AM1500	NiO, MgAl ₂ O ₄ , NiAl ₂ O ₄	Ni, MgAl ₂ O ₄ , NiAl ₂ O ₄	-	
N6AM1600	NiO, MgAl ₂ O ₄ , NiAl ₂ O ₄	Ni, MgAl ₂ O ₄ , NiAl ₂ O ₄	-	
N6M1100	MgNiO ₂	-	-	
N6M1200	MgNiO ₂	-	-	
N6M1300	MgNiO ₂	MgNiO ₂	-	

As indicated in Table A.1.2.1, three oxygen carriers did not show any significant reactivity at all, these were M4S1100, M4S1200 and N6M1300. The reason for this is most likely associated with the formation of irreversible compounds through solid state reactions that occurred between metal oxide and inert material during heat treatment. This was also confirmed through analysis with x-ray powder diffraction, see Table A.1.2.2. For this reason these three particles are not considered to be suitable for chemical-looping combustion.

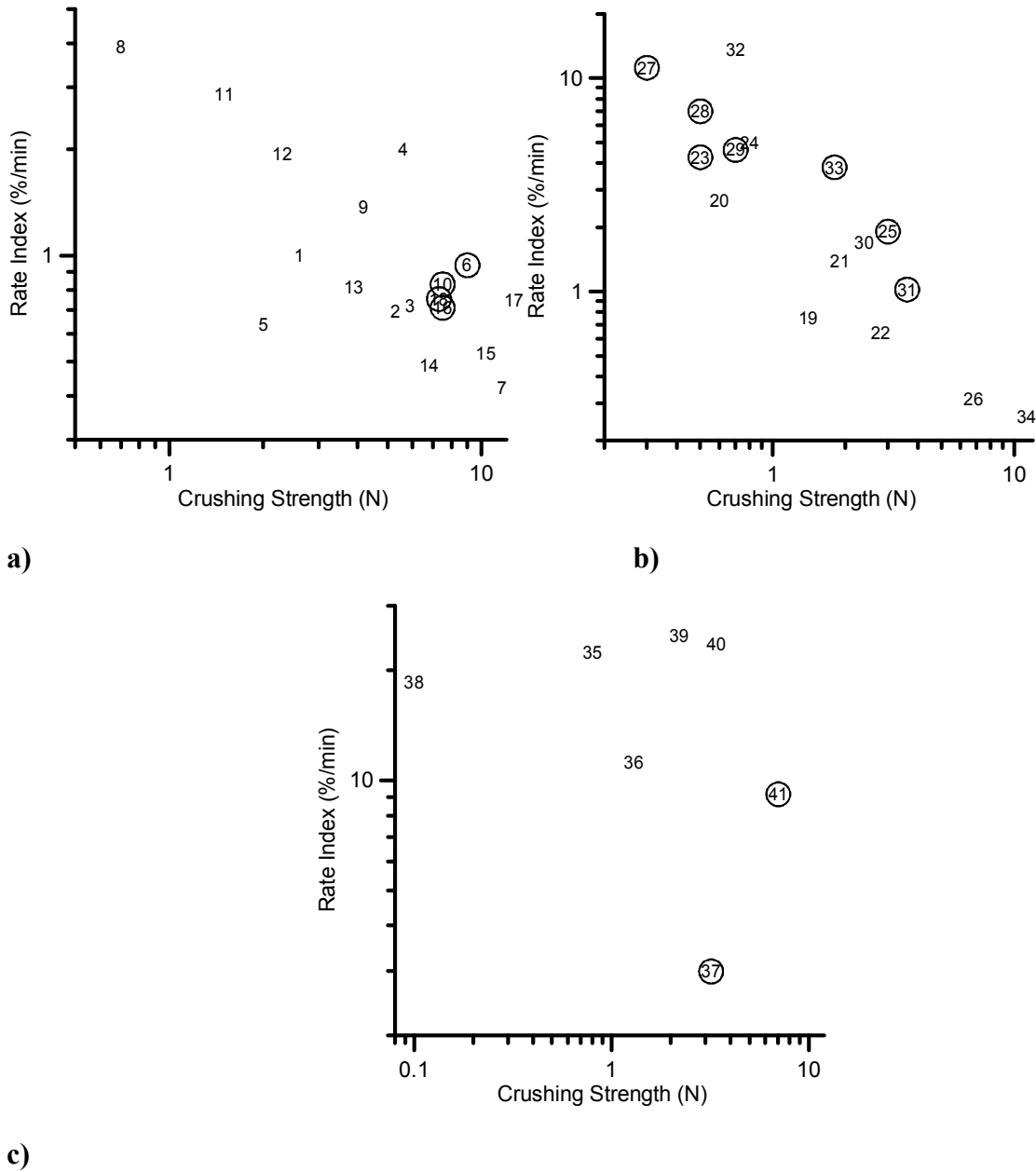


Figure A.1.2.5a-c. Rate index as a function of crushing strength for a) Iron-, b) Manganese- and c) Nickel based oxygen carriers. Numbers are taken from Table A.1.2.1. Circle around number indicates de-fluidization during reactivity investigation.

In Figure A.1.2.5 a-c the rate index vs. crushing strength is shown for iron, manganese and nickel based oxygen carriers. Note that the scales are logarithmic and differs significantly between the three figures. Also included in the figures are the particles which de-fluidized at some point during reaction, represented by circles. De-fluidization here means that a small force was necessary to separate the particle from each other after an experiment. The phenomenon of de-fluidization of oxygen carriers is not easy to define or understand, it was however clear that no severe agglomeration occurred at any of the investigated particles. Furthermore, experiments on the same particles in other reactors indicate that the problem of de-fluidization can be avoided by using larger height/width ratio of the bed, or by simply avoiding the reduction of the particles to too low degrees of conversion. Cho et al. found that iron oxide particles on alumina de-fluidized only when there was significant FeO formation. (Cho et al., 2005) Further Cho et al. investigated the 40% Mn₃O₄ on Mg stabilized ZrO₂ sintered at 1150°C, i.e. oxygen carrier #29, in more detail in the same paper, and found no signs of agglomeration independent of the time under reducing conditions. Thus, de-fluidization may not necessarily have to be a problem at scale-up. The tendency that hard particles are less reactive is clearly seen for the iron- and manganese particles. Since hard particles normally are less porous, it is not surprising that their reactivity is lower. For iron, F6A1300, F4AM1100 and F6AM1100 (#4, #8 and #11), seem to best suited for chemical-looping combustion, if the properties of reactivity, strength and good fluidization-behavior are all taken into consideration. Based on the same criteria, M4CeZ950 and M4CZ1100 (#32 and #24) would be the best option for the manganese oxides. However, more particles could be considered as suitable if de-fluidization is not a problem in scale-up. For nickel, N6AM1400 and N6AM1500 (#39 and #40) are the most promising particles; although both N4AN particles (#35 and 36) showed relatively high strength and reactivity. N4AB1300 (#38) is also very reactive but may be too soft to be suitable in a real application.

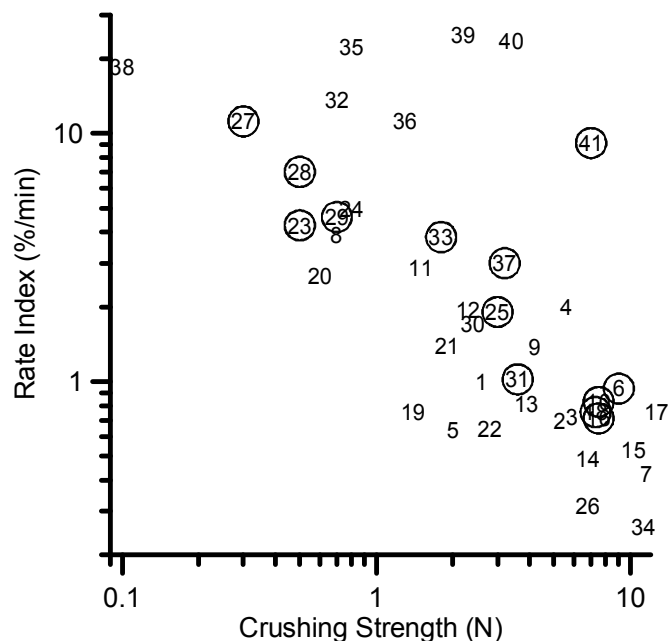


Figure A.1.2.6 Rate index as a function of crushing strength for all the investigated particles. Numbers are taken from Table A.1.2.1. Circle around number indicates de-fluidization.

When comparing all oxygen carriers it becomes clear that the nickel oxides are by far the most reactive ones. This can be seen in Figure A.1.2.6 where all investigated particles are displayed in one graph as rate index vs. crushing strength. Furthermore, the reactivities of the

most reactive nickel oxides are limited by the supply of incoming methane in the experiments, as can be seen in Figure A.1.2.4c. This means that the rate indexes presented for some nickel oxides are underestimated. The iron oxides are in general the hardest but not very reactive, whereas the manganese based carriers seem to be somewhere in-between nickel and iron in strength and reactivity. In general, de-fluidization mainly seems to concern manganese based oxygen carriers.

A.1.2.3 Conclusion

In this phase of the more than fifty oxygen carriers based on iron-, manganese- and nickel oxides on different inert materials were prepared. The carriers were tested with respect to parameters which are important for use in a chemical-looping combustor, i.e. reactivity, crushing strength as well as physical and chemical characterization. Reactivity tests under alternating oxidizing and reducing conditions were performed in a laboratory fluidized bed-reactor of quartz. Reduction was performed in 50% CH₄/50% H₂O while the oxidation was carried out in 5% O₂ in nitrogen. In general nickel particles are the most reactive, followed by manganese. Iron particles are harder but have a lower reactivity. An increase in sintering temperatures normally leads to an increase in strength and decrease in reactivity. Several particles investigated display a combination of high reactivity and strength as well as good fluidization behavior, and are feasible for use as oxygen carriers in chemical-looping combustion.

A.1.3 Selected particles for further testing

A vast number of oxygen carriers were tested at CSIC and Chalmers using three different type of preparation methods. Particles of all investigated transition state metals Fe, Cu, Ni and Mn were found which could feasible be used as oxygen carriers. More specifically the following particles were selected and tested further:

1. 10 wt% CuO on Al₂O₃ prepared by impregnation (C1A-I)
2. 60% Fe₂O₃ with Al₂O₃ prepared by freeze granulation (F6A-FG)
3. 40% NiO with Al₂O₃ prepared by freeze granulation (N4A-FG)
4. 60% NiO with MgAl₂O₄ prepared by freeze granulation (N6AM-FG)
5. 40% Mn₃O₄ with ZrO₂ (doped with Mg) (M4MZ-FG)

A.2 Task 2. Comprehensive testing of oxygen carrier particles

A.2.1. Work performed at CSIC

After the selection of the most feasible oxygen carriers to be used in a CLC, a detailed reactivity of the materials was carried out to determine their behaviour during the reduction with CO and H₂, and oxidation reactions at different operating conditions, and to determine the kinetic parameters. The oxygen carriers selected for this study were C1A-I, F6A-FG, and N4A-FG, which properties are showed in Table A.2.1.1.

Table A.2.1.1. Properties of the oxygen carriers.

	C1A-I	F6A-FG	N4A-FG
Active MeO content (wt %)	10	45	40
Particle size (mm)	0.17	0.15	0.2
Porosity	0.57	0.30	0.36
Specific surface area BET (m ² g ⁻¹)	41.3	2.5	0.8
Apparent density (kg m ⁻³)	1800	3257	3446
Oxygen transport capacity, R ₀	2.0	1.3	8.4

A.2.1.1. Task 2.1. Detailed reactivity analysis

The kinetic of the reduction and oxidation reactions has been carried out in a CI thermobalance (see section A1.1). The composition of the gas used for the reduction reaction was varied to cover the great majority of the gas concentrations present in the fuel reactor of a CLC system (Fuel (CO, H₂): 5-70 vol. %; H₂O: 0-48 vol. %; CO₂: 0-40 vol. %). For the oxidation reaction, oxygen concentrations from 5 to 21 vol. % were used. Moreover, several temperatures from 773 to 1223 K were used to determine the kinetic parameters of the different oxygen carriers.

Kinetic model. There are several resistances that can affect the reduction reaction rate of the oxygen carrier with the fuel gas or the oxidation with air. Previous calculations showed that both external and internal mass transfer resistances were not important in the reactions involved in CLC systems. Moreover, the reaction heat did not affect the particle temperature, and isothermal particles were considered (García-Labiano et al., 2005). For the oxygen carriers produced by freeze-granulation or mechanical mixing, it was assumed that the grains of the reactive material are homogeneously distributed inside the particle together with the grains of the inert material. In this case, the changing grain size model (CGSM) used to determine the kinetic parameters considered that the oxygen carrier was composed by independent grains of metal oxide and inert. However, when the oxygen carriers were prepared by impregnation, it seems more feasible to think that the metal oxide was homogeneously distributed all over the particle covering the surface of the pores (García-Labiano et al., 2004b). In this case, the shrinking core model for plate-like geometry in the

porous surface of the particle was used for the kinetic determination. Table A.2.1.2 shows the CGSM equations used for the kinetic determination. These equations also consider the thermodynamic limitations existing in the gas concentration when the Ni-based oxygen carriers are used, and the effect of the gas product in the diffusion resistance. Table A.2.1.3 shows the kinetic parameters determined for the different oxygen carriers and reactions including the reduction with CO and H₂, and the oxidation with air.

Cu-based oxygen carrier. (C1A-I). In the fuel and air reactors of a CLC system, the oxygen carrier will react with the fuel gas (CO or H₂) or the oxygen under different gas concentrations at different locations of the reactor. To determine the effect of the fuel gas concentration on the reduction reaction rate, several experiments were carried out at 1073 K

Table A.2.1.2. Equations used for the kinetic determination

Chemical reaction	
Spherical grains	
$\frac{t}{\tau_r} = 1 - (1 - X)^{1/3}$	$\tau_r = \frac{\rho_m r_0}{b k (C^{n_1} - C_{eq}^{n_1})}$
	$k = k_0 e^{-E/RT}$
Plate-like geometry (for oxygen carriers prepared by impregnation: Cu-based oxygen carriers)	
$\frac{t}{\tau_r} = X$	$\tau_r = \frac{\rho_m L}{b k C^{n_1}}$
Product layer diffusion	
$\frac{t}{\tau_d} = \left[1 - (1 - X)^{2/3} + \frac{1 - [Z + (1 - Z)(1 - X)^{2/3}]}{Z - 1} \right]$	$\tau_d = \frac{\rho_m r_0^2}{2 b D_e C^{n_2} (1 + k_{H_2O} C_{H_2O}^{n_3})}$
$D_e = D_{e,0} e^{-k_x X}$	$D_{e,0} = D_{e,00} e^{-E/RT}$
	$k_x = k_{x,0} e^{-E/RT}$

with CO and H₂. Figure A.2.1.1 shows the results obtained with the oxygen carrier as a function of the fuel gas concentration. The experimental data are represented by symbols and the model predictions with the kinetic parameters finally obtained are plotted in all the figures as continuous lines. Similar experiments were carried out to know the effect of the oxygen concentration. These experiments were used to determine the reaction order of the different reactions, which are showed in Table A.2.1.2.

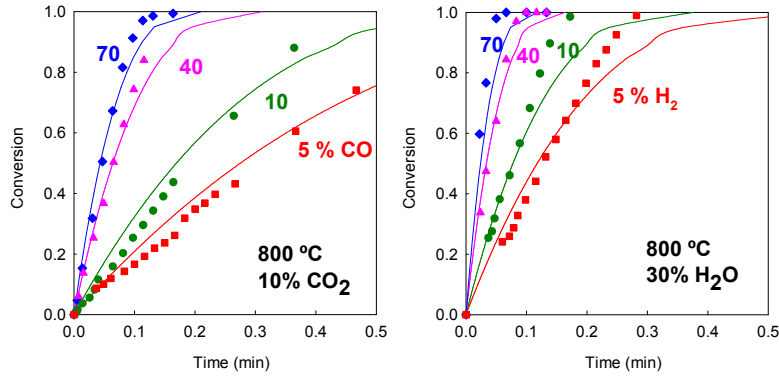


Figure A.2.1.1. Effect of gas concentration on the reduction reaction of the C1A-I oxygen carrier. P=1 atm.

Table A.2.1.3. Kinetic parameters of the oxygen carriers.

	C1A-I			F6A-FG			N4A-FG		
	H ₂	CO	O ₂	H ₂	CO	O ₂	H ₂	CO	O ₂
Physical parameters									
ρ_m (mol/m ³)	80402	80402	140251	32811	32811	22472	89290	89290	151520
r or L (m)	4.0 10 ⁻¹⁰	4.0 10 ⁻¹⁰	2.3 10 ⁻¹⁰	2.6 10 ⁻⁷	2.6 10 ⁻⁷	2.6 10 ⁻⁷	6.9 10 ⁻⁷	6.9 10 ⁻⁷	5.8 10 ⁻⁷
b	1	1	2	3	3	4	1	1	2
Kinetic parameters *									
k_0 (mol ¹⁻ⁿ m ³ⁿ⁻² s ⁻¹)	1.0 10 ⁻⁴	5.9 10 ⁻⁶	4.7 10 ⁻⁶	2.3 10 ⁻³	6.2 10 ⁻⁴	3.1 10 ⁻⁴	9.3 10 ⁻³	5.2 10 ⁻³	1.8 10 ⁻³
E (kJ/mol)	33	14	15	24	20	14	26	25	7
n	0.6	0.8	1.0	0.8	1.0	1.0	0.5	0.8	0.2
$D_{e,00}$ (m ² /s)							1.5·10 ⁻⁷		
E (kJ/mol)							0		
n ₂							0		
$k_{x,0}$							40.3		
E (kJ/mol)							17.6		
k_{H_2O} (m ³ /mol) ³							-0.6		
n ₃							0.25		
Effect of pressure									
d	0.53	0.83	0.68	1.03	0.89	0.84	0.47	0.93	0.46

The effect of the temperature on the reaction rate of the oxygen carrier was later investigated. Figure A.2.1.2 shows an example of the conversion versus time data obtained at temperatures from 773 to 1073 K for the different gases. It is remarkable the high initial reaction rates of the oxygen carrier even at low temperatures. The reduction reaction was normally composed by two different steps at temperatures below 973 K. The initial stage was characterized by a high reaction rate, which was followed by a sharply decrease in the reactivity. These steps would be associated to different resistances to the global reaction, that is, the chemical reaction and the product layer diffusion, respectively. However, the decrease in the reaction rate did not take place at typical temperatures used in CLC systems (> 1023 K), and the full conversion was reached at a nearly constant reaction rate. In these cases, it can be considered that the chemical reaction controls the reduction of the oxygen carrier. Therefore, only the parameters corresponding to this resistance were determined in this study.

On the other hand, the oxidation reaction was very quick even at the lowest temperature tested, 773 K. Oppositely to the reduction reaction, no decrease in the reaction rate was observed during the oxidation reaction, and the oxygen carrier was completely oxidized in a very short period of time.

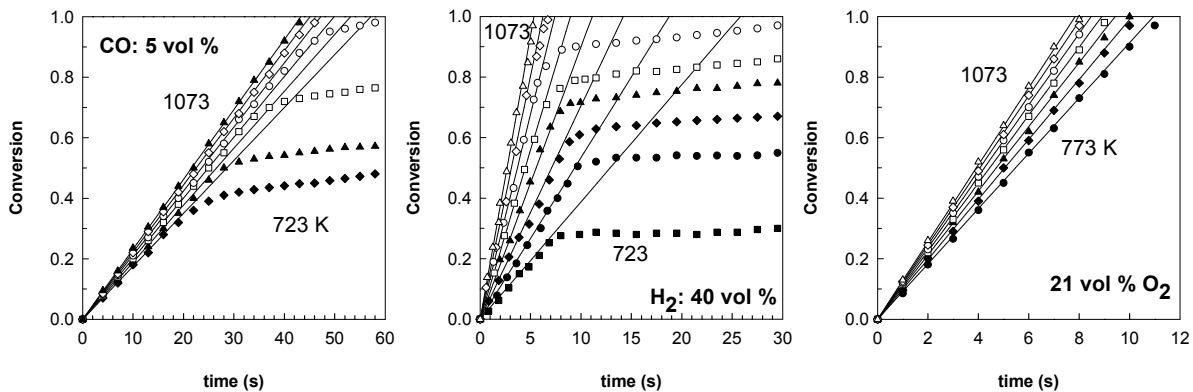


Figure A.2.1.2. Effect of temperature on the reduction reaction of the oxygen carrier with different fuel gases; temperature (K): ■ 723, ● 773, ◆ 823, ▲ 873, □ 923, ○ 973, ◇ 1023, △ 1073; — model predictions.

In the fuel reactor of a CLC system, the oxygen carrier is also in contact with the H₂O and/or CO₂ produced during the reaction. Several experiments carried out with different gas product concentrations showed that these gases did not affect the reaction rate of the CuO impregnated on alumina with CO or H₂.

Fe-based oxygen carrier. (F6A-FG). This oxygen carrier was prepared by freeze-granulation at Chalmers. The particles were prepared using 60% Fe₂O₃ and 40% Al₂O₃. Experiments in the TGA showed that not all of the oxygen in the Fe₂O₃ was active, but rather that it contained 45% of active Fe₂O₃ under these reaction conditions. This is likely due to that the reduced state is FeO. Iron compounds needs special attention due to their different oxidation states (Fe₂O₃-Fe₃O₄-FeO-Fe). Depending on gas composition, the reduction of Fe₂O₃ can finish in one of the above products, and consequently, the value of R₀ will be very different depending on the reaction considered. However, only the transformation from hematite to magnetite (Fe₂O₃ - Fe₃O₄) may be applicable for industrial CLC systems. Further reduction to FeO would produce a high decrease in the CO₂ purity obtained in the fuel reactor because of the increase in the equilibrium concentrations of CO and H₂ (Copeland, 2001). Because in the TGA system it was not possible to stop the reaction in the Fe₃O₄ product, the first part of the

experimental curves was used to determine the kinetic of the reaction from Fe₂O₃ to Fe₃O₄. On the other hand, the oxidation curves depended on the final products obtained during the reduction step. In this work, only the oxidations corresponding to the transformation FeO-Fe₂O₃ were considered.

Figure A.2.1.3 shows the results obtained with the Fe-based oxygen carrier as a function of the fuel gas concentration. The oxygen carrier exhibited a high reactivity both for reduction and oxidation with full conversion to Fe₃O₄ in times lower than 0.5 minute in the majority of the conditions. Figure A.2.1.4 shows the conversion versus time data obtained at temperatures from 1073 to 1223 K for the different fuel gases (CO, H₂) and air. This oxygen carrier exhibited very low dependence on temperature in all cases, which gave very low activation energies, as can be observed in Table A.2.1.3.

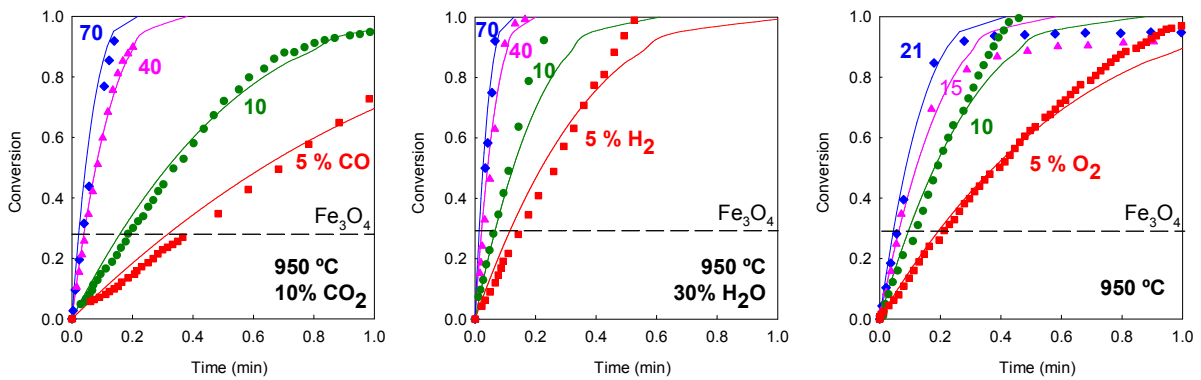


Figure A.2.1.3. Effect of gas concentration on the reduction and oxidation reactions of the Fe-based oxygen carrier. Transformation Fe₂O₃-Fe₃O₄.

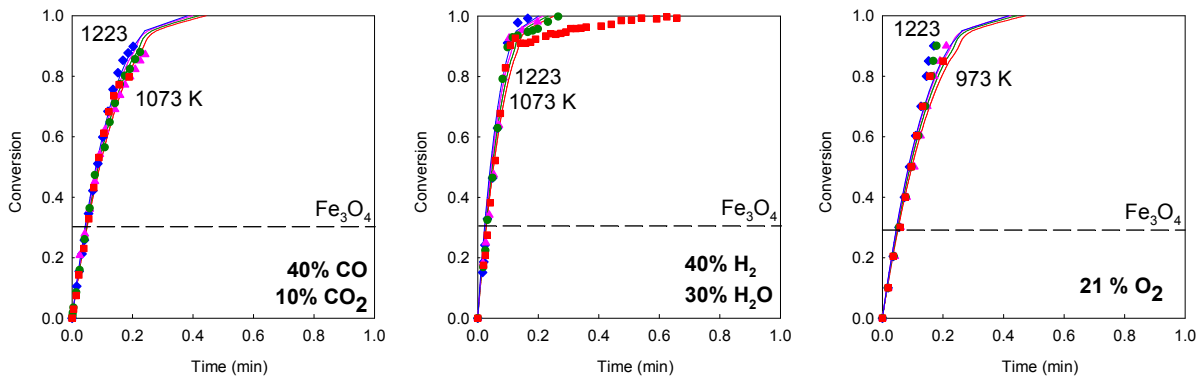


Figure A.2.1.4. Effect of temperature on the reduction and oxidation reactions of the Fe-based oxygen carrier. Transformation Fe₂O₃-Fe₃O₄.

Ni-based oxygen carrier. (N4A-FG). This oxygen carrier was prepared by freeze-granulation at Chalmers, and contained a 40% of active NiO. When a Ni-based oxygen carrier is used in a CLC system, it is not possible to achieve the complete fuel gas conversion because of thermodynamic limitations. The equilibrium constants for the reduction reactions are the following:





In this case, it is necessary to consider the gas concentration at the equilibrium in the kinetic study, as can be observed in the equations showed in Table A1.2.1. To determine the effect of the fuel gas concentration on the reduction reaction rate, several experiments were carried out at 1223 K with CO and H₂. Figure A.2.1.5 shows the results obtained with the Ni-based oxygen carrier as a function of the fuel gas concentration. Similar experiments were carried out to know the effect of the oxygen concentration. The reaction order for the different reactions obtained from these experiments is showed in Table A.2.1.3.

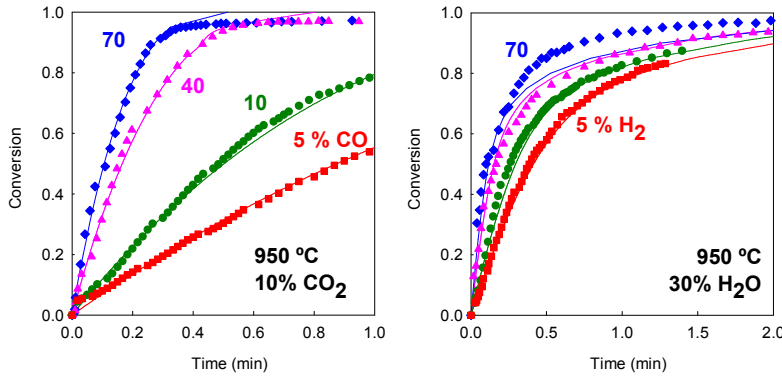


Figure A.2.1.5. Effect of gas concentration on the reduction reaction of the Ni-based oxygen carrier.

The effect of the temperature on the reaction rate of the Ni-based oxygen carrier was later investigated. Figure A.2.1.6 shows the conversion versus time data obtained at temperatures from 1073 to 1223 K for the different fuel gases (CO, H₂) and air. As was the case with the Cu-based oxygen carrier, this carrier also exhibited high initial reaction rates even at low temperatures, reaching a conversion of 50% at times lower than 30 seconds. However, the reaction rate decrease a lot for the last part of the curve. These two steps were associated again with the different resistances affecting to the global reaction, that is, the chemical reaction and the product layer diffusion, respectively. The mixed effect of both resistances made that the curves corresponding to the reduction with H₂ at different temperatures were crossed. The initial part of the curves (up to conversions above 60%) was well predicted with chemical reaction control but for the prediction of the whole reduction curve it was necessary to add the parameters corresponding to the product layer diffusion resistance.

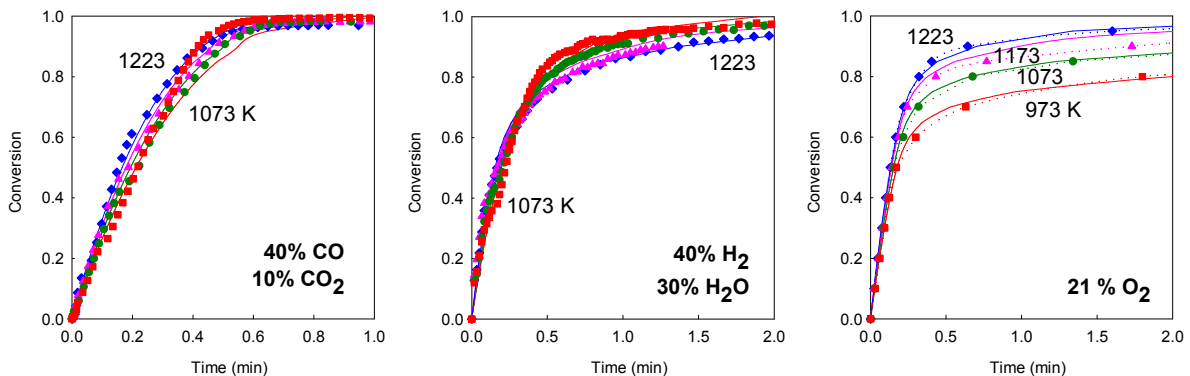


Figure A.2.1.6. Effect of temperature on the reduction and oxidation reactions of the Ni-based oxygen carrier.

On the other hand, the oxidation reaction was very quick at all temperatures in the initial stages. However, the decrease in the reaction rate started at different conversions depending on the temperature tested. In this case, it was necessary to use a product layer diffusivity depending on the conversion, increasing the number of parameters necessary for the prediction of the experimental curves in the whole range of time.

Effect of pressure. The present trend in the syngas production in power plants is towards the pressurized operation, as it is normal in the integrated gasification combined cycle (IGCC) systems because, allows the increase of the thermal efficiencies (Takematsu, 1991). The use of a pressurized CLC system would have also several advantages. First, the efficiency of the cycle in the CLC power plant will be increased (Wolf et al., 2001); second, recovering of the CO₂ as a high-pressure gas requires only a very small amount of additional power for further compressing the CO₂ to pipeline (35 atm) or sequestration pressure (100 atm), (Copeland et al., 2001). However, very little work can be found in the literature about the pressure operation of CLC (Copeland et al., 2001; Jin and Ishida, 2002, 2004; Ryu et al., 2002; Wolf et al., 2005).

To analyse the effect of total pressure on the behaviour of the oxygen carriers, several experiments were carried out in a pressurised Cahn TG-2151 thermobalance (Figure A.2.1.7). The thermobalance consists of a quartz tube (31 mm i.d.) placed in an oven that can be operated at pressurized conditions. To reduce mass transfer resistance around the sorbent sample, the sample holder was a wire mesh platinum basket (11 mm diameter and 4 mm height). Temperature, pressure, and sample weight were continuously measured and recorded on a computer. The reacting gas mixture (83 cm³ s⁻¹ STP) containing H₂/N₂, or CO/CO₂/N₂, or O₂/N₂ were controlled by electronic mass flow controllers. Condensation problems in the lower part of the PTGA prevent the H₂O feeding in the system. On the other hand, CO₂ was introduced together with CO to avoid carbon formation by the Boudouard reaction.

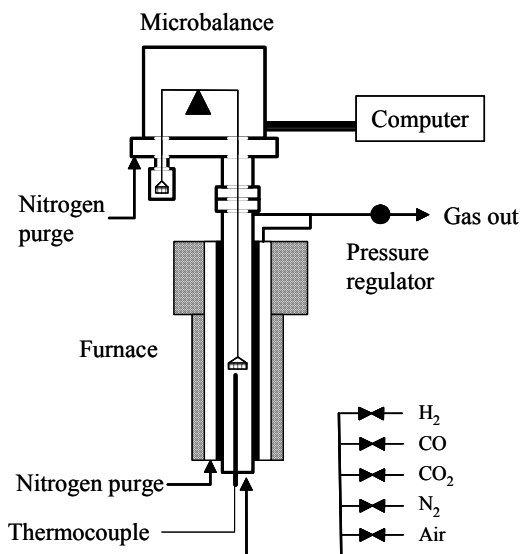


Figure A.2.1.7. Scheme of the pressurised thermogravimetric analyzer (PTGA).

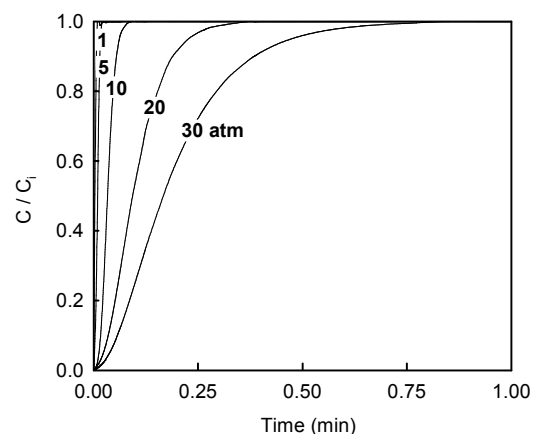


Figure A.2.1.8. Real gas concentration around the sample particles in the PTGA.

Gas dispersion in the PTGA. A common problem in the use of PTGA is that the inlet gas flow is limited by the disturbances produced in the weight signal when high pressures are used. For the maximum gas flow used in the PTGA system at high pressures, the assumption of gas plug flow is not correct and the gas concentration around the particles is not constant during the initial stages of reaction. To determine the gas dispersion in the PTGA system, a gas analyzer was located at the outlet of the system, after the pressure control valve. A step gas tracer input allowed us to determine the F curve at different total pressures, and the gas dispersion in the sample location was calculated with the equations for non-ideal flows in practical reactors (Danckwerts, 1958; Levenspiel, 1981). Figure A.2.1.8 shows the gas concentration around the sample particles as a function of time for different pressures, working at the maximum stable flowrate (4 l/m STP). The times necessary to reach the desired concentration varied from ≈ 1 s at atmospheric pressure up to ≈ 40 s at 30 atm.

To analyze the effect of total pressure on the behaviour of the oxygen carriers, two kinds of experiments were carried out in the PTGA. First, experiments with a constant molar fraction (10 vol %) of reducing gas, CO or H₂, and different total pressures up to 30 atm were performed at 1073 K. Figure A.2.1.9 shows, as an example, the results obtained during the reduction of the Cu-based oxygen carrier. Since an increase in the operating pressure represents also an increase in the reacting gas partial pressure, an increase in the reaction rate of the oxygen carriers would be expected. However, a small decrease in the reaction rate with increasing pressure was detected for all the oxygen carriers and reactions analyzed in this work. It must be considered, however, that the experimental data is the result of several effects acting together as total pressure, partial pressure, and gas dispersion.

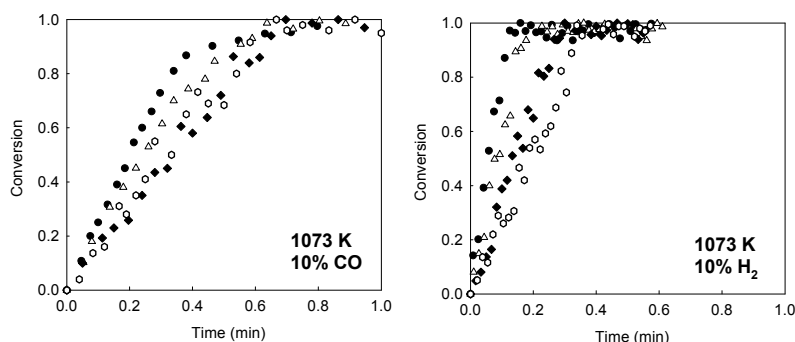


Figure A.2.1.9. Effect of total pressure on the reduction reactions with CO and H₂ of the Cu-based oxygen carrier for a constant molar fraction of reacting gas. Experimental data: \square 1 atm, \bullet 5 atm, \triangle 10 atm, \blacklozenge 20 atm, \circ 30 atm.

To deeply analyze the effect of total pressure, other experiments were performed with a constant gas partial pressure of 1 atm. Figure A.2.1.10 shows the results obtained at 1073 K for the different oxygen carriers and reaction gases. A sharp decrease of the reaction rate with increasing total pressure was observed in all cases. This negative effect of pressure has been also observed by other authors in several gas-solid reactions (Agnihotri et al, 1999; Qiu et al., 2001; Adánez et al., 2004a; García-Labiano et al., 2004b).

Because of the gas dispersion existing in the PTGA system at high pressures, the reactivity data was obtained with a non-constant concentration, and equations of Table A.2.1.2 could not be directly used to determine the kinetic parameters. However, it was possible to know the instantaneous reaction rates, dX/dt , obtained with the real gas concentrations around the

sample particles showed in Figure A.2.1.8. The theoretical conversions versus time curves were obtained by integration of the instantaneous reaction rate values.

The use of CGSM and the kinetic parameters obtained at atmospheric pressure together with the real gas concentrations around the particles, which were obtained considering the gas dispersion in the system, were unable to predict the experimental results obtained at higher pressures. Changes in the diffusivity values, within normal ranges, by the effect of pressure

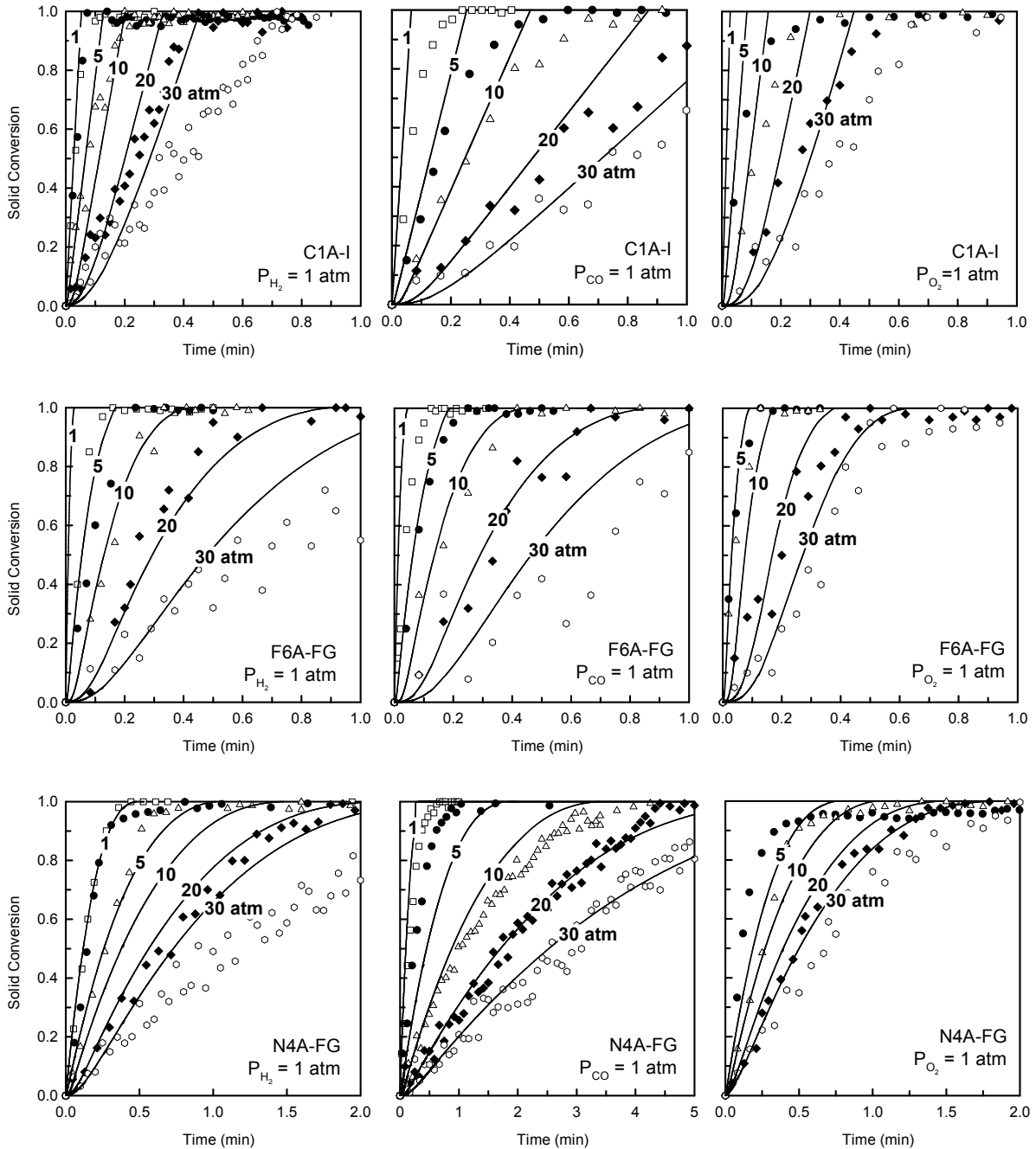


Figure A.2.1.10. Effect of total pressure on the reduction and oxidation reactions of the oxygen carrier for a constant partial pressure of reacting gas. Experimental data: \square 1 atm, \bullet 5 atm, \triangle 10 atm, \blacklozenge 20 atm, \circ 30 atm. Continuous lines = model predictions considering the effect of pressure and gas dispersion.

were not valid to predict the experimental results at pressurised conditions. The most probable reason of the pressure effect was the changes suffered by the oxygen carriers in their internal structure during pressure operation (Chauk et al., 2000) although this aspect was not be corroborated in this work. To know the magnitude of the effect of total pressure on the decrease of the reaction rates, an empirical fit was done. The value of the preexponential factor at pressurized conditions, $k_{0,p}$, which best fit the experimental data considering the gas dispersion was obtained for each oxygen carrier and reaction. Figure A.2.1.11 shows the $k_{0,p}/k_0$ values obtained for all reactions as a function of total pressure. In the majority of the cases, a sharp decrease in the value of $k_{0,p}$ was observed when the pressure changed from 1 to 5 atm, with a smoother decrease for increasing pressures. For some reactions the decrease was softer, although in any case the values of $k_{0,p}$ at 30 atm were between 5 and 95 times lower than at atmospheric pressure. Finally, an apparent preexponential factor was determined as a function of total pressure and the preexponential factor obtained at atmospheric pressure

$$k_{0,p} = \frac{k_0}{P^d} \tag{A.2.1.3}$$

Table A.2.1.3 shows the values of the parameter "d" obtained for the different oxygen carriers and reacting gas. In this way it was possible to predict the experimental results, showed as continuous lines in Figure A.2.1.10, within the range of total pressures used and when the molar fraction or the partial pressure of the reacting gas was maintained constant.

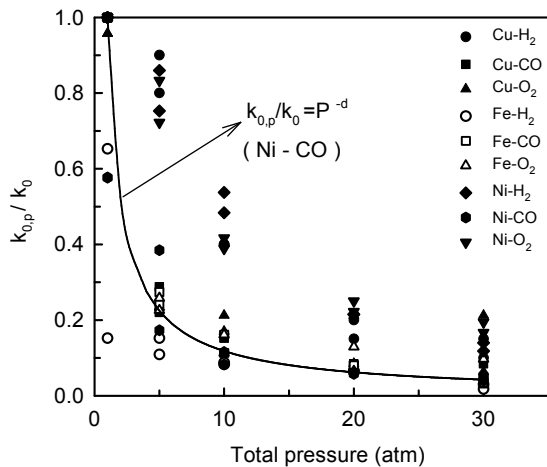


Figure A.2.1.11. Effect of total pressure on the decrease of the preexponential factor for the different oxygen carriers and reactions.

Application of reactivity to design criteria. The kinetic data above obtained at atmospheric pressure were used to calculate some design parameters of a CLC system, as the recirculation rate and the total solid inventory. More information about the detailed mathematical equations can be found in García-Labiano et al. (2004b). The oxygen carrier used for this study was the C1A-I.

Recirculation rate. The CLC concept is based in the transport of oxygen from the air to the fuel reactor by means of a carrier. The recirculation rate of oxygen carrier can be calculated from a mass balance in the fuel reactor, and it mainly depends on the conversion variation obtained by the oxygen carrier in the fuel and air reactors. Figure A.2.1.12 shows the recirculation rate as a function of the solid conversion variation to obtain complete conversion

of fuel gas ($\Delta X_f=1$), and taking as reference a power plant of 1 MW_f. To obtain 1 MW_f, a flow of 1.25 mol CH₄ s⁻¹, 3.53 mol CO s⁻¹, or 4.14 mol H₂ s⁻¹ are necessary, as a consequence of their different combustion heat ($\Delta H_{c,CH_4} = -802$ kJ mol⁻¹, $\Delta H_{c,CO} = -283$ kJ mol⁻¹, $\Delta H_{c,H_2} = -242$ kJ mol⁻¹). It must be also considered that to obtain 1 MW_f from the use of CH₄, H₂, or CO it is necessary to transport 5, 4.14, or 3.53 mol O s⁻¹, respectively. Obviously, the solid flow was higher as the transport of oxygen needed for the reaction became higher, although the differences between the three fuel gases were small. The lowest solids flow per MW_f of fuel gas corresponded to the N4A-FG oxygen carrier due to the high oxygen transport capacity of the NiO and to the high active metal oxide content (40 wt%). The other oxygen carriers showed similar recirculation rates. The values found for the C1A-I oxygen carrier is a combination of the high oxygen transport capacity of the CuO and the low active metal oxide content (10 wt%), while the Fe45Al-FG oxygen carrier has a high active metal content (45 wt%) and low oxygen transport capacity.

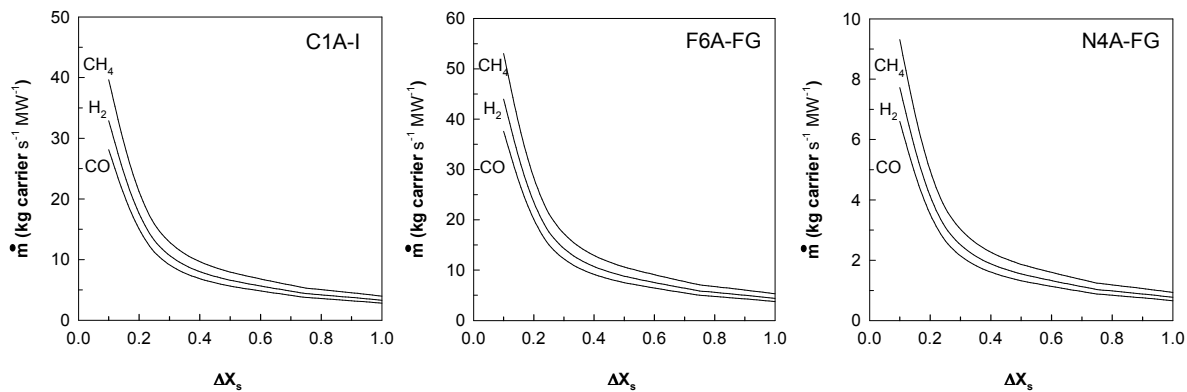


Figure A.2.1.12. Recirculation rate as a function of the oxygen carrier conversion (oxygen carrier C1A-I; 1 MW_f of fuel gas).

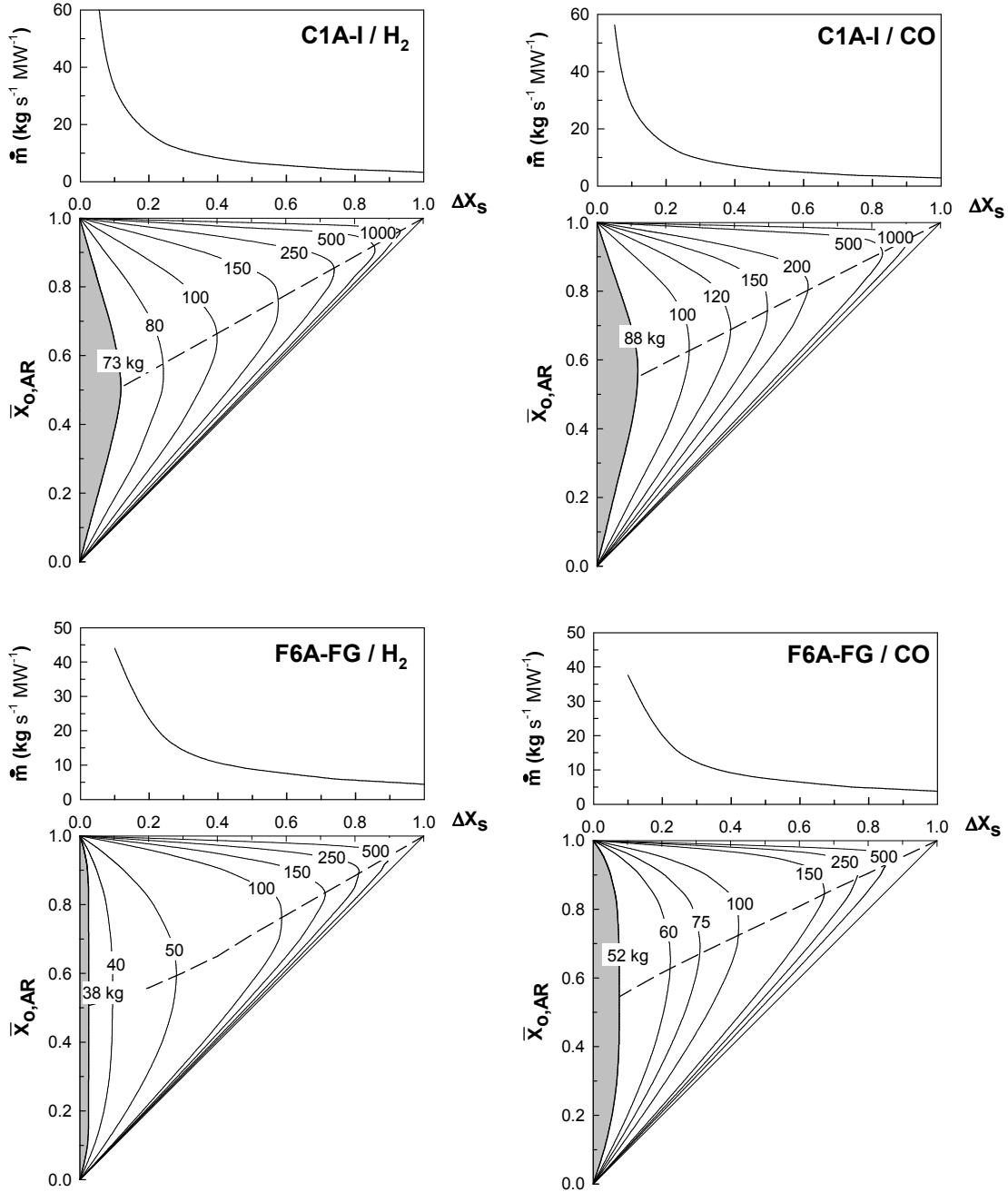
It must be considered however that for the Cu-based oxygen carriers the recirculation rate is not limited by the heat balance, as it happens with the Fe and Ni- based oxygen carriers, because both the reduction and the oxidation reactions are exothermic. The heat transport from the air reactor to the fuel reactor necessary to fulfill the heat balance in the system when using Fe- and Ni-based oxygen carriers forces in these cases to the use of high recirculation rates.

Solids inventory. The solids inventory in the CLC system for any fuel conversion can be obtained from a mass balance to the solid and gas in the fuel and air reactors. Therefore, the solid inventory for a given oxygen carrier depends on the recirculation rate and on the solid conversion at the inlet to each reactor, as well as on their metal oxide content and reactivity.

For preliminary estimations, it has been considered that the reactions between the gas fuel and air with the oxygen carrier take place in a bubbling fluidized beds (fuel reactor) or in the dense zone at the bottom of the riser (air reactor). Therefore, it was assumed perfect mixing of the solids, gas plug flow in the beds, no resistance to the gas exchange between the bubble and emulsion phases, and complete conversion of the gas fuel.

Figure A.2.1.13 shows the total inventory of oxygen carrier per MW_f of CO and H₂ in the CLC system as a function of the oxidation conversion in the air reactor, $\bar{X}_{o,AR}$, and the

variation of solid conversion between the two reactors, ΔX_s . Obviously, $\bar{X}_{o,AR}$ is the same to the solid conversion at the inlet of the fuel reactor, $\bar{X}_{o,inFR}$. The solid conversion at the inlet of the air reactor, $\bar{X}_{o,inAR}$, can be calculated directly from $\bar{X}_{o,inFR}$ and ΔX_s . The level curves indicate conditions with a same total solid inventory of oxygen carrier in the CLC system.



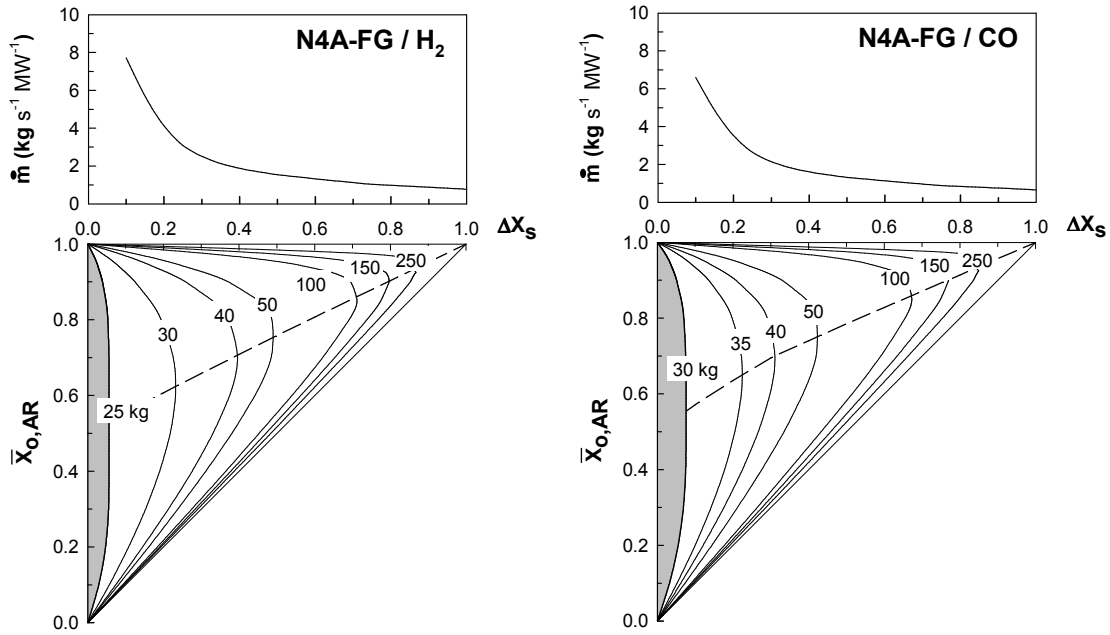


Figure A.2.1.13. Total solids inventory of oxygen carrier (fuel and air reactors) for the combustion of 1 MW_f of CO and H₂. Zone with the same solid inventory; - - - minimum solid inventory at a fixed ΔX_s.

It can be observed that, for a given ΔX_s, the total solid inventory presents a minimum with $\bar{X}_{o,AR}$. On the other hand, for a given $\bar{X}_{o,AR}$, the solid inventory in each reactor, and therefore in the whole CLC system, increases as ΔX_s increases. At values of ΔX_s lower than 0.1, there are different pairs of values ($\bar{X}_{o,AR}$, ΔX_s) that fulfill the minimum solids inventory in the

Table A.2.1.4. Minimum solid inventories for different fuel gases at atmospheric pressure.

	Cu10Al-I			F6A-FG			N4Al-FG		
Fuel gas	CH ₄	H ₂	CO	CH ₄	H ₂	CO	CH ₄	H ₂	CO
Solid inventories (Kg of oxygen carrier)									
Minimum	112	73	88	130	38	52	32	25	30
Minimum at ΔX _s =0.3	133	86	104	175	52	71	44	35	40
Solid inventories (Kg of MeO used)									
Minimum	14.5	9.5	11.5	78	22.8	31.2	19.2	15	18
Minimum at ΔX _s =0.3	17.3	11.2	13.5	105	31.2	42.6	26.4	21	10.8

system. Table A.2.1.4 shows the minimum solids inventory per MW_f of CH₄, H₂ and CO. Although the oxidation rate is the same independently of the gas used for the reduction, the differences observed among gas fuels are due to the different oxygen flow necessary to fulfill the mass balance in the system. However, low values of ΔX_s gave high recirculation rates. Oppositely, high values of ΔX_s gave high solid inventories. The optimum values of ΔX_s to get low recirculation rates and low solid inventories should be about 0.2-0.4. Table A.2.1.4 shows the minimum solid inventories in the CLC system at ΔX_s equal to 0.3 for different fuel gases. This value has been expressed as amount of oxygen carrier and as amount of metal oxide used in the preparation of the oxygen carrier. The lowest solid inventories of oxygen carrier corresponded to the N4A-FG because the NiO presents a high oxygen transport capacity and the oxygen carrier has a high NiO content (40 wt%). The F6A-FG presents higher values due to the lower oxygen transport capacity of the Fe₂O₃ (to Fe₃O₄). The higher inventories corresponds to the C1A-I because, although the CuO can transport a lot of oxygen, the oxygen carrier present a low active metal oxide content (10 wt%). However, if we consider the amount of metal oxide used in the oxygen carrier manufacture we observed that the lowest values correspond to the Cu-based oxygen carrier. This is because in the preparation of the Fe- and Ni-based oxygen carriers, a part of the metal oxide reacts with the support during the preparation and it is not useful for oxygen transport. In any case, the values of solids inventories are not high and the three oxygen carriers could be used in a CLC system. It must be remembered however that these values correspond to preliminary data, where the resistance to the gas exchange between the bubble and emulsion phases, which can be important in a fluidized bed, has been ignored.

The results obtained in this work can also very useful for the design of pressurized CLC systems considering that the reactivity of the carrier material must allow sufficient reduction and oxidation rates to fulfill the mass and energy balances. These balances are not affected by the pressure, and are only dependent on the type and content of metal oxide existing in the oxygen carrier.

Taking as reference the same thermal power and using the same gas velocity, the diameter of the reactors in a pressurized CLC plant are smaller than in an atmospheric CLC plant. Oppositely to the expected, we have found that an increase in the operating pressure produced a small decrease in the reaction rates of the oxygen carriers. The solids would need higher residence times to fulfill the mass balance and taller beds would be necessary in a pressurized CLC plant. The solids inventory in the system should be also higher although the exact values will depend on the oxygen carrier used. To better know these values it is not satisfactory to use the kinetic parameters obtained at atmospheric pressure. Although an initial approach has been made in this work to consider the effect of the total pressure on the kinetic parameters, it is advisable to determine them at the operating pressure of the CLC plant.

A.2.1.2 Investigation of M4MZ-FG and N6AM-FG

The reactivity of the two additional samples which showed good behavior at Chalmers was performed. These corresponds to the samples N6AM-FG, i.e. 60 wt% NiO and MgAl₂O₄ (sintered at 1300, 1400, and 1500 °C), and M4MZ-FG, i.e. 40 wt% Mn₃O₄ and Mg-ZrO₂ (sintered at 1100, 1150, and 1200 °C), and for several particle sizes (0.09-0.125, 0.125-0.18, 0.18-0.25 mm). Figures A.2.1.14 and A.2.1.15 shows the conversion versus time curves obtained during the reduction and oxidation in the TG. The reduction was carried out with H₂ (40 vol%) or CO/CO₂ (40/10 vol%), and the oxidation was carried out with air.

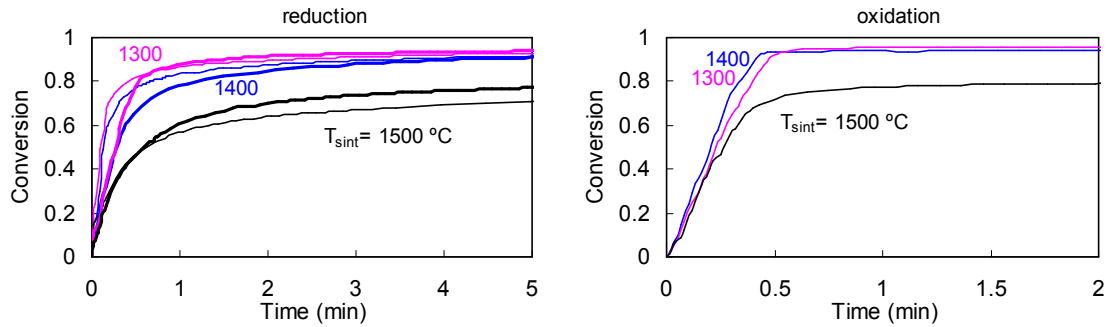


Figure A.2.1.14. Conversion curves obtained for the oxygen carrier NiO/MgAl₂O₄ sintered at different temperatures. Thin lines = H₂, gross lines=CO/CO₂. dp=0.125-0.18 mm.

The reactivity of the oxygen carrier NiO/MgAl₂O₄ depended on the sintering temperature and on the gas used for the reduction. A higher sintering temperature produced a lower reduction and oxidation reaction rate, decreasing a lot for the highest sintering temperature (1500 °C). On the other hand, the reaction rate of the reduction with H₂ was higher than the reduction with CO. The particle size did not affect the reactions.

The reaction rate of the Mn-based oxygen carrier was very high and it was not affected by the particle size or by the sintering temperature.

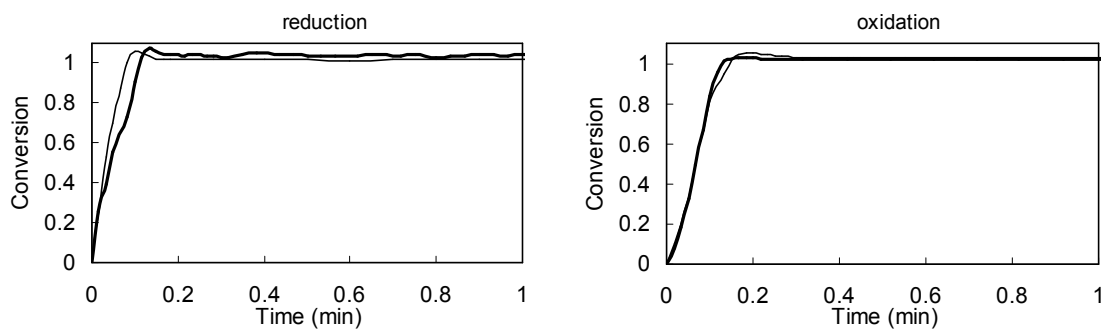


Figure A.2.1.15. Conversion curves obtained for the oxygen carrier Mn₃O₄/Mg-ZrO₂ sintered at 1150 °C. Thin lines = H₂, gross lines=CO/CO₂. dp=0.125-0.18 mm

A.2.2. Work performed at Chalmers

A.2.2.1. Introduction

Of the extensive amount of tested oxygen carriers within the screening phase of the project, three particles were selected for further testing in the batch fluidized bed at Chalmers as well as the continuous working prototype of CLC, see section A.4.1.

1. 40% Mn₃O₄/60% Mg-ZrO₂, M4MZ-FG, sintered at 1100°C; particle number 27 in Table A.1.2.1.
2. 60% NiO/40% MgAl₂O₄, N6AM-FG, sintered at 1400°C; particle number 38 in Table A.1.2.1.

3. 60% Fe₂O₃ and 40% Al₂O₃, F6A-FG, sintered at 1100°C. Note that the particle tested in the screening phase, i.e. number 4 in Table A.1.2.1, was sintered at a higher temperature. A somewhat lower sintering temperature was chosen to increase porosity of the particle.

These three particles showed the combination of high reactivity under many oxidation and reduction cycles, relatively high strength and limited or no particle breakage during the fluidized bed tests. Below follows a discussion of the investigation in the batch fluidized bed reactor of these oxygen carriers using both syngas and methane.

A.2.2.2. Experimental

The selected three types of particles were tested in the laboratory fluidized bed with a syngas composed of 50% H₂ and 50% CO at different temperatures. For comparison, fluidized bed tests were also conducted with 100% CH₄. The reactivity experiments in the fluidized bed were performed in a similar way as with methane/steam explained in section A.2.1 and the details of the data evaluation is also given there. The amount of bed material as well as the fuel flow was the same for both methane and syngas, i.e. 15g and 450 ml/min respectively, and this would correspond to 57 kg/MW_f for methane and 173 kg/MW_f for syngas.

Two gas yields were defined as the ratio of the H₂ and CO added which reacted to H₂O and CO₂ respectively and were calculated from

$$\gamma_{CO} = \frac{x_{CO_2}}{x_{CO} + x_{CO_2}} \quad (A.2.2.1)$$

and

$$\gamma_{H_2} = \frac{x_{H_2O}}{x_{H_2O} + x_{H_2}} = 1 - \frac{x_{H_2}}{x_{CO_2} + x_{CO}} \quad (A.2.2.2)$$

For the experiments conducted with 100% CH₄, the gas yield was defined as

$$\gamma_{CH_4} = \frac{x_{CO_2}}{x_{CH_4} + x_{CO} + x_{CO_2}} \quad (A.2.2.3)$$

A gas yield was defined for the oxidation period as,

$$\gamma_{ox} = \frac{p_{O_2,in} - p_{O_2,out}}{p_{O_2,in}} \quad (A.2.2.4)$$

where $p_{O_2,in}$ and $p_{O_2,out}$ are the inlet and outlet partial pressures of O₂ respectively. Thus a gas yield of unity would mean that there is no measurable concentration of O₂ from the exit of the reactor, i.e. a high rate of reaction with the reduced metal oxide.

A.2.2.3. Results

Reduction. Figure A.2.2.1-A.2.2.3 shows the outlet gas concentrations from the second reduction period and third oxidation period for the experiment with the three selected oxygen carriers at 950°C. In addition to being estimated by equilibrium, the hydrogen concentration was measured using a gas chromatograph. For the manganese based oxygen carrier, there

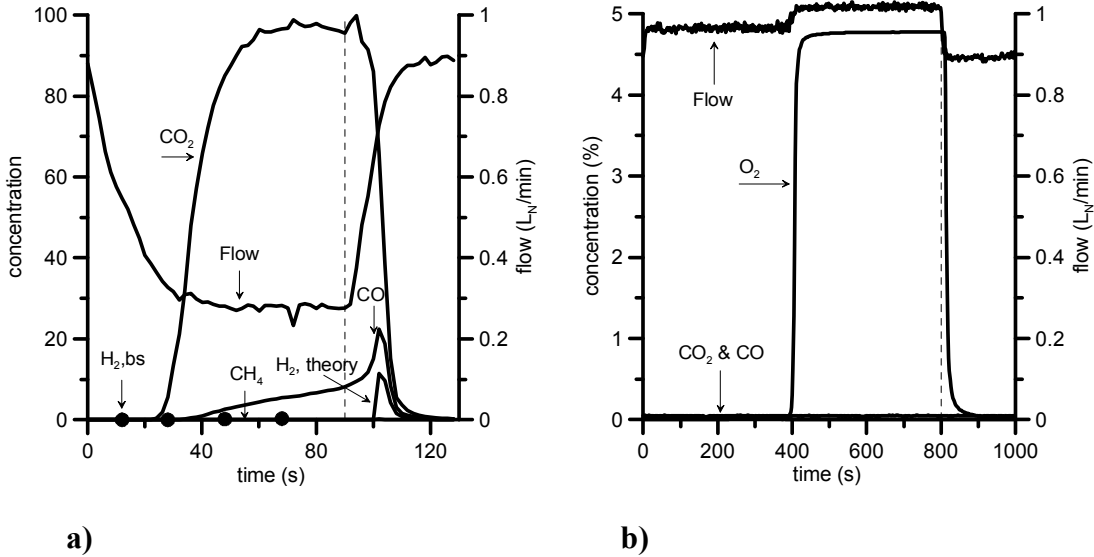


Figure A.2.2.1. Outlet gas concentrations for the iron based oxygen carrier at 950C using syngas a) the second reduction period and b) the third oxidation period. The H₂ concentration as measured with a gas chromatograf is indicated by (●).

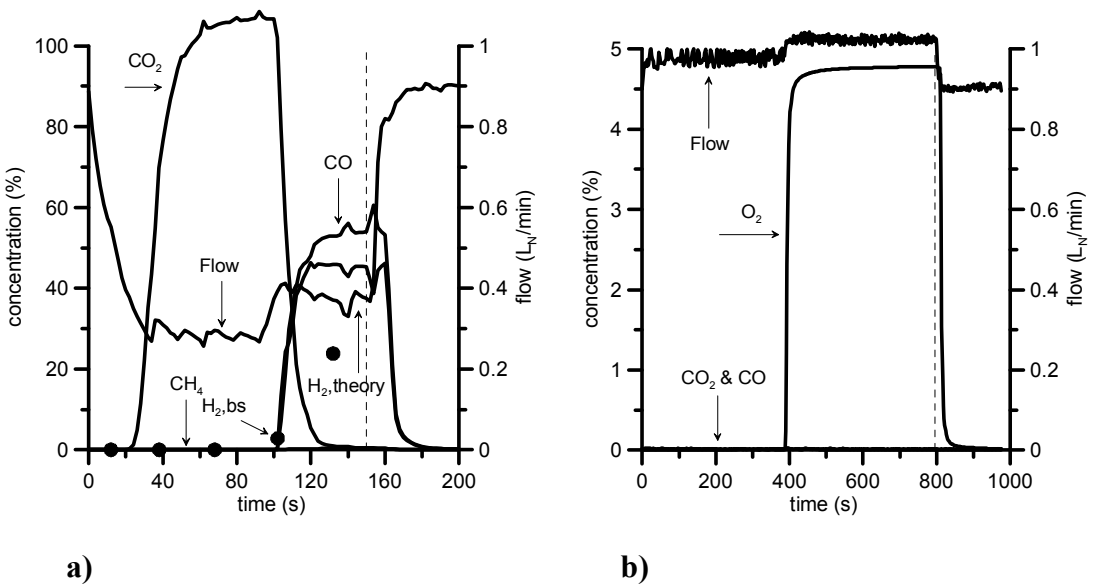


Figure A.2.2.2. Outlet gas concentrations for the manganese based oxygen carrier at 950C using syngas a) the second reduction period and b) the third oxidation period. The H₂ concentration as measured with a gas chromatograf is indicated by (●).

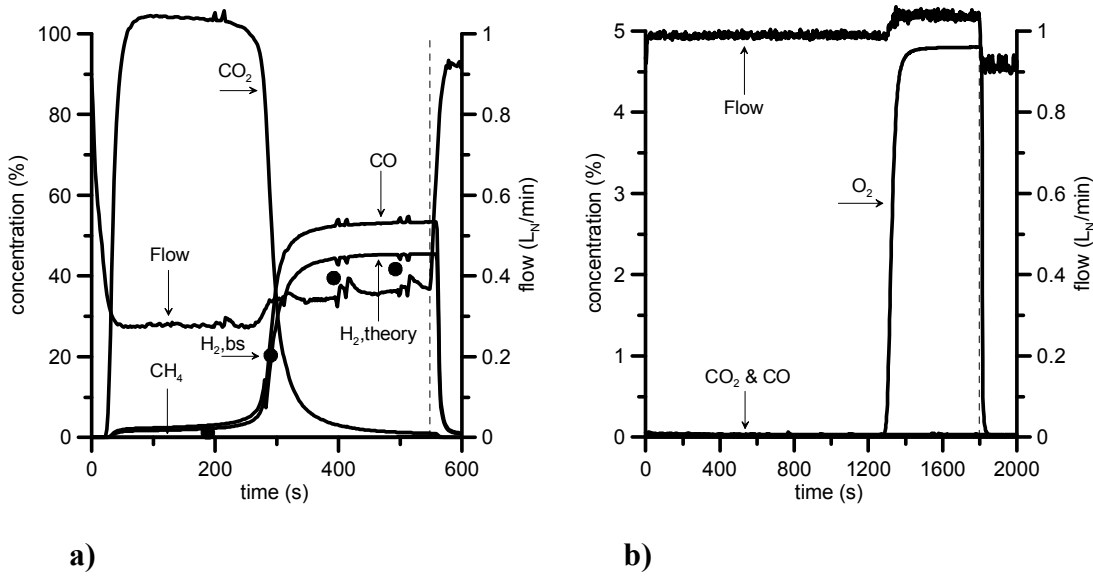


Figure A.2.2.3. Outlet gas concentrations for the nickel based oxygen carrier at 950C using syngas a) the second reduction period and b) the third oxidation period. The H₂ concentration as measured with a gas chromatograph is indicated by (●).

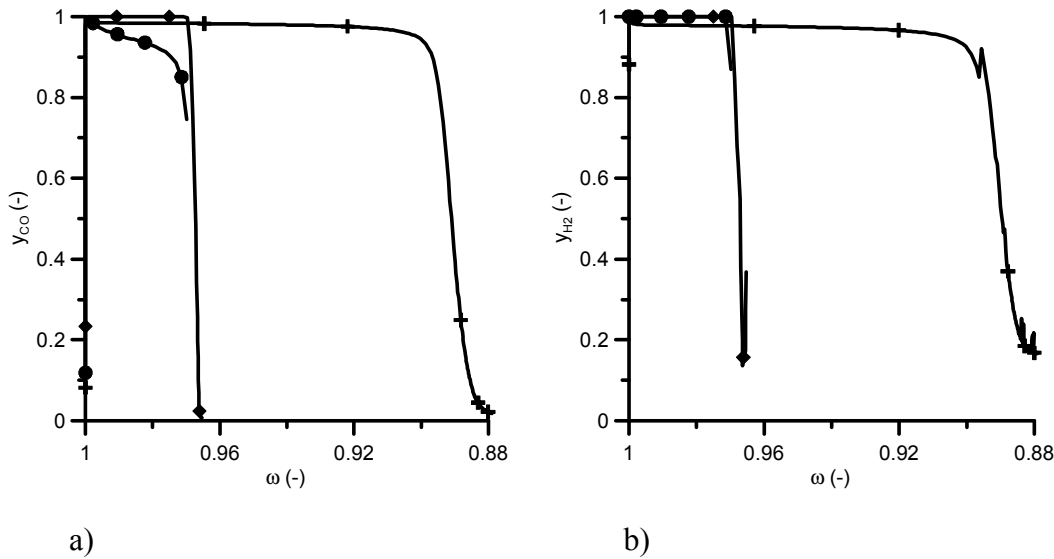


Figure A.2.2.4. The gas yield for a) CO, γ_{CO} , and b) H₂, γ_{H2} , as a function of ω for the second reduction period using Ni (+), Mn (◆) and Fe (●).

was complete conversion of the fuel gas. Similarly, the iron based oxygen carrier had an almost complete conversion of the fuel gas to carbon dioxide, although there was some CO out from the reactor. This was the case even at very high degrees of oxidation of the oxygen carrier, when the thermodynamic gas yield is complete. However, as seen from figure A.2.2.1 and A.2.2.2 no hydrogen was measured at these high degrees of gas yield for both iron and manganese. As for the Ni-carrier there is also a high gas yield, albeit there is some CO and H₂ from the outlet even at these high yields, see Figure A.2.2.3. This is due to the thermodynamic limitation for NiO to fully convert syngas to CO₂ and H₂O, see reactions

(A.2.1.1) and (A.2.1.2). Figure A.2.2.4 shows the gas yield of H₂ and CO as a function of the mass-based degree of conversion, ω , for the second reduction period for the three investigated oxygen carriers at 950°C. For iron it is clear that the hydrogen reacts at a fast rate in comparison to the carbon monoxide. This confirms the findings in the TGA at CSIC for the iron based oxygen carrier, where a somewhat faster reaction rate was measured using hydrogen, see Figure A.2.2.4. Full gas yield was seen for manganese for both CO and H₂, while Ni had a gas yield less than unity for both CO and H₂, most likely due to the thermodynamic limitations. For comparison the gas yield is shown for experiments conducted with methane at 950°C in Figure A.2.2.5. Clearly, there is considerable difference with respect to the gas reactivity, and only Ni has a nearly full yield to carbon dioxide. As metallic Ni is a good catalyst for both methane decomposition and steam reforming of methane, the methane is most likely easily reformed to CO and H₂ on the external and internal pore structure of the particle where Ni sites are present. The CO and H₂ then react at a high rate with the NiO. On the other hand, Fe and Mn do not catalyze pyrolysis and reforming reactions at such a high rate, which means that the overall reaction will proceed at a slower rate.

Figure A.2.2.6 shows the mass-based rate of reaction, $d\omega/dt$, as a function of the conversion for the Mn, Fe and Ni based carriers using syngas and methane. At full yield of the syngas to CO₂ and H₂O, the particles in the bed have the highest reactivity, corresponding to a rate of 0.00037/s in Figure 2.2.2.6a. The rate is here limited by the access to gaseous reactant. A comparison between the two figures A.2.2.6a and b shows that the reaction rates are higher for the oxygen carrier when using methane, which can be explained by the stoichiometry of the reactions; whereas four moles of metal oxide reacts with one mole of methane only one mole of metal oxide reacts per mole syngas (CO/H₂). If the reaction rates were normalized per mole of solid reactant, the rates in Figure 2.2.2.6a would increase by a factor 4 and thus be comparable to that of Ni in Fig. 2.2.2.6b. However, because the solids inventory is inversely proportional to $d\omega/dt$ this will have implications for a real system. (Garcia-Labiano et al., 2004).

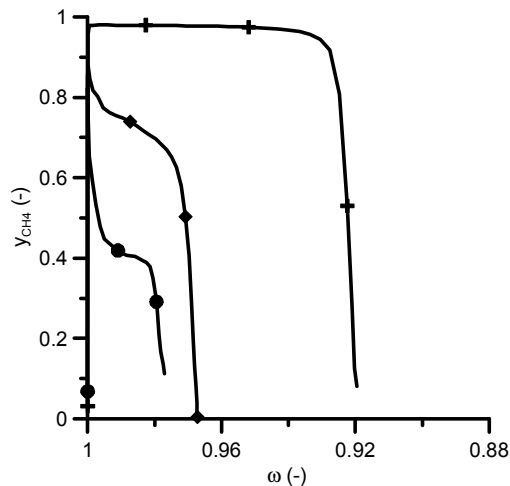


Figure A.2.2.5. The gas yield for CH₄, γ_{CH_4} , as a function of ω for the second reduction period using Ni (+), Mn (◆) and Fe (●). The fuel was 100% CH₄.

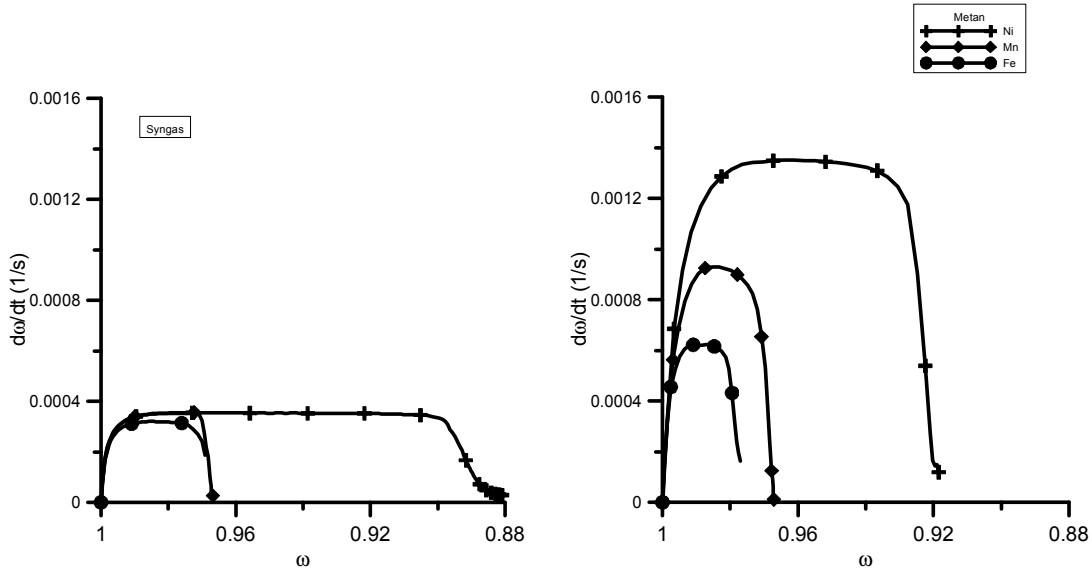
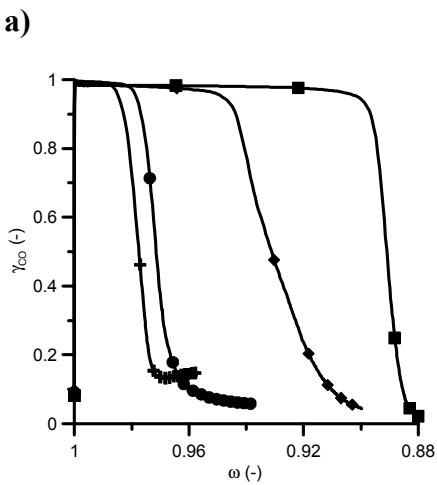
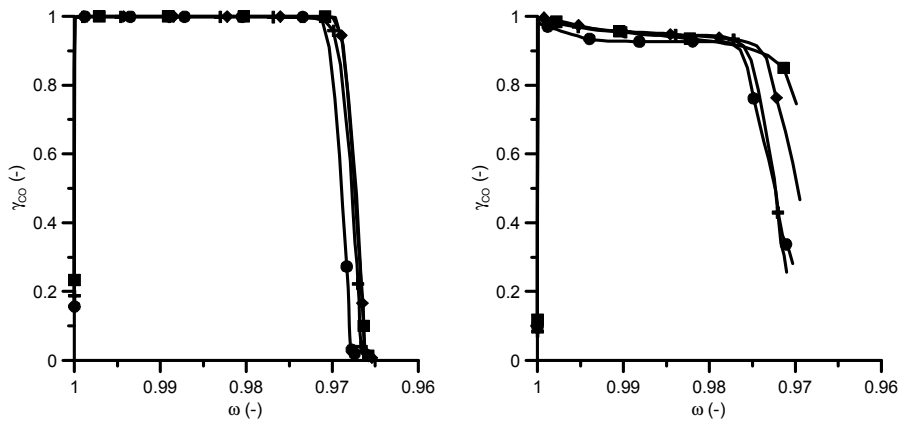


Figure A.2.2.6. The mass based rate as a function of conversion for a) syngas and b) methane for experiments conducted at 950°C. Ni (+), Mn (◆) and Fe (●).



a)

b)

c)

Figure A.2.2.7 The gas yield for CO, γ_{CO} , as a function of ω for the second reduction period using syngas for a) M4MZ, b) F6A and c) N6AM. Temperatures: 950°C (■), 850°C (◆), 750°C (●), 650°C (+)

The reactivity with syngas was investigated for different temperatures in the range 650-950°C. Fig. 2.2.2.7 shows the gas yield of CO to CO₂, γ_{CO} , for the three investigated oxygen carriers. Manganese showed no difference in reactivity as a function of temperature, for iron small differences were found, but still a high gas yield was achieved independent of the temperature. For Ni however, there was a clear decrease in reactivity at lower degrees of conversion, see Figure. A.2.2.2.7c.

A.3 Task 3. Fluidisation conditions.

A.3.1 Work performed at VUT

The objective of task 3, carried out by the Institute of Chemical Engineering, Vienna University of Technology, was the determination of the effects of reactor design, solid properties and fluidisation conditions on the fluid dynamics (solids circulation rate, gas leakage) of CLC reactor designs. To this end, three reactor concepts, differing in scale and operating conditions, were designed and tested experimentally by means of scale models operated at ambient temperatures. The relationships of the operating parameters obtained from experimental work were integrated into mathematical models. Such, the reactor system characteristics could be made independent on size and reliable scale-up tools for future chemical-looping combustion plants are available. From the results of the cold-model testing a hot prototype CLC reactor was constructed and operated at Chalmers. Further, a number of small mathematical models facilitating the design procedure were developed.

A.3.1.1 Laboratory scale CLC unit

From previous research arose a need to study smaller amounts of different oxygen carrier particles in a continuous mode and to demonstrate the CLC process for the coal syngas application. The purpose of the first CLC reactor design at laboratory scale was therefore to develop a small CLC laboratory reactor to be used for i) the study of the process, and ii) testing of different oxygen carriers. The unit is characterised by a simple design and a small bed inventory. The design (Figure A.3.1.1b) chosen for this CLC system is a two-compartment fluidised bed having a thermal power range of 100 – 300W_{th} for the original reactor.

Four different reactor layouts were designed, constructed, and tested in respect of the solids flow and the gas leakage (Table A.3.1.1). A final design, optimised in terms of solids flow and gas mixing, was constructed and put into operation.

Table A.3.1.1. Design variations and main dimensions

design	FR dimension	AR dimension (bottom)	downcomer width	slot height	slot profile
	[mm]	[mm]	[mm]	[mm]	
A	19 x 19	19 x 27	9	8	I
B	19 x 19	19 x 27	9	4.5	I
C	19 x 19	19 x 27	11	1.5	I
D	19 x 19	19 x 27	11	1.2	T

Results of pressure drop measurements

Pressure drop measurements were carried out at up to nine positions at the cold flow model. Figure A.3.1.1 shows some results. It can be observed that as a consequence of the different gas velocities in the reactors ($u_{AR} = 1.6 \cdot u_t$, and $u_{FR} = 18 \cdot u_{mf}$) large differences in the bed porosity follow, causing a lower pressure gradient in the “slow-fluidised” bed. The “fast-fluidised” bed, on the other hand, shows a pressure profile which is similar to typical CFB risers, having a higher pressure drop in the bottom zone followed by a dilute zone. The

pressure and the solids flow loops are closed by the downcomer. A particle column balances the pressure differences between the air reactor and the fuel reactor at the height of the particle return orifice. The solids column also minimises gas leakage through the downcomer in both directions. At the height of the bottom return slot the pressure is higher in the fuel reactor and the pressure difference causes particles to flow from the fuel reactor to the air reactor

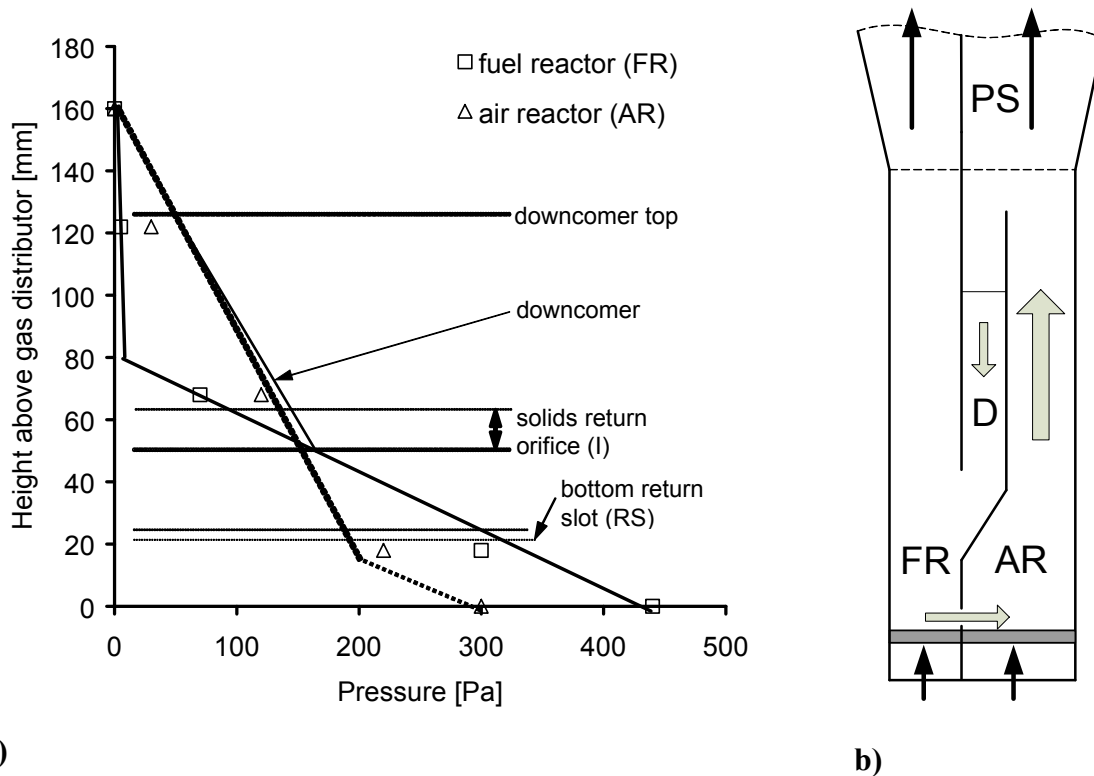


Figure A.3.1.1. Pressure loop of the two-compartment fluidised bed.

Solids circulation rate measurements

Solids circulation rate measurements were carried out at different total solid inventories (TSI=40 to 70g, material FCC powder and glass beads), several design variations and velocities in the reactors.

Figure A.3.1.2. shows the solids circulation rate against the velocity in the air reactor, for the four different designs and FCC as bed material. The velocity in the air reactor (u_{AR}) refers to the velocity in the upper, narrow part, along the downcomer. Since two of the designs, C and D, have a more narrow section, they will have higher velocities for the three volume flows used. The velocity in the fuel reactor (u_{FR}) is held constant at 18 times u_{mf} , which corresponds to 100 W in the hot laboratory unit. In general, it can be seen that the solids circulation rate increases with increasing velocity in the air reactor. The trend for the geometry influence is that the smaller the slot height, the lower the solids flow between the reactors. However, the design with the largest slot, A, did not have the highest recirculation. Similar tests with glass beads gave solids flow rates higher by almost an order of magnitude and an indirect proportionality between the solids flow and the slot height was found.

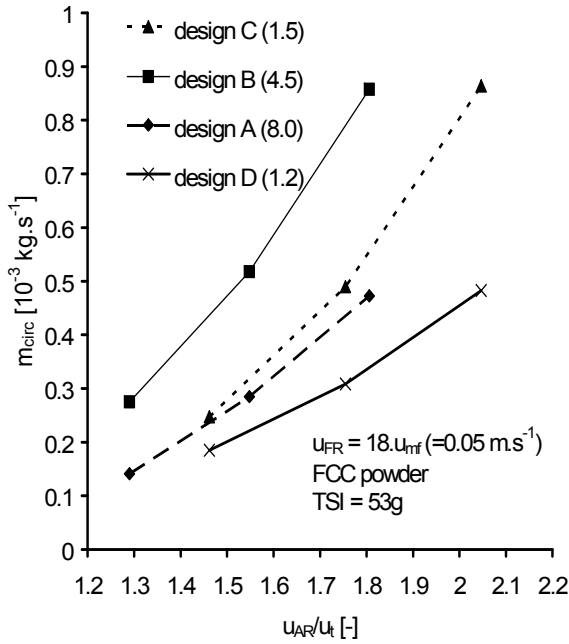


Figure A.3.1.2. Solids circulation rate for all designs (slot height in mm in bracket), and FCC powder. $u_{FR} = 18 \cdot u_{mf} (=0.05 \text{ m}\cdot\text{s}^{-1})$, TSI = 53 g.

Gas leakage measurements

For large-scale units very low values on gas leakage between the reactors are required, but in the laboratory model, higher leakages can be accepted. The main purpose of the unit is not to demonstrate a very highly effective CO₂ separation but rather to test particles in a continuously operating unit.

In general it was found that gas leakage is directly related to the cross section area of the slot opening. It is likely that the main mechanism of leakage is the exchange of gas bubbles reaching the other reactor accidentally through the opening. This is also supported by the observation that there is simultaneous leakage in both directions. Design D gives a lower gas leakage. The horizontal plate reduces this gas exchange and also visual observation supports the assumption that fewer gas bubbles cross the orifice and move into the other reactor. Comparing the designs one can see that an increased solids circulation rate is correlated with a higher gas leakage. Specific values can be found in Table A.3.1.2..

Table A.3.1.2. Comparison of leakage flows for design C and D, $u_{FR} = 0.05 \text{ m}\cdot\text{s}^{-1}$, $u_{AR} = 0.35 \text{ m}\cdot\text{s}^{-1}$

		leakage flow [L.min ⁻¹]	fraction of air flow [-]	fraction of fuel flow [-]
design C	leakage into FR	0.21	3.6%	19.5%
	leakage into AR	0.13	2.1%	11.7%
design D	leakage into FR	0.037	0.6%	3.3%
	leakage into AR	0.069	1.2%	6.3%

A final design, optimised in terms of solids flow and gas mixing, was constructed and put into operation, see A.4.1 for details of these experiments.

A.3.1.2. Atmospheric CLC demonstration unit - mathematical modelling and experimental results

CFB system description. The CFB experimental rig used in this sub task is a flow model of a demonstration scale CLC plant. It consists of a 1.18 m high rectangular riser with inner dimensions of 0.105 m by 0.160 m. Experiments were conducted at ambient temperature and pressure. The fluidisation gas used in all experiments was air, and bronze powder with 54 μm mean particle diameter and 8750 $\text{kg}\cdot\text{m}^{-3}$ density was used as bed material. This gas/bed material combination was the result of the downscaling of a pre-demonstration scale CLC power plant (2 MW_{th}), applying scaling criteria of Glicksman (1993). In general the design in Figure A.3.1.3 follows a “close to real system” approach. It includes features specific for the large-scale CFB unit like air staging (secondary air injection) for better control of the solids circulation rate and advanced loop seal designs for the prevention of gas mixing between the two reactors. A summary of property data and dimensions of the cold flow model is given in table A.3.1.3.

Table A.3.1.3. Data of cold flow model and pilot scale plant

	flow model	pilot scale plant	unit
riser dimension (L x W x H)	0.105 x 0.16 x 1.18	0.7 x 0.45 x 5	m
FR dimension ((L x W x H)	0.09 x 0.11 x 0.15	0.43 x 0.5 x 0.65	m
AR dimension (L x W x H)	0.09 x 0.08 x 0.15	0.43 x 0.4 x 0.4	m
bed-material	bronze powder	oxygen carrier	
d_p	54	119	μm
ρ_p	8750	2250	$\text{kg}\cdot\text{m}^{-3}$
ρ_g	1.28	0.3	$\text{kg}\cdot\text{m}^{-3}$

The operating superficial gas velocity of the riser, u_{RIS} , and mean solids flux, G_s , are 1.6 - 3 $\text{m}\cdot\text{s}^{-1}$ and up to 100 $\text{kg}\cdot\text{m}^{-2}\cdot\text{s}^{-1}$, respectively. The fuel reactor operating regime for the pre-demonstration at 2MW_{th} scale was selected to follow a turbulent regime with u_{FR} around 1 $\text{m}\cdot\text{s}^{-1}$. For simplicity reasons, however, this was not directly scaled to the flow model but a lower velocity was chosen. Omission of particle separator at the fuel reactor exit was compensated by installation of a valve for simulation of the gas-solid separator pressure drop and its effect on the system behavior. The loop seal fluidisations were all set to 1.5 times u_{mf} but variations were carried out for optimisation of the gas leakage. For the gas distribution in the riser a perforated plate with 30 holes (6 mm in diameter) was used. The loop seals, air reactor, fuel reactor, and loop seals were fluidised through porous glass plates.

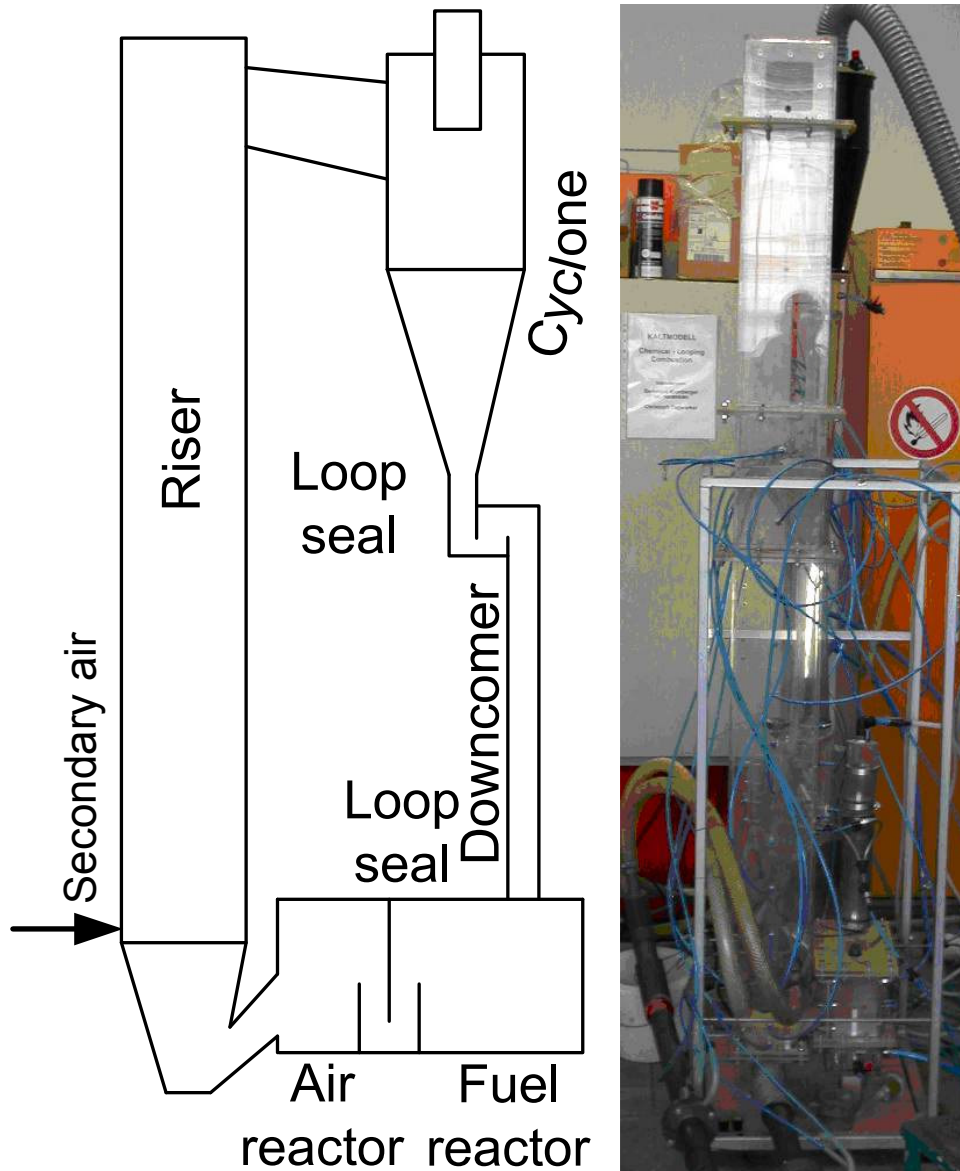


Figure A.3.1.3 Schematic diagram and photo of flow model.

Experimental results of solids circulation rate. In the current CFB system adjustment of the solids flux for part load behaviour can be achieved by variations of the air staging, i.e. the ratio of bottom air to secondary air flows. Since the superficial velocity in the riser section above the secondary air injection is significantly higher than the terminal velocity of particles in all test series, conditions in the riser are assessed as being fast fluidised. Therefore, a strong influence of the riser superficial fluidisation gas velocity on the solids circulation rate can be expected.

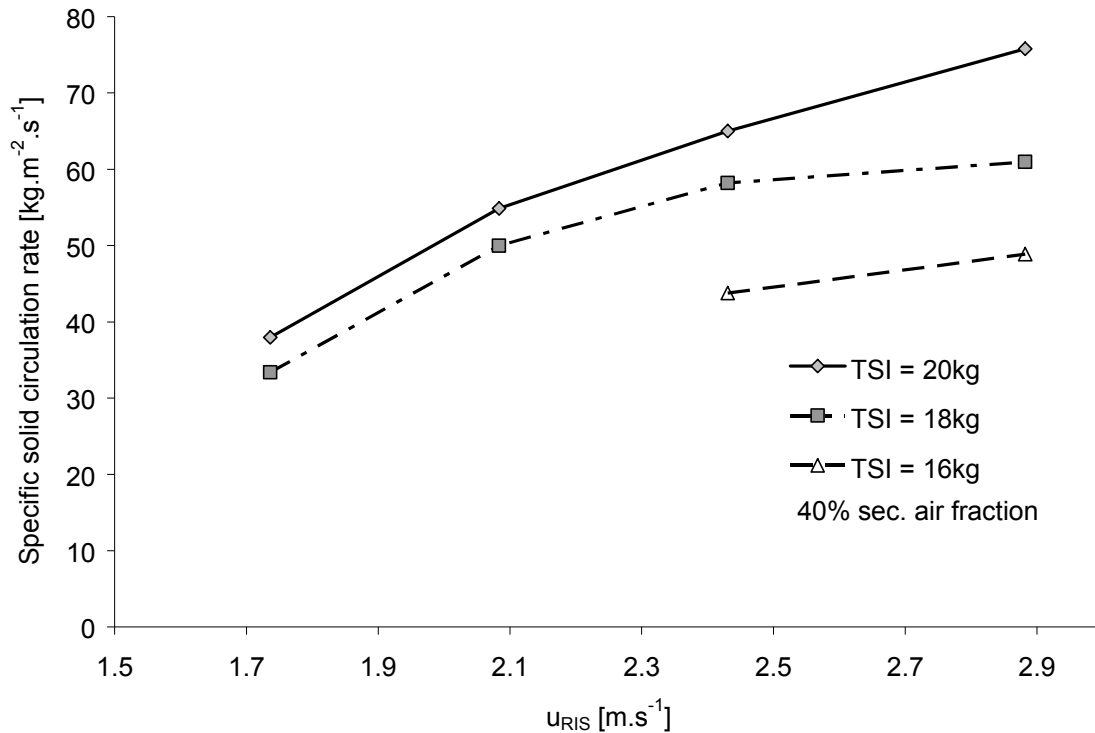


Figure A.3.1.4. Specific solids circulation rate vs. fluidisation gas velocity in the riser for different total solid inventories (TSI)

The graph in Figure A.3.1.4 shows that the solids circulation rate is influenced by both the gas velocity in the riser and the total solids inventory. However, the increase with respect to the TSI riser velocity was lower than expected. This can be explained by the fact that due to higher solids flux, bed material is accumulated in other components of the CFB-system. In the downcomer of the cyclone it is caused by higher flow resistance of the loop seal at higher solids flow rates. Therefore, the material inventory and the return flow at the bottom of the riser are reduced and the solids circulation rate is limited.

Mathematical description. The CFB fluid dynamics of the large-scale concept studied experimentally in the previous reporting period were transformed into a mathematical model. The intended application is to form an instrument that supports design and scale-up of the CLC reactor. Input parameters for the model are fluidisation conditions (volume flows, temperature, total mass load, secondary air injection etc.), physical material properties and geometry data of the system. After calculation of the riser solids flow and pressure drop these values are used to calculate pressure drop and solids inventory sequentially for each CFB loop component. Mass and pressure balances are used to connect the components of the system to each other and therefore adjust the values in an iterative procedure. This loop calculation (Figure A.3.1.5) is stopped when mass and pressure balances for the loop are converged and deviation is within a given increment.

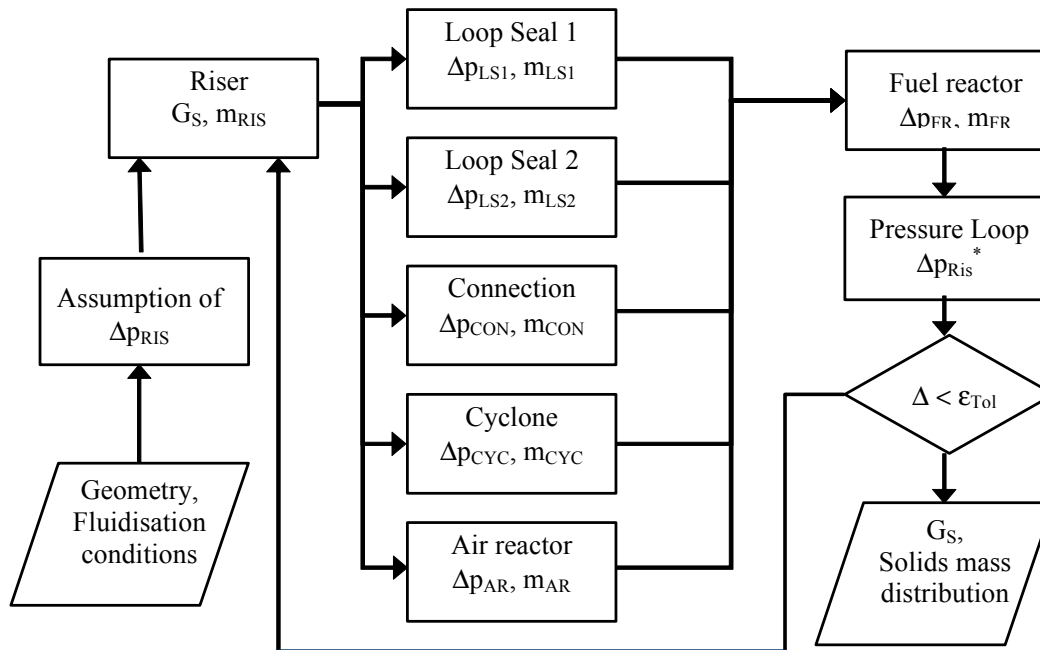


Figure A.3.1.5. Structure of the program

CFB-components models. Component models were developed for the riser, the fuel reactor, the loop seals and the cyclone. A detailed description is given here only for the riser model.

The riser model

The riser is split into a transport zone, an exit zone, a bottom zone. Characteristic model details for each zone are presented in the following section

Transport zone

The model for the riser transport zone was developed based on the assumption of a core-annulus flow structure as e.g. proposed by Pugsley and Berruti (1995). The solids flow structure of the transport zone is formed by a dilute core zone, an upward solids flow, and a dense annulus (a downward solids flow at the riser walls). The gas is assumed to flow upward only in the core region. The axial mean voidage profile in the transport zone is calculated according to the exponential voidage profile correlation as proposed by Zenz and Weil (1958).

$$\frac{\varepsilon(h_i) - \varepsilon_\infty}{\varepsilon_0 - \varepsilon_\infty} = \exp[-a \cdot (h_i - h_0)] \quad (\text{A.3.1.1})$$

Kunii and Levenspiel (1991) suggest that the decay constant “a” in equation (A.3.1.1) is a product of “a” times “u”, depended only on the particle size. (equation (A.3.1.1))

$$a \cdot u \cdot \text{const.} = \begin{cases} 2 \sim 5 \text{ s}^{-1} & \text{for } d_p < 70 \mu\text{m} \\ 4 \sim 12 \text{ s}^{-1} & \text{for } d_p > 88 \mu\text{m} \end{cases} \quad (\text{A.3.1.2})$$

This assumption was found to cover well the experimental results of this study and the value of 4 s⁻¹ for a mean particle diameter of 54 μm.

The second parameter for determining the axial voidage profile according to equation (A.3.1.1) is the voidage above TDH, ϵ_{TDH} . The evaluation of the experimental results of this study showed that the correlation of Geldart et al. (1985) best fits this model.

The momentum balance for gas and solids in the transport zone. equation (A.3.1.3), was used to determine the pressure at each riser height. The terms on the right side of the equation are covering the solids acceleration, the hydrostatic head of solids and the wall friction of the two-phase flow.

$$-\frac{dp}{dh} = \left(\frac{d(m_{s,up} \cdot u_{c,s})}{dh} + \frac{d(m_{s,down} \cdot u_{a,s})}{dh} \right) + (1 - \epsilon) \cdot (\rho_p - \rho_g) \cdot g + \frac{dp_{fric}}{dh} \quad (\text{A.3.1.3})$$

The wall friction, covered by the term dp_{fric}/dh , was considered following the recommendation of Capes and Nakamura (1973) for the friction coefficient.

Exit zone

The T-shaped exit of the riser severely influences the solids hold-up. As the riser of the demo unit is very short this is even more important. The separation effect of the riser was implemented by using the approach of Gupta and Berruti (2000). The concept is based on the definition of a reflection coefficient for the correction of the slip factor. The corrected slip factor then allows the calculation of a corrected particle velocity at the exit zone, giving the net solids flux.

Bottom bed

The momentum balance as given in equation A.3.1.3 causes a situation where the entire upwards solids mass flux is accelerated at the height of the solids return, which results in a drastic overestimation of the dynamic gas pressure drop. Because of this and following the geometric situation of the riser, a bottom zone was included. This allows a gradual increase of the mass flow to be accelerated at the bottom area of the riser. The model is based on work by Schlichthaerle et al. (1999).

Most industrial CFB risers are designed to have a bottom section with an increase of the cross section. It has been observed during flow modelling that a solids accumulation occurs in this region. Visual observations of this study confirm that the region behind a certain angle consists of the downward solids flow of the annulus. In the present configuration the geometric angle of the inclined walls is 20° and the maximum angle where particles can follow the gas flow is determined by fitting the model to experimental data as 10°.

Results of riser model

In Figure A.3.1.6 detailed results of the solids concentrations and the total pressure drop for the standard case of 35% secondary air fraction and a superficial riser velocity of 2.74 m·s⁻¹

are shown and compared to experimental results. In Figure A.3.1.6b) it can be seen that the pressure profile can be well reproduced, which results also in agreement of the apparent solids concentration values in Figure A.3.1.6a). The pressure profiles shown in this study are levelled to the measured pressure of the top experimental value, which is located at the height of the riser exit. In Figure A.3.1.6 the solids concentration of overall mean, core and annulus are depicted. It is remarkable that the apparent solids concentration and the mean solids concentration are equal already at a height of about 0.2 m. An analysis of the particle acceleration showed that the small cross section at the bottom zone gives very high gas velocities, resulting in a very high particle drag. The core concentration is lower than the mean solids concentration, which is a consequence of the exit effect. The annulus at the riser exit is not zero but equivalent to a flow predicted from the exit coefficient. Because the model is intended to be used as scale-up tool it should be mentioned here that scale-up of the exit effects needs to be done carefully as some authors (Lackermeier et al., 2002, Pugsley et al. 1994) conclude that the increase of the solids concentration near the exit is a scale effect.

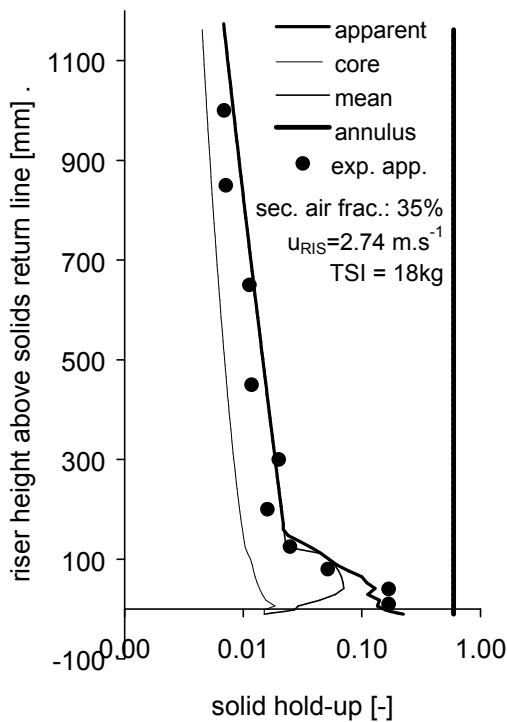


Figure A.3.1.6a)

Solids hold-up (a) and static pressure (b) vs. height for reference case ($u_{RIS} = 2.74 \text{ m}\cdot\text{s}^{-1}$, 35% sec. air fraction, TSI = 18kg)

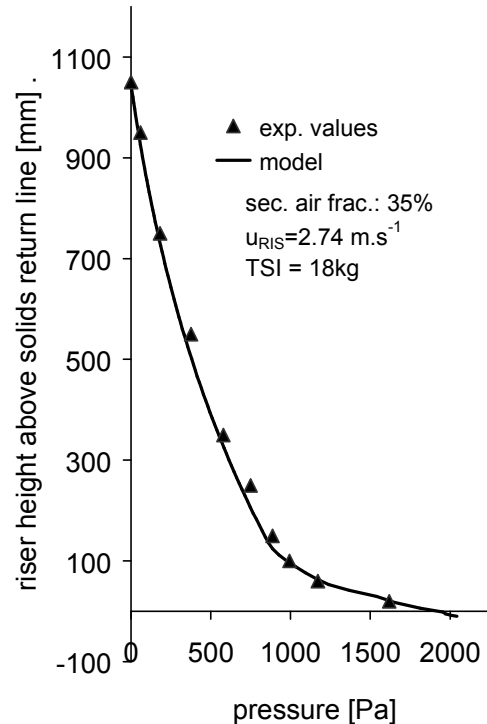


Figure A.3.1.6b)

Riser parameter mapping

The most important output of riser models is the correct prediction of the solids circulation flow rate. This can be seen in Figure A.3.1.7 for the standard case conditions over a wide range of riser pressure drop and riser velocity values. A strong dependency of the solids flux on the riser pressure drop and the superficial gas riser velocity was found. Although

experimental result show the same tendency a direct comparison is not possible as for the simulations for the graph below only single parameters (Δp_{RIS} and u_{RIS}) were varied, whereas the experimental results were obtained for the riser when integrated into the overall CFB loop.

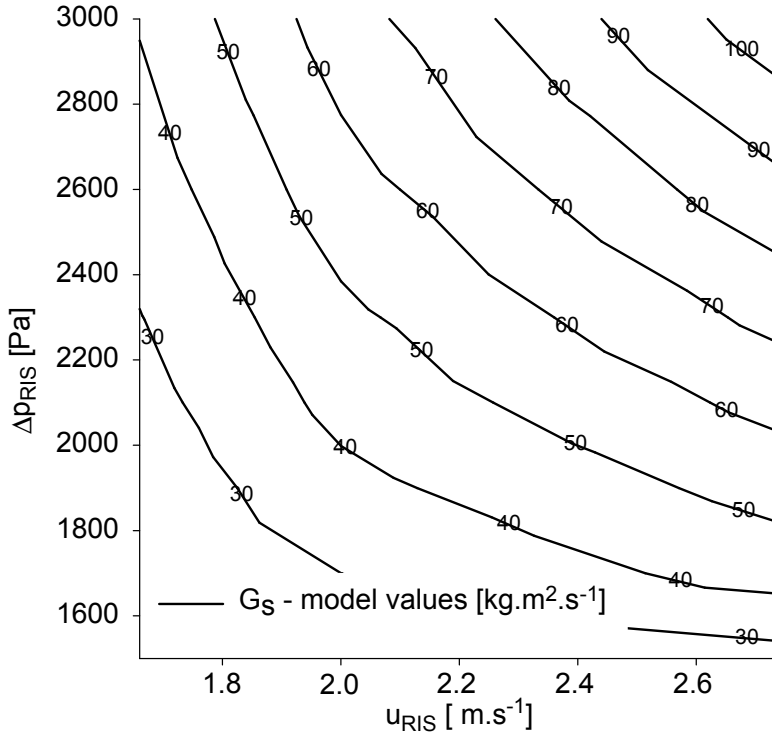


Figure A.3.1.7. Parameter mapping for the riser model. (35% sec. air fraction)

Simulation results and discussion

Static pressure distribution - pressure loop

The component models were integrated into the global model and a large number of simulation runs were carried out. Input values are the geometries and the parameters as described above as well as the gas pressures at the cyclone and fuel reactor outlet. The pressure drop for the riser is determined from the pressure balance along the pressure loop. This, written for the loop including the riser is:

$$p_{CYC,Outlet} - p_{FR,Outlet} = \Delta p_{CYC,inlet} + \Delta p_{RIS*} - \Delta p_{LSI,Dow} - \Delta p_{LSI,Hor} + \Delta p_{FR} \quad (A.3.1.4)$$

It was already found during experimental work that the pressure situation is stable at all tested operating conditions, which could also be confirmed during simulation work. All component models gave the expected results. The relationship between the static pressure (measurement values and model prediction) and the CFB system height is presented for a defined standard case. The total loop is at elevated pressure because of the filter equipment installed for de-dusting of the gas flows of the flow model.

In the diagram the pressure loss of each component is presented. It can be seen that the loop seals between oxygen carrier oxidation zone and “combustion” zone are operating at a higher pressure level, which avoids gas mixing between these zones.

The diagram also allows the description of the riser pressure drop Δp_{RIS^*} used in equation (A.3.1.4). The situation at the riser solids return line at the height of the air reactor bed surface is such, that the pressure at this location is equal to the pressure of the riser at the same height. The riser pressure drop Δp_{RIS^*} therefore is the pressure drop between the riser exit and the riser height equal to the air reactor bed surface.

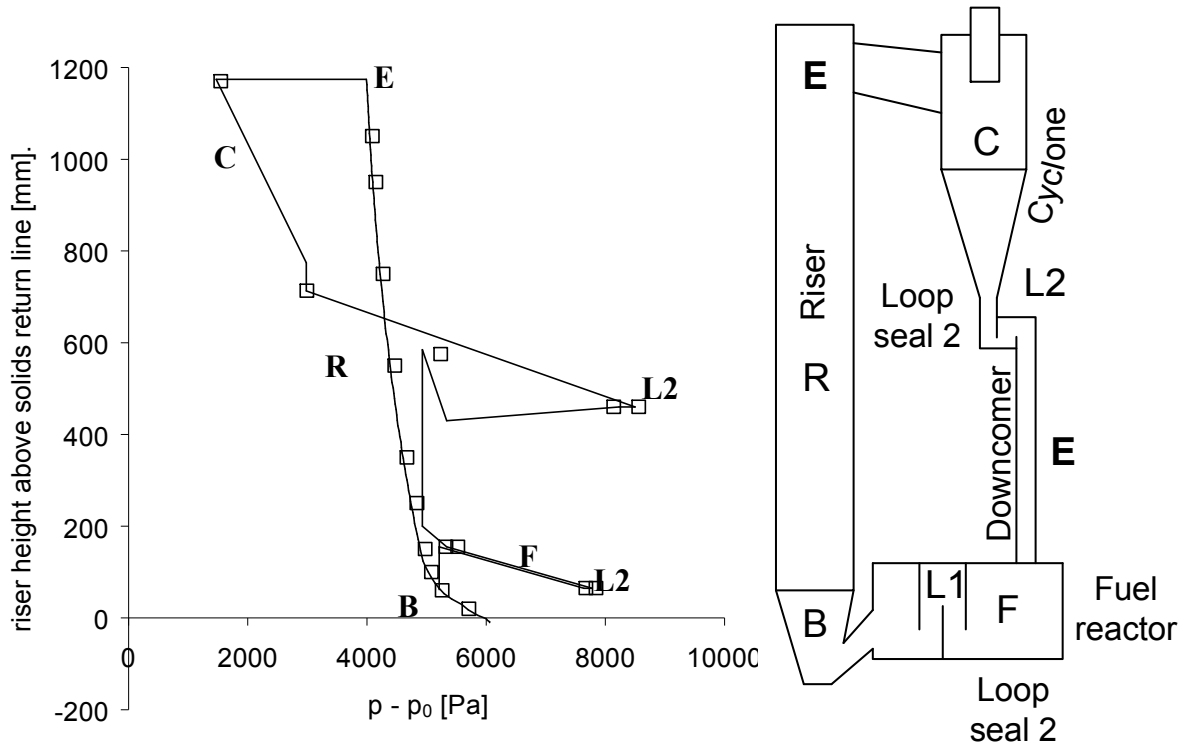


Figure A.3.1.8. Pressure profile of the CFB loop (experimental and modelling data for TSI = 18kg, sec. air fraction = 35%, $u=1,74m \cdot s^{-1}$, $G_s=62.5 \square m^{-1} s^{-2}$).

Solids circulation rate

In Figure A.3.1.9 the solids circulation rate is shown for different operating conditions versus the riser pressure drop $\Delta p_{RIS^{**}}$. The riser pressure drop $\Delta p_{RIS^{**}}$ is the pressure value taken immediately above the gas distribution plate because no experimental data exist for the total riser. The air staging in the presented case is 35% secondary air of the total air flow in the riser. The riser fluidisation velocity was altered between 1.66 and 2.74 m·s⁻¹ and the total solids inventory for the CFB system was varied between 14 and 20 kg.

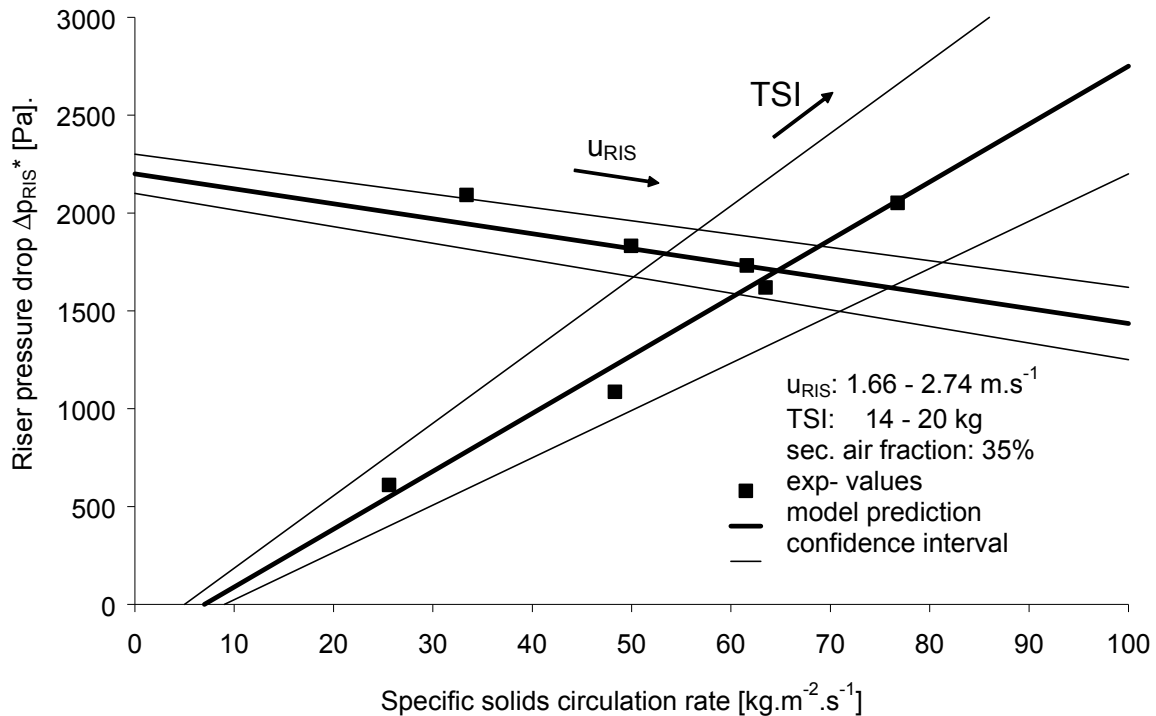


Figure A.3.1.9. CFB loop parameter plot.

Bold lines show results from simulation runs. However, as presented in equation (A.3.1.4) the pressure loop includes the modified riser pressure drop Δp_{RIS}^* . As the absolute value is small in comparison to the measurement inaccuracies of the outlet pressures this is a significant source and gives a high sensitivity of the model to the pressure values at the outlets.

The simulation results in Figure A.3.1.9 include deviation indicators. The maximum deviation between the measured and predicted values of Δp_{RIS}^* is determined from comparison of model predictions and experimental results as 6%. As shown in figure A.3.1.4 the solids circulation rate is highly dependent on the riser pressure drop, which gives a deviation of maximum 15% for the model. With equal accuracy the model allows determination of mass inventories from the reactor volumes, operating conditions and the solids flux.

A.3.1.3. Design of pressurized CLC demonstration plant

The third CLC reactor design forms the basis for future employment of CLC for coal combustion power plants featuring combined cycle power processes. This shall allow a significant increase of the energy efficiency but numerous aspects need to be studied before this can be realised. The present study focused on the fluid dynamics and the basic design of a pressurized CLC demonstration plant.

To this end, a flow model, based on a pressurized CLC of interconnected fluidised beds was designed and tested. The unit represents a $60kW_{th}$ bench scale reactor and experimental tests correspond to three different pressure levels, i.e. 1bar, 4.1bar, and 10 bar. In addition the experimental work allowed a mathematical description of the effects of pressurised conditions on the fluid dynamics of CFB CLC systems. It was shown that the proposed design (Figure A.3.1.10) is suitable for PCLC, which can be realised in a future CLC development project.

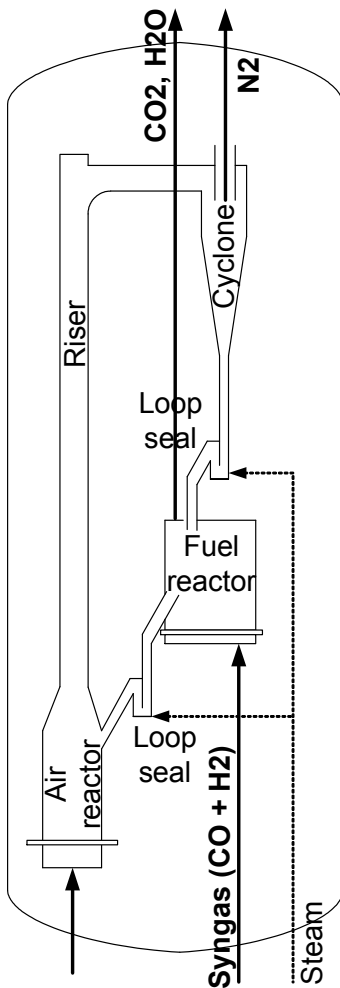


Figure A.3.1.10. PCLC combustor

Scaling of results for bench scale unit (“hot unit”)

The results of the intensive experimental programme were scaled to the operating conditions of the pressurized bench scale unit by application of common scaling relationships. A main difficulty thereby was missing data for high riser fluidisation velocities for the case of 10 bar pressure.

This problem was overcome by the use of approximation functions for the relation of the solids circulation rate vs. TSI and the riser fluidisation velocity, which also facilitate the handling of the experimental results. The characteristic velocity chosen for this approach is the particle velocity u_p , which is equal to the superficial gas velocity minus the slip velocity, in this case assumed as the particle terminal velocity.

Although other authors (e.g. Kehlenbeck, 2000) have tried to establish general correlations, the validity of them is still limited to the specific system. For this reason an empirical approximation was made for this system taking into account the variation of the total solids inventory (TSI) and the influence of the gas density. Whereas for the TSI relation a linear approach showed satisfactory results ((A.3.1.5)-(A.3.1.7)), the evaluation of the pressure dependency was not possible. The values derived from the min square root fit are presented in Table A.3.1.4 and the obtained curves given in (A.3.1.11).

$$G_s = C_1 \cdot u_p^a + C_2 \cdot u_p \quad (\text{A.3.1.5})$$

$$C_1 = c_1 \cdot \text{TSI} + d_1 \quad (\text{A.3.1.6})$$

$$C_2 = c_2 \cdot \text{TSI} + d_2 \quad (\text{A.3.1.7})$$

Table A.3.1.4. Approximation functions constants

	C	d
He/air	2,28E-03	1,46E+00
	-5,01E-03	1,31E+01
air	3,27E-03	1,46E+00
	-7,74E-03	2,09E+01
SF6/air	1,02E-02	-5,56E+00
	-1,50E-02	3,44E+01

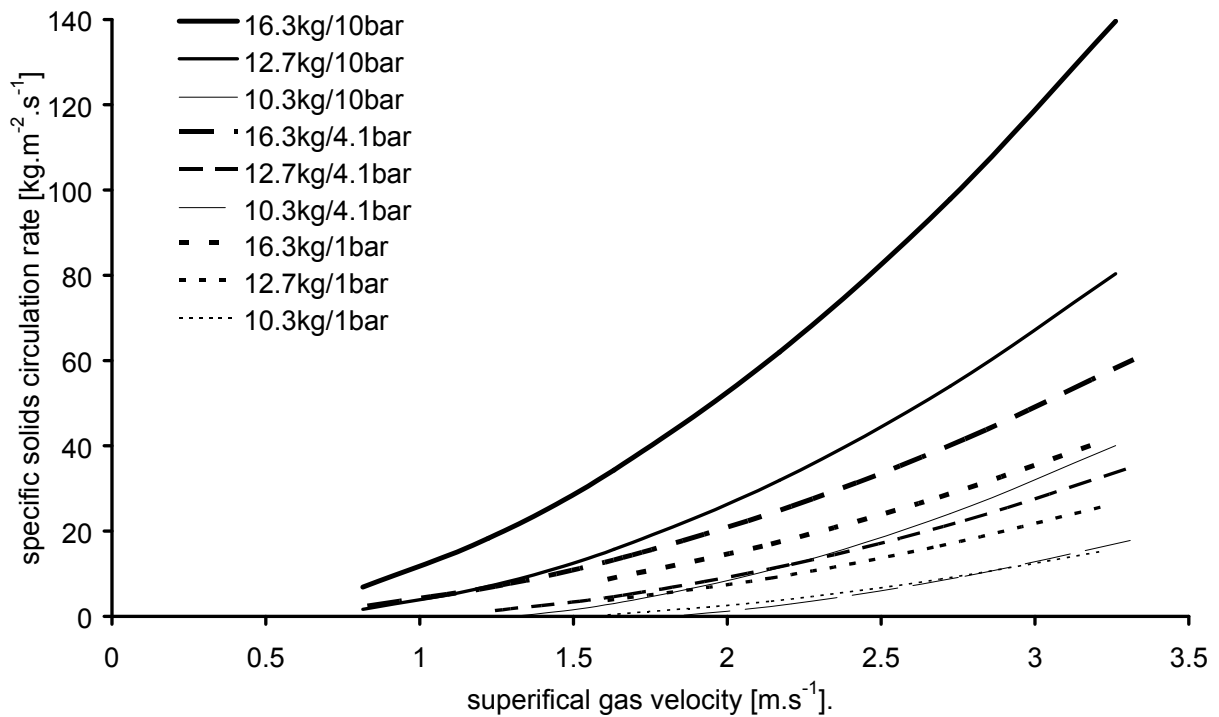


Figure A.3.1.11. Approximation functions of solids circulation rate vs. u_{RIS} for different TSI and pressures.

Figure A.3.1.11 shows a comparison for the three different pressure levels for equal bed material. The bed mass is calculated with a standard fuel reactor mass of 5.7kg. However, it will be shown later that this mass is too low for pressurized conditions and an increased fuel reactor with additional bed material must be provided.

Effect of gas density on CFB fluid dynamics

In Figure A.3.1.12 and Figure A.3.1.13 the effect of the gas density on the vertical pressure profiles is shown. Thereby the height z' is made dimensionless with the total riser height and the dimensionless static pressure is given according to equation (A.3.1.8).

$$p' = \frac{(p - p_0)}{\rho_p \cdot g \cdot D} \tag{A.3.1.8}$$

Each figure shows the dimensionless pressure profiles vs. height for different gas densities for constant Froude number (=constant riser velocity, because of constant d_s), constant volumetric flow rates M/R .

In contrary to the results of Louge et al (1999), the graphs do not show very clearly that the pressure gradient in the upper riser is generally smaller for denser gases. In both figures this seems to be true for atmospheric conditions (He/air) and the pressurized conditions at 4.1 bar (air), but the pressurized case of PCFB-SF6 only qualitatively fits into this assumption. A later analysis will show if their assumption was correct if the significantly different Fr and M/R numbers are reason for this deviation.

The dense acceleration zone at the base of the riser is found smaller for gases with higher density. An explanation for this is the higher drag caused by denser gases, which leads to a

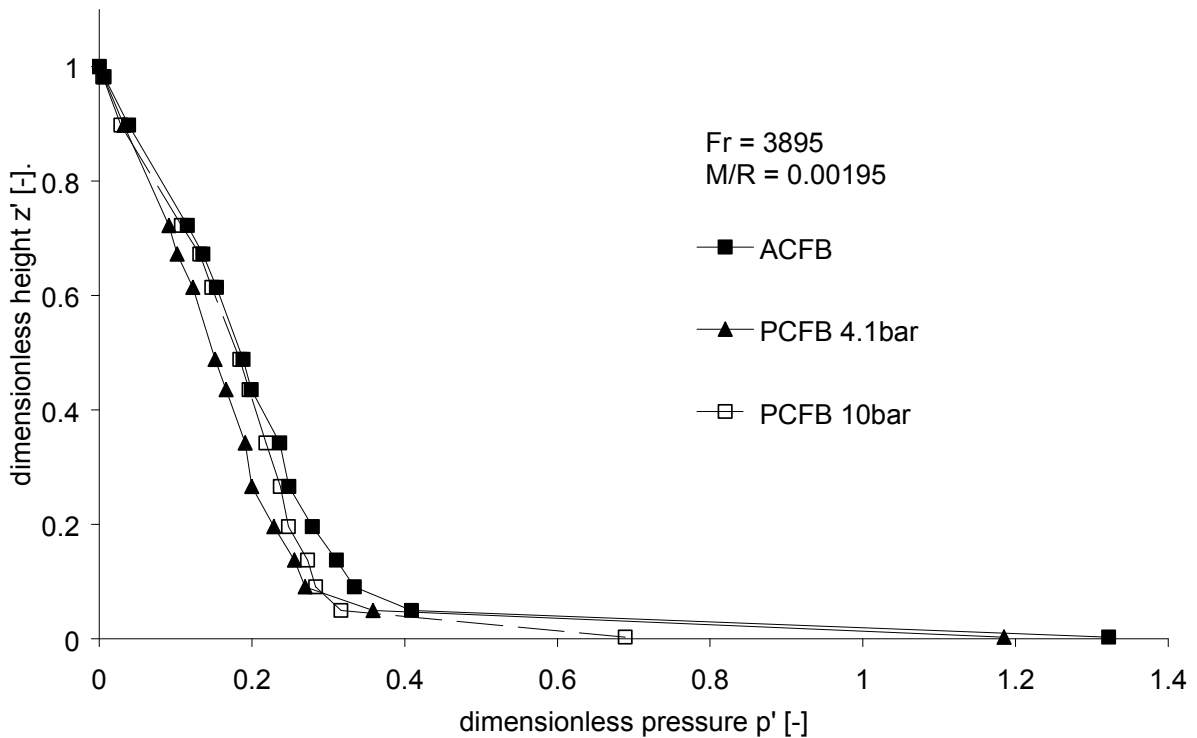


Figure A.3.1.12. Vertical gas pressure profile comparison for $FR = 3895$ and $M/R = 0.00195$

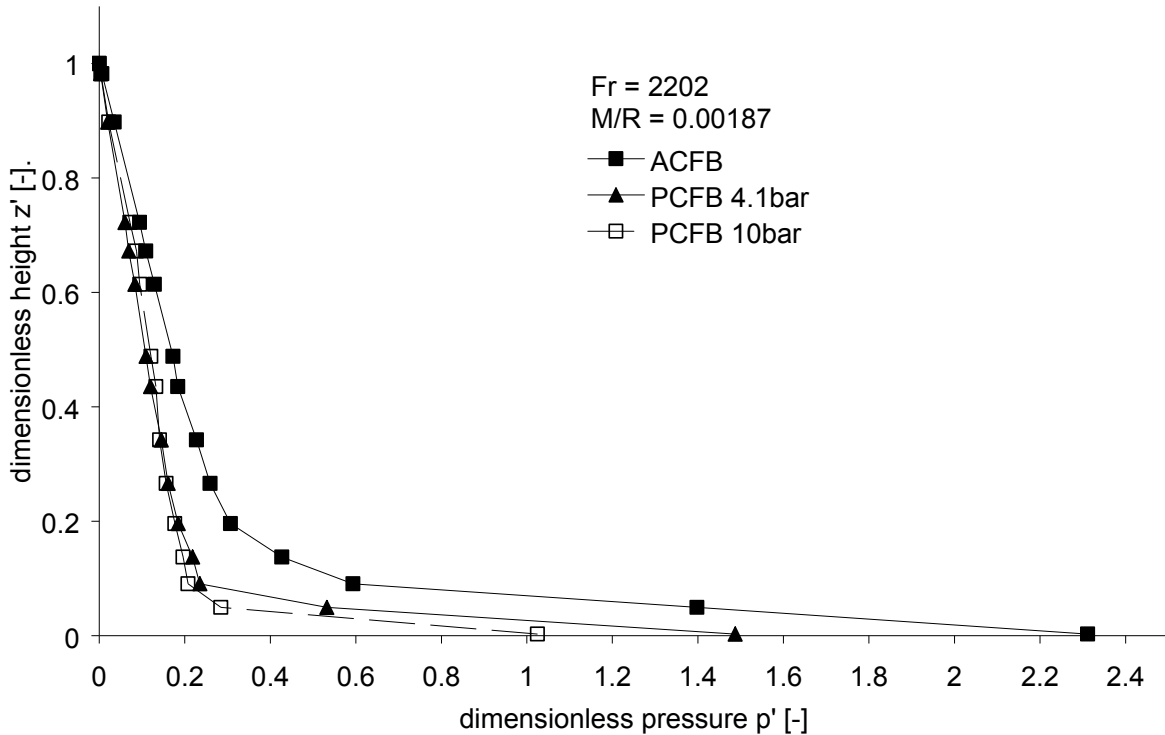


Figure A.3.1.13. Vertical gas pressure profile comparison for FR = 2202 and M/R = 0.00187

smaller height of this zone for the fluidisation gases SF₆-mixture and air in comparison to the Helium mixture.

A mathematical model for parameter studies on CLC thermodynamics

The choice of the oxygen carrier type depends on a number of aspects. A crucial parameter is the thermodynamic behaviour of the oxygen carrier in reaction with a fuel gas. For a systematic analysis of this issue a mathematical model of a CLC system with an integrated solution of the mass and energy balances was developed. Evaluation of the effect of numerous design and operating parameters, such as fuel gas composition and reactor cooling arrangement, were carried out for different oxygen carrier types (Figure A.3.1.14). From this analysis it appears that the conversion and the fraction of active material determine the necessary solids circulation rate. In Figure A.3.1.14 the temperature difference between the two reactors is shown versus the specific solids circulation rate for the syngas model fuel. Additionally, the purity of CO₂ in the FR exit gas flow (dry basis) is plotted in separate charts.

At the given conditions (cooling of 60% in the AR) Cu and Ni cause a larger temperature difference than Fe and Mn. For the latter two a specific solids flow of about 0.002 kg s⁻¹ kW⁻¹ is sufficient to maintain a temperature difference lower than 50°C, whereas for Cu and Ni about 0.008 kg s⁻¹ kW⁻¹ is required for the same limitation. The CO₂-purity as the second characteristic determining the choice of an appropriate solids mass flow shows that for Cu full gas conversion is always achieved and for Mn for mass flows above 0.002 kg s⁻¹ kW⁻¹. Ni has a constant CO₂-purity of about 98%. For Fe, however, circulation rates lower than 0.005 kg s⁻¹ kW⁻¹ cause a dilution of the CO₂ - H₂O mixture to about 90% purity.

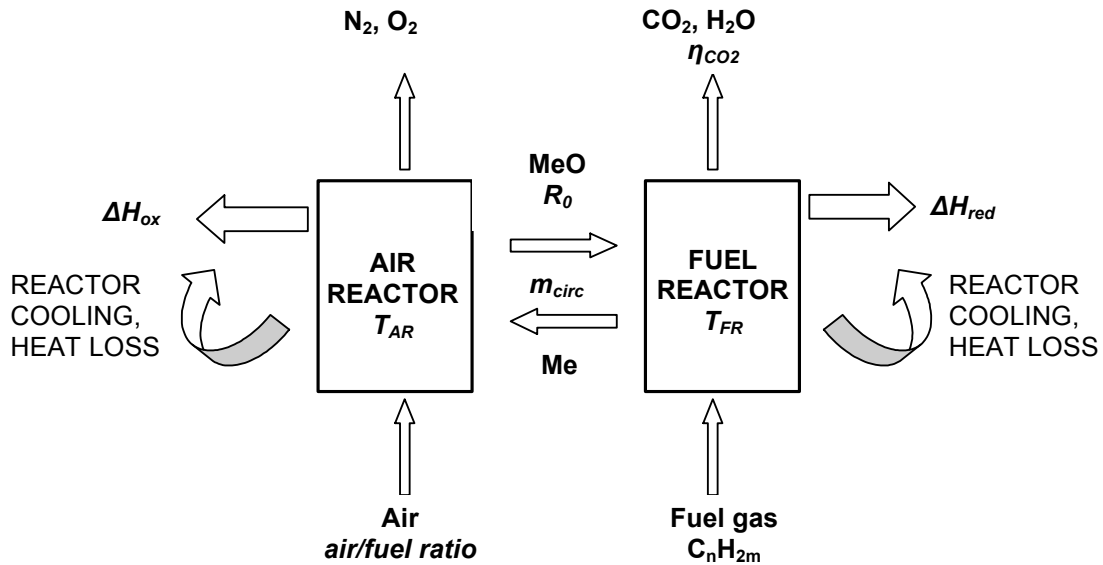


Figure A.3.1.14. Principle of chemical-looping combustion. MeO and Me denote oxidised and reduced oxygen carriers.

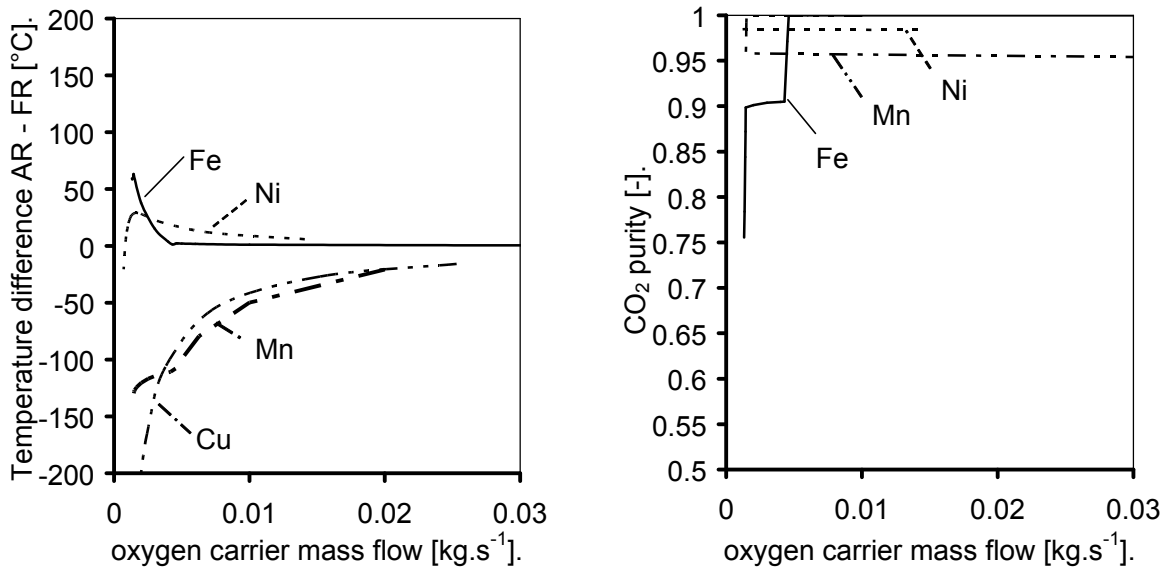


Figure A.3.1.15. Comparison of temperature difference (a) and CO₂ purity (b) between AR and FR and fuel gas conversion for base cases for CO/H₂

From the analysis, it follows that for oxides of the metals Fe, Cu, Ni, and Mn, and for reasonable small temperature differences between the two reactors, an oxygen carrier mass flow of about 0.005 kg.s⁻¹.kW⁻¹ is sufficient for combustion of synthesis gas from coal gasification.

A.4 Task 4. Construction and operation of a laboratory chemical-looping combustor.

A.4.1 Work performed at Chalmers

A laboratory size continuously operated chemical-looping combustion reactor has been designed, built and operated. This system was designed for an input power between 100 and 250 W using syngas as the fuel. Also, the unit was suitable for natural gas as fuel, which is a gas with volume expansion. The relatively low inventory of oxygen carrier needed in this unit make it feasible for testing of different types of oxygen-carriers.

A.4.1.1 Criteria for design

Firstly the fundamental criteria that have to be met in the construction of a chemical-looping combustor are discussed. These criteria are:

- i) Sufficient particle bed mass
- ii) Sufficient particle recirculation
- iii) Proper temperature
- iv) Particle retention
- v) Little gas mixing

Bed mass. The first criterion is that each of the two reactors has to have a sufficient amount of bed material to be able to convert the gas sufficiently.

Particle recirculation. In order to transport enough of oxygen between the two reactors and to attain proper temperature in the fuel reactor, a sufficient flow of particles is needed. The method for particle recirculation is to use a high velocity in the air reactor to carry off particles and then separate them from the gas. The rest of the circulation through the system is accomplished by means of gravity.

Proper temperature. Both reactors need to have a sufficient temperature for the reactions, e.g. 800-900 °C or more. Furthermore the temperature should not be so high that the reactor material or the particles are adversely affected.

Particle retention. The loss of particles from the system has to be minimized.

Little gas mixing. The leakage between the two reactors has to be minimized. This is fundamental to achieve the CO₂ in pure form. However, larger leakages would be acceptable in this testing unit, than in a real unit. It is preferred that leakage goes from the fuel reactor to the air reactor in order to facilitate evaluation of the combustion tests.

In order to maximize the usefulness of the unit it should be designed to give a maximum freedom in choosing running conditions. The following conditions are important:

Particle size. It is important to have some flexibility in the choice of particle size. The range possible to use should be 100 - 200 μ m.

Temperature flexibility. This is desired in order to be able to study the effect of temperature. It should also be noted that the various metal oxides differ when it comes to possible temperature ranges for reasons like melting, thermodynamic stability, kinetics etc.

Pressure. Although this may not be possible within this limited project it would be an advantage if the unit can be modified to be run at increased pressure.

Low bed inventory. The cost of making larger particle batches in small scale presently used in the project, e.g. freeze granulation, is very significant. It would be an important advantage if tests can be made with batches of hundreds, instead of thousands, of grams.

A.4.1.2 Description of the unit

Several possible designs for a hot laboratory reactor of Chemical-Looping Combustion were thoroughly investigated, and the design chosen is shown in Figure A.4.1.1. The idea in this design was to reduce the amount of particles, and also to reduce the complexity of the process. This design is similar to the one proposed by Chong et. al., 1986, and further investigated by Fang et. al., 2003.

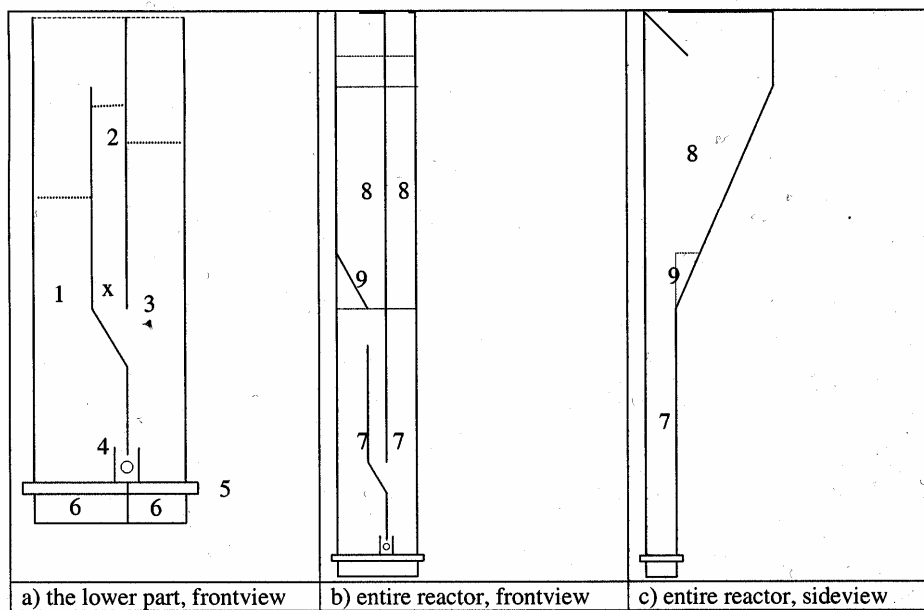


Figure A.4.1.1. The principal sketch of the chemical-looping reactor. 1) air reactor, 2) downcomer, 3) fuel reactor, 4) slot, 5) gas distributor plate, 6) wind box, 7) reactor part, 8) particle separator, 9) leaning wall. Fluidization in the downcomer (x) and slot (o) is also indicated. The dashed lines indicate the bed heights during combustion.

The reactor system was designed for a fuel flow corresponding to a thermal power between 100 and 250 W using syngas as fuel. The prototype is a two-compartment fluidized bed. One compartment is the air reactor (1), with a cross section area of 4x2.5 cm at the bottom and 2.5x2.5 cm at the upper part; the other compartment is the fuel reactor (3), with a cross

section area of 2.5x2.5 cm. The height of the reactor part (see 7 in Figure A.4.1.1) is 20 cm. On top of this section, both reactors increase in width in order to decrease the gas velocities and allow particles to fall back into the reactors. The total height is 44 cm. Due to the size of the reactor, the required solids inventory will be small, which is preferable since the cost of particle production in laboratory scale is high. In order to maintain the temperature in both reactor chambers the whole reactor will be placed in an oven. The gases enter in two separate wind boxes (6), and two porous quartz plates (5) act as distributors for the gases entering the reactors. The air reactor has a high enough velocity for particles to be thrown upwards, with a certain fraction of them falling into a downcomer (2), leading to the fuel reactor. The feeding of particles into the fuel reactor will increase the bed height, which will provide a driving force for returning particles to the air reactor through a slot (4) in the wall between the two reactors. The needed recirculation is determined by the oxygen transfer capacity of the oxygen-carrier. To improve particle circulation argon can be injected through two pipes in the downcomer and in the slot (see symbols x and o in Figure A.4.1.1).

The gas flows leaving the reactors are each connected to gas analysers. The on-line analysers measure carbon monoxide, carbon dioxide and methane with IR technique, and oxygen with paramagnetic technique. The hydrogen content of the exiting gas from the fuel reactor was also analyzed using a gas chromatograph (Varian Micro-GC 4900 equipped with a Molsieve 5A and PoraPLOT Q column). In addition, CO and CO₂ were measured by GC to corroborate the results obtained with the IR analyzer.

A.4.1.3 Leakage tests

In order to understand and evaluate combustion experiments, the gas leakage between air and fuel reactors was first investigated. The leakage was minimized by controlling the pressure in the fuel reactor by a water trap connected to the exit stream from fuel reactor, i.e. the total pressure in the fuel reactor is controlled by the height of the water column. However, there is some gas flow between both reactors. The gas flow from the fuel reactor to the air reactor produces a loss in the CO₂ capture efficiency, and it is named leakage. The gas flow from the air reactor to the fuel reactor dilutes the CO₂ flow at the exit of the fuel reactor, and it is named dilution.

Leakage tests with non-combustible gases were performed in the reactor using the oxygen carrier composed of 60wt% NiO with 40wt% MgAl₂O₄, see particle 39 in Table A.1.2.1, as bed material. Particles of 90-212 μ m were used and the solid inventory was 340 g, giving an overall bed height of about 12 cm. Five different test series were made, and in each one or two of the gas flows were varied. A summary of the test conditions and the corresponding power is shown in Table A.4.1.1. In all the leakage tests the temperature of the fuel reactor was 850 °C.

The values of the flows were set to match the flows used in real combustion tests as closely as possible. A first series of tests to measure leakage was made with carbon dioxide as fluidization gas in the fuel reactor, air in the air reactor and argon in the downcomer and slot. A second series was made with carbon dioxide instead of argon in the downcomer and slot, nitrogen in the fuel reactor and air in the air reactor. These tests were made primarily to investigate how the gas in the downcomer and slot are divided between the reactors. In both outgoing gas streams the concentration of carbon dioxide and oxygen was measured. From a mass balance over the system the dilution and the leakage between the reactors can be

Table A.4.1.1. Leakage test series.

Test number	U _{FR}	U _{AR}	U _{DC}	U _{SL}	T _{FR}	Corresponding power	
	L/min	L/min	L/min	L/min	°C	CO/H ₂ W	CH ₄ W
L1	0.15-0.9	6	0.01	0.02	850	30-170	100-530
L2	0.35	4-6.5	0.01	0.02	850	70	200
L3	0.15-0.55	1.7-6.3	0.01	0.02	850	30-110	100-300
L4	0.35	4	0-0.04	0.02	850	70	200
L5	0.35	4	0.01	0.01-0.04	850	70	200

determined. The leakage is related to the incoming flow in the fuel reactor, thus indicating the percentage of carbon which is lost to the air reactor and the leakage in the other direction, i.e. dilution, is also related to the incoming fuel flow.

The leakage and dilution are shown in Figures A.4.1.2 as a function of the flow rate to the fuel reactor or the air reactor respectively (tests L1 and L2). Both the leakage and dilution are highly dependent on the fuel flow as seen in test series L1, Figures A.4.1.2a, where the leakage varies from 35 to 15% while the dilution varies from 25 to 10%. A higher velocity in the fuel reactor significantly decreases both the leakage and dilution. However, the absolute leakage flow in both directions increases. A higher gas flow leads to larger pressure fluctuations, which may result in higher flows of leakage. All the same, the leakage and dilution, which are related to the fuel flow, may decrease. The leakage from the fuel reactor increases as the velocity in the air reactor increases as seen in test series L2, Figures A.4.1.2b, and varies in the range 13-22% for leakage and 5-10% for dilution. Several mechanisms could explain this behaviour. Firstly, a higher particle circulation causes a higher pressure in the fuel reactor. Secondly, a higher air flow gives higher particle circulation, and could cause an increase in the leakage because some gas is expected to follow the particles. Thirdly, an increase of pressure fluctuations should favour the gas exchange through the slot. In these tests, the leakage from the fuel reactor is roughly twice as large as the dilution of the fuel reactor. A reason for this is believed to be the higher pressure in the fuel reactor than the air reactor.

In the leakage experiments where the air to fuel ratio was held constant (tests L3), the leakage in both directions goes through a minimum. This fact involves the combined effects of increased air and fuel flow. A change in gas flow in the downcomer or in the slot (tests L4 and L5) does not affect the gas leakage between the reactors significantly, except for the leakage from the fuel reactor that goes through a minimum when the fuel flow in the downcomer is varied. It was preferable to keep the gas flow in the downcomer low, but not zero. Higher gas flow in the downcomer increases the voidage in the particle column, and this might facilitate a leakage from the fuel reactor to the air reactor. The tests with carbon dioxide in the downcomer and slot showed that about 50% of this flow enters the fuel reactor.

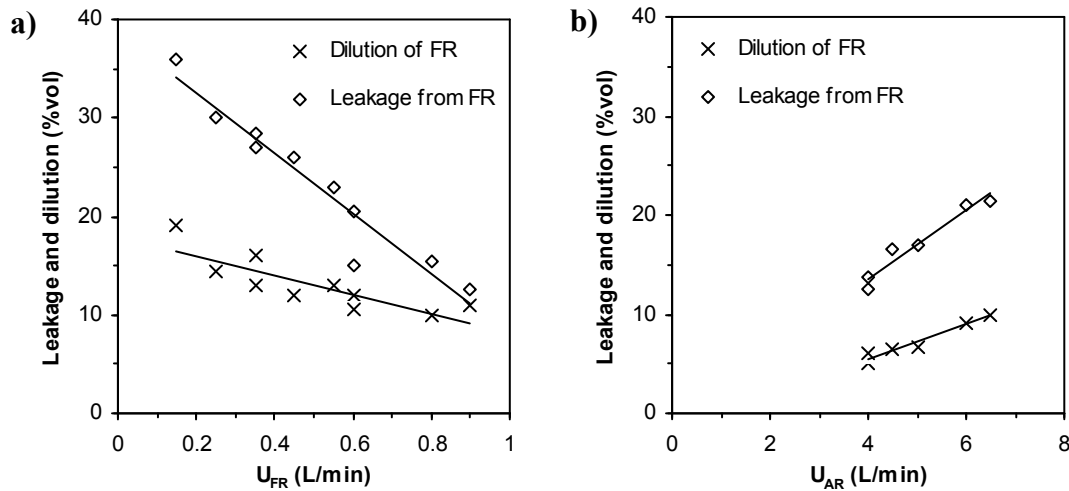


Figure A.4.1.2. The leakage and dilution as a function of the volume flow in a) the fuel reactor, U_{FR} , or b) the air reactor, U_{AR} .

The dilution and leakage has to be considered when the combustion results are interpreted. According to the data shown above, about 1-4% of the oxygen supplied comes from air leaking into the fuel reactor when syngas or natural gas is used as fuel. The analysis of the cold model (Kronberger et al., 2004) showed that the dilution was mainly through the slot. It is likely that most of the oxygen will react with the fuel and the particles in the lower part of the reactor, and thus, the air dilution is expected to have a rather small effect on the final conversion.

A.4.1.4 Combustion tests

Combustion test series were performed with two fuels, simulated syngas consisting of a mixture of 50% CO and 50% H₂, and for comparison, natural gas. The natural gas consists of 88% methane, and has a H/C ratio of 3.7. The fuel flow, the air flow and the temperature in the reactors were varied one at a time. Four tests series were made with syngas (S series) and three tests series were made with natural gas (N series). The test conditions are described in detail in Table A.4.1.2.

From the screening tests performed in section A.2.1, three different oxygen carriers were chosen to be studied in the continuous reactor. Approximately 400 g of these new particles were prepared by freeze granulation for use in the reactor. First, a Ni-based oxygen carrier composed of 60% NiO and 40% MgAl₂O₄, particle number 39 in Table A.1.2.1.1. Second, a Mn-based oxygen carrier, composed of 40% Mn₃O₄ and 60% Mg-ZrO₂, number 29 in the same table. The third oxygen carrier tested was a Fe-based oxygen carrier, composed of 60% Fe₂O₃ and 40% Al₂O₃ and sintered at 1100°C. Because the Mn- and Fe- based oxygen carrier particles have a smaller density in comparison to the Ni-based carrier, the air reactor was operated with a lower gas flow when using Mn and Fe. This was done in order to prevent oxygen carriers from leaving the reactor with the exit gas streams. The solid inventory was 340 g for NiO/MgAl₂O₄ particles, 295 g for Mn₃O₄/Mg-ZrO₂ particles and 300 g for the Fe₂O₃/Al₂O₃ particles, and thus the bed height was the same in all tests, about 12 cm.

Table A.4.1.2. Combustion test series.

Test number	U _{FR} L/min	U _{AR} L/min	U _{DC} L/min	U _{SL} L/min	T _{FR} °C	Power W	Air ratio
S1	0.5-1.3	6 ⁽¹⁾ -5 ⁽²⁾	0.01	0.02 ⁽¹⁾ -0.01 ⁽²⁾	850	100-250	1.6-5.0
S2	0.9	3.5-6	0.01	0.02 ⁽¹⁾ -0.01 ⁽²⁾	850	175	1.6-2.8
S3	0.5-1.3	2.5-6.5	0.01	0.02 ⁽¹⁾ -0.01 ⁽²⁾	850	100-250	2.1
S4	0.9	3.5	0.01	0.02 ⁽¹⁾ -0.01 ⁽²⁾	800-950	175	1.6
N1	0.15-0.55	6 ⁽¹⁾ -5 ⁽²⁾	0.01	0.02 ⁽¹⁾ -0.01 ⁽²⁾	850	100-360	1.1-3.8
N2	0.35	4-6.5	0.01	0.02 ⁽¹⁾ -0.01 ⁽²⁾	850	230	1.1-1.8
N4	0.35	4	0.01	0.02 ⁽¹⁾ -0.01 ⁽²⁾	800-950	230	1.1

⁽¹⁾ using NiO/MgAl₂O₄; ⁽²⁾ using Mn₃O₄/Mg-ZrO₂ and Fe₂O₃/ Al₂O₃

The investigated particles have been fluidized with recirculation in hot conditions for approximately 150 h for Ni particles, 130 h for Mn particles, and 60 h for Fe particles. During the operation of the reactor no signs of agglomeration of the particles were observed. For NiO/MgAl₂O₄ oxygen carrier there was a loss in the bed mass of 13 g. This corresponds to a loss of 0.027% per hour. However, no measurable amounts of particles were found in the filters. Minor losses could be associated with deposits in the ducts leading to the filters. For Mn₃O₄/Mg-ZrO₂ particles a mass loss in the system of 15 g was observed at the end of the experimental series. This corresponds to a loss of 0.039% per hour. The main quantity of the mass loss was collected in the filter at the air reactor exit during the first hour of operation at hot conditions. This mass loss could be related to elutriation of small particles, either present in the original sample or from primary fragmentation, from the air reactor where the fluidization was vigorous. No loss of material was observed after the experimental series when Fe carrier was used as bed material. These results suggest that attrition was low and the Ni-, Mn- or Fe-based oxygen particles used in this work have a high durability.

A.4.1.5. Combustion with syngas

Combustion test series S1-4 were carried out with syngas using NiO/MgAl₂O₄, Mn₃O₄/Mg-ZrO₂, and Fe₂O₃/Al₂O₃ oxygen carriers. For these experiments, the CO is presented below as the fraction of carbon products leaving the fuel reactor:

$$f_{\text{CO}} = \frac{x_{\text{CO}}}{x_{\text{CO}_2} + x_{\text{CO}}} \quad (\text{A.4.1.1})$$

and H₂ is presented in a similar way, i.e. as the fraction of total hydrogen leaving the reactor. Since the fuel consists of 50% CO and 50% H₂, the total molar flow of H₂+H₂O leaving the reactor is equal to CO+CO₂.

$$f_{\text{H}_2} = \frac{x_{\text{H}_2}}{x_{\text{H}_2\text{O}} + x_{\text{H}_2}} = \frac{x_{\text{H}_2}}{x_{\text{CO}_2} + x_{\text{CO}}} \quad (\text{A.4.1.2})$$

Figures A.4.1.3a-d show the CO and H₂ fractions as a function of the flow in the fuel reactor, the flow in the air reactor or the temperature. For Ni-based particles, the fraction of CO and H₂ was in the range 0-2.3%. Using the Mn-carrier the conversion of fuel was complete, with no CO and H₂ in the flue gas for all tested cases. In this case, the values for the thermodynamic equilibrium were only represented. For Fe-based particles, the fraction of CO was considerably higher than the fraction of H₂.

Figure A.4.1.3a shows that an increase in the fuel flow increased the amount of CO and H₂. This is expected, firstly because the amount of oxygen-carrier in the fuel reactor, and the oxygen supply into the fuel reactor were constant, but the flow of fuel increased. The circulation of the particles, and thereby oxygen supply, is determined by the velocity in the air reactor, which was constant. Secondly, there is also a less efficient contact between the particles and the gas at higher velocities when a larger fraction of the gas will be in the bubble-phase. In tests using Ni-based particles, at the two lowest velocities of the fuel, both the fraction of CO and H₂ was lower than the corresponding equilibrium values of 0.71 and 0.64%. One possible explanation for these low fractions are that all of the oxygen leaking from the air reactor does not react on the way up through the bed, but reacts with CO and H₂ above the bed. As seen in Fig A.4.1.2a the dilution increases at low fuel flows.

An increase of the gas flow in the air reactor decreases the concentration of CO and H₂ in the flue gas from the fuel reactor slightly (Figure A.4.1.3b). This might be explained by a higher recirculation flow of particles, and thereby more oxygen is carrying from the air reactor to the fuel reactor. When the air ratio is held constant, and both fuel flow and air flow increases, the amount of unburnt increases, see Figure A.4.1.3c. This indicates that the effect of the increase in the fuel flow is higher than the effect of the increase of the air flow.

Figure A.4.1.3d shows the effect of the temperature of reaction on the fraction of CO and H₂ at the gas flue exit and for equilibrium conditions. For Ni, the fractions of CO and H₂ was higher than the equilibrium at 800 °C, and at temperatures from 850 °C the fraction of CO and H₂ reaches equilibrium. However, even at a low temperature of 800 °C the conversion of syngas was high. Tests with this carrier and syngas in the batch fluidized bed also found high reactivity initially at these temperatures, although there was a clear decrease in reactivity at low degrees of conversion, see section A.2.2. The Mn-carrier has complete gas yield at all temperatures. For the Fe, the fraction of CO decreases from 2.2 at 800 °C to 0.5 at 950 °C. The fraction of H₂ was below the fraction of CO. This tendency was also observed with Ni particles. This indicates that H₂ reacts faster with the oxygen carrier than CO.

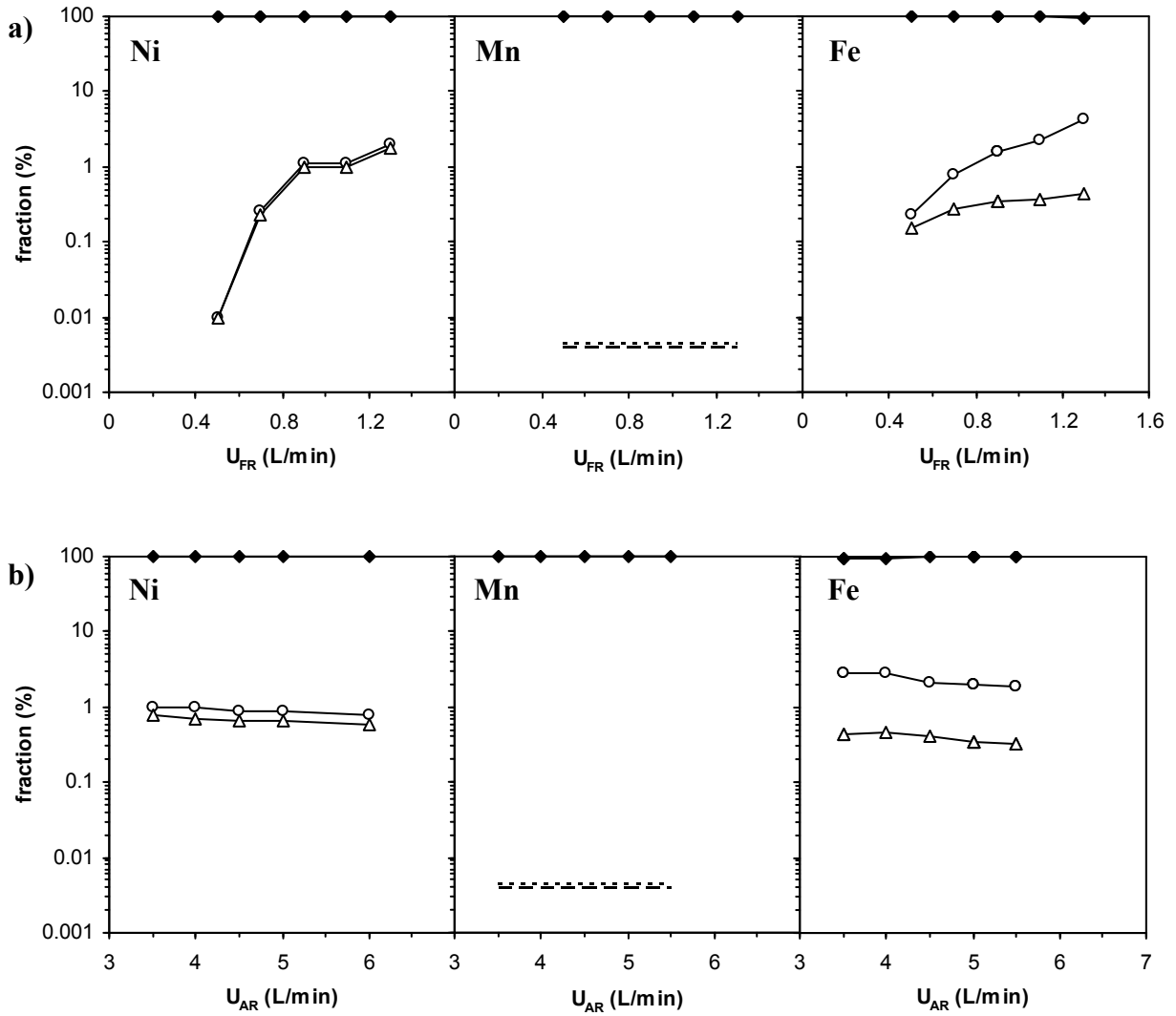


Figure A.4.1.3. The fraction of CH₄, CO, H₂ and CO₂ in the combustion products of syngas as a function of a) the flow in the fuel reactor (S1), b) the flow in the air reactor (S2), c) the flow in the fuel reactor at constant air ratio (S3), and d) the reactor temperature (S4). Symbols: —○— CO; —△— H₂; —◆— CO₂; CO at equilibrium; — — H₂ at equilibrium.

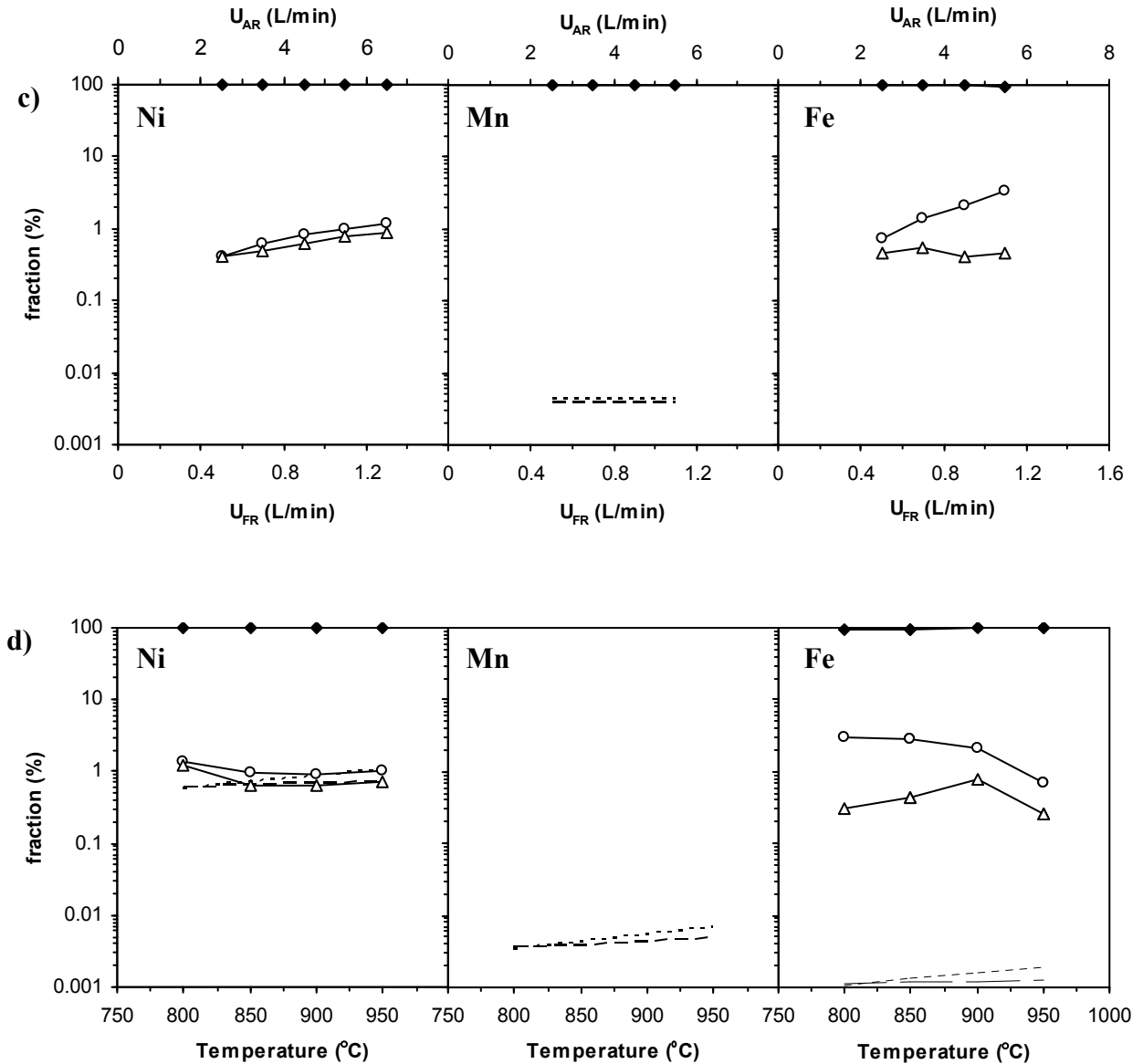


Figure A.4.1.3 (cont.). The fraction of CH₄, CO, H₂ and CO₂ in the combustion products of syngas as a function of a) the flow in the fuel reactor (S1), b) the flow in the air reactor (S2), c) the flow in the fuel reactor at constant air ratio (S3), and d) the reactor temperature (S4). Symbols: —○— CO; —△— H₂; —◆— CO₂; CO at equilibrium; — — H₂ at equilibrium.

Figure A.4.1.4 shows the combustion efficiency as a function of the reactor temperature for Ni-, Mn- and Fe-based oxygen carriers. Because of thermodynamic limitations the combustion efficiency for Ni particles was limited at 0.994 at 800 °C or 0.991 at 950 °C. In contrast to Ni-based oxygen carriers, there is no thermodynamic limitation for the system Mn₃O₄-MnO or Fe₂O₃-Fe₃O₄. The Mn carrier showed efficiencies near to unity at all temperatures. However, combustion efficiency with Fe particles was higher than 0.98, but efficiencies near to 1 could be possible at equilibrium conditions. In comparison to the batch tests done with these oxygen carriers, manganese and iron showed high reactivity at temperatures as low as 650°C while a clear decrease in reactivity at high degrees of conversion was seen for Ni at temperatures of 850°C and below.

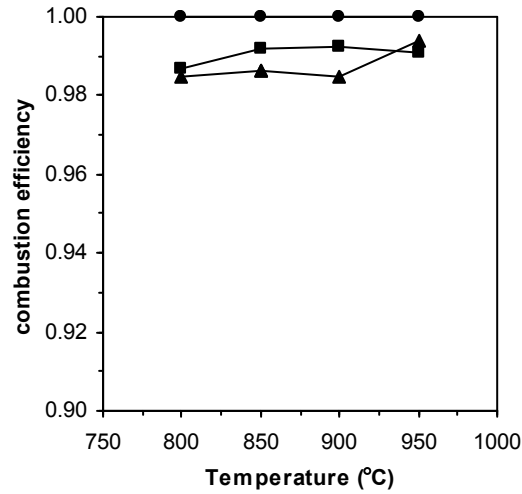


Figure A.4.1.4. The combustion efficiency for natural gas as a function of the reactor temperature (N4). Symbols: —■— Ni; —●— Mn; —▲— Fe.

When syngas is used as fuel, particles tested are well suited as oxygen carriers. They give a high conversion of the fuel with small amounts of unburnt from the fuel reactor. For many of the tests with NiO/MgAl₂O₄ equilibrium is reached and combustion efficiency was 0.994 at 850 °C. For Mn₃O₄/Mg-ZrO₂ the CO and H₂ concentrations were below the detection level of the gas analyzer or GC. At 850 °C, combustion efficiency at equilibrium conditions is 0.9996. Fe-based oxygen carrier showed high conversion of the fuel with a combustion efficiency of 0.988 at 850 °C.

A.4.1.5 Combustion with natural gas

In general, the combustion tests with natural gas showed the presence of CO and H₂ in the exit gas stream from the fuel reactor. Higher amounts of methane were detected using Mn- and Fe-based oxygen carriers, but no methane was detected in tests carried out with Ni-based oxygen carrier.

The fraction of carbon monoxide in the gas from the fuel reactor is presented below as the fraction of total carbon leaving the fuel reactor:

$$f_{\text{CO}} = \frac{x_{\text{CO}}}{x_{\text{CO}_2} + x_{\text{CO}} + x_{\text{CH}_4}} \quad (\text{A.4.1.3})$$

where x_i is the molar fraction of i in dry exit gas. The methane, hydrogen and carbon dioxide fractions are calculated in a similar way.

The fraction of CH₄, CO and H₂ in the flue gas as a function of the fuel flow is shown in Figure A.4.1.5a for the oxygen carriers used in this work. In all cases, these fractions increased with the fuel load. This is the same trend as with combustion with syngas, and can be explained in the same way, see discussion above.

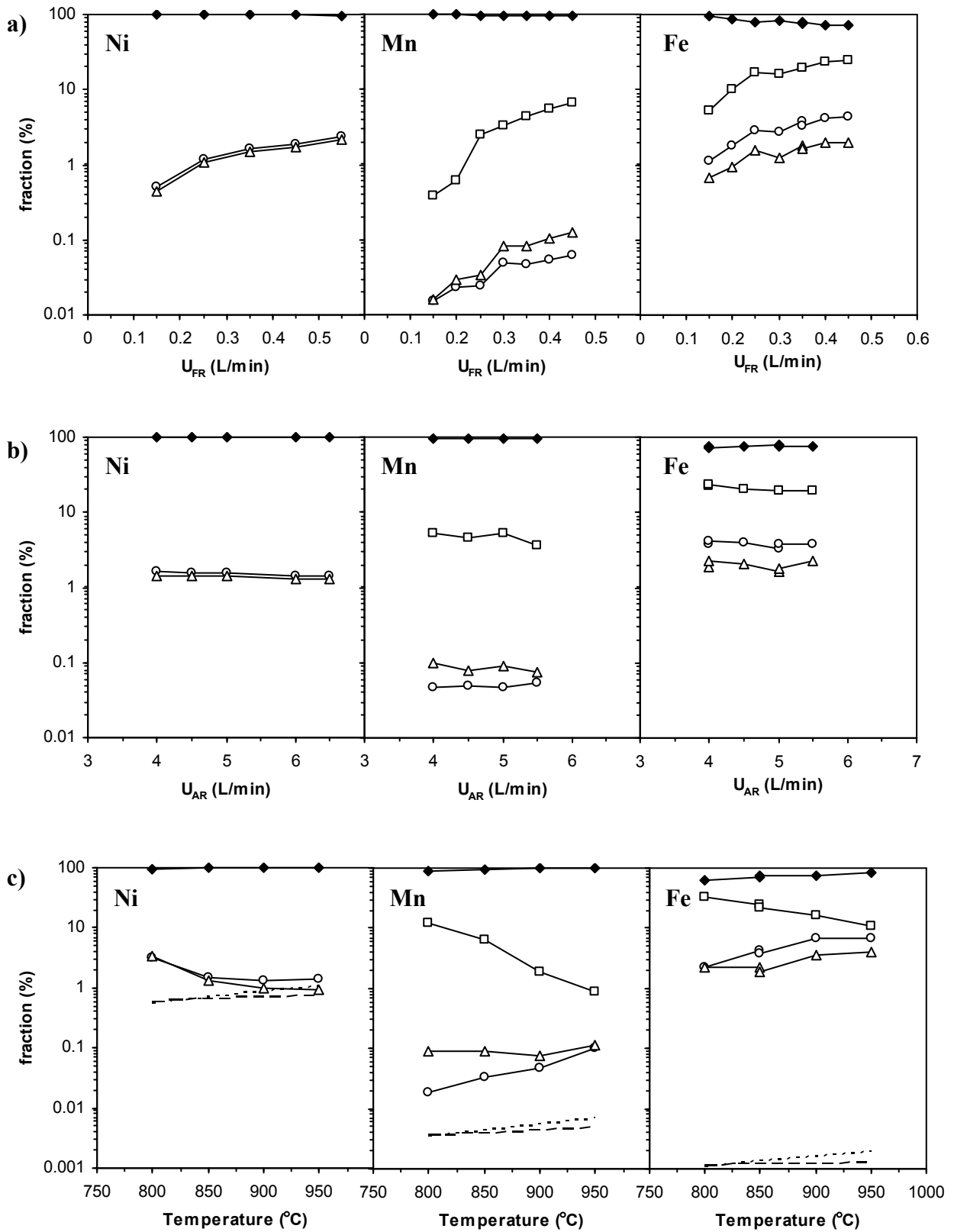


Figure A.4.1.5. The fraction of CH₄, CO, H₂ and CO₂ in the combustion products of natural gas as a function of a) the flow in the fuel reactor (N1), b) the flow in the air reactor (N2), and c) the reactor temperature (N4). Symbols: —□— CH₄; —○— CO; —△— H₂; —◆— CO₂; CO at equilibrium; — — H₂ at equilibrium.

Figure A.4.1.5b shows that an increase in the air flow gives a slight decrease in the fraction of CH₄, CO and H₂. This fact could be caused by increased circulation of the particles, which increases the oxygen transfer to the fuel reactor as well as the bed height.

The fraction of CH₄, CO and H₂ as a function of the temperature is shown in Figure A.4.1.5c. The equilibrium lines for the fraction of CO and H₂ are also shown in the figure. Methane concentration for the equilibrium conditions was very close to zero in all cases. For Ni-based oxygen carrier, there was no methane found in the gas from the fuel reactor. At the lowest temperature, 800 °C, the fraction of CO and H₂ is approximately 3%. At the higher temperatures, it is rather stable at 1.5% in the range 850-950 °C. At the highest temperature equilibrium is approached. For Mn₃O₄/Mg-ZrO₂ particles the fraction of CH₄ was about 12% at 800 °C, but this fell to 0.9% at 950 °C. On the contrary, the fractions of CO and H₂ were maintained at low values (below 0.1%), although higher than equilibrium concentrations.

A similar behaviour for the outlet CH₄, CO and H₂ fractions was obtained with the Fe-based oxygen carrier, although the actual fractions were higher than those obtained with the Mn-based particles. The fraction of methane was higher than 10%, meanwhile the fractions of CO and H₂ were in the range 2-7%. In Figures A.4.1.5a-c the fraction of CO₂ is shown, which is the degree of methane yield to carbon dioxide. It can be seen that high CO₂ fractions were obtained with Ni and Mn, but lower values, from 65 to 95%, was seen with Fe.

For comparison purposes Figure A.4.1.6 shows the combustion efficiency, based on the heating value, for the different oxygen carriers as a function of the reactor temperature. The combustion efficiency increases as the temperature increases, but the behaviour depends on the oxygen carrier. Ni oxygen carrier shows combustion efficiencies about 0.99 in the range 850-950 °C. These particles are acting as a catalyser for the methane reforming. Thus, the fraction of fuel non-converted is the fraction of CO and H₂. The efficiency was limited at 0.992 at 950 °C because of the concentration of CO and H₂ at equilibrium conditions.

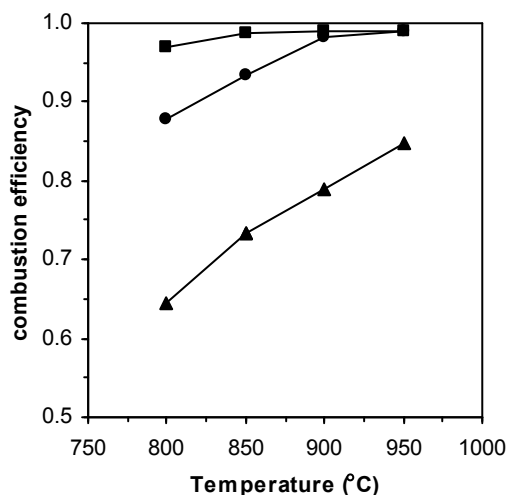


Figure A.4.1.6. The combustion efficiency for natural gas as a function of the reactor temperature (N4). Symbols: —■— Ni; —●— Mn; —▲— Fe.

For the Mn-based oxygen carrier a strong effect of the temperature on the combustion efficiency was observed. For these particles there is a decrease in the methane concentration

as the temperature increases, meanwhile the CO concentration was low. Unconverted CH₄ can be due to the slow reforming reaction of CH₄. It is likely that CO and H₂ are intermediates in the reaction between the metal oxide and methane. An increase in the reaction temperature increases the CH₄ reforming rate. Consequently, the CH₄ concentration decreases, and the combustion efficiency increases. In the present tests, an increase in the reactor temperature increased the combustion efficiency from 0.88 at 800 °C to 0.99 at 950 °C.

The combustion efficiency obtained with the iron based particles was rather low. Similar to Mn particles, there is a strong increase in the combustion efficiency as the temperature increases from 800 to 950 °C. However, a maximum efficiency of 0.85 was obtained at 950 °C. The low oxygen ratio for this carrier, besides the slow CH₄ reforming rate, could be the reasons for the poor efficiency obtained for Fe-based particles. The oxygen ratio, R₀, is the mass fraction of oxygen that can be used in the oxygen transfer, and is defined as:

$$R_0 = \frac{m_{\text{ox}} - m_{\text{red}}}{m_{\text{ox}}} \quad (\text{A.4.1.4})$$

For the oxygen carriers used in this work, the oxygen ratio was 0.13 for Ni particles, 0.028 for Mn particles, and 0.018 for Fe particles. For the Fe based particles the oxygen ratio is based on the system Fe₂O₃/Fe₃O₄. The formation of lower forms of iron oxide, such as FeO, is not desired since the thermodynamic conversion of methane is low.

When natural gas is used as fuel, Ni particles are better suited for the use in a chemical looping combustion system. To increase the combustion conversions for methane with Mn- and Fe-based oxygen carriers a higher amount of oxygen carrier could be used in addition to a high temperature.

A.5 Task 5. Characterisation of sorbent (CaO) performance in the LCCC

This task was a fundamental part of the project as it had to supply the key information to define the different process operating conditions in quantitative form (solid circulation flow between units, fresh sorbent requirements and purge rates all depend on sorbent capture capacity along cycling). The main activity in this task has been carried out by CSIC, with relevant input from Cranfield (for the “in duct” carbonation option, as described in A6.1) and VTT (section A.5.2 below).

Before detailing the experimental and modelling work under this task, and in order to put a frame to the work conducted in this project, we describe in the next paragraphs the fundamentals of the carbonation-calcination chemical loop and the state of the art when the project started.

Equilibrium data for the calcination of CaCO₃ is represented in Figure A.5.1 using the correlation of Baker, (1962) in the temperature intervals of interest for this project. Attending to the equilibrium, and for coal combustion gases with partial pressures of CO₂ around 0.12 atm, there is a suitable temperature window for carbonation (between 600 and 750 °C) that can achieve substantial reduction in CO₂ emissions. At pressures higher than the atmospheric, this temperature range increases to 800-850°C. Also, calcination at temperatures higher than 900 are needed to deliver a pure stream of CO₂ in the calciner at atmospheric pressure (the use of vacuum/steam in the calciner to lower the partial pressure of CO₂ and will be considered later). The conditions expected in the reactors considered in this project are beyond the regions where liquid phases may appear in the calciner or carbonator (Curran, 1967; Paterson et al., 2001), that where a problem of melts appeared under the high pressure and reducing conditions in the the Acceptor Gasification Process (Gorin, 1980), that used a similar carbonation-calcination cycle to increase the H₂ yield in a coal gasifier (Curran et al, 1967).

In addition to a favourable equilibrium, it is also essential that sufficiently high reaction rates occur in the carbonator and calciner for these reactors to have meaningful dimensions. The calcination of CaCO₃ is perhaps the most intensively studied solid decomposition reaction in the scientific literature. Well validated experimental methodologies and data are available to derive rate expressions suitable for a wide range of conditions depending on the particular application, including those to be used in a LCCC system. Also, there is a wide range of industrial applications where calcination is taking place under similar conditions. Two close examples within the coal-energy sector are the in-duct sorbent injection to PF boilers and the limestone addition to FBCs to capture SO₂. Large number experimental and theoretical studies on calcination for these conditions have been reported in the literature, many of which have been reviewed and compared recently by Garcia Labiano et al. (2001). In view of this experience and these studies, we have assume that calcination can be completed and achieved in very short times in a LCCC system, designed to allow enough solid residence time in a calciner operating at temperatures over 50°C (at least) higher than the equilibrium temperature given in Figure A.5.1.

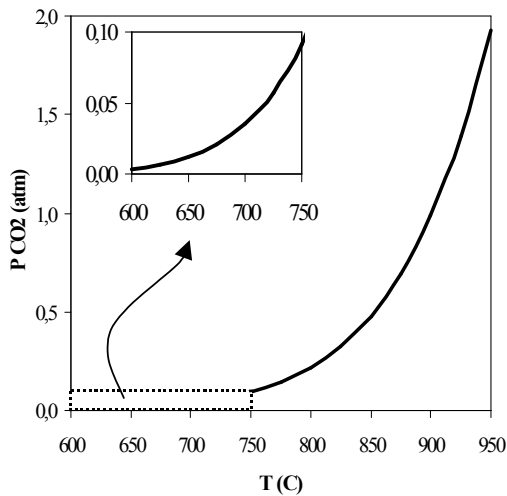


Figure A.5.1. The equilibrium pressure of CO₂ on CaO.

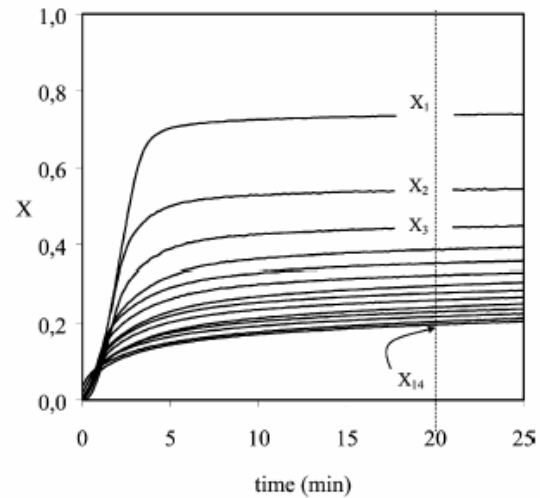


Figure A.5.2. Example of carbonation conversions curves (T=650°C, 10%v CO₂, limestone "la blanca" calcined at 900°C, 0.4-0.6 mm)

The recarbonation reaction of CaO to form CaCO₃ has received far less attention than the reverse calcination reaction and is obviously the critical "capture step" in any LCCC system. An example of the recarbonation results from this project, using samples of CaO particles with increasing number of carbonation calcinations cycles is presented in Figure A.5.2. The investigation of the recarbonation reaction has been the key subject of all sorbent performance studies in this project as will be shown below, with thousands of experiments in TG and fixed bed reactors like the few presented in Figure A.5.2.

Bathia and Perlmutter (1983) reviewed the scarce data on recarbonation kinetics previously published and carried out an extensive experimental and modelling work of direct relevance for this project. They showed, in agreement with several previous findings, that the kinetics of the recarbonation follows an initial fast stage reaction followed by a much slower stage controlled by diffusion through a product layer of CaCO₃. Their experimental results with limes of different origin, pore structure, particle sizes and at different temperatures and concentration of CO₂ are modelled reasonably well with a reaction mechanism based on their random pore model (Bathia and Perlmutter, 1980). They also showed that the reaction rates in this fast stage part of the conversion curve are independent of particle size, but dependent on textural properties of the sorbent (initial surface area and porosity). They found a very good agreement between this maximum conversion attained during fast carbonation (onset of the slow reaction regime) with the fraction of porosity that corresponds to pore sizes lower than 100 Å.

For the purposes of this project, the most interesting part in the carbonation conversion curves will be the fraction of the curves that correspond to the rapid reaction stage. This is because this will be the only relevant to achieve sufficiently high reactor intensities in the carbonator (understood as units of CO₂ captured per unit volume of the reactor). Mess and Sarofim (1999) have studied the slow stage of the carbonation curve under very high pressures of CO₂, and concluded that the diffusion mechanism of CO₂ through the product layer becomes even slower with increasing conversion, which puts recarbonation after the first fast stage, well beyond any practical interest, even as a sorbent regeneration option. It will be shown below that reaction rates to achieve maximum conversion in the order of 10 seconds are essential for the options

using entrained mode gas-solid contact, while reaction rates in the order of several minutes are sufficient for those using fluidised bed gas-solid contact. However, the fast reaction rate clearly finishes in a value of conversion that decays with the number of cycles (as can be already seen in Figure A.5.2). Thus, the key phenomena in the carbonation/calcination reaction for the purpose of this project is the decay in activity of the sorbent in the subsequent cycles carbonation/calcinations which is an area where the information is particularly scarce and this project has made the largest contribution to date. Therefore, the target for task 5 was to supply information on how fast, but specially in what extent, goes the conversion in the carbonation reaction of the sorbent, as a function of operating conditions (calcination temperatures, partial pressure of CO₂ and other gases during carbonation, particle size, etc) at different cycle numbers and for different type of materials.

A.5.1 Work carried out at CSIC

The experimental studies have been carried out in two different types of equipment: a thermogravimetric analyser (CSIC-ICB) and a fixed bed reactor suspended in a tube furnace (CSIC-INCAR). The latter provided sufficient amount of sample to allow the collection of small intermediate sub-samples for their characterisation under the SEM. A review of existing literature on this subject was completed by compiling all the published results on sorbent performance and putting them in a consistent base to allow comparison (see below and also Abanades and Alvarez, 2003).

The TGA used to investigate the cyclic carbonation and calcination reactions consist of a quartz tube placed in an oven, which can be operated at temperatures up to 1000 °C. The sample-holder was a platinum basket (8 mm diameter and 2 mm height). The temperature and the sample weight were continuously recorded in a computer. The reacting gas mixture contained CO₂, O₂ and N₂ in different proportions set by mass flow controllers. For each run in the TGA experiments, around 10 mg of limestone were loaded in the basket. After complete calcination, the temperature to the carbonation temperature (650°C in all the experiments) and the calcines were exposed for at least 20 min to the simulated carbonation gas mixture, consisting of the desired CO₂ concentration in air. The system was changed to allow more rapid and automatic operation in multicycle test (see Figure A.5.1.1).

The fixed bed reactor is a 1m high vertical furnace surrounding an alumina tube where a basket containing the sample is suspended along its vertical axis. The reacting gases are axially injected at the base of the tube, are forced to pass through the basket and leave the furnace by the upper end of the tube. The depth of the particulate bed was limited to about 5 mm (~5 g of parent limestone). Solids were allowed to react 10 min for calcination and 30 min for carbonation. A fast change of the experimental conditions between calcination (900 °C, air) and recarbonation (650 °C, 20% CO₂) was achieved by taking advantage of the temperature profiles along the furnace. Thus, when the furnace was operated at 930 °C (temperature at the surface of the heating elements), the temperature of the sample was 900 °C at the vertical centre of the tube, but only 650 °C when the sample was placed 5 cm below the top of the tube. The sample was therefore alternated between these two positions along the cycling experiment. Selected sub-samples were taken from the basket while in its upper position, either before (calcined samples) or after recarbonation (carbonated samples). The actual temperature of the sample was measured with a thermocouple placed in the centre of the particulate bed.

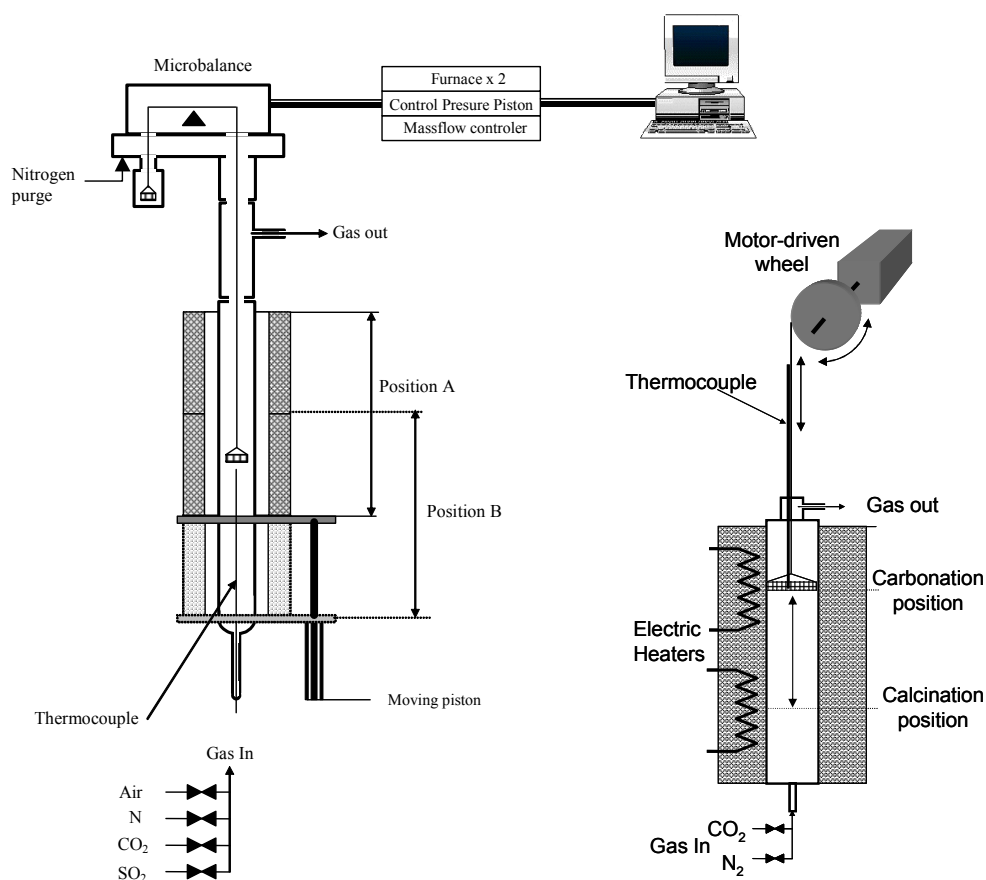


Figure A.5.1.1. Experimental installations used for sorbent performance testing at CSIC. Left: multicycle sorbent testing (two ovens moving with a pneumatic system to different cyclic positions-temperatures). Right: small fixed bed apparatus with a movable sample system between two different positions (and temperatures)

A scanning electron microscopy (SEM, Zeiss DSM-942) was the technique used for the examination and imaging of the calcines and recarbonated samples. Small sub-samples (~50 particles) were mildly crushed by pressing them between two pieces of glass, in order to expose their inner parts to the electron beam. The fragmented particles were dispersed on a graphite adhesive tab placed on an aluminium stub, and coated with a thin film (~20nm thick) of gold in order to get a better electronic signal and, besides, prevent the hydration of the calcines. In addition, a Hg porosimetry was used to follow the textural evolution (pore size distribution change) along cycling of selected samples as well as a determinations of sorbent surface area with the BET.

Table A.5.1.1 compiles the range of experimental conditions used during sorbent characterisation tests, including the main variables studied. The experimental work has generated a database of several thousand thermograms (each cycle point in subsequent figures is a full thermogram), several hundred fixed bed cycles of carbonation-calcination and associated samples for SEM observation and quantitative texture determination by Hg porosimetry.

Table A.5.1.1. Summary of reaction conditions during different experimental series. Grey shadows show the referece conditinos, fixed when the others are varied.

Type of limestone	dp (mm)	t calcination (min)	T calcination (°C)	% CO ₂ vol. (carbonation and calcination)	% sulfation of limestone	Number of cycles, N
Blanca	0.1-0.25	3	800	3	0	up to 500
Havelock	0.25-0.4	5	850	6	0.048	
Cadomin	0.4-0.6	10	900	10	0.063	
Wolica	0.6-0.8	20	950	12	0.12	
Gotland	0.8-1	30	1000	24	0.25	
Dolomite (Sierra de Arcos)		60		50		
				100		

The key results of this experimental work are described in the following paragraphs. Also, the discussion to interpret the data and put them in suitable form for the design of the units and systems carried out in subsequent sections. Most of the experiments were carried out with a Spanish limestone (“la Blanca”/Omyacarb) because it was clear by reviewing literature data and with the first series of experiments (see Figure A.5.1.2 and Abanades and Alvarez, 2003 for details) that the effect of limestone type, although detectable in some cases, was a second order effect respect to the key mechanism of deactivation along cycling. Limestone la Blanca is almost pure CaCO₃, yielding 56.2 % of calcined material. Also, particle size and carbonation temperature, where investigated only at the beginning of the test programme because it was clearly seen that (for the purpose of the maximum conversion achieved at the end of the fast reaction period) they did not affect much the results.

Figure A.5.1.2 presents some representative series of experiments referred in Table A.5.1.2, as a function of the number of cycles. Table A.5.1.2 compiles the range of conditions employed in these experiments and in those conducted by other authors. The results in these figures show a striking similarity in several of the series of experimental points. This is despite the large differences in sorbent characteristics, particle sizes, reactor characteristics, reaction conditions and calcination and carbonation times in the original experiments (see Table A.5.1.2).

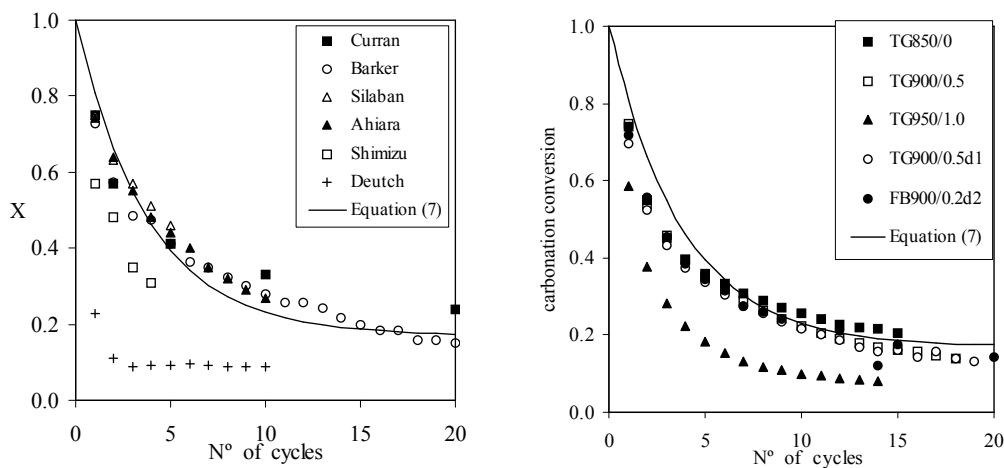


Figure A.5.1.2. The decay in maximum carbonation conversion with the number of cycles. Left, several authors sources reviewed in Abanades and Alvarez (2003). Right: this project at calcinations temperatures and partial pressure of CO₂ (atm) as indicated in the key.

Table A.5.1.2. Outline of Reaction Conditions during the Series of Experiments of Figure A.5.1.2.

reference	carbonation		calcination		dp (mm)
	T (K)	P _{CO₂}	T (K)	P _{CO₂}	
TG850/0	923	0.1	1123	0.0	0.1–0.25
TG900/0.5	923	0.5	1173	0.5	0.1–0.25
TG950/1.0	923	1.0	1223	1.0	0.1–0.25
TG900/0.5d1	923	0.1	1173	0.5	0.6–0.8
FB900/0.2d2	923	0.21	1173	0.21	0.4–0.6
Curran et al. ^a	1089	1.3	1333	4	> 1
Shimizu et al. ^b	873	0.05	1223	1	0.5
Silaban et al. ^c	1023	0.15	1023	0	<0.01
Barker ^d	1139	1.0	1139	0	0.02
Aihara et al. ^e	1023	0.2	1023	0	10 (pellet)
Deutch et al. ^f	823	1	1543	1	finest?

In order to get a visual indication supporting the calcinations/recarbonation pattern, we shall now describe the textural changes undergone by the limestone along the subsequent calcination/carbonation cycles carried out in our fixed bed experiment (FB900/0.2d2 in Table A.5.1.2). The microscopic examination of the parent material under the transmitted light microscope revealed (Figure A.5.1.3a) that the limestone particles are composed of microcrystals displaying a wide range of sizes, typically 10–20 μm diameter, although much bigger grain sizes were also detected, some even forming monocrystal particles (~0.5 mm diameter). When moving to a higher magnification within one of these fragmented grains, it can be seen (Figure A.5.1.3d) that the CaO is arranged in small (~100 nm breadth, variable length) parallel rods, which leave in between a network of quasi-cylindrical pores. When this material is submitted to recarbonation conditions, the microgranular structure of the grains is lost, and only some pores typically 100 nm diameter are observed in an apparently dense groundmass (see Figure A.5.1.3e). The grain surfaces show the stone-paved appearance illustrated in Figure A.5.1.3f. This image alone suggests that the recarbonation might have ceased due to the sealing of the outer surfaces of the grains, but the equally dense appearance of the material in the inner of the grains suggests that the reacting gas must have penetrated before the full closing of the external layer of micrograins or proceeded through smaller pores than the resolving power of the microscope. In summary, the reaction does not stop as a consequence of the sealing of an outer layer in the grain, but due to the lack of useful porosity where the CaCO₃ might grow, as a consequence of the different molar volumes of CaCO₃ and CaO (36.9 and 16.9 cc/g, respectively). The observations support the concept of a limiting microporosity for all the carbonation cycles at a grain level, similarly to how Bathia and Perlmutter (1983) interpreted the carbonation conversion after a single calcination. The volume fraction associated with these small pores seems to decrease as the number of calcination/carbonation cycles increases, due to micrograin sintering and/or grain shrinkage as will be discussed below. In the large voids, the limiting factor for further reaction is not the lack of space but the rapid increase in the resistance to gas diffusion through the product layer, as measured by Mess *et al* (1999). Figure A.5.1.4 summarizes the mechanism of recarbonation discussed in the previous paragraphs.

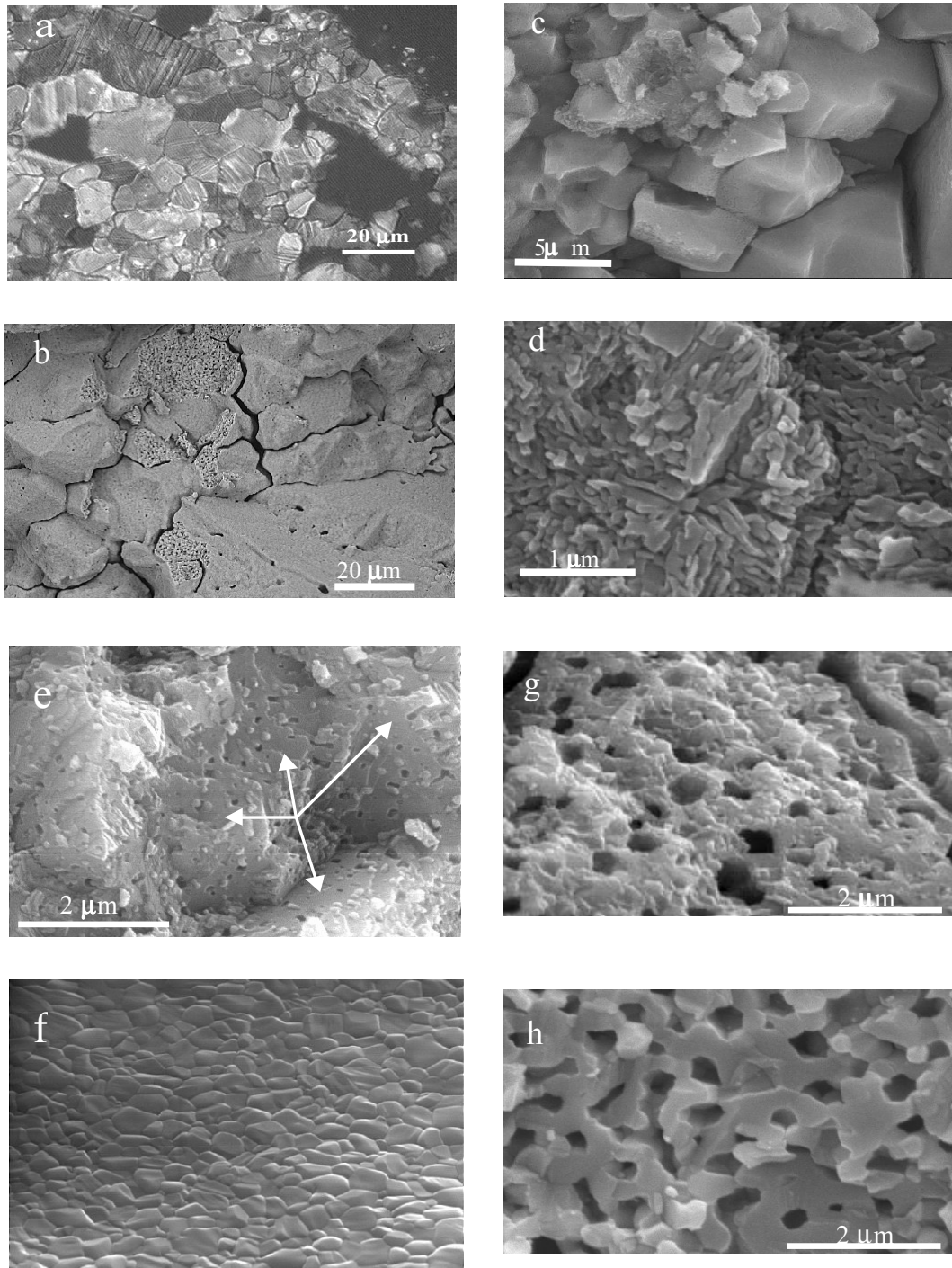


Figure A.5.1.3. Images from the transmitted light (a) and SEM (b-h) microscopes. a) observation of grain crystals in the parent limestone, b) crystalline domains after the carbonation in cycle 40, c) grain structure after the first calcinations, d) micro grains of CaO inside the grains, e) interior of the grains after the first carbonation, f) exterior surface of the grains after carbonation, g) larger voids formed in the interior of the grains after first calcination and (h) after calcinations in cycle 40.

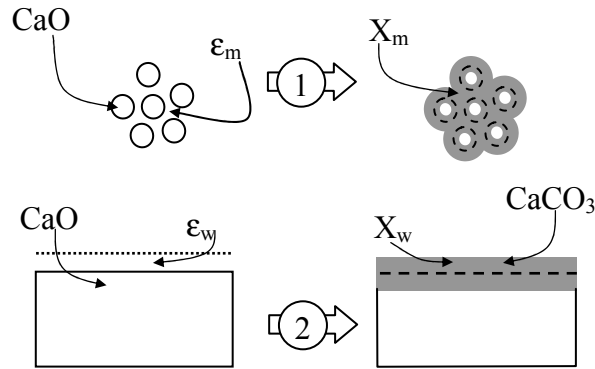


Figure A.5.1.4. Scheme of the complete filling up by CaCO₃ of the small inter-micrograin voids (1) and the formation of a product layer of CaCO₃ in the wall of large voids (2). The dotted line in 2 (left) indicates the maximum growth of the product layer. The dashed lines in 1 and 2 (right) indicate the boundary of the CaO zones before carbonation.

A simple mathematical model has been developed to account for the decay in carbonation conversion with the number of cycles, based in the changes in texture described above (Abanades and Alvarez, 2003):

$$X_N = f_m^N (1 - f_w) + f_w \quad (\text{A.5.1.1})$$

with $f_m=0.77$ and $f_w=0.17$ for the solid lines of Figure A.5.1.2

The model is able to fit also the data from other authors compiled in A.5.1.2 (see solid line in Figure A.5.1.2) and can be easily incorporated into the simulation tools being developed in Task8 to predict system performance in terms of CO₂ capture efficiencies.

Fundamental sorbent characterization work included detailed studies of the Hg intrusion curves of selected samples. In Figure A.5.1.5 calcined (left) and recarbonated (right) samples from two series of experiments carried out using 5 minutes carbonation time, without (top) and with initial pre-sintering (bottom) times of 10 and 90 minutes are presented as an example. In this figure, it can be readily noticed that the extended residence time of the CaO during the first calcination indeed provoked important changes in its pore network, with a pore size distribution peaking at 189 nm, more than twice the size of the pores (85 nm) in the fresh CaO, calcined for 10 minutes. However, in spite of this initial difference, the behavior of both systems rapidly converges to become virtually indistinguishable from each other after the 30th cycle. This is due to the fact that the calcium carbonate formed during carbonation does not keep a memory of its previous calcinations and recarbonations, as regards its texture development. Thus, when the sintered CaO is recarbonated and then calcined (but not sintered) again, the texture development of this newly formed CaO is essentially the same as in the fresh calcine of the non-sintered series. As the recarbonation progresses from the free surfaces inwards, the unreacted CaO after completion of the first cycle will presumably be situated in the skeleton of the former CaO arrangement. When this recarbonated sample is calcined again, a network of small pores (~85 nm) is formed on the surface of the larger pores formed during the first calcination+sintering. And the large pores will continuously increase in size with the number of cycles as a consequence of the internal sintering that takes place during calcination. This mechanism explains why the initial pore size distribution splits into

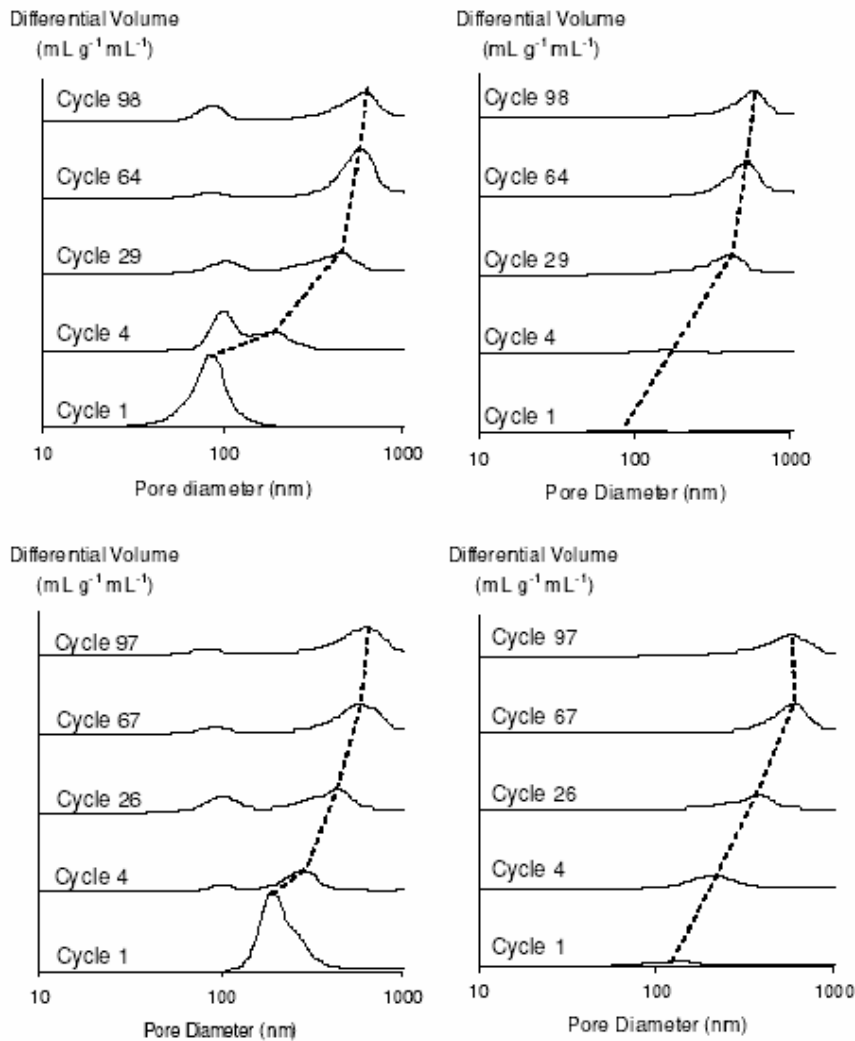


Figure A.5.1.5. Intrusion curves of selected samples from the fresh CaO series (top) and the pre-sintered series (bottom). Curves on the left correspond to calcine samples and those on the right were obtained from their recarbonated counterparts.

two different populations of pores: a decreasing one, always peaking at about 90 nm and attributable to the calcination of the newly formed calcium carbonate, and the other continuously shifting to bigger sizes and due to the sintering of the unreacted CaO.

Fundamental sorbent characterization work also explored other barriers for the carbonation conversion that appeared in some sorbents and conditions: the early pore closure of the external surface of the grains of the calcines when particles have experienced several cycles with extensive carbonation times. The results of these studies have been recently published in Alvarez and Abanades (2005). We observed (Figure A.5.1.6a) that the pore size distributions of the data series with extended carbonation times (30 min) peaked at remarkably lower pore diameters than their 5 min recarbonation counterparts. These calcines, even after 100 cycles, had a single population of pore sizes peaking at about 80-105 nm, in the same range as the pore sizes in the fresh CaO. The Hg intrusion curves of the corresponding recarbonated samples are not shown because they are just straight horizontal lines, indicating virtually no pore volume, and this is clear proof that these recarbonated samples had undergone extensive pore mouth blockage. The Hg porosimetry technique sees a highly microporous material

when conversion data only shows modest conversions (around 12%) typical of highly degraded samples. Figure A.5.1.7a is a medium magnification image of the outer surface of a calcined particle (pre-sintering: 90 minutes, recarbonation time: 30 min., 30 cycles), where it can be seen that the fine-grained surface reveals behind a regular pattern of dark spots ~1 micron diameter corresponding to the internal pore network. The observation of this surface at a higher magnification (Figure A.5.1.7b) shows the presence of smaller pores connecting the internal macropores to the exterior of the grain. These bottle neck pore structure conciliates the conversion data with the porosimetry and SEM observations.

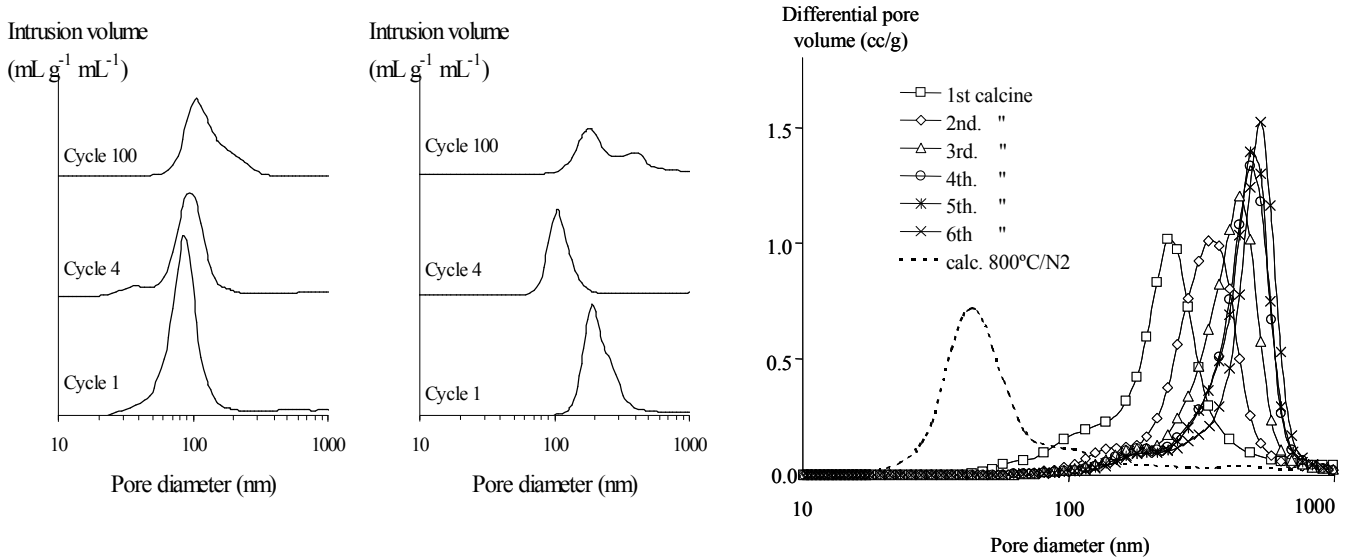


Figure A.5.1.6. Intrusion curves of calcined samples. Left, “la blanca” (recarbonation 30 min) no pre-sintering. Central: Pre-sintered samples. Right: Calcined Cadomin samples from tests in a pilot fluidised bed carbonator (see section A8).

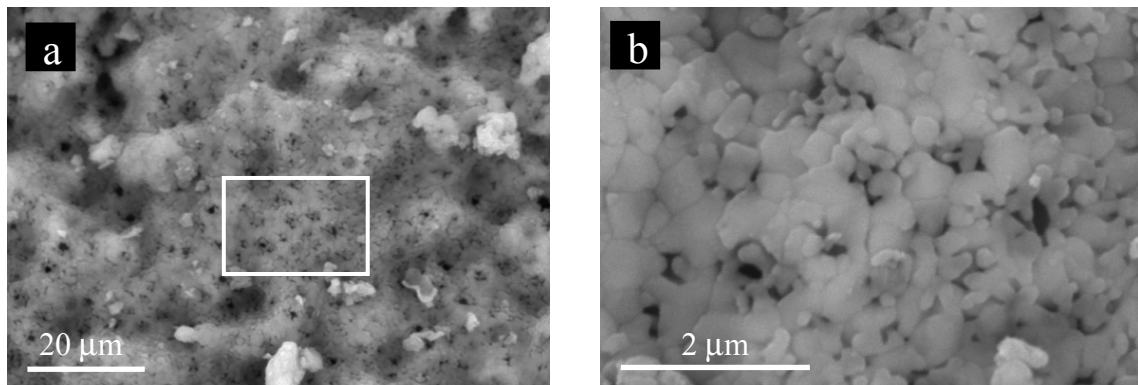


Figure A.5.1.7. View of the external surface of a large grain of calcined sample (30 cycles, non pre-sintered, recarbonation time: 30 min.). The dark spots in the top left image (a) indicate that a network of larger inner pores exists, very close to the outer of the particle. A zoom of this image (b) shows the micrograins responsible for pore blocking on extended carbonation times.

Support work of sorbent characterisation was also required to interpret data coming from a fluidised bed carbonator (see section A8 and Abanades et al 2004). As an example, the right hand side of the Figure A.5.1.6 presents Hg porosimetries of the calcines of several Cadomin(limestone) samples taken from the fluidized bed after experiencing several calcinations-carbonation cycles in the bed. They are compared against a calcine obtained in mild conditions (N₂ at 800°C) from fresh Cadomin limestone. The huge textural differences between the calcines of samples from the bed and from the laboratory can only be explained accepting that, despite the nominally mild calcination conditions during the Cadomin calcination tests (850°C in air, see Abanades et al 2004 for details), sufficiently strong sintering mechanisms were present during the first calcination cycle, that yielded much poorer texture (and sorbent performance) during the subsequent cycles. In contrast, other limestones not presented here (Havelock) was more insensitive to bed calcination conditions. It is interesting to note that Curran et al. (1967) observed that the large differences in deactivation rates of different acceptors measured in a batch unit were not confirmed in the continuous unit, where calcination rates at the particle level were much higher. It seems important (at least for some limestones) to conduct carbonation-calcination tests in the laboratory at high heating rates (as it is the case in the experimental rigs built for this project with a fast moving oven zones around the sample).

The work measuring the decay in sorbent capacity along cycling was completed later with long duration testing of some sorbents (hundreds of cycles, lasting for more than two weeks in continuous for one test) and in the effect of sulphur (as CaSO₄ in the sorbent) in the decay curves of the sorbent. As will be seen below in sections A8 and A9, an overall objective in the system may be to minimise the need of make up flow (although high make up flows are feasible because the low cost of limestone as shown in A10). Low make up flows of limestone imposes a higher number of cycles for the sorbent particles carbonating and calcining in the system.

Figure A.5.1.8 shows the results of the multicycle tests, showing that the sorbent performance is poorer than expected in the range of number of cycles >50 from previous studies; with a second, very slow decay in capture capacity in the materials studied towards conversions of around 5%. Results confirm that dolomites ("S Arcos") perform better in terms of CO₂ capture capacity than limestone. However, sufficiently long number of cycles bring dolomites conversions to similarly low values than those obtained by limestone. The effect of an inert part (main fraction) of inert solids (not carbonated CaO and or MgO) in the heat requirements in the calciner is studied in section A9 but it can be anticipated from Figure A.5.1.8 that the better performance of dolomites is not sufficient to justify their use.

The effect of sulphur was studied in the TGA on sorbents with different level of CaSO₄ obtained by reaction of SO₂ with the calcined sorbent in air. The sorbent sample was first calcined and then sulphated to different levels (Ca conversion to CaSO₄ is the keyword of Figure A.5.1.9). The partially sulphated samples were then submitted to repetitive carbonation calcination cycles. As expected, the carbonation conversion suffered in the first cycle from a large drop in carbonation conversion to below 30% for highly sulphated sample. This limestone (La Blanca) is known to develop during sulfation a strong core-shell structure at particle level that must be preventing the CO₂ from accessing large portions of the particle with free CaO. The effect of sulphur is however substantially less important in subsequent cycles. This may be an indication that only a certain volume fraction of the sorbent is actually affected by the sulphur uptake (in the exterior shell of the particles). When the shell is not completely sealed with CaSO₄ (for instance when large pores have developed after a few cycles), the CO₂ can penetrate to the interior of the sorbent and carbonate as in normal carbonation/calcinations conditions the free surfaces of CaO.

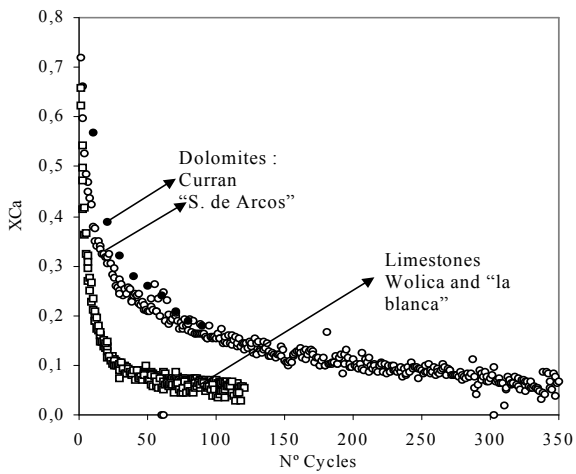


Figure A.5.1.8. Multicycle testing of three different sorbents including a comparison with data from Curran et al (1967) for dolomites. The experimental data noted as “Curran” are from a large pilot (Acceptor Process) while the remaining data are from the TG studies in this project. Limestone la Blanca, 0.4-0.6 mm, Tcarb 650 °C, Tcal=900 °C, 10% vol CO₂ during carbonation and calcinations

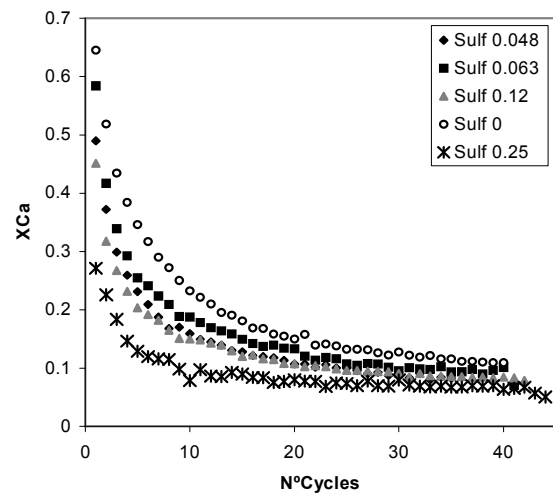


Figure A.5.1.9. Effect of partial sulfation of a calcine on the multi cycle performance in carbonation-calcination tests. Limestone la Blanca, 0.4-0.6 mm, Tcarb 650 °C, Tcal=900 °C, 10% vol CO₂ during carbonation and calcination.

For samples with low sulfation level (conversion to sulphate below 0.1) pore blockage by CaSO₄ may not be present/complete and the access to the sorbent allows sorbent performance comparable to the fresh sorbent without sulphur (see Figure A.5.1.9). It is important to bear in mind that since the target in the LCCC system is to capture the CO₂ generated in combustion, and the molar flow of CO₂ is typically two orders of magnitude higher than SO₂ in flue gases, particles with low sulfation conversion are most likely in a real system. This means that, for the high make up flows of sorbent required to maintain the activity in the CO₂ capture-regeneration loop, the sorbent will be an effective SO₂ sorbent without a large detrimental effect on performance respect to CO₂ capture.

Finally, and in support of activities to develop the “in duct” carbonation options, where especially high reactions rates are required, a closer examination on the carbonation reaction rates under kinetic controlling conditions was carried out. In particular the effect of CO₂ partial pressure and effect of the number of carbonation-calcination cycles on the rate of carbonation was investigated. Figure A.5.1.9 are examples of reaction rates measured in conditions where no external resistance exists to the progress of reaction (about 10mg of sample with around 15 l/min of gas in the TGA of 20mm id) in the exterior of the particles. As discussed in previous reports, the reaction rates are always sufficiently high (full conversions achieved between one to five minutes) to effectively capture CO₂ from in a fluidized bed (see section A.8.2). However, the entrained bed carbonator envisaged for “in duct” carbonation options (see A.6.1) is far more sensitive to reaction rates, because the limited gas solid contact times. In these conditions, the results above cannot supply good enough information, as the particle sizes are much smaller and the rates of reaction are much higher than those that can be

measured in a TG apparatus (but not the maximum conversions achieved after, say, several minutes that remain governed by equation A.5.1.1). Efforts to model the carbonation reaction at particle level in these conditions have been the subject of intense investigation by CSIC and Cranfield (in entrained bed tests as described in A.6.1) and also by VTT incorporating pore diffusion effects on the recarbonation reaction of large particles.

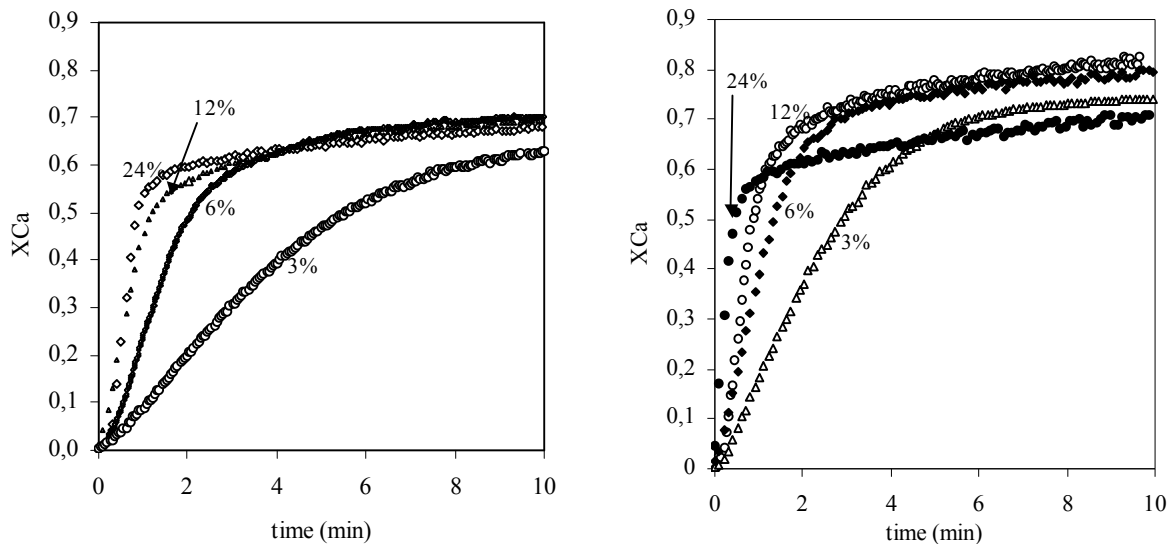


Figure A.5.1.10. Reaction rates measured in TGA for limestone “la Blanca” (left) and dolomite (right) “Sierra de Arcos” at different vol% of CO₂. $d_p=0.4-0.6$ mm, $T=650^\circ\text{C}$.

The model by Bathia and Perlmutter (1983) was adopted as a first approximation to the problem and adapted to the sorbent after several cycles. To calculate the reaction rate in this model, we assumed that after achieving the carbonation conversion limit, $X_{b,N}$, the carbonation reaction completely ceases (Abanades and Alvarez, 2003). It is also assumed that in the active part of the conversion curves (below $X_{b,N}$), the carbonation reaction follows a shrinking core model at grain level, consistent with our observations by SEM. As the number of carbonation-calcination cycles increases, the decreasing value of $X_{b,N}$ changes the value of effective surface of reaction ($S_0X_{b,N}$) of the calcines. This can be interpreted either as an increase in the grain size or as a decrease of the total amount of reactive CaO micrograins. However, the decay in activity for a given limestone, as the number of carbonation-calcination cycles increases, seems to be more linked with a reduction in the fraction of CaO in the particle in the form of micrograins. This will require more detailed textural investigations in the future and more elaborate model predictions. The simple approach described above was considered sufficient to supply the key information needed for interpretation of pilot test results from entrained and fluidised bed carbonation experiments described in section A.6.

A.5.2 Work performed at VTT

Activities in this task have been progressing at VTT as planned, by using “Sorbent performance” (SOPE) test rig and TGA for characterisation of sorbent nature and properties on CO₂ separation activity. The focus was to determine optimum circumstances for CO₂ separation, like temperature, reaction time, gas velocity, sorbent volume and particle size.

A.5.2.1 CO₂ reduction tests at SOPE

The SOPE test rig consists of quartz tubes as sample line placed in heat casing (Figure A.5.2.1). The sample line and sorbent bed are electrically heated, and gas streams (mixture of nitrogen and CO₂) are controlled by mass flow meters. Homogeneous gas mixture is achieved in mixing chamber. Temperatures are measured with thermocouples, placed along the sample line. Temperatures are recorded continuously by computer and exhaust gas concentrations can be measured if needed. A schematic operation diagram of the sorbent performance test rig is presented in figure A.5.2.2.

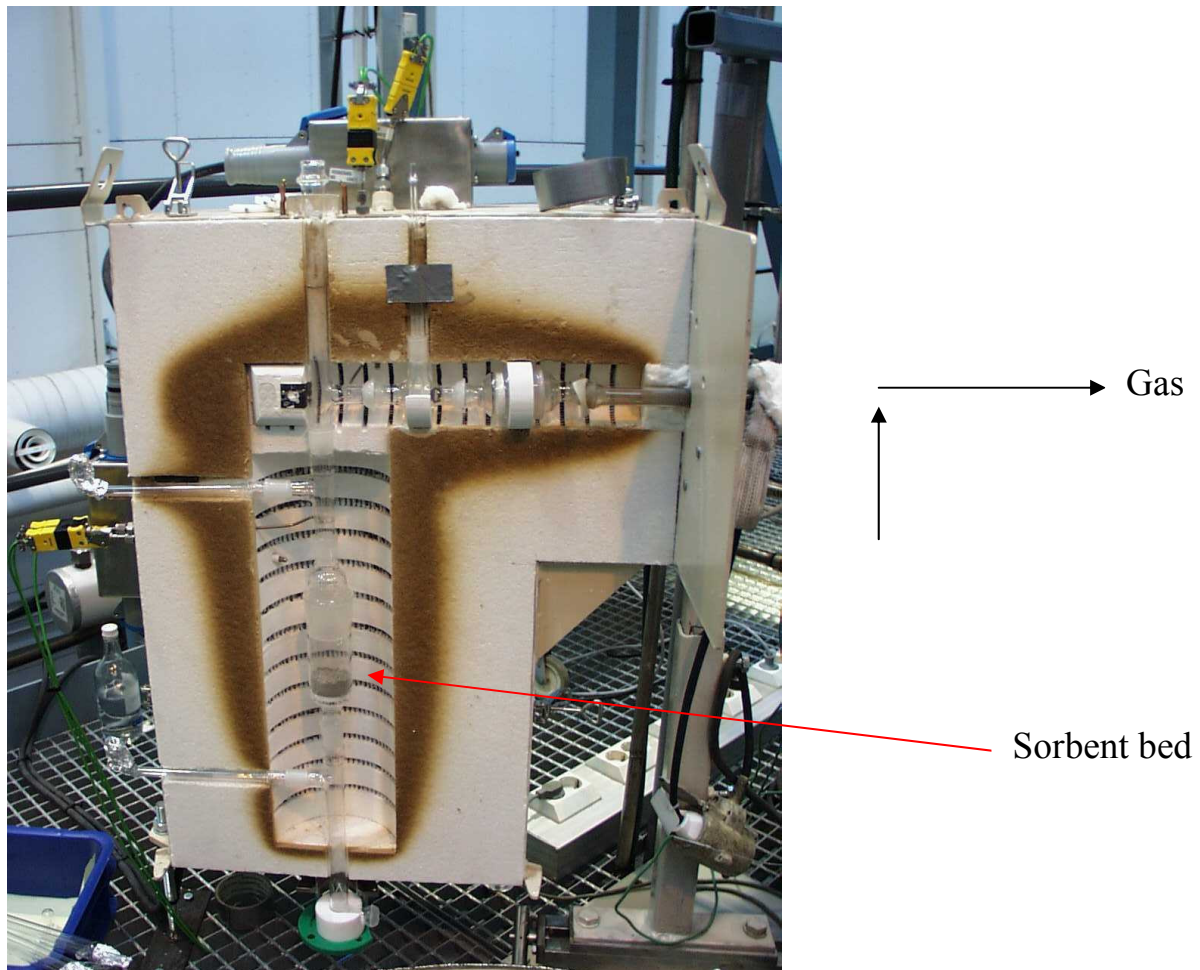


Figure A.5.2.1. VTT's sorbent performance test rig.

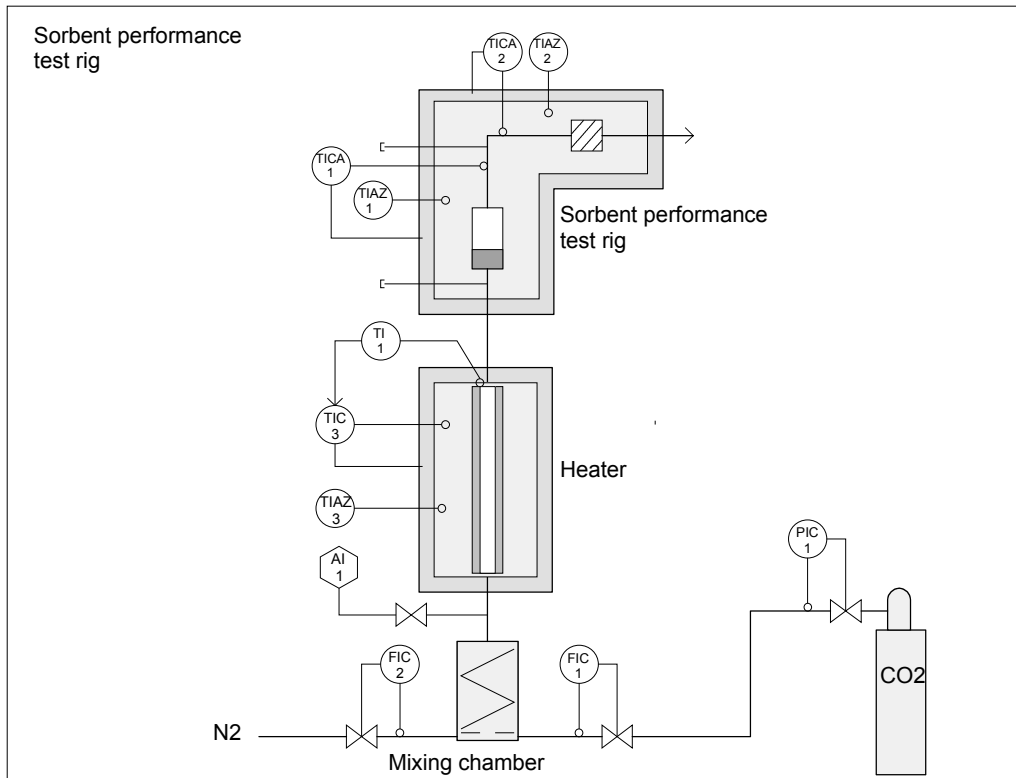


Figure A.5.2.2. VTT's sorbent performance test rig operating principle.

Sorbent used in experiments were Finnish limestone from Partek Nordkalk Oyj Abp. The composition of limestone according to the manufacturer, announced as oxides, were MgO 1–2 %, Fe₂O₃ 0.2–0.4 %, SiO₂ 1–3 %, Al₂O₃ 0.3–0.6 % and CaCO₃ content of limestone were 95–96 %. Investigated particle sizes were 0.5–1.0 mm, 1.0–2.0 mm and 2.0–4.0 mm. All limestone fractions were calcinated at laboratory oven at temperature 900 °C for about 16 hours before CO₂ capture tests.

The all carbonation experiments were carried out with SOPE test rig so that 10 grams of calcinated limestone was loaded as bed material. After that the reactor was electrically heated to temperature of 420–760 °C. When sorbent achieved adjusted temperature, CO₂ and N₂ in different proportions were lead to the sample line and through the sorbent bed. CO₂-concentrations of 10–15 % were allowed to react with solids about 5–30 minutes. During the experiments the average gas feed through the sorbent bed was 0.3–0.79 m/s. CO₂ inlet and exhaust concentrations was measured with FTIR-spectrometer, however change of CO₂-concentrations was low due to small amount of sorbent compared to inlet CO₂.

The carbonation rates of limestone were determined after carbonation by TGA, thermogravimetric analysis. TGA technique measures the change in the weight of a sample as it is heated at a known rate. At these experiments temperature were raised at 5 °C/min from 105 °C up to 900 °C. It is known that calcium carbonates released approximately at 550–750 °C temperature, at that time CaCO₃ convert to CaO. Magnesium carbonates released at temperature 210–480 °C. Samples were mixed and powdered properly before analysis. Sample volume used in analysis was about 4 mg and atmosphere was pure nitrogen. The variations in sample temperature and weight losses were continuously recorded with computer (Figure A.5.2.3

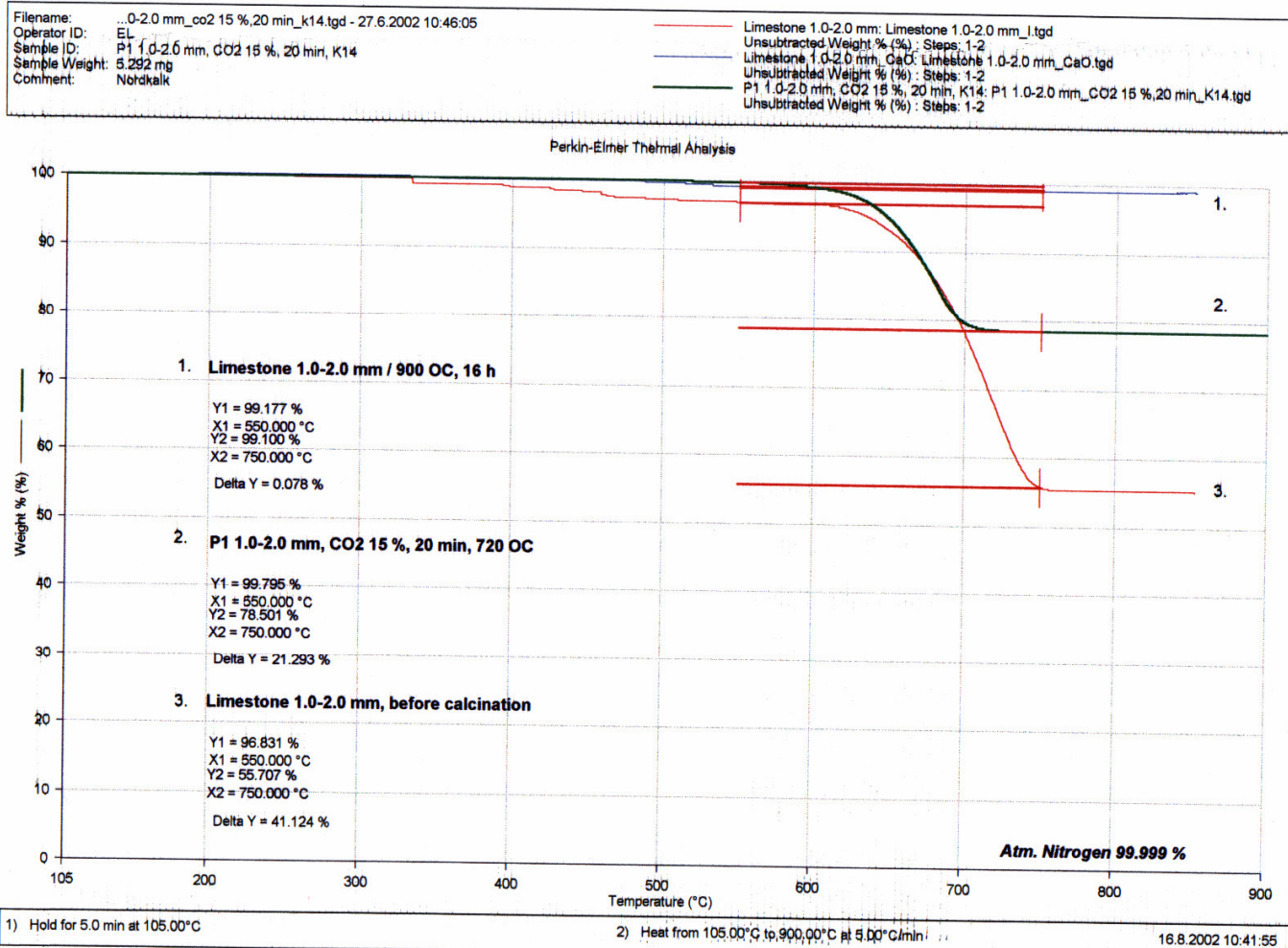


Figure A.5.2.3. Weight losses as a function of temperature (tg-curves from the analysis of limestone fraction 1.0 – 2.0 mm).

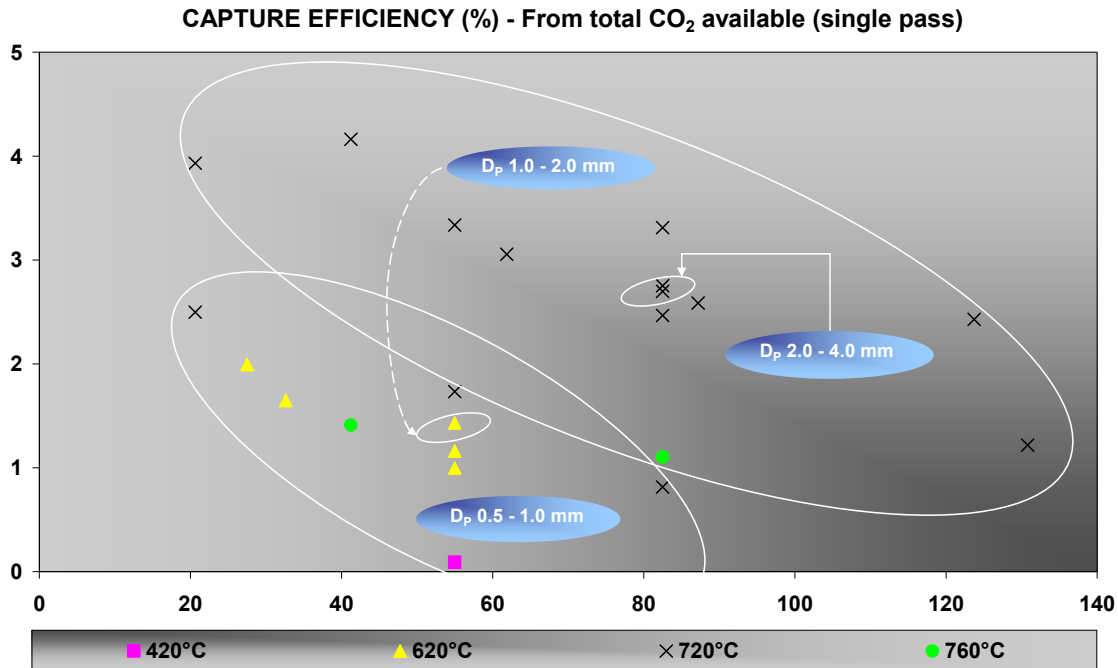


Figure A.5.2.4. Capture efficiency (%) from total amount (g) CO₂ fed through the sorbent.

According to fixed bed experiments, the results indicate that particle size distribution 0.5–1.0 mm has minimal effect on the CO₂ separation, but instead coarser particle size fraction 1.0–2.0 mm proved to be more effective (Figure A.5.2.4). Observation may be due to more uniform gas flow distribution with larger particles.

Experiments with fraction 1.0–2.0 mm showed by TGA-analysis as follows:

- When temperature was 720 °C instead of 620 °C weight losses (TGA) were two times bigger meaning higher carbonation degree and higher capture efficiency. Higher temperature than 720 °C is not necessary.
- Weight losses (TGA) were 15–40 % of a higher grade when CO₂-concentration was 15 % than 10 %.
- Reaction time 5 minutes has quite low effect on the CO₂ separation but when time was raised to 30 minutes results were three times better.

As a summary of above test programme gave us detail design parameters to perform sorbent experimentation with CFB pilot reactor at proper process conditions.

A.5.2.2 Thermogravimetric analysis of lime stones – CO₂ exposure tests

Thermo gravimetric CO₂ exposure tests and analysis gave information on:

- Effect of particle size on reaction rate and maximum degree of conversion (pore plugging)
- Effect of temperature on reaction rate and maximum degree of conversion
- Effect of CO₂ concentration
- Effect of type of CaO (density, porosity, internal surface area)

Thermogravimetric experiments were started in the fifth reporting period and have been finished by the end of the project. TGA results have been utilised in modelling work.

Test sets consisted of almost 30 tests. In the first test set, five different lime stone were exposed to similar conditions:

- CO₂ concentration 15 %
- Gas temperature 650 °C
- Particle size 75-90 µm

Heating rate was 50 °C/min, as in all subsequent tests. The results are in Figure A.5.2.5. Maximum conversion rate refers to the maximum slope value in a weigh graph. Analyser software enables calculating and printing of the derivative curves as function of time.

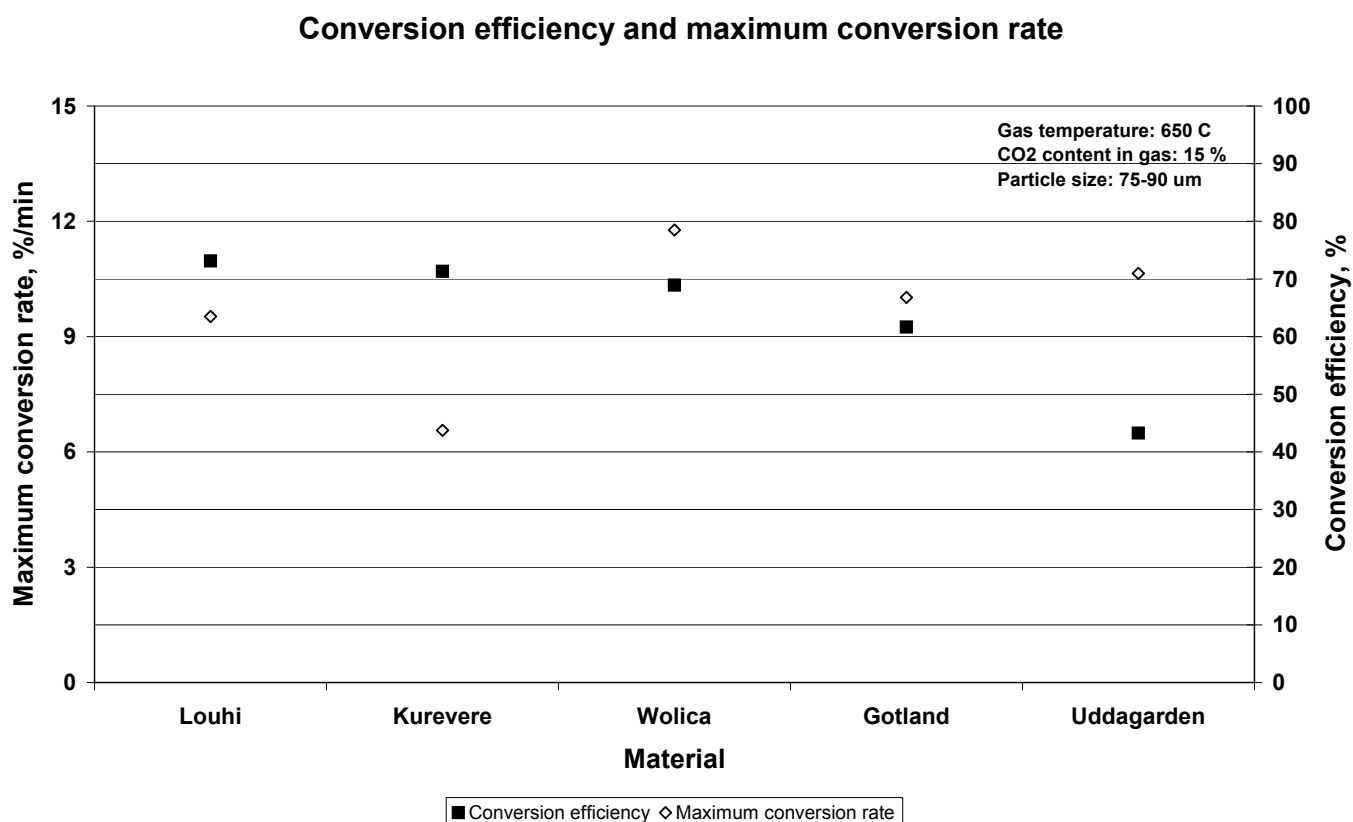


Figure A.5.2.5. Conversion characteristics of test materials.

First figure in the appenx of the annual report for 2004 gives an example of weigh curve for the entire experiment, whereas the second figure shows a six-minute period when the conversion rate attains its maximum at about 39 minutes.

The materials, in Figure A.5.2.5, are presented in decreasing order of the maximum conversion rate. The maximum rate is almost the same for all materials excluding Uddagarden lime with clearly lower maximum value. Conversion efficiency varies from about 40 to 80 %, and it does not correlate with the maximum conversion rate. For practical reasons, Wolica

lime might be the best one, since its conversion efficiency is high. Besides, its conversion rate is high too, enabling fast and effective circulation in an industrial carbonator.

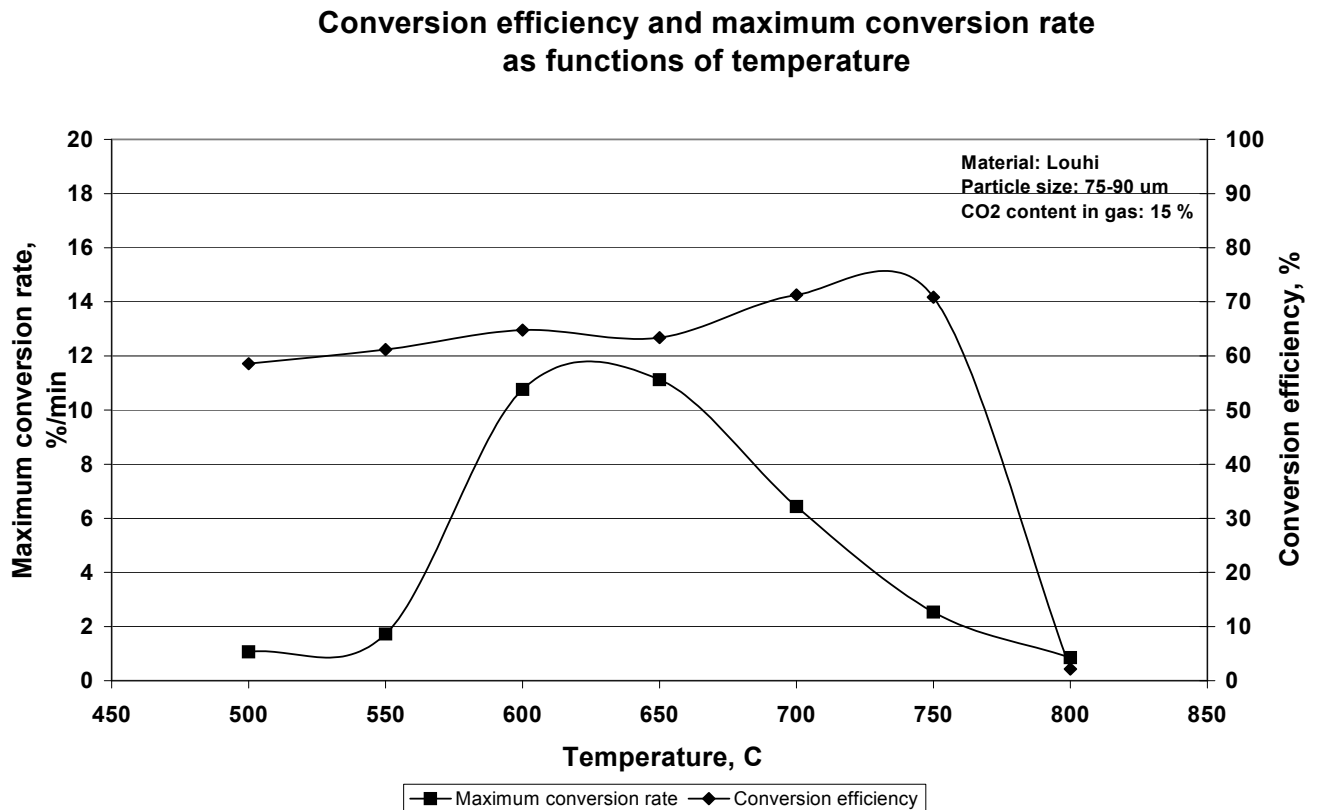


Figure A.5.2.6. Effect of gas temperature on conversion.

Figure A.5.2.6. shows how the gas temperature affects conversion. Maximum conversion rate is reached at about 600-650 °C, whereas the highest attainable efficiency is at about 700-750 °C. However, the efficiency does not depend very strongly on the gas temperature in the studied range.

Figure A.5.2.7 shows that the CaO particle size has a very straightforward effect on conversion efficiency. This contradicts with the results by Ranade et al., 1979, which indicate no significant effect of particle size. However, in those tests only two particle fractions with average sizes 81 and 137 μm were studied. The fractions were relatively close to one another. Similarly, Figure A.5.2.8 shows that the difference in conversion efficiency is insignificant in such a short range. Maximum conversion rate depends on the particle size to some extent too. The clearly higher rate for 75-90 μm fraction is somewhat surprising. It may be due to an error of some sort and the test should be repeated.

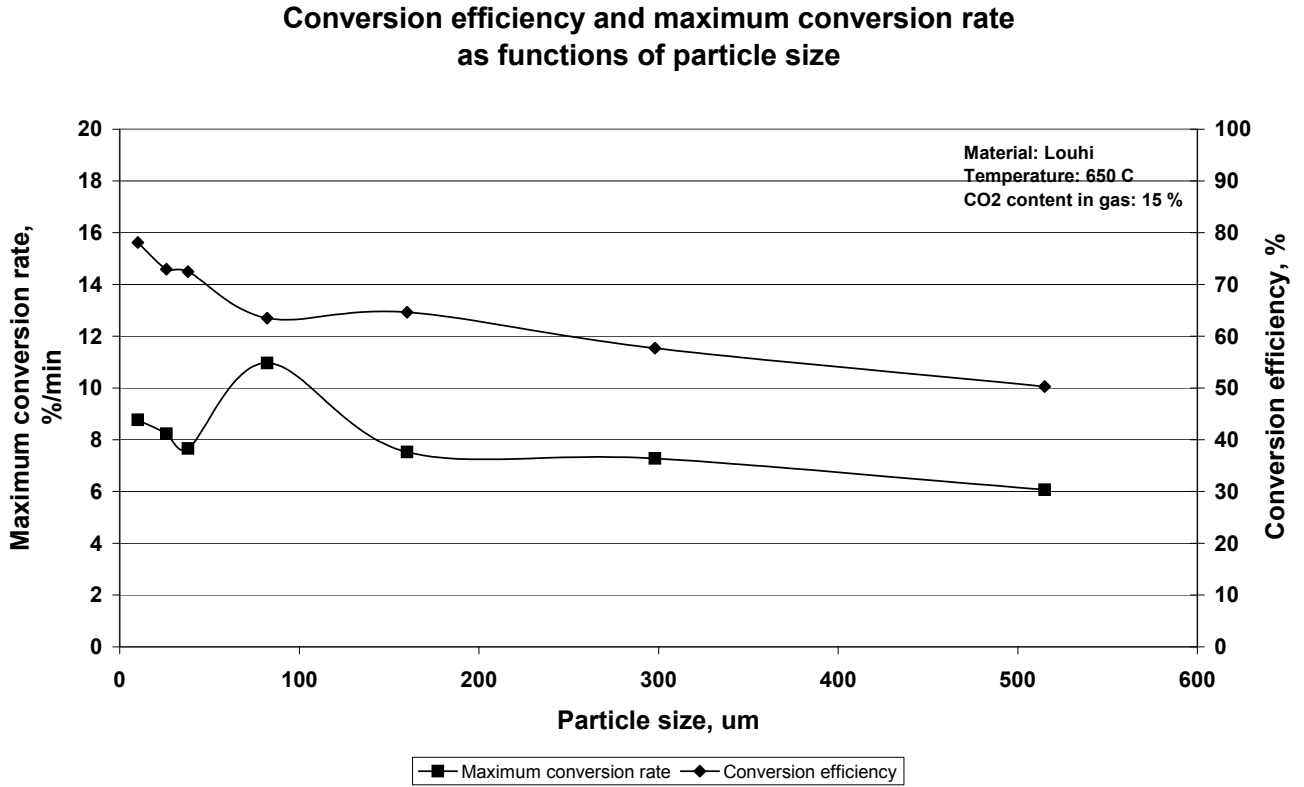


Figure A.5.2.7. Effect of CaO particle size on conversion.

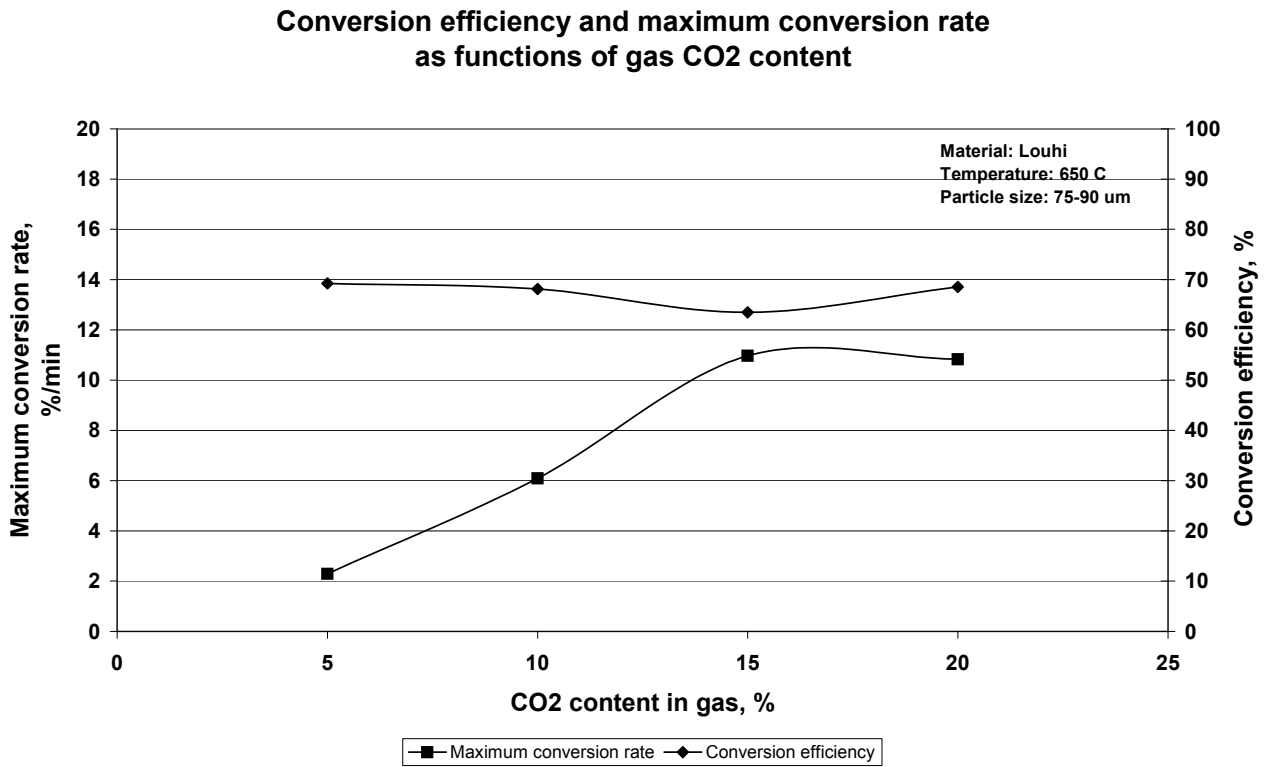


Figure A.5.2.8. Effect of CO₂ concentration on conversion.

Figure A.5.2.8 shows clearly that CO₂ content in gas has no effect on the conversion efficiency under the conditions used, but has almost linear effect on the maximum rate. Especially if taking into account that the data point at 15 % is the same deviating one as in Figure 5.2.2.VTT7..

A.5.2.3. Capture by CaO - Modelling

General

In the following modelling of CO₂ capture is discussed. The diffusion and reaction of CO₂ inside the particle can be described by

$$\frac{\partial \rho_{CO_2}}{\partial t} = \frac{1}{r^2} \left(\frac{\partial}{\partial r} D r^2 \frac{\partial \rho_{CO_2}}{\partial r} \right) - \dot{\rho}_{CO_2} \quad (A.5.2.1)$$

The term on the left describes the storage. t is time and ρ_{CO_2} is concentration of CO₂ (kg m⁻³) or its difference to the equilibrium concentration. The first term on the right hand side describes diffusion inside the particle. D is diffusivity of CO₂ inside the particle and r is radial co-ordinate. The second term describes the local disappearance of CO₂ due to reaction with CaO by the carbonisation reaction



The molar weights are $M_{CaO}=56.08$, $M_{CO_2}=44.01$ and $M_{CaCO_3}=100.09$. Then theoretically 1 kg can absorb 0.785 kg CO₂ producing 1.785 kg CaCO₃. The energy release in the process is 4.16 MJ/kgCO₂. The optimum temperature is about 650°C. The optimum temperature is affected by the competing of the rate of reactions and diffusion. At high temperatures CO₂ is again released due to competing reactions. Shimizu et al., 2003 gives the value 2700 kg m⁻³ for the true density of typical Japanese limestone. The measured loose density for Volica limestone particles (<75µm) was 722 kg m⁻³, which increased to 1003 kg m⁻³ by applying vibration. If we assume the shape of the particles as spheres having the minimum with porosity 36 % in the packing then 1567 kg m⁻³ is obtained. Then the density of CaO particles will be 888 kg m⁻³. This is just a rough estimate, since the smaller particles may fill the voids between large ones. The density of the reacted solid ρ_p will increase due to CO₂ capture in the reaction, Eq. (A.5.2.2),

$$\frac{\partial \rho_p}{\partial t} = -\dot{\rho}_{CO_2} = (\rho_{CaCO_3,0} - \rho_{CaO,0}) \frac{\partial X}{\partial t} \quad (A.5.2.3)$$

X is local conversion. Both CaCO₃ and CaO can be locally present. The index 0 refers to pure substance. If the rate of reaction is fast, pore plugging or significant increase in the diffusion resistance may take place before much capture has taken place. The increase in density of the outer layer may cause pore plugging preventing diffusion of CO₂ inside the particle before the interior of the particle has been reacted and further capture of CO₂. The CaO particle can be considered to consist of smaller grains. There may be also a limit of conversion of an individual grain inside the particle, if the pores of this grain are plugged or parts of the grains are unachievable.

The boundary condition at the surface of the particle with radius R_p is

$$h_m(\rho_{CO_2,g} - \rho_{CO_2,s}) = D \left(\frac{\partial \rho_{CO_2}}{\partial r} \right)_s \quad (A.5.2.4)$$

where h_m is the mass transfer coefficient between the gas and the surface of the particle. Index s denotes particle surface and g gas far from the particle. The symmetry condition in the centre of the particle is

$$\left(\frac{\partial \rho_{CO_2}}{\partial r} \right)_{r=0} = 0 \quad (A.5.2.5)$$

In practical cases the effect of storage is small and the term on the left side of Equation (A.5.2.1) can be neglected. Then the rate of process is determined by interplay of diffusion and chemical kinetics.

Equation (A.5.2.1) with its boundary condition can be solved numerically, if the diffusivity D and the local chemical reaction rate are known. The local chemical reaction rate could be described for example by first order reaction with respect to concentration of solid CaO and gaseous CO₂

$$\dot{\rho}_{CO_2} = k_1 \rho_{CaO} \rho_{CO_2} \quad (A.5.2.6)$$

where the reaction rate coefficient k_1 depends on temperature and may also depend on local conversion. Then reactions rate coefficient includes the effect of internal surface area, which is changing. Two different ways to describe the reduction of the coefficient k_1 of a corresponding coefficient in the progress of the conversion has been presented. One way is to use exponential decay. (Dogu, 1981)

$$k_1 = k_{1,0} \exp(-bt) \quad (A.5.2.7)$$

due to deactivation or sintering and decrease of reaction surface. The form of Eq.(A.5.2.7) would predict different reaction rates for different particle sizes, since diffusion in a large particle takes more time. If the rate is decreased due to formation of a product layer, then a relation $k_1=k_1(X)$ would be better. The form of Equation (A.5.2.7) would be better suited to describe the decrease of reactivity (and reactive surface area) due to sintering. (Rande and Harrison, 1979) The grain model is another way to describe the reduction of the local reaction rate with conversion. The particle is considered to be consisted of small grains, in which the conversion takes place by the shrinking core concept.

If D is constant and we assume that $k_1 \rho_{CaO} = k \rho_p \approx \text{constant}$ (in the initial stage when not much CaO has been converted to CaCO₃), Equation (A.5.2.1) can be solved analytically

$$\rho_{CO_2} / \rho_{CO_2,s} = \frac{R_p}{r} \frac{\sinh[3\Phi(r/R_p)]}{\sinh(3\Phi)} \quad (A.5.2.8)$$

where R_p is particle radius and

$$\Phi = \frac{R_p}{3} \sqrt{\frac{\rho_p k}{D}} \quad (\text{A.5.2.9})$$

is Thiele modulus. The surface concentration, in Equation (A.5.2.8), is obtained from the boundary condition (A.5.2.4),

$$\rho_{CO_2,s} = \frac{\rho_{CO_2,\infty}}{1 + (1/Bi_m)[3\Phi \coth(3\Phi) - 1]} \quad (\text{A.5.2.10})$$

where $Bi_m = h_m R_p / D$. The reaction rate of CO₂ per mass of CaO is

$$r = \frac{\dot{m}_{CO_2,s}'' S}{\rho_{CaO} V} = \frac{3D}{R_p \rho_p} \left(\frac{\partial \rho_{CO_2}}{\partial r} \right)_s = \eta k \rho_{CO_2,s} \quad (\text{A.5.2.11})$$

where the effectiveness factor (actual rate for the whole particle/rate evaluated at outer surface conditions) is

$$\eta = \frac{1}{\Phi} \left[\frac{1}{\tanh(3\Phi)} - \frac{1}{3\Phi} \right] \quad (\text{A.5.2.12})$$

Rate limited by diffusion

An unreactive CaO can be good with respect to conversion (but not with respect to rate of conversion), since the internal parts will be reacted before pore plugging on the surface of the particle. There is interplay between reaction rate, pore size and reaction surface area. Physically the process is analogous to sulfation. Three sulfation patterns were observed in different limestones are unreacted core, uniformly sulfated and network. (Laursen et al., 2001) The same patterns may also be present in carbonisation depending on the nature and porosity of CaO particles.

If the rate of diffusion is slow compared to the rate of reaction, the process can be described by the shrinking unreacted core model. A layer of reacted solid will be formed on the unreacted core of CaO having radius R_c . Then the concentration of carbon dioxide inside the surface layer of the particle is obtained as the solution of Equation (A.5.2.1) with boundary condition (A.5.2.4)

$$\rho_{CO_2} / \rho_{CO_2,s} = (1/r - 1/R_c) / (1/R_p - 1/R_c) \quad (A.5.2.13)$$

where the surface concentration of CO₂ is

$$\rho_{CO_2,s} = \rho_{CO_2,\infty} / [1 + (1/Bi_m) / (R_p / R_c - 1)] \quad (A.5.2.14)$$

The rate of the reduction of the radius of the shrinking core is related to the mass flux of carbon dioxide to the reaction front

$$\dot{m}_{CO_2,c}'' = D \frac{\partial \rho_{CO_2}}{\partial r} = - \frac{D}{R_c^2} \frac{\rho_{CO_2,s}}{1/R_p - 1/R_c} = -f \rho_{CaO} \frac{dR_c}{dt} \quad (A.5.2.15)$$

where $f = M_{CO_2} / M_{CaO} = 44.01 / 56.08 = 0.785$. Equation (14) can be integrated to give the relationship between time t and conversion X

$$\frac{6D\rho_{CO_2,\infty}t}{f\rho_{CaO}R_p^2} = 3 - 2(1 - 1/Bi_m)X - 3(1 - X)^{2/3} \quad (A.5.2.16)$$

where $X = 1 - (R_c / R_p)^3$ is the conversion. Usually the Biot number for mass transfer is large ($1/Bi_m \rightarrow 0$) and Equation (A.5.2.15) becomes

$$\frac{6D\rho_{CO_2}t}{f\rho_{CaO}R_p^2} = 1 + 2(1 - X) - 3(1 - X)^{2/3} \quad (A.5.2.17)$$

In the other extreme case the chemical reaction rate is low compared to the rate of diffusion. Then the CO₂ concentration inside the particle is the same as in the gas and the whole particle

is reacting uniformly. Eq. (A.5.2.17) might also be used to the case where the rate is controlled by the diffusion into separate grains of then particle, if the diffusion rate in the voids between grains is high. Then the radius R_p should be replaced by the grain radius. In the work of Mess et al., 1999 measurements were carried out for 15-20 μm CaO powder. The diffusivity of the product layer was $D=A\exp(-B/T)$, where $A=0.65\times 10^{-4}\text{ m}^2\text{s}^{-1}$ and $B=28654\text{ K}$.

Rate limited by chemical kinetics

When rate diffusion is fast compared to the rate of chemical reactions, the conversion takes place uniformly in side the particle. A simple way to describe it is

$$\frac{dX}{dt} = k(1-X)^n \quad (\text{A.5.2.18})$$

where k is function of temperature and concentration of CO₂. Equation (A.5.2.17) can easily be integrated to give resulting to the expression between time t and conversion X

$$X = 1 - [1 - (1-n)kt]^{1/(1-n)} \quad \text{when } n \neq 1 \quad (\text{A.5.2.19})$$

$$X = 1 - \exp(-kt) \quad \text{when } n = 1 \quad (\text{A.5.2.20})$$

In principle Eqs. (A.5.2.18), (A.5.2.19) or (A.5.2.20) can be used as global models even if the reaction does not take place uniformly inside the particle. Then, however, reaction rate constant k depends on the particle size.

The simple relation between time and conversion

$$t = t_c(X) + t_d(X) \quad (\text{A.5.2.21})$$

where the times are summed up, might be a reasonable approximation accounting both for kinetics and diffusion.

Discussion

A fluidised bed batch experiment could be used to study the CO₂ capture. Then mixture of nitrogen and CO₂ flows through the batch and the change in CO₂ concentration in the outlet is monitored. The bed can also be quenched and the particles analysed. Thermobalance tests with a single large particle or a thin bed of pulverised particles could also be applied.

Thermobalance tests with very fine material, for which the process is controlled by the chemical kinetics diffusion being fast, can be used to find the parameters for the chemical kinetics.

The capability of the CaO particles to capture CO₂ depends on the structure of the particles (porosity, internal area) and the particle size. The fragmentation of the CaO particles due to thermal shock may affect the particle size. Particle size is important, since it affects on the rate of CO₂ capture

the degree of conversion (if pore plugging takes place)

Attrition is not much affecting in a single conversion step, but in the long run it will reduce the particle size. The two extreme hypotheses, controls by diffusion and by chemical kinetics, can be tested using different sizes of particles in a thermobalance. There should no effect of particle size in the control by chemical kinetics. This is also the case, if the rate is controlled by the diffusion in individual grains inside the particle. On the other hand, in product layer diffusion control, Equation (A.5.2.16) indicates, that the conversion time is proportional to particle radius power two ($\sim R_p^2$).

Particle size may also affect the degree of conversion reached with very long residence time, if pore plugging takes place. Then the dense product layer formed on the particle prevents further diffusion of CO₂ inside the particle and conversion is ceased. This behaviour depends on the structure of the particle. An interesting point is also how high degree of conversion can be reached compared to the theoretical maximum, which is 0.785 kg CO₂/1kg CaO.

According to Abanades et al., 2004 there are two limits in terms of CO₂ capture efficiency from the gas phase in the carbonator. The first limit arises from the equilibrium in the carbonation-calcium reaction. The equilibrium allows for CO₂ capture efficiencies higher than 90% for typical conditions (12-15 vol % of CO₂) at atmospheric temperatures and temperatures around 650°C. The second limit is the very rapid drop in the reaction rate after a given value of conversion reported by Bhatia and Perlmutter, 1983 and others. The slow reaction regime, Ness et al., 1999, has no practical interest from the perspective of a CO₂ capture device.

The shapes of all the CO₂ capture curves measured at VTT using CaO particles produced from different limestones by calcination show first a rapid reaction and then a slow rate and total ending of the process before complete conversion.

One way to correlate the time dependent behaviour is to apply a diffusivity (in Equation (A.5.2.1)) that decreases with the increase of local conversion such as

$$D/D_0 = f(X) = (1 - X/X_{max})^n \quad (\text{A.5.2.22})$$

This predicts local pore plugging at local conversion $X = X_{max}$. The chemical reactivity seems to be high shown by the rapid initial reaction. However, it is not well-known which type of diffusion and product layer is influential here. Is it the product layer on the surface of the particle or the product layers on an individual grains inside the particle.

The shape of the curves for CO₂ can be obtained by using the simplified model Eq. (A.5.2.17) with the conversion dependent diffusivity, Eq. (A.5.2.22) giving

$$t/\tau = [1 + 2(1 - X) - 3(1 - X)^{2/3}] / f(X) \quad (\text{A.5.2.23})$$

where $\tau = f\rho_{CaO}R_p^2 / (6D_0\rho_{CO_2})$. As an example the case $X_{cr} = 1$, $n = 2$ and $\tau = 360$ s is shown in Figure A.5.2.9.

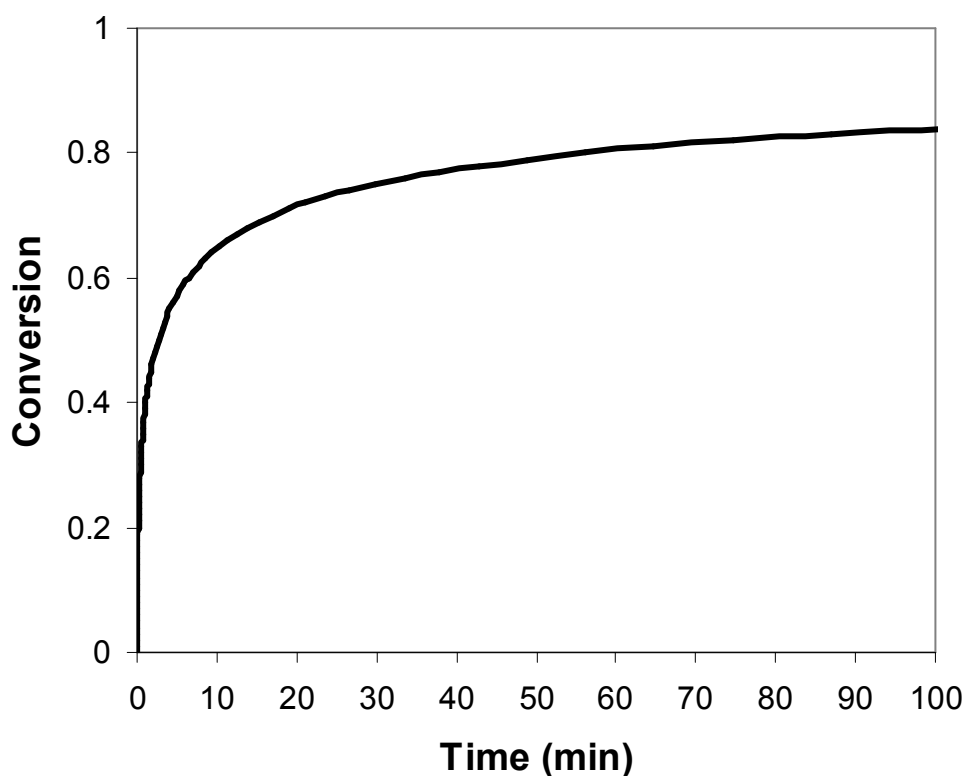


Figure A.5.2.9. Simulated conversion of CaO to CaCO₃ as function of time with conversion-dependent diffusivity.

However, experiments show that the conversion was independent on particle size from 81 to 137 μm meaning that the process was under the control of chemical kinetics. (Abanades et al., 2004) In this case, the diffusion control may take place in the individual grains and not on the surface of the particle. VTT's experiments with different particle sizes in a thermobalance show particle size dependency of the rate of conversion and of the extent of conversion. Then both diffusion from the surface inwards the particle and inside in the grains are affecting.

The control by chemical kinetics, Eq. (A.5.2.18) with $n=0$ seem well predict the fast initial stage. For example for Gotland limestone (75-90 μm) at 15 % CO₂ at 650°C, $k \approx 0.0027 \text{ s}^{-1}$. The reaction rate coefficient seems to be almost proportional to CO₂ concentration (Louhi, 75-90 μm). First order reaction is also suggested by Shimizu et al., 1999. It is seen that the initial reaction rate coefficient k rate is highest at 600°C (Louhi 20 μm , 15 % CO₂), lower at 700°C and lowest at 750°C, but the degree of conversion is highest at 700°C. The reaction rate is almost the same for particle sizes <20 μm and 75-90 μm (Louhi, 15 % CO₂, 700 °C) indicating kinetic control, but then the reaction rate starts to cease with increasing particle size indicating transition into partial diffusion control (in the whole particle level).

Figure A.5.2.10 shows the mass increase of small CaO particles. The mass scale is that of the thermobalance applied in the measurements. The increase of the rate is high at the beginning, but the rate does not reach the high value instantaneously. The lag may be due to lags and mixing in the experimental device. Then CO₂ does not enter to the reactor in a plug flow manner as it is assumed in later simulation. Corresponding curves for large particles are shown in Figure A.5.2.11. The comparison of these cases is shown in Figure A.5.2.12.

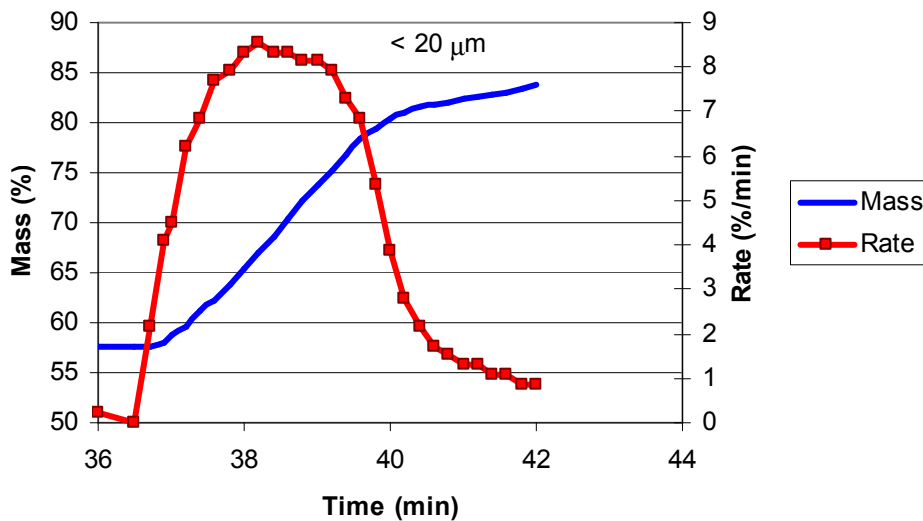


Figure A.5.2.10. Mass and rate of mass change for CaO particles <20 μm (Louhi) at 15 % CO₂ and 650°C.

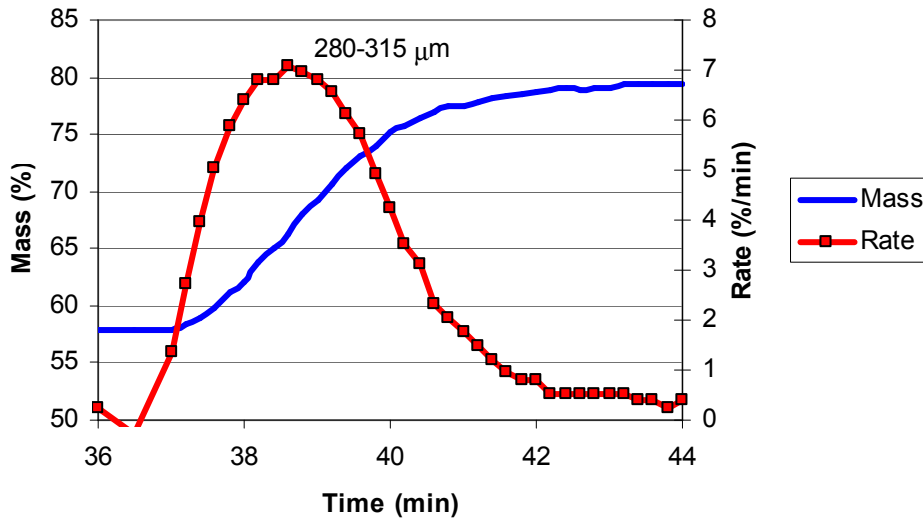


Figure A.5.2.11 Mass and rate of mass change for CaO particles 280-315 μm (Louhi) at 15 % CO₂ and 650°C.

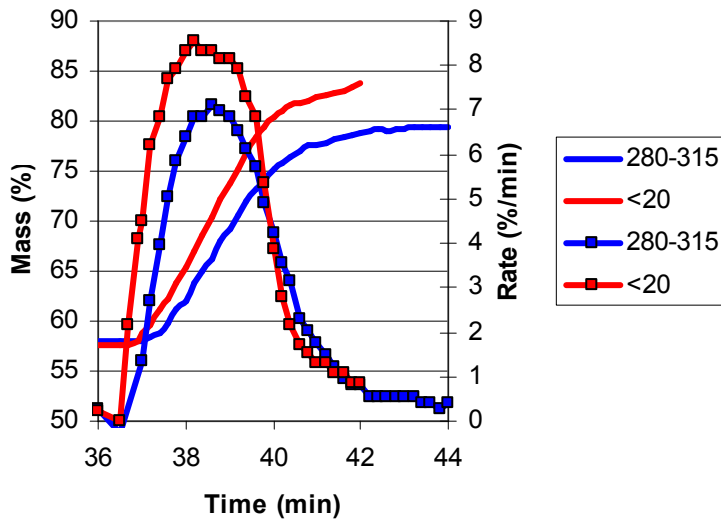


Figure A.5.2.12. Comparison of mass increase of CaO particles with different sizes (Louhi) at 15 % CO₂ and 650°C.

Shimizu et al., 1999 used fixed bed reactor to measure the rate of carbonization of CaO. The particles (0.42-0.59 mm) were diluted using quartz sand in 1 g CaO in 5 g of sand . The global reaction rate coefficient was described by

$$\frac{dX}{dt} = kC(X_{\max} - X) = kCX_{\max} \exp(-kCt) \quad (\text{A.5.2.24})$$

where C is concentration of CO₂, X_{\max} is the maximum conversion at which the rate approached zero, and k is a reaction rate coefficient. CO₂ concentration affected neither k nor X_{\max} . X_{\max} decreased with increasing number of cycles, but the degree became less with increasing number of cycle. k was not affected by the number of cycle. In their reactor design k was fixed at 25 m³kmol⁻¹s⁻¹ and X_{\max} was treated as a parameter less than 0.3, which was observed in the 4th cycle. This model equation, Eq. (A.5.2.24), could describe the reaction rate of the particles of certain size range (0.42-0.59 mm).

Using a similar approach but extending it to account the high initial rate and for the local conversion rate instead of whole particles, we get

$$\frac{dX}{dt} = k\rho_{\text{CO}_2}\rho_{\text{CaO}} \quad \text{when } X < X_c \quad (\text{A.5.2.25})$$

$$\frac{dX}{dt} = k\rho_{\text{CO}_2}\rho_{\text{CaO}} \frac{X_{\max} - X}{X_{\max} - X_c} \quad \text{when } X > X_c \quad (\text{A.5.2.26})$$

where the local CaO concentration (mass/volume) is $\rho_{\text{CaO}} = \rho_{\text{CaO},0}(1 - X)$. The first of these equations can describe the fast initial reaction rate before critical conversion X_c . The latter one can describe the decrease of the reaction rate and the final extinction of the reactions at $X = X_{\max}$. However, a model, where the local reaction rate is function of the local conversion $dX/dt \sim g(X)$ cannot explain why the final conversion is smaller for larger particles. This particle size dependency indicates that diffusion (in the particle level) and pore plugging on the external surface of the particle may play some role. The local diffusivity here is described by equation

$$D = D_0 f(X) \quad (\text{A.5.2.27})$$

where $f(X) = 1$, when $X < X_c$ and $f(X) = (X_{\max} - X)/(X_{\max} - X_c)$, when $X_c < X < X_{\max}$. This model can produce the measured trend.

The local reaction rate is described by the grain model, where CO₂ diffuses through the surface layer of grains and reacts on a shrinking cores in grains inside particles. The mass flow rate of CO₂ between through two concentric spheres (grain surface and reaction surface) is

$$\dot{m} = \frac{4\pi D_{gr}(\rho_{CO_2} - \rho_v)}{\frac{1}{r_v} - \frac{1}{r_{gr}}} = 4\pi r_v^2 k f \rho_v \quad (\text{A.5.2.28})$$

where r is radius, k is the reaction rate coefficient, f is the stoichiometric coefficient, gr denotes the grain surface and v the core surface. The concentration on the core surface can be solved

$$\rho_v = \frac{\rho_{CO_2}}{1 + Da \frac{r_v}{r_{gr}} \left(1 - \frac{r_v}{r_{gr}}\right)} \quad (\text{A.5.2.29})$$

where the grain Damköhler number is defined as $Da = k f r_{gr} / D_{gr}$. It describes the ratio of chemical and diffusion rates. The mass flow rate of CO₂ through the product layer is

$$\dot{m} = 4\pi D_{gr} r_{gr} Da \rho_{CO_2} g(X) \quad (\text{A.5.2.30})$$

where

$$g(X) = \frac{(1-X)^{2/3}}{1 + Da(1-X)^{1/3}[1 - (1-X)^{1/3}]} \quad (\text{A.5.2.31})$$

We get the mass flow rate of recovered CO₂ in Eq. (A.5.2.1) becomes

$$\dot{\rho}_{CO_2} = -g(X)\rho_{CO_2} / \tau_k \quad (\text{A.5.2.32})$$

where the time constant for chemical reactions is $\tau_k = r_{gr} / [3kf(1 - \epsilon_0)]$, where ϵ_0 is initial porosity. Thus Eq. (1) becomes

$$\frac{\partial \rho_{CO_2}}{\partial t} = \frac{1/\tau_d}{x^2} \frac{\partial}{\partial x} \left(f(X)x^2 \frac{\partial \rho_{CO_2}}{\partial x} \right) - g(X)\rho_{CO_2} / \tau_k \quad (\text{A.5.2.33})$$

where time constant for diffusion is $\tau_d = R^2 / D_0$. Boundary conditions are

$$Bi_m(\rho_{CO_2,g} - \rho_{CO_2,s}) = \left(\frac{\partial \rho_{CO_2}}{\partial x} \right)_s \quad (\text{A.5.2.34})$$

and

$$\left(\frac{\partial \rho_{CO_2}}{\partial x}\right)_{x=0} = 0 \tag{A.5.2.35}$$

Equation (A.5.2.33) can be expressed as

$$\frac{\partial \rho_{CO_2}}{\partial t} = \frac{1}{\tau_d} \left[\left(\frac{df}{dx} + \frac{2f}{x} \right) \frac{\partial \rho_{CO_2}}{\partial x} + f \frac{\partial^2 \rho_{CO_2}}{\partial x^2} \right] - g(X) \rho_{CO_2} / \tau_k \tag{A.5.2.36}$$

At $x = 0$, $df/dx = 0$ and we get using L'Hospital's rule

$$\left(\frac{\partial \rho_{CO_2}}{\partial t}\right)_{x=0} = \frac{1}{\tau_d} \left(3f(X) \frac{\partial^2 \rho_{CO_2}}{\partial x^2} \right)_{x=0} - g(X) \rho_{CO_2} / \tau_k \tag{A.5.2.37}$$

which is more suitable in the numerical discretization than Eq. (A.5.2.35). The local conversion is

$$\frac{dX}{dt} = g(X) \frac{\rho_{CO_2} / \tau_k}{\rho_{CaCO_3,0} - \rho_{CaO,0}} \tag{A.5.2.38}$$

Figure A.5.2.13 shows the reaction rate function g as function of conversion. For large grain diffusion control (small D_{gr} , large Da) the rate would decrease rapidly with increasing

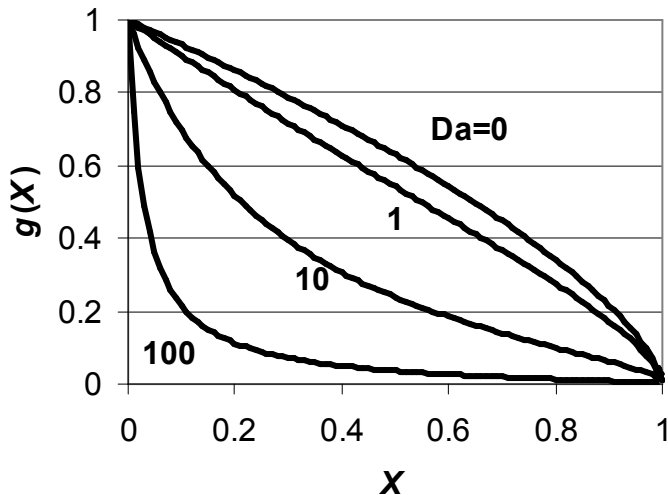


Figure A.5.2.13 . Reaction rate function $g(X)$ for a grain.

product layer on the grains. Note that here the diffusivity of the product layer, D_{gr} , is assumed constant. For $Da = 0$ the decrease is only due to decrease in the reaction surface area.

For a small particle the reaction is controlled by chemical kinetics and the concentration of CO₂ on the grain surface is the same as in the gas. Then equation for conversion can be integrated

$$\frac{\rho_{CO_2} t}{(\rho_{CaCO_3,0} - \rho_{CaO,0}) \tau_k} = -3(1-X)^{1/3} - \frac{3}{2} Da(1-X)^{2/3} + Da(1-X) + \frac{1}{2} Da + 3 \quad (A.5.2.39)$$

The value for the time constant for the reaction kinetics τ_k was estimated from Figure A.5.2.14. At the initial stage ($X = 0$) the rate is about 9%/min, which gives

$$\left(\frac{dX}{dt} \right)_{X=0} \approx (0.09/60) \frac{100\%}{100\% - 56.657\%} = 0.00346 \text{ s}^{-1} \quad (A.5.2.40)$$

The CO₂ concentration corresponding to volume fraction 0.15 is

$$\rho_{CO_2} = x_{CO_2} M_{CO_2} p / (RT) = 0.15 \times 44.01 \times 101300 / (8314 \times 923.15) = 0.0871 \text{ kg m}^{-3}$$

where p is pressure, T is temperature, x_{CO_2} mole fraction of CO₂ in gas and R is the universal gas constant. Then τ_k can be solved

$$\tau_k = \frac{\rho_{CO_2}}{\rho_{CaCO_3,0} - \rho_{CaO,0}} / \left(\frac{dX}{dt} \right)_{X=0} = \frac{0.0871}{(1567 - 888) \times 0.00346} \text{ s} = 0.0371 \text{ s} \quad (A.5.2.41)$$

for CaO produced from Louhi limestone. The reaction rate of the small 20 μm particle is dominated by chemical kinetics and the spatial conversion profile is smooth. However, even for that eventually pore plugging takes place. The critical conversion can be estimated from the long run thermobalance test for a small particle. After 426 min, the reading of the thermobalance was 90.554 % and the reactions were close to total extinction. This gives the maximum value $X_{max} = (90.554 - 56.657) / (100 - 56.657) = 0.782$ for the conversion. The case $Da = 0$ calculated with Eq. (A.5.2.39), is presented in Figure A.5.2.14.

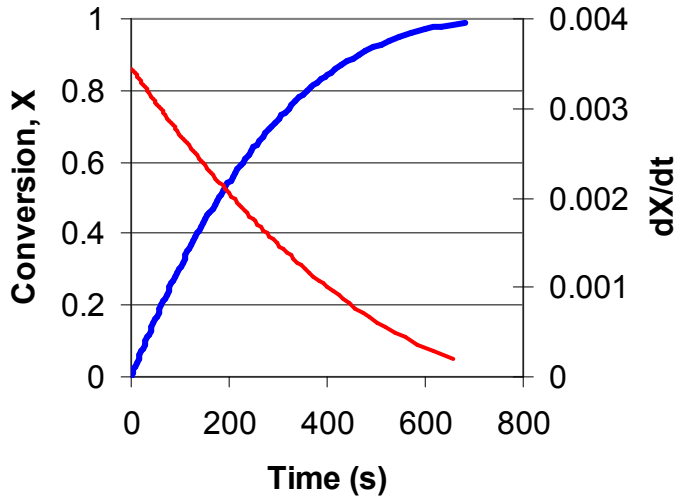


Figure A.5.2.14. Conversion of particle as function of time calculated by the grain model in regime of kinetic control.

The solution of Eqs. (A.5.2.36), (A.5.2.37) and (A.5.2.34) can be done numerically using equations ($p = \Delta t / (\tau_D \Delta x^2)$)

$$\rho_k^{s+1} = p \{ [f_k(1-1/k) - (f_{k+1} - f_{k-1})/4] \rho_{k-1}^s + [f_k(1+1/k) + (f_{k+1} - f_{k-1})/4] \rho_{k+1}^s \} + (1-2p) f_k \rho_k^s + \dot{\rho}_k \Delta t \quad (\text{A.5.2.42})$$

for internal points ($k = 1, 2, 3, \dots$). For centre ($k = 0$) using Eq. (A.5.2.37)

$$\rho_0^{s+1} = (1-6p) \rho_0^s + 6p \rho_1^s + \dot{\rho}_0 \Delta t \quad (\text{A.5.2.43})$$

For particle surface ($k=K$) the parabolic estimation of the derivate is used. Then

$$\rho_K = \frac{2\Delta x Bi_m \rho_{CO_2,g} + 4\rho_{K-1} - \rho_{K-2}}{3 + 2\Delta x Bi_m} \quad (\text{A.5.2.44})$$

For a larger particle the overall critical conversion is lower than X_{max} , since the reactions inside the particle are ceased, when the conversion at the surface reaches X_{max} preventing further diffusion of CO₂ inside the particle.

Eq. (A.5.2.33) with boundary conditions was solved numerically with $Bi_{m0} = 4$, $X_c = 0.553$, and $X_{max} = 0.782$. The value $D_0 = 3.75 \times 10^{-7} \text{ m}^2 \text{ s}^{-1}$ gave a reasonable agreement. The calculations for 20 μm particle showed a very rapid evolution of an even concentration profile of CO₂ inside the particle. Simulation results for CO₂ concentrations inside a larger particle are shown in Figure A.5.2.15. Here also the concentration profiles are quite even. At about 4 minutes the concentration of CO₂ decreases due to increase in the diffusion resistance in the particle surface. Simulation of the time dependent conversion curves with conversion dependent diffusivity is presented in Figure A.5.2.16. The conversion profiles are also quite even. Figure A.5.2.17 shows calculated conversion and rate of conversion for a 300 μm particle as function of time. After about 4 minutes, the rate is decreased. Particle size dependent conversion could also be obtained with constant diffusivity D , if the reaction rate would depend on time t (see Eq. (A.5.2.7)), but not if it depends on the conversion X .

The calculations were carried out with a sparse grid, where the spherical particle was divided into ten layers. The small number is due to the great calculation time required, since the time step is proportional to $(\Delta x)^2$. The accuracy is good, when time is less than 240 s. After that a denser grid would be needed on the surface, where the effective diffusivity decreased. The same calculations were carried out later using pseudo-steady model neglecting storage term as small, which is good approximation, and using 100 layers. This was carried out in another project concerning SO₂ capture to test the numerical model. The trends were the same, but change took place little later than 240 s. In the end the concentration on the particle surface increased and a steep concentration gradient was formed on the surface until total stop of reactions. In reality, the particles are not of the same shape and may have cracks so that the tail for somewhat non-homogeneous particle populations used in experiments will be longer. The form of the diffusivity may suggest that the size of the grains inside the particle remain constant for some time. Then they swell hindering the diffusion until total plugging or pores.

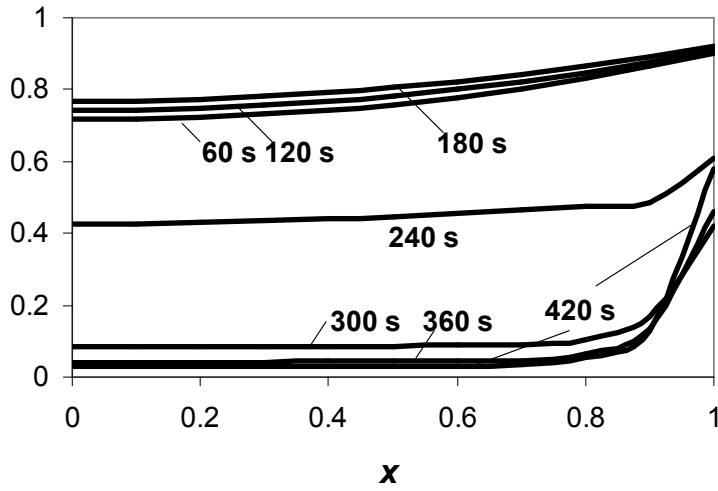


Figure A.5.2.15. Calculated concentration of CO₂ (divided by concentration in gas) inside a 300 μm particle at some time instants.

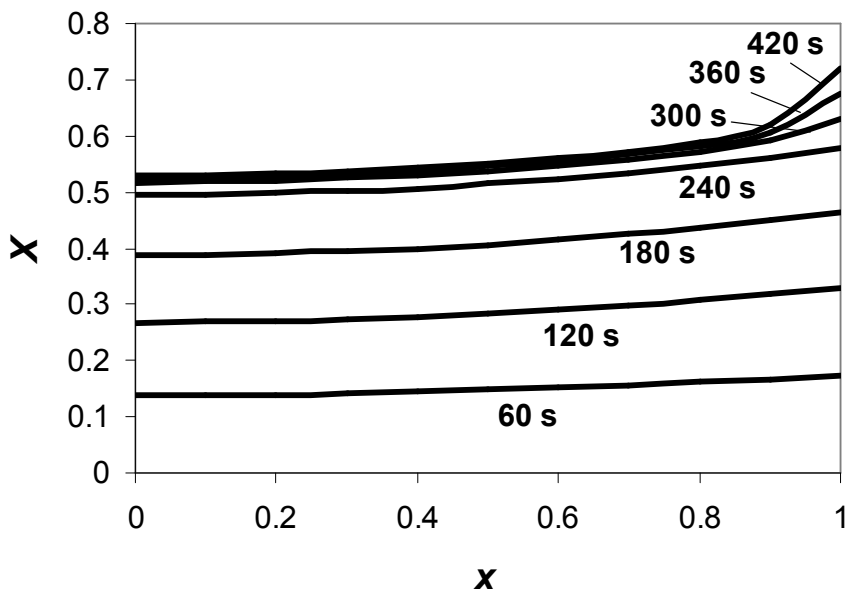


Figure A.5.2.16. Calculated local conversion inside a 300 μm particle at some time instants.

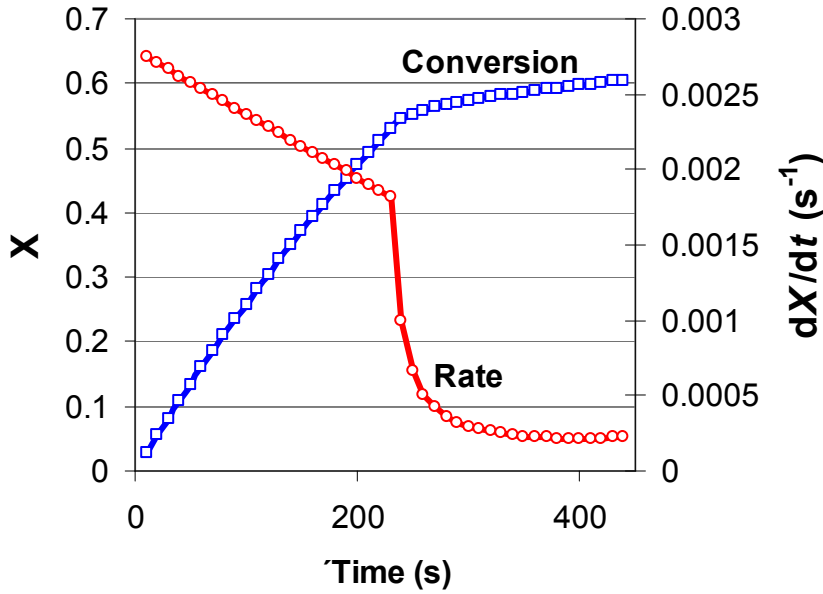


Figure A.5.2.17. Calculated conversion and rate of conversion for a 300 μm particle.

It should be noted that if the pore plugging (in the particle level) takes place on the particle surface, the diffusion will eventually affect also the conversion rate of small particles, since the diffusion starts to limit the conversion rate. Equations (A.5.2.37) and (A.5.2.38) show that

$$\left(\frac{dX}{dt}\right)_{x=0} = \frac{3D_0}{R_p^2(\rho_{CaCO_3,0} - \rho_{CaO,0})} \left(f(X) \frac{\partial^2 \rho_{CO_2}}{\partial x^2} \right)_{x=0} \quad (\text{A.5.2.44})$$

showing that the reaction rate at the centre of the particle will cease, when $f(X) \rightarrow 0$.

The decrease of the mass when CaCO₃ particles are heated can be calculated by an analogous pyrolysis model. (Alvarez and Abanades, 2005) During a single cycle attrition does not have much effect due to the relatively short cycle time, but in long term with several cycles attrition will decrease the particle size of the sorbents.

Conclusions of Modelling

A model accounting for radial diffusion and reaction inside lime particle was developed.

By using the grain model and diffusivity depending on conversion, the trends with decreasing rate and extent of carbonisation with increase in the particle size could be predicted. The measurements at VTT were for the first carbonation cycle.

The decay of the of the CO₂ capture capacity of CaO particles after several cycles has been discussed.(Alvares and Abanades, 2005a,b; Wang and Anthony, 2005) There will be textural changes in the limestone after several cycles. (Alvares and Abanades, 2005a,b) Photographs show that a fresh calcined limestone seems to consist of grains, but the same limestone after 100 cycles seems to consist more like a concrete structure with large pores [10]. Then instead of a spherical grain, a grain of the shape of a hollow cylinder with an impermeable outer surface would be better. Then the reaction rate function $g(X)$ is

$$g(X) = \frac{[1 + (1/\varepsilon - 1)X]^{1/2}}{1 + Da[1 + (1/\varepsilon - 1)X]^{1/2} \ln[1 + (1/\varepsilon - 1)X]^{1/2}} \quad (\text{A.5.2.45})$$

where $Da = kfr_p / D_{gr}$, $\tau_k = r_p / (2kf\varepsilon_0)$ and r_p is the pore radius. CO₂ in the pore diffuses through the inner surface and product layer. Also the physical behaviour may change after several cycles, since the small pores will be filled and pores become larger. The tests were carried with one particle size interval (Alvares and Abanades, 2005a,b) so that no particle size effect could be noticed and the model considers no radial effects. This might be true after several cycles, since probably CO₂ can easily diffuse through large pores formed and the rate will be controlled by the product layer. However, the thermobalance experiments with fresh limestone for the first cycle showed particle size effect, which can be accounted for by considering radial diffusion inside the particle and pore closure at the surface of the particle.

A.6 Task 6. Pilot plant evaluation of the CO₂ separation concept.

A.6.1 Work performed at VTT

VTT's contribution to the project includes CO₂ capture efficiency studies employing a laboratory CFB reactor. To this topic included:

preliminary CO₂ removal tests

design of the additional modifications for test procedure

planning of the final CFB test programme

CO₂ reduction tests by using gas feed (CO₂, N and air)

VTT has a CFB reactor that consists of an air/water-cooled ceramic chamber enclosing a fluidised bed (Figure A.6.1.1). Reactor is used to study combustion behaviour of different fuels, deposit formation, formation of pollutants and ash behaviour under CFB conditions.

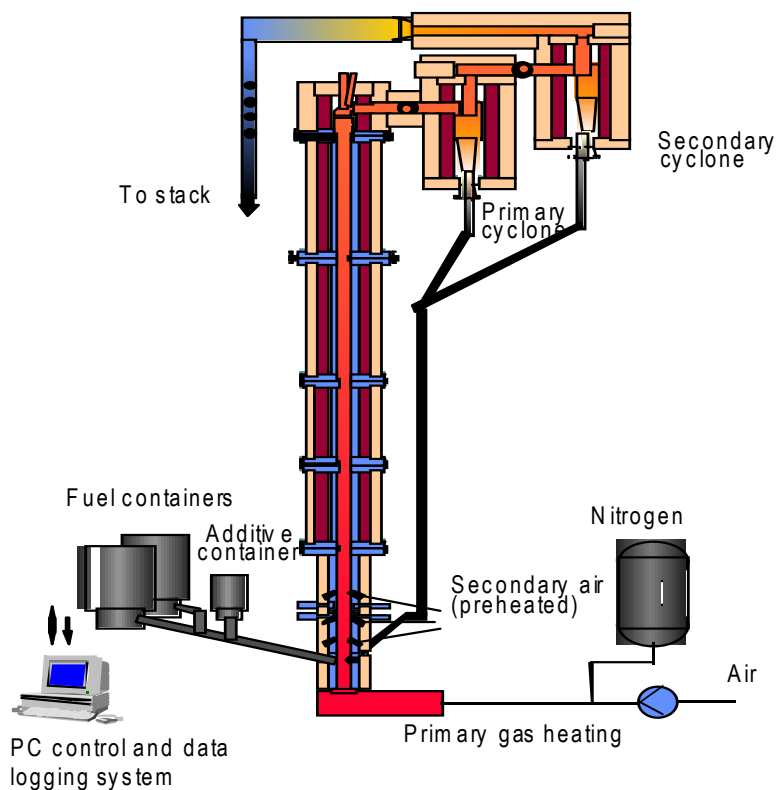


Figure A.6.1.1. VTT's CFB reactor.

Desired temperature in the reactor can be maintained with electrical heaters, cooling system and by staging air feed. The amount of primary- and secondary air fed from three levels is controlled and measured by thermal mass flow meters. Riser height of the reactor is eight meters, ensuring a sufficient residence time for combustion also at high flue gas velocities. Sampling ports at different locations enable the determination of combustion profile as a function of residence time. Samples of solid material can be taken for analysing their quality and particle size. Particulate matter is separated from flue gases in the primary and secondary cyclones and in a fabric filter. Main characteristics of the reactor are:

- i) fuel input 50 kW on an energy basis, ii) riser height 8 m, diameter 167 mm, iii) option for fuel feed with two separate feeding lines, iv) fuel additive feed through a separate feeding line, v) gas and solids sampling at different locations along the riser and vi) fly ash sampling after both cyclones

A.6.1.1. CO₂ capture studies using bio fuel in CFB reactor

Prior to the combustion tests, lime feed was tested to ensure its proper functioning and capacity. Lime was blended with fuel by feeding it from the secondary fuel container into the primary fuel line. The tests showed that maximum fuel and lime feeds were 3.8 and 2.9 g/s, respectively. In addition, calibration curves for fuel and lime feed were obtained by measuring the mass flow rates as a function of frequency converter settings. Eventually in the tests the fuel and lime containers were continuously weighed and mass flow rates calculated from that data.

Preparatory calculations were made before the tests to foresee the mass flow rates of ash, required CaO, removed CO₂, and CaCO₃ corresponding the maximum fuel feed 3.8 g/s (2.75 g/s on a dry basis). The results including the CO₂ and O₂ contents in flue

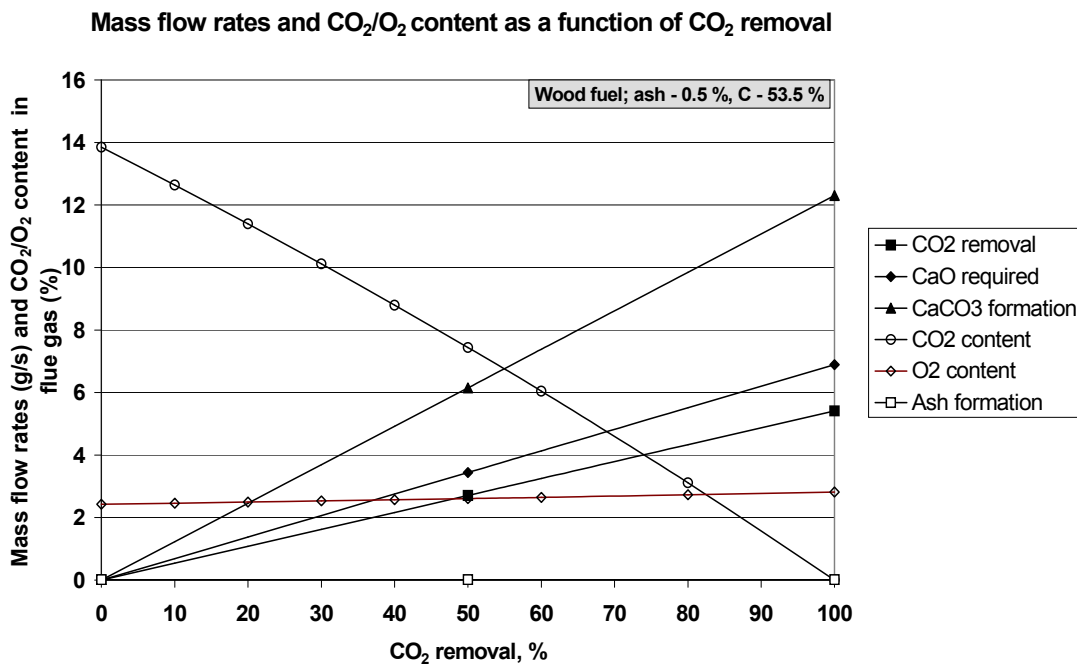


Figure A.6.1.2. Results of the preliminary calculations.

gas are presented in Figure A.6.1.2. The mass flow rates and the contents of gas species are presented as a function of CO₂ removal. Required CaO mass flow rate corresponds to a calculated theoretical rate when all CaO reacts with CO₂ forming CaCO₃. Mass flow rates of CaCO₃ and removed CO₂ simply come from mass stoichiometry CaCO₃:CO₂:CaO ~ 100:44:56. Mass flow rate of ash is constant and as shown in Figure A.6.1.2 is insignificant (~ 0 on the applied scale) in comparison with the other mass flows. Therefore, it was preliminarily presumed that virtually all solids removed from the secondary cyclone are CaCO₃ and CaO, at least when CaO feed corresponds to a higher theoretical CO₂ removal than about 10 %.

Test fuel was milled bark-free pine. This fuel was selected as a sulphur free fuel to produce CO₂ without SO₂ formation. Calcium oxide has stronger tendency to form sulphate than carbonate. The main characteristics of used biomass fuel are shown in Table A.6.1.1. It can be shown by simple calculations that sulphur content in the fuel is low enough to be neglected in CaO mass balance calculations. Similarly calcium input in fuel is insignificant beside calcium input in lime feed.

Table A.6.1.1. Fuel characteristics.

Moisture, %	27.6
Lower heating value (dry fuel), MJ/kg	19.5
Ash content, %	0.44
Elemental analysis, %	
C	51.3
H	6.2
O	42.4
N	0.07
S	0.01

Three one-hour-tests were carried out. Table A.6.1.2 shows fuel and lime feed rates in all tests. Lime feed in test 3 could have decreased CO₂ emissions by 29 % if all CaO would have formed CaCO₃.

Table A.6.1.2. Test parameters.

Test	Fuel feed, g/s	Lime feed, g/s	Theoretical maximum CO ₂ removal, %
1	3.8	--	--
2	-- ['] --	1.1	16
3	-- ['] --	2.0	29

Gas temperature in the riser was maintained in about 750 °C along the whole length of the riser. It was measured at three heights and varied between 740 and 770 °C during the entire test period. Temperatures in the first and second cyclone were 670 and 640 °C, respectively. Both temperatures varied less than ±20 °C during the tests. Excess of air was slightly higher than indicated in Figure A.6.1.2, resulting in flue gas O₂ content about 7 %.

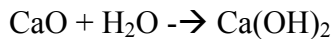
Table A.6.1.3. Measured mass flow rates and deposited material.

Mass flow rate (kg/h)/Test		1	2	3
In	Fuel	13.7	13.7	13.7
	Ash	0.04	0.04	0.04
	CaO	--	3.9	7.2
Circulating	1 st cyclone	42.5	40.3	53.3
Out	2 nd cyclone	0.02	0.055	~ 0
	Filter	0.02	0.007	1.69
Deposited material after the tests, kg	Fluidized bed	4.25		
	Riser tube	1.09		
	1 st cyclone	0.25		
	2 nd cyclone	0.63		
	Heat exchanger	1.90		
	Total	8.12		

Solid material samples were taken during all tests in order to determine CO₂ capture efficiency. Samples were taken from beneath both cyclones and from the filter that is in the flue gas line after the heat exchanger. Samples were weighed and later analysed in thermogravimeter. Table A.6.1.3 presents the measured mass flow rates. Supposing that all or almost all combustible material in fuel burns in the combustor, only compounds of calcium would be collected from the second cyclone and the filter in addition to minor amounts of ash and fluidising sand. In the first test, when no lime was fed, the ash mass input equals the total material removal. In the second test the total CaO and ash mass input was slightly over 3.9 kg, but only 0.06 kg was removed from the gas cleaners. It implied that most of CaO or formed calcium compounds are just circulating between the combustor and the first cyclone or are deposited somewhere between the fluidised bed and the filter. Mass flow rate of the combustor/first cyclone cycle was measured at the end of each test. It was not increased by the end of test 2, rather it was decreased slightly, Table A.6.1.3. It indicates that calcium compounds would have deposited almost entirely.

In the last test, almost 1.7 kg of solids was collected from the gas cleaners, whereas about 7.2 kg (CaO+ash) was fed into the fluidised bed. Recirculation from the first cyclone was now about 53 kg/h that was somewhat higher than in the first tests. It may indicate that some of the increased feed remained in the combustor/cyclone cycle. On the other hand, this mass flow rate measurement is not very accurate and the mass flow rate normally fluctuates to some extent even during a relatively stable test period. Therefore it is more probable that most of the above-mentioned feed was deposited again.

After the tests the entire line between the fluidised bed and the filter was cleaned and solid material collected from different sections of the line, as shown in Table A.6.1.3. Lime feed (CaO) formed calcium hydroxide with water that originates from fuel:



Calcium hydroxide melts in about 580 °C, which temperature the particles can reach soon after being fed into the fluidised bed. Calcium hydroxide releases water mainly between 350 and 450 °C and later in conjunction with its melting in about 580 °C. Therefore, particles containing melted calcium hydroxide may land on the walls of the combustor line where the temperature range is between 640 and 770 °C, as mentioned, and form deposits there. Probably only a small fraction of lime has to form hydroxide to enable the deposit formation, especially since the absolute mass feed rate is high.

The primary objective of the experiments was to test if this method could be a applicable test procedure to be employed later when a more comprehensive set of tests will be carried out. Lime was blended with wood fuel prior to feeding it into the fluidised bed in order to separate the reacted lime in form of calcium carbonate from the gas cleaners and remove CO₂ from flue gas in this way. It was observed that most of the solid material deposited on the walls of the riser tube, the cyclones and other sections of the combustor. This was to be due to calcium hydroxide formation in blending and feeding lime with the fuel. Solid material particles carrying a fraction of calcium hydroxide and landing on the combustor walls, may deposit there because of the low melting point of calcium hydroxide. Therefore the employed method proved inapplicable and will not be used later. Calcium hydroxide formation can be prevented by replacing fuel and air feed with a gas feed consisting of a blend of pressurised air or nitrogen and carbon dioxide as showing in following section.

A.6.1.2 CO₂ capture studies using gas feed to CFB reactor

The method used first proved to be inapplicable, since mixing of fuel and lime led to calcium hydroxide formation resulting in solid deposit problems in the entire combustion line. Therefore the procedure was modified to remove those problems and to improve reactor's performance in CO₂ capture. Previously employed fuel, lime, and air feed to generate a constant suspension flow of CO₂ and lime was replaced with a gas feed consisting of a blend of pressurised air and carbon dioxide. Lime was fed as before through the line from the fuel container. In this way, the calcium hydroxide formation that caused problems in the previous tests could be avoided. A pre-heater was used to raise the temperature of the gas mixture onto an appropriate level.

The effect of the following parameters on CO₂ capture has been studied:

carbon dioxide content in gas

temperatures along the fluidised bed reactor

particle size of lime

lime feed rate

Solid particle samples are analysed in order to determine the extent of carbonation in different process conditions. Gas and mass balance calculations enable the determination of the overall CO₂ separation efficiency.

Carbon dioxide feed from a set of CO₂ gas bottles was used. CO₂ was diluted in desired ratios with pressurised air. The CO₂ content of the gas mixture was set to 10 or 20 % and it remained on the desired level very well during the tests, as the test results below indicate. The CO₂ content in flue gas before and after the combustor was continuously measured. This allowed the determination of CO₂ capture efficiencies. Lime was fed from one of the fuel

Table A.6.1.4. Test parameters and results.

Test	Gas feed, l/min	CO ₂ in gas, %	Lime feed, g/s	Max. CO ₂ capture, %	CO ₂ capture achieved, %	CO ₂ capture efficiency, %
1	550	10	1.1	48	1-3	~ 4
2	--"--	--"--	--"--	--"--	2-4	~ 6
3	500	20	--"--	26	3-4	~ 13
4	380	--"--	--"--	35	8-10	~ 26
5	800	--"--	1.0	15	1-3	~ 13
6	--"--	--"--	2.0	30	5-15	~ 33

containers and introduced into the gas mixture just above the gas inlet. The lime feed can be controlled in a range between 0 and 2.9 g/s. In all, five tests were made. Table A.6.1.4 shows the test parameters and some tests results. The average gas temperature in the riser tube and cyclones was in all tests 650 °C. All the measured temperatures varied less than ± 20 °C during the tests.

Solid material samples were taken during all tests in order to determine the CO₂ capture efficiency. Samples were taken from beneath both cyclones and from the filter that is in the flue gas line after the heat exchanger. The samples were weighed and were to be analysed later in a thermogravimeter. However, since it turned out that the CO₂ capture efficiency in these tests could be determined reliably from the gas content measurements, the samples have not been analysed so far.

In addition to the test parameters, Table A.6.1.4 shows the calculated and measured values of maximum and achieved CO₂ capture, and the CO₂ capture efficiency. Maximum CO₂ capture corresponds to a theoretical case when every single CaO molecule reacts with a CO₂ molecule. The achieved captures are the results of the measurements. Finally, the CO₂ capture efficiency shows the ratio of achieved and theoretical values.

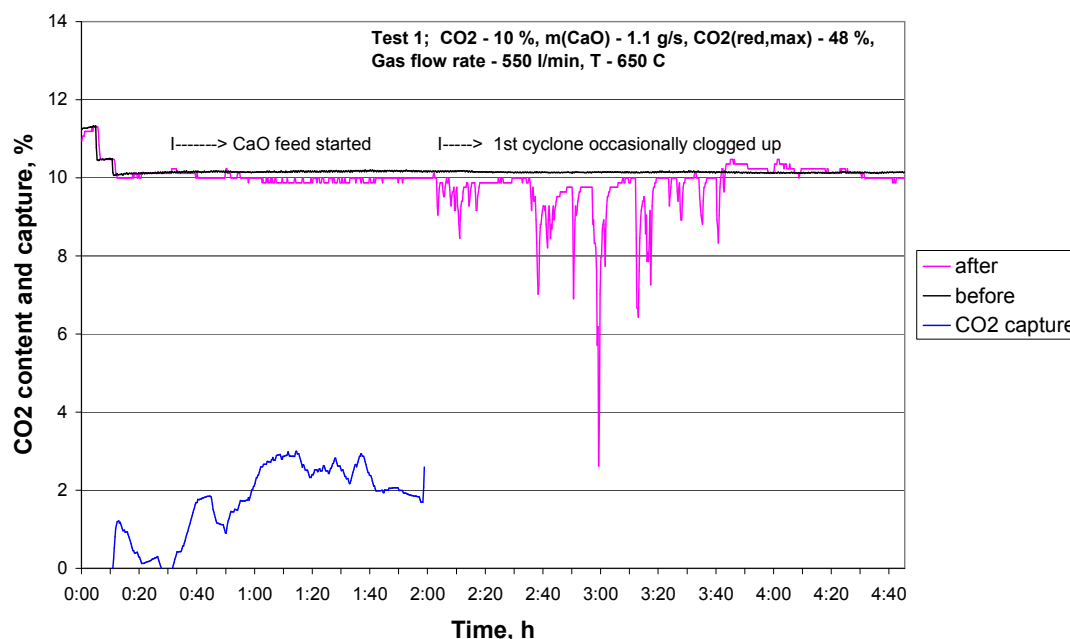


Figure A.6.1.3. CO₂ contents and capture as a function of time, test 1.

Figure A.6.1.3 shows the measured CO₂ contents and the capture efficiency as a function of time in the first test when no bed material was used in the reactor. Some time after starting the lime feed the cyclones started to become occasionally clogged up (see high fluctuation in CO₂ content after the reactor, Fig A.6.1.3) and the test was therefore stopped. The CO₂ capture efficiency in this test was only about 4 %, Table A.6.1.4.

In the next test the gas conditions were exactly as in the first one, but 2.5 kg of bed material was inserted into the reactor in the beginning of the test. The clogging was significantly reduced when bed material was used. Consequently the capture efficiency was slightly higher, but still not more than about 6 %.

The CO₂ content of flue gas was raised up to 20 % for the following tests, Figure A6.1.4. This resulted in about doubled capture efficiency, test 3. The capture efficiency could be still doubled by decreasing the gas feed from 500 to 380 l/min. A decrease in gas feed should indeed result in a higher capture efficiency because of several effects. Firstly, the lime particle concentration in flue gas increases due to the lower gas feed. Secondly, the particle concentration increases also because the velocity difference between the gas velocity and the terminal settling velocity of particles becomes smaller, resulting in longer particle residence times. Furthermore, the gas residence time in the reactor increases also.

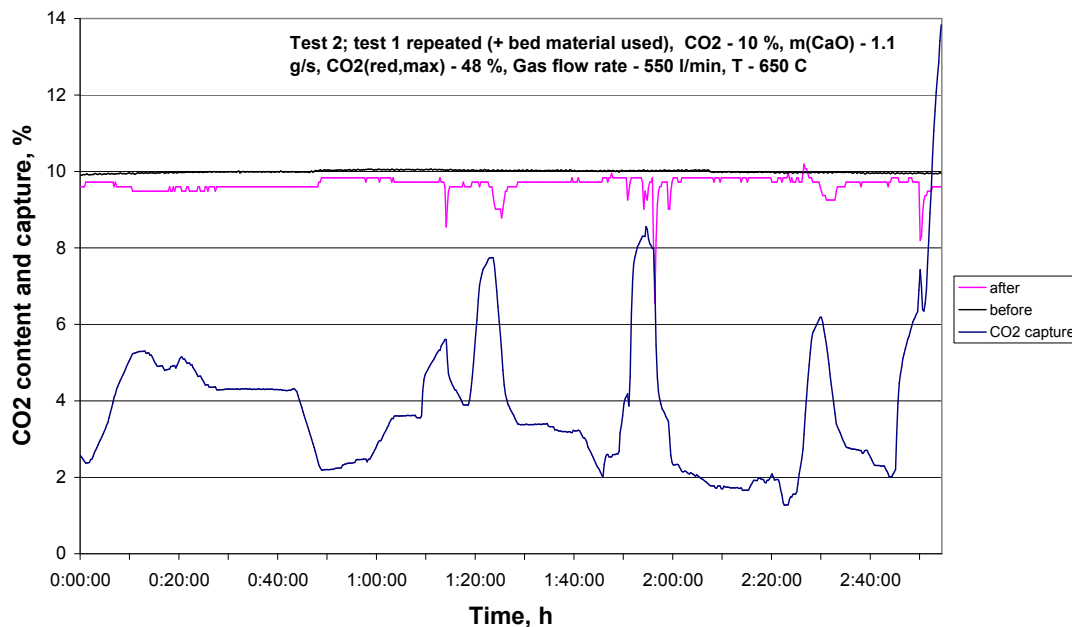


Figure A.6.1.4. Measured results, test 2.

Figure A6.1.5 shows the results of the tests 5 and 6. The conditions in the test 5 were similar as in the test 4 excluding the gas feed rate that was higher. Consistently with what was mentioned before, the capture efficiency decreased in comparison with respect to the test 4. However, now it analogously should have been even lower than in the test 3, since the conditions were otherwise the same excluding the higher gas feed rate. This behaviour can not be reliably explained, but may be due to a different, more favourable flow pattern or simply to uncertainty, since the measured differences in CO₂ contents before and after the reactor are in both cases small. Besides, the tests were quite short.

The lime feed was increased from 1 to 2 g/s in the last test. It had supposedly a very clear impact on the CO₂ capture, see Figure A.6.1.6 and Table A.6.1.4, since the conditions in the reactor were changed only with respect to the particle concentration that was doubled. Consequently, the total particle surface in the suspension is doubled as well as the collision rate between the particles and CO₂ molecules, at least during the very first moments when the particles are entering the reactor. Farther away, downstream in the reactor the collision rate is not necessarily double any more, since the fraction of the most reactive CO₂ molecules decreases fastest along the gas route simply because they react faster with the lime particles. It is supposed that the reactivity of individual CO₂ molecules is a function of their velocity. Furthermore, obviously the surface reactivity of an individual particle is not constant all around the particle as well as the overall reactivities of single particles are not the same. Correspondingly, the particles are less reactive downstream, since the most reactive particles and the most reactive parts of the particles have already reacted. Before-mentioned facts are valid qualitatively, but since we do not have any quantitative measures for these changes in the reactivities, we can not know if the differences are great enough to cause any real, significant change in the overall reaction rate in the suspension on its route in the reactor. This matter will be studied during the next reporting period.

Conclusions

An improved method for lime carbonation in a laboratory-scale fluidised bed reactor was tested, since the method tested before did not prove to be applicable. This time no fuel was used, but the carbon dioxide was fed into the reactor in a mixture with air. This proved to be an effective way to reduce clogging problems in the first cyclone, especially when bed material was used in conjunction with the gas-lime suspension.

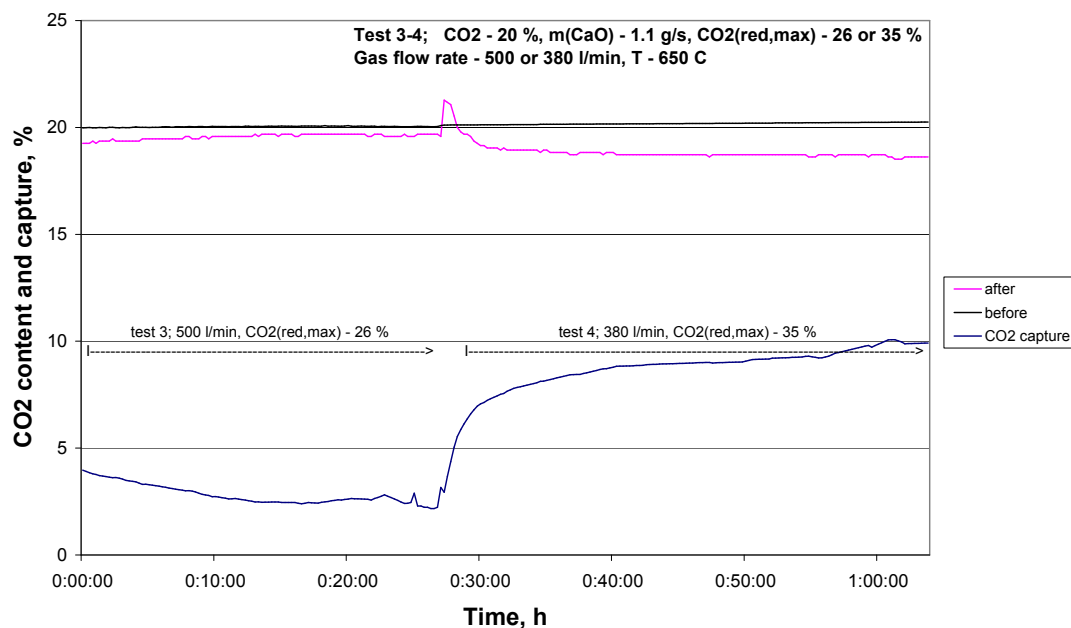


Figure A.6.1.5. Measured results, test 3 and 4.

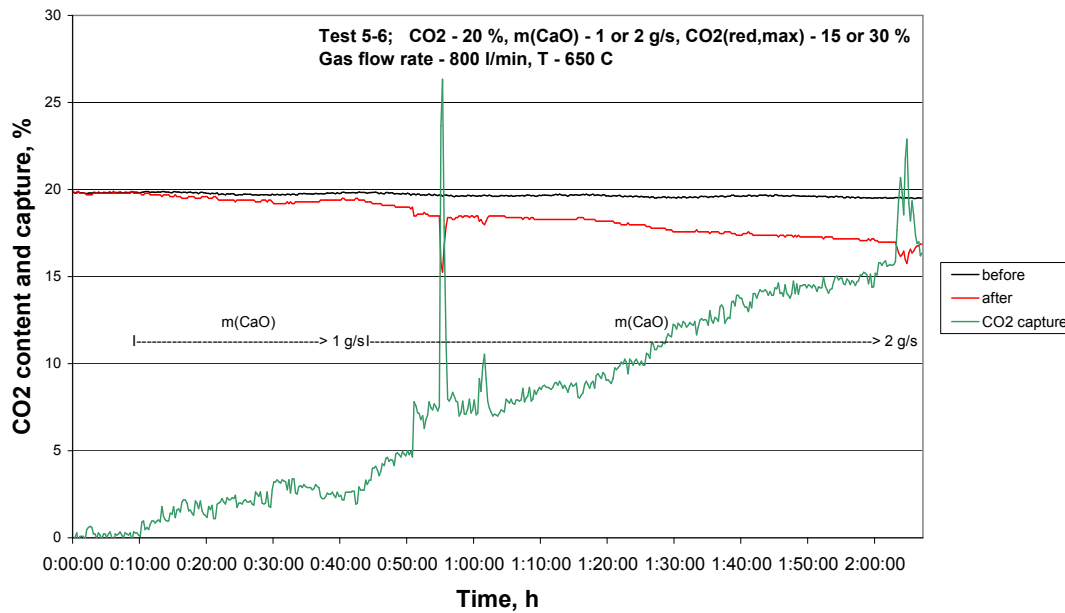


Figure A.6.1.6. Measured results, test 5 and 6.

Three variables were used in the tests; gas and lime feed rates, and initial CO₂ content in the gas. The highest capture efficiency 33 % was achieved when these variables were 800 l/min, 2 g/s, and 20 %, respectively. In all, the measured capture efficiencies did obey supposed trends quite well; higher gas feed rate decreased and higher CO₂ content increased efficiency. However, when the lime feed was doubled from 1 to 2 g/s, the capture efficiency increased from 13 to 33 %. There is no logical reason why the capture efficiency should change, since the absolute number of captured CO₂ molecules should increase roughly in proportion to the increased lime feed resulting in almost a constant capture efficiency.

A.6.2. Work performed at Cranfield. In duct testing.

As was mentioned in previous parts of this report, one of the options considered to capture CO₂ in existing power stations is the injection of sorbent (lime) in the flue gas path. In order to use this entrained mode, lime particle size must be small enough to maximise contact with the flue gas. With this configuration, the residence time for gas-solid contact will be limited to a few seconds. This implies that high carbonation rates have to be achieved.

Cranfield University activities within this task involved the development and use of a laboratory scale entrained flow reactor and a pilot scale combustion facility to measure the performance of finer CO₂ sorbent particles.

A.6.2.1 Laboratory scale entrained flow reactor

Rig design

The carbonation reaction in entrained mode has been simulated with in preliminary modelling exercise to determine the specifications for the rig. Typical combustion atmospheres from coal combustion are around 13-15% in volume of CO₂. Kinetic constants have been extracted from literature (Bathia and Perlmutter, 1983), and typical specific surfaces for calcined material have been used (20 m²/g) as initial parameters for this model. The upper limit for the extent of carbonation will be given by the equilibrium pressure for CO₂. Figure A.6.2.1 simulates the effect of temperature on the CO₂ removal efficiency for a given CO₂ concentration and gas flow in the entrained flow reactor, an assumed particle conversion of 0.2, a solid specific surface of 20 m²/g (typical for calcined limestone), and a fixed ratio Ca/C.

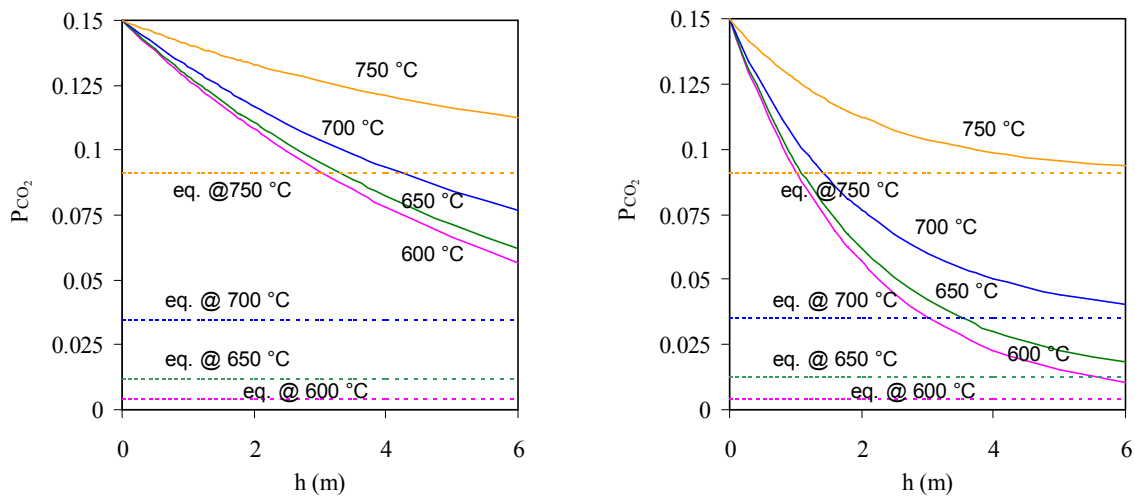


Figure A.6.2.1. Effect of temperature on CO₂ capture in entrained flow vs. reactor length for two different Ca/C ratio; a) Ca/C=1, b) Ca/C=3.

The carbonation reaction has two different stages; there is a first step where the carbonation rate is fast, and then a second step where the carbonation rate decreases. From the initial

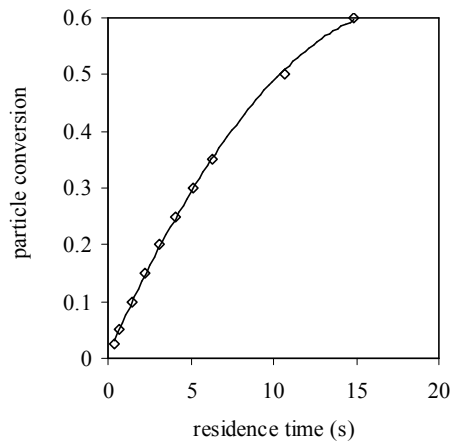


Figure A.6.2.2. Theoretical particle residence time in the entrained flow reactor versus mean particle conversion.

model, based in the kinetic constants extracted from the literature, the residence time needed to reach a given particle conversion can be calculated. This residence time is plotted against particle conversion in Figure A.6.2.2.

The data extracted from these results have been used in the design of the carbonator entrained flow reactor. To achieve a reasonable level of conversion, the residence time has to be in the range of a few seconds, and this, combined with the minimum gas flow in the line needed to avoid the effect of gas dispersion, gave the required length for the reactor. Dispersion module in the entrained flow reactor can be observed in Figure A.6.2.3

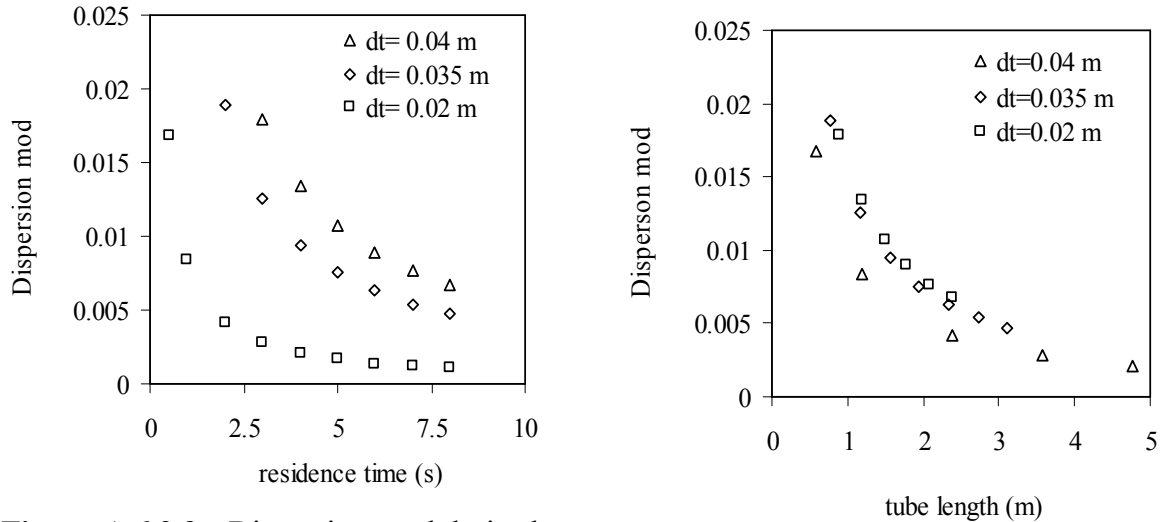


Figure A.6.2.3. Dispersion module in the entrained flow reactor vs tube length.

The final scheme of the installation is given by Figure A.6.2.4 and a picture of the test rig is shown in Figure A.6.2.5. The main features of the experimental rig and the solid injection system and the length of the heated zone (6 m) which gives reasonable flexibility in terms of gas/solid contact time. A powder dispersion generator has been used to create the solid-gas dispersion. The particle disperser operates with particle sizes less than 100 μm .

After the particle injection, the air/solids gas stream joins a CO₂ containing gas stream coming from a commercial gas bottle. The combined gas/particle stream then enters a coiled pipe (which forms the reaction tube) which is immersed in a fluidised bed (Techne, IFB 101) filled with alumina. The good heat transfer characteristic of fluidised beds is used to obtain a uniform heated zone in the reaction tube. The temperature in the reaction tube is controlled by the temperature of the fluidising alumina. After the fluidised bath the reacted gas/solids stream is cooled down, in a coiled pipe immersed in water bath, to stop the carbonation reaction. Then the carbonated particles are captured in two filters working in parallel.

There are two sampling points in the system to measure CO₂ concentration, before and after the reaction zone in the coiled tube. The solids were collected from the filters and stored in a dessicator for further analysis.

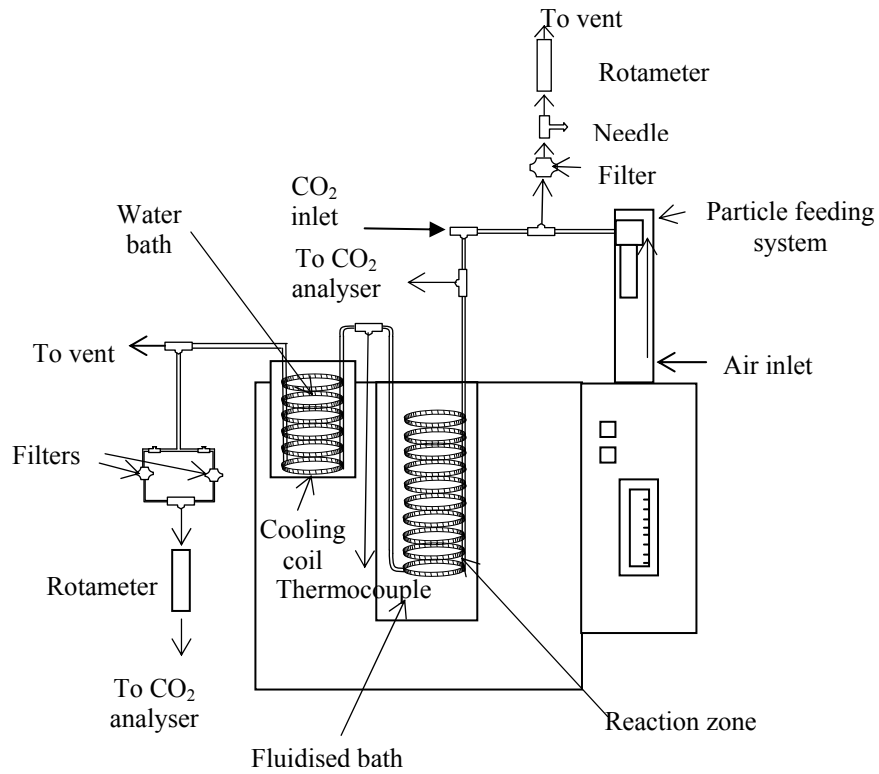


Figure A.6.2.4. Scheme of the installation for CO₂ capture experiments in entrained bed.



Figure A.6.2.5. Picture of the entrained flow rig for CO₂ capture.

Solids

Natural limestone (99.95 % CaCO₃) has been used to prepare lime for these experiments. Starting material has been ground to reduce the initial particle size to obtain a distribution with a mean particle diameter of 60 μm. Figure A.6.2.6 shows the typical solids particle size distribution.

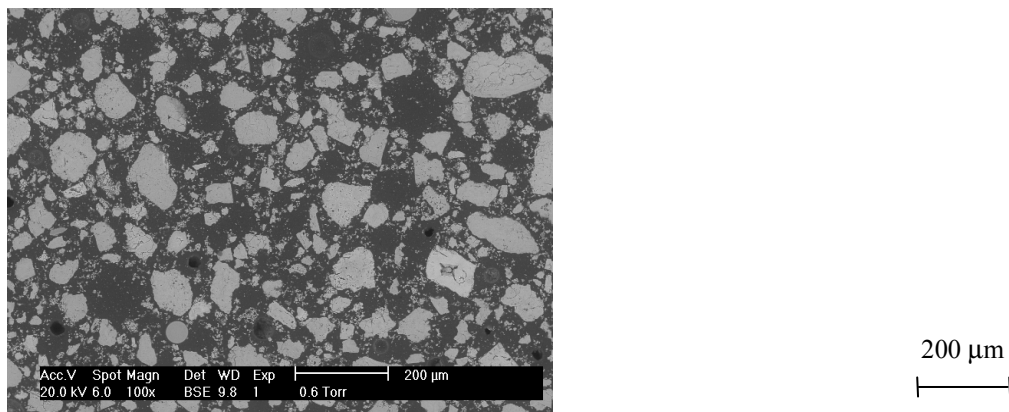


Figure A.6.2.6. SEM picture showing the typical particle size distribution used in the experiments.

Due to the amount of lime (of consistent quality) required further test programme it was not possible to prepare it by flash calcination. In order to obtain lime, limestone has been calcined in an oven at 850 °C for 30 minutes. Samples were spread on plates and introduced into the oven. The calcined solids are stored in a dessicator and placed directly in the particle feeding system ready for the carbonation experiments. Samples of these solids were stored for later characterisation. Lime obtained using this method will be less reactive than that prepared by flash calcination. This will be due to the different surface areas developed in both cases and the risk of sintering when limestone is calcined in an oven.

To evaluate the efficiency and obtain the conversion of the calcination process from this fresh limestone, a controlled calcination experiments in a thermobalance in a N₂ atmosphere were carried out. Calcined solids were placed in a platinum basket in a quartz reactor, heated up (10 K/min) and kept one hour at the peak temperature of 850 °C to ensure the complete calcination of the material. A typical curve is shown in Figure A.6.2.7 in this graph the fractional mass change is plotted against temperature. Two big steps can be observed, the first mass loss represents the water absorbed by the fresh lime (a very hygroscopic material) and the second corresponds to the CO₂ still remaining in the solids calcined in the oven.

The conversion in the calcination process has been calculated from these graphs, and as can be seen the calcined solids in the oven still retain 14% in weight (9% in moles) of CO₂. This means that the calcination of limestone is not complete. However it is expected that most of the unconverted limestone will be found in the centre of particles, so it will not have an important influence in carbonation process.

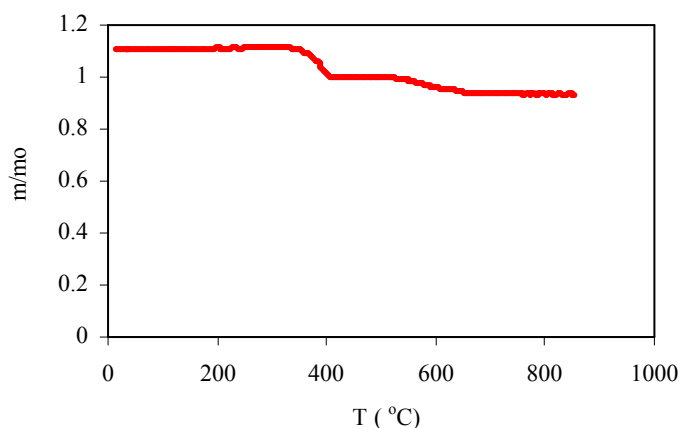


Figure A.6.2.7. Mass lose versus temperature obtained in thermobalance, in calcinations carried out over solids pre-calcined in the oven.

Carbonation experiments

Carbonation experiments have been carried out in a wide range of conditions. The carbonation temperature has been modified between 550 °C to 670 °C, these values are reasonable in the practical application of the capture technique, where the sorbent injection would be located in the exhaust duct of a boiler. Residence times of the order 1-3 s were used and total molar ratios of CaO/CO₂ between 0.85-2.15. The experimental conditions for the carbonation experiments are compiled in Table A.6.2.1 together with the reduction in CO₂ concentration achieved after the sorbent injection.

As can be seen the percentage of efficiency in CO₂ capture oscillates in most cases between 20 and 30 % (% of reduction in volume concentration of CO₂ in the gas stream). A surprisingly high value of CO₂ capture was achieved in the experiment carried out at 670 °C. Although there is uncertainty about the size distribution of particles used in this test. The rest of the experiments have been carried out with a more homogeneous particle size distribution. Residence times in the order of 2.5-3 s give in all cases reductions in the CO₂ concentration over 20 %.

After the carbonation experiment, the gas/solid stream is cooled down when it leaves the fluidised bath and the solids are captured in two filters in parallel. Calcination experiments have been carried out in a thermobalance in N₂ atmosphere to analyse the average particle conversion of these carbonated solids. A known amount of solids is placed in a platinum basket, inside the quartz tube which is heated up in a N₂ stream at 10 K/min up to 850 °C and then stays there during one hour, to ensure complete calcination of the solids. Figure 2.6.Cran8 shows one example the mass change obtained in these calcination test, against temperature. Calcination tests were carried out for the solids captured in both filters in the system.

Table A.6.2.1. Experimental conditions and results obtained for the carbonation experiments carried out in the entrained bed reactor.

T (°C)	air (l/min)	CO₂ (l/min)	% CO₂(init)	% CO₂(after)	grs CaO/min	CaO/CO₂ (molar)	t_r (s)	% reduction
671	4.00	0.60	13.60	8.18	1.62	1.08	3.07	39.9
636	4.83	0.75	13.44	10.81	2.03	1.08	2.63	19.6
626	4.53	0.75	14.22	10.35	2.43	1.30	2.81	27.2
617	3.62	0.60	14.22	10.66	2.84	1.89	3.55	25.0
617	3.76	0.60	13.75	10.81	2.84	1.89	3.43	21.4
612	4.07	0.40	8.96	6.33	1.62	1.62	3.37	29.4
607	6.04	0.95	13.60	12.05	2.03	0.85	2.17	11.4
599	6.87	0.90	11.59	8.96	2.43	1.08	1.97	22.7
599	7.25	0.95	11.59	9.88	2.43	1.02	1.87	14.7
587	4.54	0.55	10.81	7.25	2.43	1.77	3.05	32.9
587	5.77	0.60	9.42	5.71	2.84	1.89	2.43	39.4
587	5.38	0.60	10.04	7.10	3.24	2.16	2.59	29.3
586	7.36	0.95	11.43	8.96	2.03	0.85	1.87	21.7
581	4.85	0.55	10.19	7.41	2.03	1.47	2.89	27.3
541	6.83	0.95	12.21	9.58	2.03	0.85	2.11	21.6

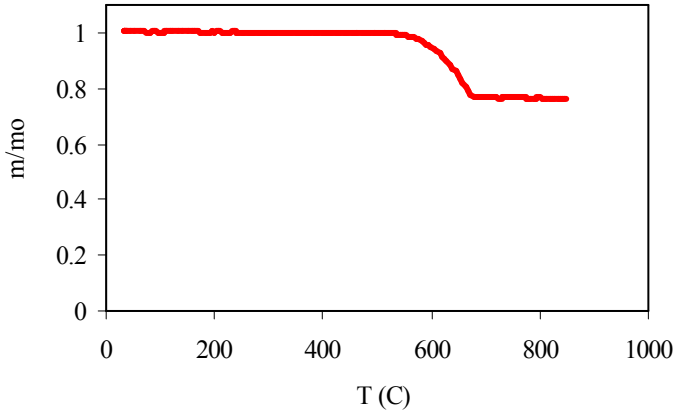


Figure A.6.2.8. Mass lose versus temperature, obtained from the calcination of previously carbonated solids, carried out in the thermobalance. Carbonation conditions: T^a 587 °C; initial C_{CO2} 10.1 % vol; final C_{CO2} 7.1 %; reduction achieved 29.3 %; t_r 2.6 s; CaO/CO₂ molar ratio 2.16; particle conversion 22.87%.

Solids conversion is obtained combining the information of these two set of calcination experiments in thermobalance. This conversion will be obtained from the initial CO₂ content of the solids (percentage of CaCO₃ in the calcined material) and then the total mass loses in the carbonated material (percentage of CaCO₃ in the carbonated solids). The calcination curves obtained in the different experiments in thermobalance are compiled in next figures:

Mass balance calculations have been carried out in all the experiments to ensure the reliability of the experimental conditions in terms of solid/gas contact time at the reaction temperature and quantity of solids injected.

$$\text{moles CO}_2 \text{ gas stream} * \text{CO}_2 \text{ reduction} = \text{moles CaO injected} * \text{particle conversion}$$

This balance closes with a good agreement in all the experiments.

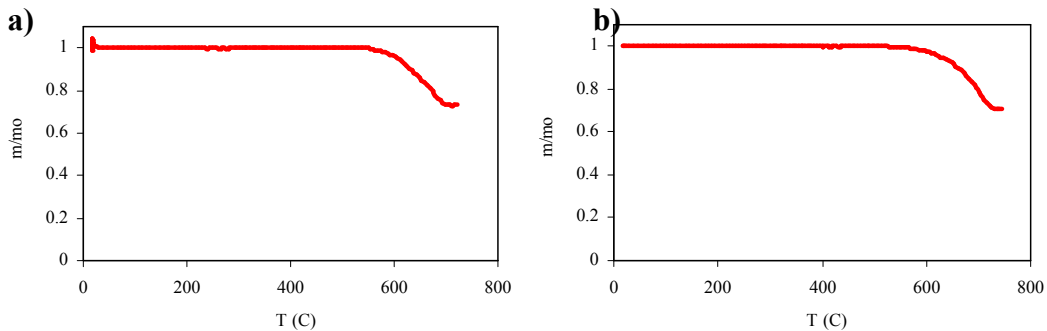
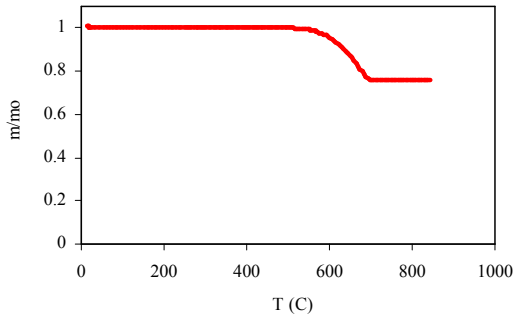


Figure A.6.2.9. Carbonation experimental conditions: T^a 607 °C; initial C_{CO2} 13.6 % vol; final C_{CO2} 12 %; reduction achieved 11.4 %; t_r 2.5 s; CaO/CO₂ molar ratio 0.85; particle conversion 29 %. a) solids from main stream, b) solids captured in the filter before the analyser.

a)



b)

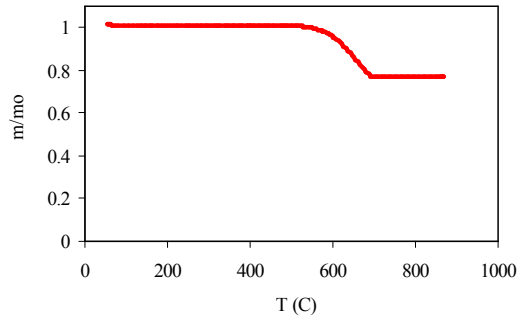
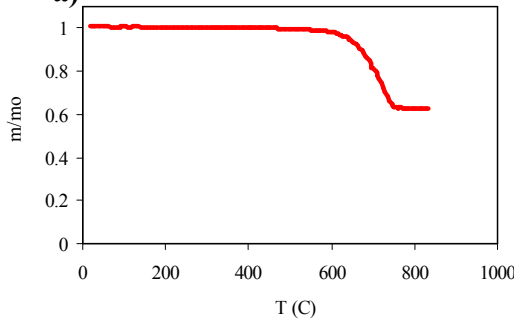


Figure A.6.2.10. Carbonation experimental conditions: T^a 599 °C; initial C_{CO₂} 11.6 % vol; final C_{CO₂} 8.9 %; reduction achieved 22.7 %; t_r 1.97 s; CaO/CO₂ molar ratio 1.08; particle conversion 23 %. a) solids from main stream, b) solids captured in the filter before the analyser.

a)



b)

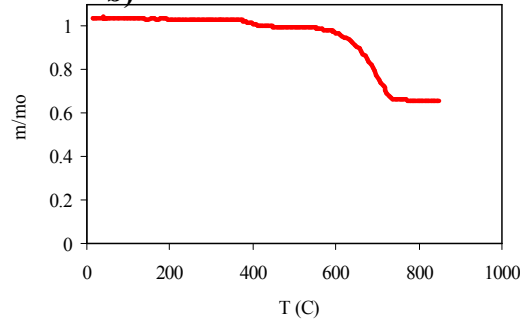
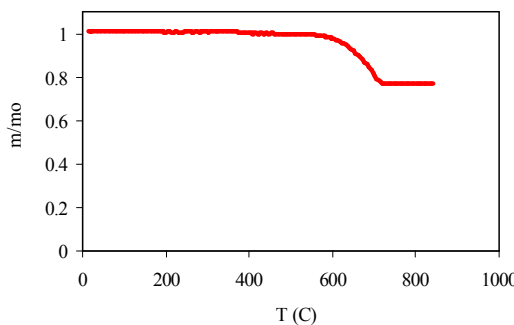


Figure A.6.2.11. Carbonation experimental conditions: a) T^a 541 °C; initial C_{CO₂} 12.2 % vol; final C_{CO₂} 9.6 %; reduction achieved 18.8 %; t_r 2.11 s; CaO/CO₂ molar ratio 0.85; particle conversion 34.3 %. b) T^a 581 °C; initial C_{CO₂} 12.3 % vol; final C_{CO₂} 10.1 %; reduction achieved 21.5 %; t_r 2.03 s; CaO/CO₂ molar ratio 0.85; particle conversion 37 %.

a)



b)

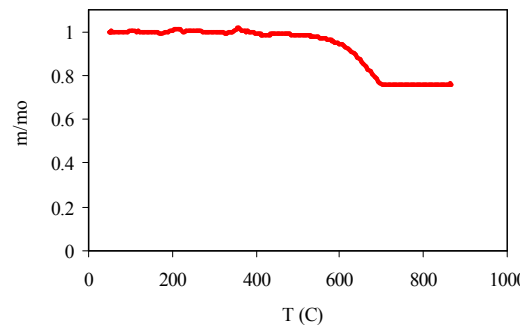


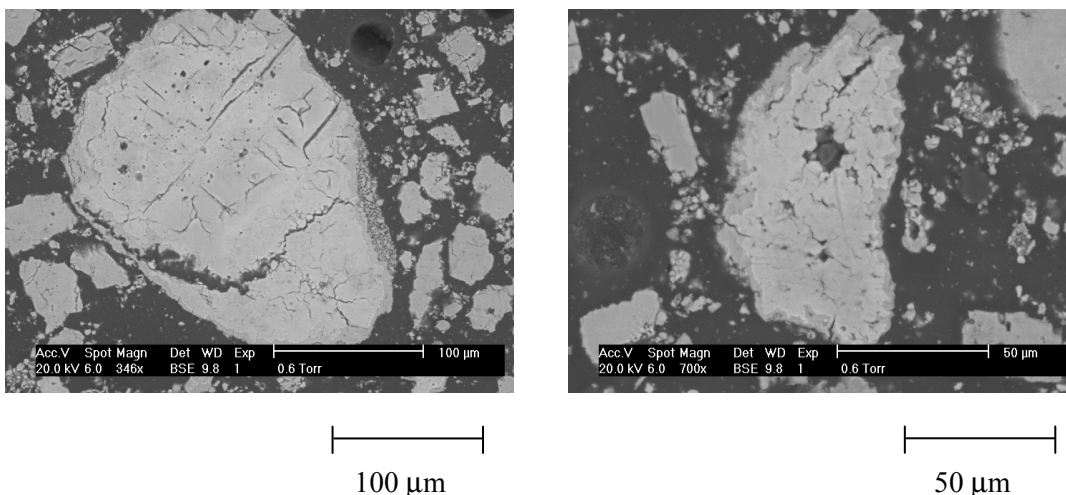
Figure A.6.2.12. Carbonation experimental conditions: a) T^a 587 °C; initial C_{CO₂} 10.8 % vol; final C_{CO₂} 7.25 %; reduction achieved 32.9 %; t_r 3.05 s; CaO/CO₂ molar ratio 1.77; particle conversion 23 %. b) T^a 587 °C; initial C_{CO₂} 9.42 % vol; final C_{CO₂} 5.71 %; reduction achieved 39.4 %; t_r 2.43 s; CaO/CO₂ molar ratio 1.89; particle conversion 24 %.

Table A.6.2.2. Experimental conditions for the carbonation experiments carried out in the entrained bed reactor.

T (°C)	% CO ₂ (init)	% CO ₂ (after)	CaO/CO ₂ (molar)	t _r (s)	% reduction	% particle conversion
617	13.75	10.81	1.89	2.17	11.4	29.0
599	11.59	8.96	1.08	1.97	22.7	23.0
587	10.81	7.25	1.77	3.05	32.9	23.0
587	9.42	5.71	1.89	2.43	39.4	24.0
587	10.04	7.10	2.16	2.59	29.3	22.9
586	11.43	8.96	0.85	1.87	21.7	34.6
581	10.19	7.41	1.47	2.89	27.3	30.0
541	12.21	9.58	0.85	2.11	21.6	34.4

Table A.6.2.2 includes the results obtained for particle conversion measured in the calcination tests carried out in the thermobalance, together with the CO₂ reduction achieved in some of the experiments.

Samples of the carbonated solids were prepared to be analysed by SEM to obtain more information on the textural characteristics of the carbonated material. The samples were prepared following the same procedure used in metallographic analysis. Figure A.6.2.13 shows some of the pictures.

**Figure A.6.2.13.** SEM pictures of carbonated solids.

These pictures correspond to the experiment carried out at 587 ° C, with an initial 10 % of CO₂ (in volume), and a molar Ca/CO₂ ratio of 2.14. The residence time of the solids in the reaction length was 2.59 s. The final CO₂ concentration after the capture was 7.1 % in

volume, giving a capture efficiency of 29.3 %. Calcination tests carried out in a thermobalance on the carbonated solids gave a mean particle conversion of 22.87% (in mass). As can be seen there is a darker layer around the particles in contrast with the lighter inner core. This outer layer is the CaCO₃ formed around the initial lime particle. This layer is especially clear in the picture on the right belonging to a smaller particle (mean particle diameter around 50 µm). This SEM analysis technique has to be improved to obtain clearer images from the smallest particles in the particle distribution.

A.6.2.2. Pilot Scale Plant Facility

Pilot scale facility modifications and description

Within this task, Cranfield University activities involved the modification of an existing pilot scale combustion facility to allow the in-duct injection of sorbent particles and the use of this system to determine the CO₂ capture efficiencies of a range of potential sorbents under different operating conditions.

Figure A.6.2.14 shows the existing pilot scale combustion facility. This rig is based around two combustion units - a bubbling fluidised bed combustor and a pulverised coal combustor – that give a total combined thermal output of ~150kW. The combustors can be operated either separately or in series. Both combustors operate on coal and have natural gas start-up burners. The rig includes facilities for routine flue gas measurements and data logging of operational parameters. Figure A.6.2.15 shows a picture of both pilot scale units

Modifications to this test facility made to:

- Enable sorbent particles to be injected at selected locations along the hot gas path duct
- Enable gas and particulate sampling to be carried out to determine the CO₂ capture performance of the sorbent (and fully characterise the exposure conditions of the particles)
- Ensure that the sorbent is removed from the gas stream before reaching the induced draft fan (as the sorbent size distribution will probably be different to the particle distribution currently produced by the combustors)

As a task in this project, a number of alternative schemes for these minor modifications were considered and designs produced for the most promising schemes. Parts of the modifications that were common to the different schemes were carried out to minimise any delays in the project.

Alternative locations for sorbent particle injection considered have been (see Figure A.6.2.14):

1. pipe between fluidised bed combustor and pulverised coal combustor
2. pulverised coal combustor burner/FBC output gas stream *instead* of coal feed
3. pulverised coal combustor *adjacent* to burner/FBC output gas stream
4. lower down pulverised coal combustion chamber
5. first set of heat exchanger probe locations after pulverised coal combustion chamber

Starting from the information about sorbent size, sorbent reactivity and residence times/temperatures, etc., the best location for sorbent particle injection appeared to be location 3.

Alternative particle feed systems and injection methods have been investigated during this task. The most appropriate for the sorbent particles was a controlled screw feeding from a

containment vessel, followed by gravity/pneumatic transport by a N₂ flow into the test rig. This alternative seemed to be the best option available as it could be applied with minor changes to existing solids feed systems. A solids feeding system was connected to inject the sorbent at location 3.

Gas and particulate sampling are needed downstream of these particle injection locations. Sampling was carried out at ports that were originally designed for the exposure of heat exchanger probes in both of the existing probe exposure test sections.

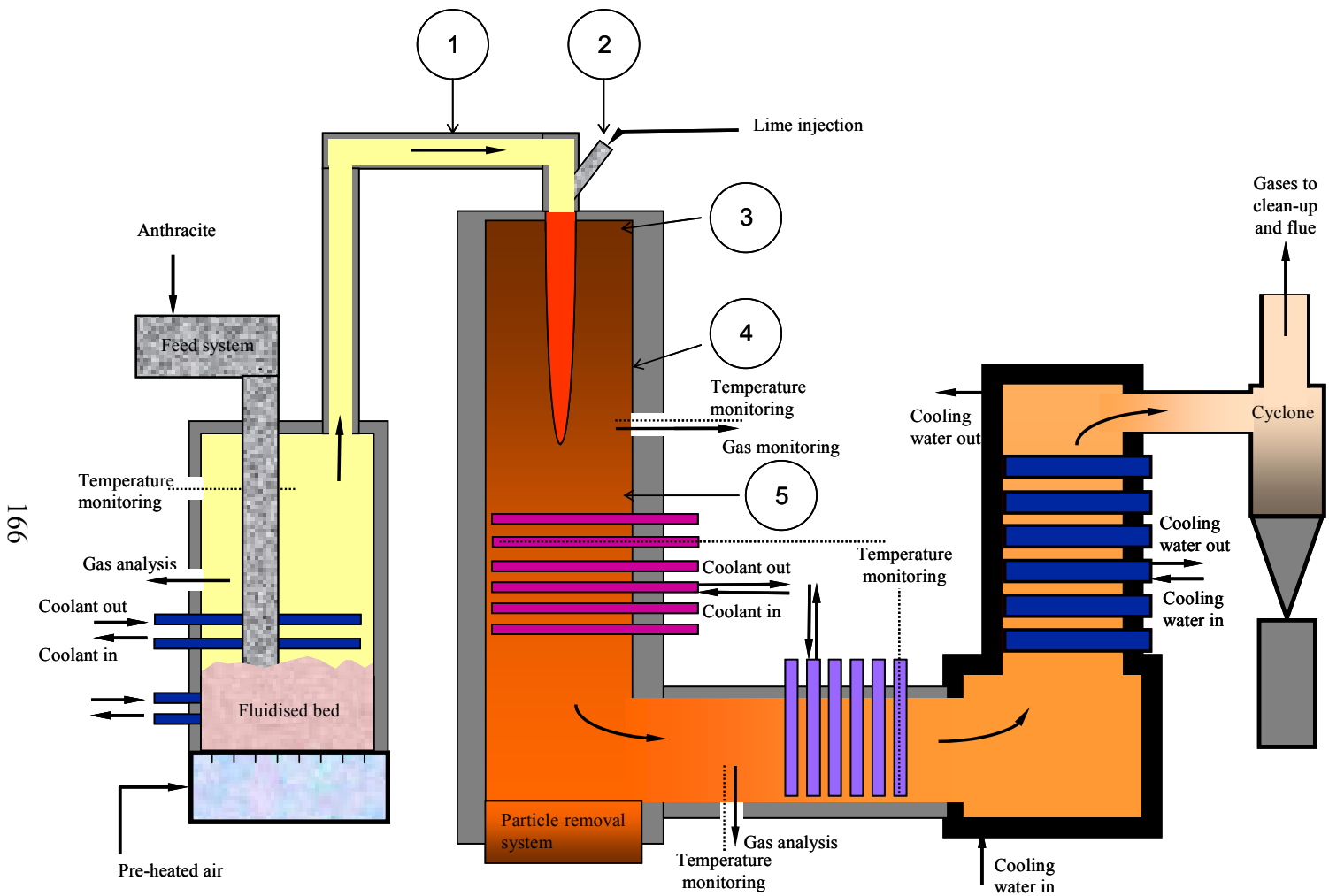


Figure A.6.2.14. Schematic diagram of existing combustion test facility

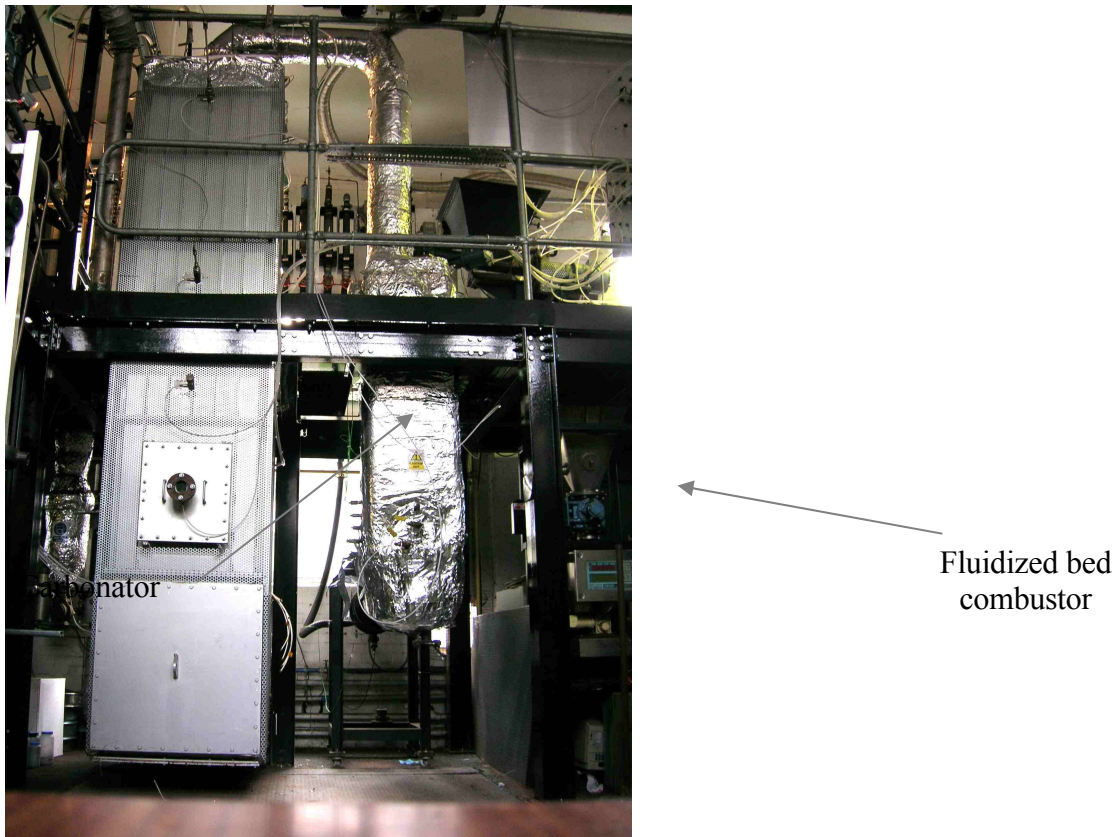


Figure A.6.2.15. Pilot scale combustion facility in Cranfield University.

Pilot-scale carbonation experiment

The fluidized bed was used during these tests as a combustion unit and the second chamber as a carbonator. The great advantage of this pilot plant and this configuration was that it allowed the performance of lime to be studied in a real combustion atmosphere.

During the experiments the bed, filled with silica sand, was operated with anthracite and fluidised with air (around 40 % excess air) to keep the temperature in the desired range. The air flow used in these experiments was 1.2 m³/min.

The temperatures in the bed and in the gas path were monitored along with the gas composition. As was mentioned, there were two sampling points for the CO₂ analysis, the first one in the exit of the fluidised bed and the second one is 2 m below the sorbent injection point.

Anthracite was used in all the experiments as fuel. The proximate analysis of the fuel used in the experiments is shown in Table A.6.2.3.

Test in the pilot scale combustion facility required large amounts lime. For this reason it was not possible to prepare it by calcinating limestone. The sorbent used in the tests was a commercial lime with 96 % CaO, 75 < \square m in size and with a specific surface between 8.5-16 m²/g (as specified by the supplier). The lime feeding rate was 3.2 kg/hr. This value was

limited by the solids injection system. The residence time of particles inside the carbonation chamber was about 2 seconds.

Table A.6.2.3. Proximate composition of the anthracite used in the fluidised bed.

% C	% H	% O	% N	% S	% Ash
0.91	0.03	0.02	0.01	0.01	0.02

The effect of temperature on carbonation process was the main focus in this study. In order to obtain this information, experiments were performed at different temperatures, from 550 °C to 750 °C. Table A.6.2.4 summarises temperatures and flows used in these tests.

Table A.6.2.4. Temperatures and flows used.

Temperature (°C)	Coal flow(kg/hr)	CaO flow (kg/hr)	CO ₂ in (%)	CO ₂ fin (%)	CaO/CO ₂
550	3.2	3.6	12.10	10.03	0.2
625	3.2	3.6	12.53	11.01	0.2
730	3.2	3.6	12.28	11.67	0.2
750	3.2	3.6	12.60	11.70	0.2

The reduction of CO₂ emissions seems low looking at these results. However it has to be noted that the CaO/CO₂ ratio is far from an optimum value, because of the low lime feed rates used. This fact implies that further analysis of the results has to be done in order to study the efficiency of the process.

Table A.6.2.5. Reduction of CO₂ emissions, lime particle conversion and minimum CO₂ concentration that can be achieved.

Temperature (°C)	% Reduction CO ₂ emission	Particle Conversion (%)	Minimum possible CO ₂ concentration	CO ₂ captured/maximum CO ₂ capture
550	17.1	99.5	9.68	85.5
625	11.7	66.0	10.02	58.6
730	4.9	19.2	9.82	24.6
750	7.1	29.7	10.08	35.7

Table A.6.2.5 shows reduction of CO₂ emissions, lime particle conversion and the minimum possible CO₂ concentration in flue gas assuming a complete conversion of particles injected. In this study particle conversion was calculated as the ratio between the CO₂ removed and the maximum value that can be achieved.

In Table A.6.2.5 also gives the ratio of the CO₂ captured to the maximum CO₂ capture possible. This parameter quantifies the CO₂ reduction that can be achieved at these experimental conditions if the lime injection was increased so that the CaO/CO₂ ratio was 1.

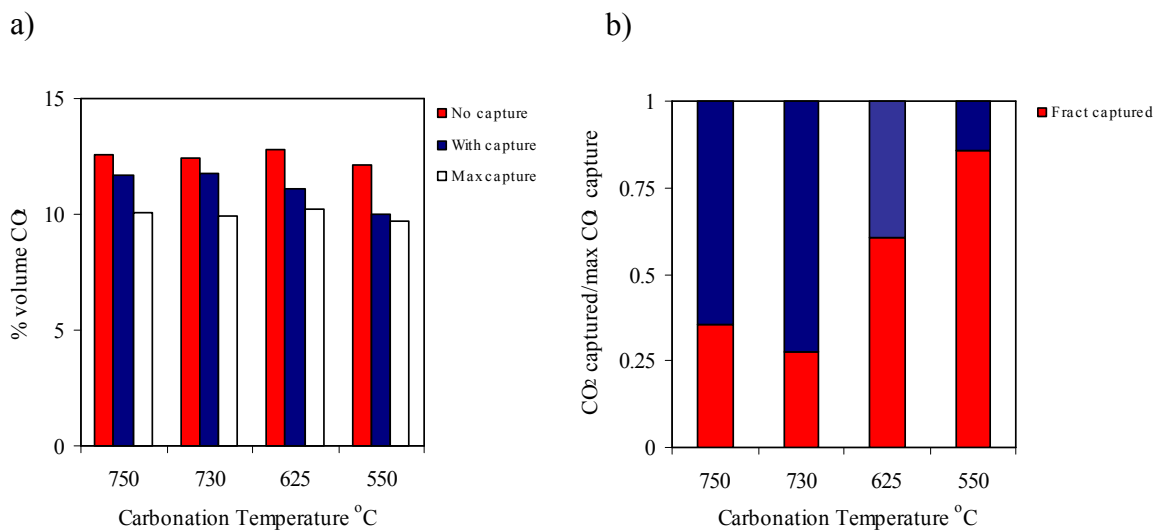


Figure A.6.2.16. CO₂ capture achieved in the pilot scale rig. CaO/CO₂ ratio: 0.2.

Results in terms of CO₂ capture are displayed in Figure A.6.2.16. The first graph, a), represents the total CO₂ capture. The red bars represent the CO₂ concentration before injecting the sorbent, the blue ones represent the concentration after the injection point and the white ones the maximum capture possible if the particle conversion, for the amount of solids injected, had been complete. Although the total capture may seem low looking at this graph, the perspective is much better when the low CaO/CO₂ ratio is taken into account. Due to this low ratio the minimum CO₂ concentration that can be achieved is between 10-11 %. The experimental value of CO₂ reduction reached when the carbonator was used at 550 °C indicates that the competing reaction with SO₂ has not significantly affected the capture of CO₂.

The second graph, b), of Fig. A.6.2.16 shows the ratio of CO₂ captured to the maximum CO₂ capture at different temperatures. As can be seen, temperature plays an important role in carbonation process. High temperatures lead to lower capture efficiencies. At 550 °C, lime particles are almost converted with a residence time of 2 seconds in the pilot scale carbonator and 85% of the CO₂ would have been captured if the stoichiometric CaO/CO₂ ratio has been used. This means that under these experimental conditions CO₂ reaction with CaO particles is fast enough to have confidence in this capture process.

Experiments made in this task show that reasonable levels of CO₂ capture can take place in real combustion environments. This fact shows that this option is worth pursuing for cycles proposed for the capture with regenerable sorbents.

A.7 Task 7. Pilot testing and design specification of the calciner.

There are different methods proposed to supply the heat required for the regeneration that tend to become more difficult and challenging as the temperature of the regeneration increases. For the CaCO₃/CaO system, Shimizu et al. (1999) proposed the calcination of CaCO₃ by burning a fraction of the fuel with O₂/CO₂ in a fluidized bed calciner. This requires an air separation unit that is almost 50% the size of the unit required to burn all the fuel with oxygen (full oxyfuel combustion). The air separation unit (as in the case of oxyfuel combustion systems) introduces a substantial energy penalty and added cost to the system. Other less developed calcination options are under consideration to avoid the use of an air separation unit, using heat carriers, such as CaO circulating between a high-temperature combustion chamber and the calciner (Abanades et al 2005). Also, an indirect calcination option has been proposed by Ziock et al. (2002) using a huge CO₂ flow of recycle gas. Other alternative routes to be explored are outlined by Levenspiel (2005).

A.7.1 Work performed at CSIC

The objective of this task was to obtain the fundamental design parameters for novel fluidised bed systems that consider the heat transfer from the combustion chamber to the calciner to drive the calcinations (regeneration) reaction of the sorbent. It was recognized from the start that these options incorporate complexities in the design, require special materials and will certainly translate into a substantial increase of the capital cost respect to a power plant without capture (although this is common for other CO₂ capture systems). However, they offer a substantial reduction in efficiency penalties (see section A9), and avoid the need for an air separation unit to supply O₂ to the calciner (to burn part of the fuel and drive the calcinations reactions). It should always be of interest to exploit, at least in part, the option of heat transfer between two fluidised beds.

Figure A.7.1.1 (left) outlines one of the options for the indirect heat transfer method proposed for case B in A9 (see also Abanades et al 2005). It includes a high temperature circulating fluidized bed combustor ($T = 1050^{\circ}\text{C}$) transferring heat through metallic walls to a fluidized bed calciner ($T = 850^{\circ}\text{C}$) operating at a CO₂ partial pressure of 0.4 bar obtained in the calciner by injecting steam. Solids in the calciner are fluidized with a mixture of steam and the CO₂ generated during calcination. The carbonator operates at 650°C after cooling the gases coming from the combustor. In these proposed arrangements, the solids fluidising in the narrow sections of the bed (fins) have to transfer the heat along the fluidised fin to the main body of the combustor and/or regeneration unit. The mixing rate of solids (specially the lateral mixing) in these narrow fluidised beds is the key mechanism to understand how far we can go increasing the length and the thickness of the “fins” between beds. This work is intended to study the mobility of the solids in the restricted geometry of the fins, as a first step to estimate the practical feasibility of the system proposed in Figure A.7.1.1 and the limits imposed by solid mixing to the (lateral) heat transfer in the fins.

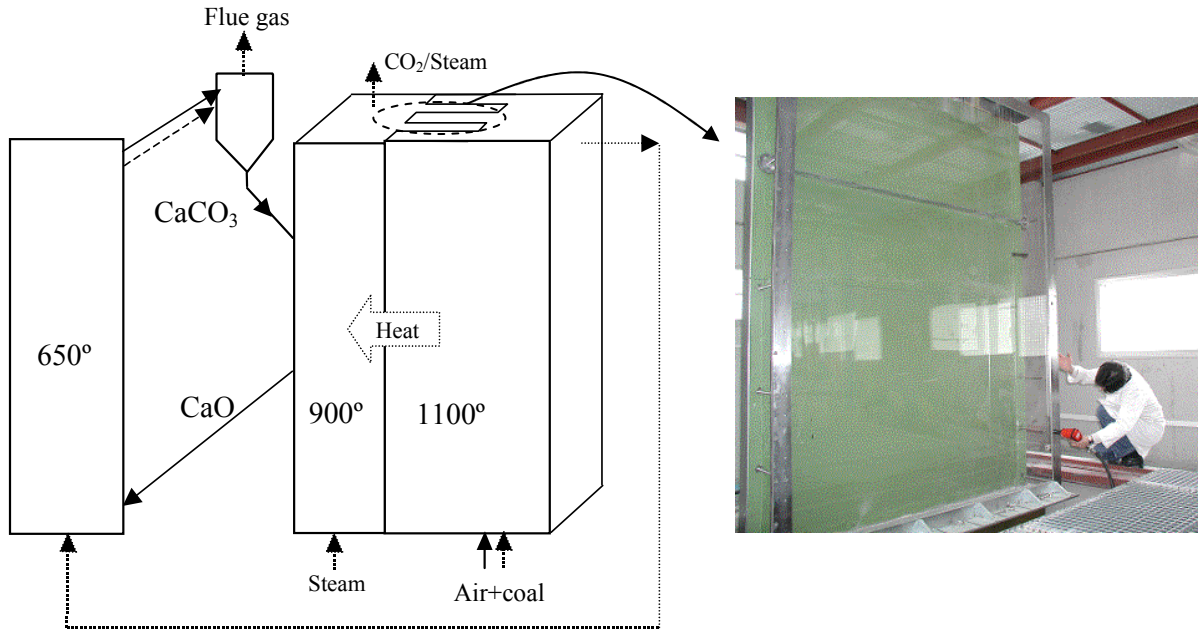


Figure A.7.1.1. Outline of an indirect heat transfer method for case B (left) and cold bed facility to investigate viability of lateral heat transfer in narrow fluidized beds.

The work has been focused on estimate heat transfer between beds which can be expressed in terms of an overall bed-to-wall heat transfer coefficient as follows:

$$Q = hA_t \Delta T_m \quad (\text{A.7.1.1})$$

The difference of temperatures between beds, ΔT_m , will be fixed by the operation conditions in both rigs (200K in Figure A.7.1.1). The bed-to-wall heat transfer coefficient (h) will depend on bed temperature and fluidisation conditions but a conservative assumption could be around 300 W/m²K. A_t between beds will be the key parameter to increase the heat transfer needed to sustain the calcinations reaction. Different options can be proposed to modify this area but a simple alternative to increase the calciner cross area consists in dividing the bed into a certain number of fins, thus increasing the area exposed to the combustor. Heat requirements in the calciner are estimated to be at least 30% of the energy input to the plant (for capture efficiencies higher than 80%) and therefore between 5-10 m² of metallic wall (per nominal Mw_{th} input to the plant) have to be allowed between combustor and calciner. The key parameter in the design of a fin for heat transfer is the effective thermal conductivity of the calciner, k (W/mK) that can be calculated from the expression:

$$k = D_{sr} C_{pe} \rho_e \quad (\text{A.7.1.2})$$

where C_{pe} and ρ_e are the calciner effective values of specific heat and density; D_{sr} is the solids lateral diffusion coefficient in the bed. There are several works studying solids mixing in lateral direction of fluidised beds but the equations describing this phenomenon predict values for the coefficient that can differ in more than one order of magnitude (Shi and Fan, 1984; Westphalen and Glicksman, 1995; Bi et al., 1995) and are not necessarily valid for the geometry of the proposed system, where more restrictions to the lateral movement of solids would exist as a result of the increase in bed external areas (fins).

Fluidisation experiments, with air, at room temperature have been carried out in a bi-dimensional fluidised bed reactor for the purpose of measuring the lateral solid diffusion coefficient in “finned” fluidised beds (see the right cold model in the right hand side of Figure A.7.1.1). The bed is a two-dimensional fluidized bed with a front-facing transparent window and a metallic back-plate (1.5 m wide, 2 m tall). A modification of an image analysis technique (applied by Abanades and Grasa 2001) has been adapted to this project making use of a long afterglow phosphor to coat the bed material. The experiments with these solids, that can emit light after activation by an UV source, are recorded and the images are translated to concentration profiles by calibration (Grasa et al. 2004). A commercial phosphor material had suitable properties for the application required in these experiments. The coated particles are limestone; the final mean particle diameter was 0.61 mm, particle density of 2700 kg/m³ and the minimum fluidisation velocity 0.27 m/s. These particles can be used inactivated as normal bed material or activated as tracer material so that there is no difference in fluidization properties when conducting tracer experiments (adding a batch of activated particles to a fluidised bed of non activated particles). The light emitted from the phosphor becomes undetectable after 1-2 h and the main solids can not be detected from the tracer and the solids can be used in a new experiment avoiding the tedious separation process.

After a calibration exercise, fluidizing different mixtures of activated and non activated solids, a linear correlation between activated tracer concentration and mean grey scale luminance in the images has been found (Grasa et al. 2004). The tracer concentration can be measured at any time from the following expression:

$$C_{FB} = \frac{I_{FB} - I_{min}}{I_{max} - I_{min}} \quad (\text{A.7.1.3})$$

Where I_{FB} is the luminance in the area of interest, I_{max} is the luminance of the fully activated solids and I_{min} is the luminance of the non-activated tracer. The bed was initially divided in two areas, non-activated solids are placed in one of them and the other one is filled with activated solids (20% mean tracer concentration in the bed). The bed was quickly fluidised with a pre-set air flow while it was recorded with a video camera. After the experiments a few

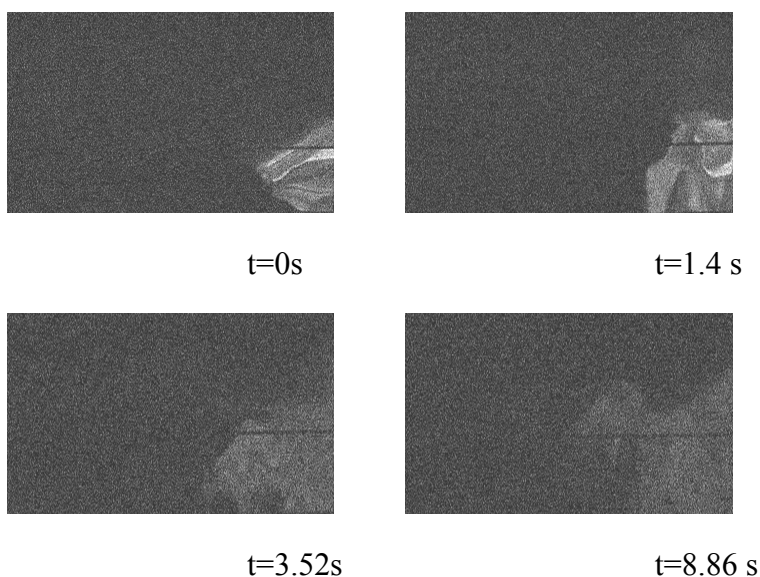


Figure A.7.1.2. Selection of images extracted from the fluidization experiments in a cold model of the calciner. $t = 0$ s, 1.4 s, 3.52 s and 8.86 s; $u_{gas} = 0.44$ m/s.

images per second were selected and tracer concentration maps vs. time were plotted after their analysis. Figure A.7.1.2 shows an example of images extracted from the experiments.

Experimental radial concentration profiles were extracted from the images and the solid Dispersion Model (DM), based on a diffusion law responsible of solids mixing in the bed, was used to fit them. There is only one adjustable parameter in this model, D_{sr} . This parameter can be calculated fitting the equation that solves the model:

$$C = \bar{C} + \frac{2}{\pi} \sum_{n=1}^{\infty} \frac{1}{n} \sin(n\pi\bar{C}) \cos(n\pi z) \exp(-n^2 \pi^2 D_{sr} t / L^2) \quad (\text{A.7.1.4})$$

The optimum dispersions coefficients, D_{sr} , ranged between $1.41 \cdot 10^{-3}$ and $1.24 \cdot 10^{-2}$ m²/s when fitting the individual experiments and as can be seen in Figure A.7.1.3 the concordance between the experimental concentration profiles and those predicted by the diffusion model is reasonably good

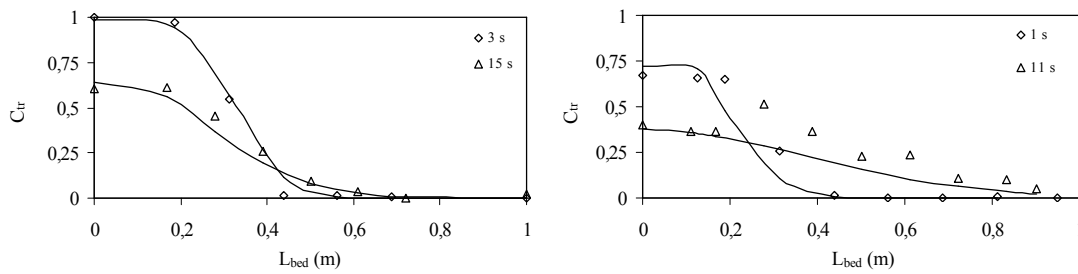


Figure A.7.1.3. Experimental and predicted concentration profiles for two different times. Experimental conditions: a) $u_{gas} = 0.44$ m/s; $D_{sr} = 3.57 \cdot 10^{-3}$; b) $u_{gas} = 1$ m/s; $D_{sr} = 1.24 \cdot 10^{-2}$.

Once it has been proved that the individual experiments fulfil the dispersion model and lateral solids mixing can be described by a dispersion coefficient, it is necessary to find a general equation capable of calculate them from operation conditions and bed and particle properties. Several equations have been found in literature (Werther et al. 1987, Shen et al. 1995, Kunni and Levenspiel 1969, Shi and Fan 1984). A good agreement was found with the equation proposed by Shi and Fan (1984) where the dispersion coefficients are calculated in terms of particle characteristics, properties of the fluidization medium and operating conditions.

$$D_{sr} = (u_{gas} - u_{mf}) h_{mf} 0.46 \left(\frac{(u - u_{mf}) d_p \rho_f}{\mu_f} \right)^{-0.21} \left(\frac{h_{mf}}{d_p} \right)^{0.24} \left(\frac{\rho_s - \rho_f}{\rho_f} \right)^{-0.43} \quad (\text{A.7.1.5})$$

Figure A.7.1.3 shows examples of the the comparison between the dispersion coefficients fitted from the experimental data and the coefficients calculated with equation (A.7.1.5).

As it can be seen, Shi & Fan (1984) equation is capable to represent solids mixing in narrow fluidised beds and is a useful tool to calculate the effective conductivity in the fins proposed for the design of the calciner. Estimated values for the effective fin conductivity calculated from equation A.7.1.5 at conditions characteristic of the fluidised bed calciner (gas velocity around 1 m/s, temperature higher than 900 ° C) yield effective k higher than 30000 (W/mK) for fluidised bed fins as narrow as 0.05 m.

In a fluidised fin there will be a temperature profile inside which will reduce the average temperature difference between beds (assumed to be 200K in early calculations). If there were strong temperature profiles, much larger exchange areas would be required to transfer the same amount of heat, and this could make the system totally impractical. To estimate these temperature profiles and confirm that they are moderate for the fin geometries expected in the system of A.7.1.1, the effective fin conductivity and heat transfer coefficient have been included in the one-dimensional equation for heat balance along the fin:

$$\frac{d}{dx} \left(-kA \frac{dT}{dx} \right) dl = Ph_w(T_c - T)dl \tag{A.7.1.6}$$

Boundary conditions:

$$X=0, T= T_b$$

$$X=d_2, -k \left(\frac{dT}{dx} \right)_{z=d_2} = h_w(T_c - T_{end}) \text{ convective end}$$

And solving this equation with the above boundary conditions, the temperature profile along a fin is:

$$\frac{T_c - T(l)}{T_c - T_b} = \frac{\cosh(m(d_2 - l)) + (h / mk)\sinh(m(d_2 - l))}{\cosh(md_2) + (h / mk)\sinh(md_2)} \tag{A.7.1.7}$$

Figure A.7.1.4 shows the ΔT between beds for a fin 2 m long and different fin thickness. As it can be seen, thinner fins will result in higher temperature profiles along the fin, reducing then the ΔT between combustor and calciner.

Fin geometries of 0.15 m thick and around 2 m long, could be a good configuration for the calciner, allowing to a good heat transfer rate between both fluidised beds and combining

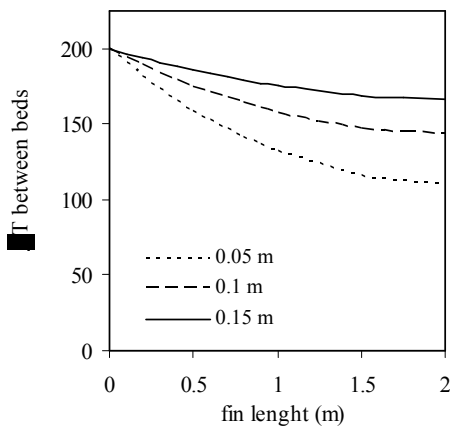


Figure A.7.1.4. Local ΔT between beds vs. fin length (for a 2 m long fin) for different fin thicknesses. Maximum ΔT between beds 200 °C.

enough area for heat transfer with low temperature profiles inside the fin and high average temperature difference between beds. As an example, for a power plant with 100 MW_{th}, 14 fins (2 m long, 0.15 m thick) would be needed to transfer 1/3 of the energy input (heat necessary to carry on the sorbent regeneration), assuming a 300 W/m²K, a 200 K delta T and a height of 10 m height of effective heat exchange between beds. The applicability of this system to the CaO/CaCO₃ cycle is therefore not restricted by fundamental heat transfer limitations but by material and construction issues due to the average high temperature required. The application of the concept of different sorption desorption cycles working at milder temperatures is discussed in Grasa et al (2005).

A.7.2 Work performed at Cranfield. Calcination in flame.

The need for a very reactive sorbent when the carbonation process is used in an entrained flow configuration makes it necessary to move away from the initial concept of carrying out calcination by indirect heat transfer. The quality of the calcined material, with a high specific surface area, depends mainly on the calcination rate. Different studies into the calcination of calcium-based sorbents show that short residence times at high temperatures are the most effective way to prepare the sorbent. The high temperature gives rapid calcination to oxide, providing the maximum surface area, while a short residence time ensures that sintering of the oxide is kept to a minimum. Specific surface areas for lime can vary from 40 m²/g in flash calcination to 18 m²/g when calcined in an oven. Moreover, specific surface area can be reduced in presence of CO₂ and H₂O as these gases encourage sintering. Also, steam will have another effect in flash calcination, as it can be used both to control and to reduce the temperature required in calciner reaction chamber to achieve the same quality of calcined sorbent. This modification will influence particle heating rates and thus in the particle texture developed.

The purpose of this task was to test the feasibility using a natural gas flame to prepare highly active CO₂ sorbent and to obtain data on the basic operating parameters. In order to gain a better understanding of the flash calcination process, the effect of temperature, particle size and CO₂ partial pressure were studied. Results obtained of this study are essential to determine the feasibility of applying flash calcination in a real plant.

In order to carry out this study, a pilot scale calciner was designed and built at Cranfield University. Figure A.7.2.1 shows schematically the design of the calciner. In this experimental device, particles are heated by means of a CH₄/O₂ flame. The reaction chamber has a length of 0.5 m and diameter of 0.10 m. Fresh limestone is fed from a hopper with a screw feeder and is then carried to an injector by a stream of CO₂ and O₂/Ar. The heat required for the calcination process is obtained by the combustion of CH₄ with O₂. Both gas flows were introduced into the reaction chamber through the injector, where they are mixed with the limestone/CO₂ stream. Inside the reactor chamber, there is a temperature profile determined by the CH₄/O₂ flame conditions. An average value of the temperature was determined measuring at two axial points in the reactor.

The calcination process takes place as the particles descend in the vertical reaction chamber. At the bottom of the calciner, a gas flow of N₂ is introduced in order to cool the particles and gases. Solids are removed from the gas stream using a cyclone situated at the end of the cool-down area. These solids were analyzed and characterised to determine the calcination efficiency and particle morphology. The calciner was designed to operate at different

temperatures; calcination experiments have been carried out at temperatures between 800 and 1000°C.

Steam is present in the reaction chamber during the experiments as it is produced during the combustion of CH₄. The effect of steam level on flash calcination was not studied in this work as modifications would be required to provide in the system. However, this variable will be taken into account.

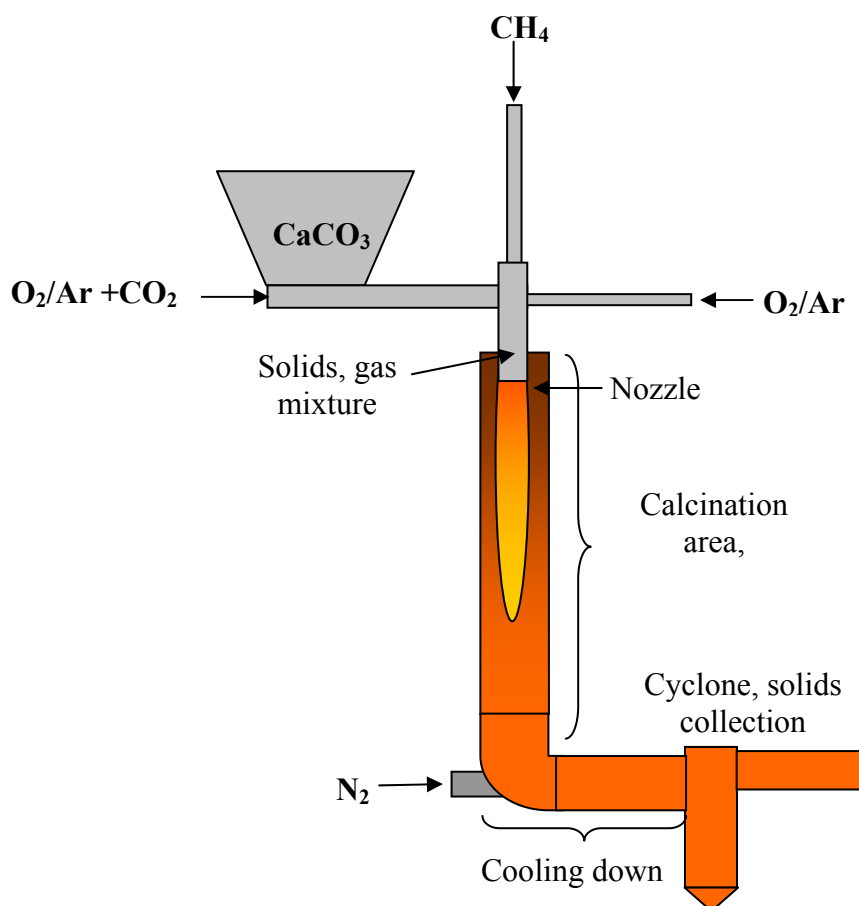


Figure A.7.2.1. Scheme of the calciner design for flash calcination of the solids.

A commercial limestone with 95.5 % CaCO₃ was used in these experiments. The original limestone was ground and sieved to prepare three particle size fractions: <100, 300-350 and 500-600 μm. The <100 μm fraction was the most homogeneous due to the nature of finer particles. For this reason the particle size distribution of this fraction was determined. The results obtained are presented in Figure A.7.2.2. As can be seen from this figure, the main part of this fraction has a particle size between 63 and 90 μm.

CO₂ partial pressure can be adjusted in the reactor by varying the CH₄, CO₂ and O₂/Ar flows. Three partial pressures were evaluated using different flow rates. The effect of feed rate on calcination process was not studied in this work and an average limestone feed rate of 10 g/min was used in all the experiments.

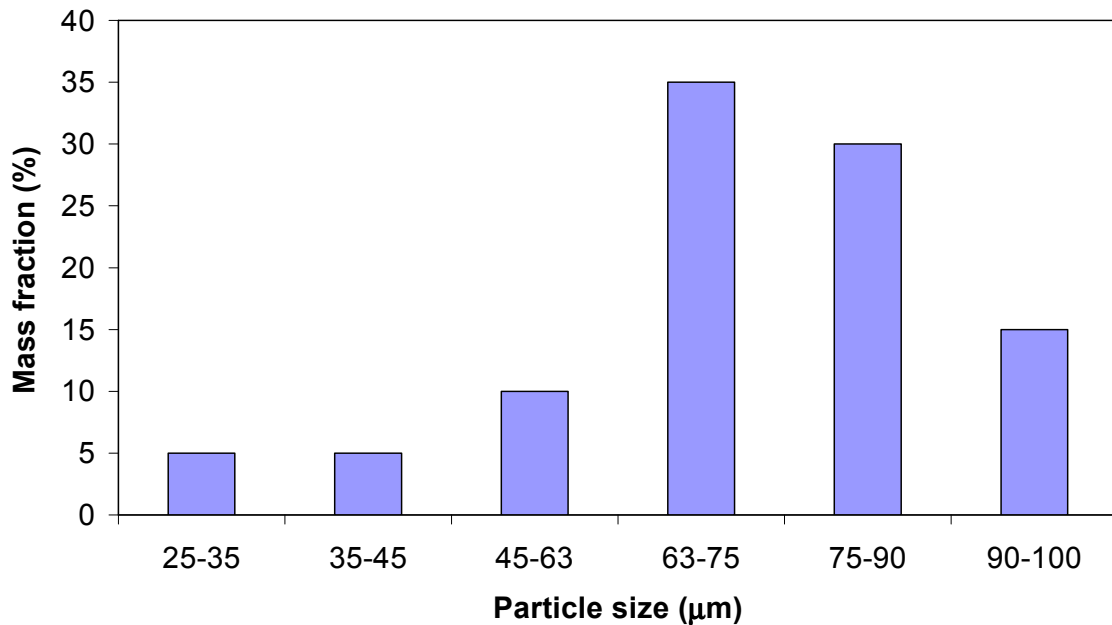


Figure A.7.2.2. Particle size distribution of fraction <100 μm

After each experiment, the calcination efficiency of calcined samples was calculated. If calcination efficiency, η , is defined as the percentage of the decomposed limestone, it can be expressed as:

$$\eta = \frac{1 - X_{CaCO_3c}}{1} \times 100$$

where X_{CaCO_3c} is the mass fraction of CaCO₃ in the calcined sample. The mass fraction of CaCO₃ is determined as the mass loss when the sample was subsequently heated at 900°C for 1h in air. Preliminary studies showed that these thermal conditions ensure a total decomposition of the remaining CaCO₃.

The morphology of samples was investigated using scanning electron microscopy in order to study of the extent of sintering in the CaO particles formed during the experiments.

The flows used and calcination efficiency obtained are summarised in Table A.7.2.1. The flows are expressed at 20°C and 1 atm.

During the experiments there were three sources of CO₂:

- the added CO₂ as a pure stream.
- CO₂ produced from CH₄ combustion.
- CO₂ produced from limestone decomposition.

The added CO₂ can be adjusted by altering the mass flow introduced into the calciner. The combustion CO₂ can be calculated assuming that the CH₄ is completely burned. This

Table A.7.2.1. Experimental flows and temperatures, calculated partial pressures and calcination efficiencies.

CH ₄ (L/min)	O ₂ /Ar (L/min)	CO ₂ (L/min)	N ₂ (L/min)	Air (L/min)	Temperature (°C)	CO ₂ partial pressure	H ₂ O partial pressure	Particle size (mm)	η (%)
2.1	20	7	1		850	0.35	0.14	<100	61.1
2.1	20	7	1		900	0.36	0.14	<100	83.5
2.1	20	7	1		950	0.37	0.14	<100	88.5
2.1	20	7	1		1000	0.37	0.14	<100	93.6
2.1	20	4	1		850	0.29	0.16	<100	77.9
2.1	20	4	1		900	0.30	0.16	<100	89.9
2.1	20	4	1		950	0.30	0.16	<100	93.0
2.1	20	4	1		1000	0.30	0.16	<100	93.8
2.1			1	35	800	0.10	0.11	<100	70.9
2.1			1	35	850	0.10	0.11	<100	81.4
2.1	20	7	1		850	0.30	0.14	300-350	0.0
2.1	20	7	1		900	0.31	0.14	300-350	9.1
2.1	20	7	1		950	0.31	0.14	300-350	13.2
2.1	20	7	1		1000	0.32	0.14	300-350	20.2
2.1			1	35	750	0.06	0.11	300-350	0.0
2.1			1	35	800	0.06	0.11	300-350	0.0
2.1			1	35	850	0.06	0.11	300-350	5.2
2.1			1	35	900	0.06	0.11	300-350	10.0
2.1	20	7	1		850	0.30	0.14	500-600	0.0
2.1	20	7	1		900	0.31	0.14	500-600	5.1
2.1	20	7	1		950	0.31	0.14	500-600	8.1
2.1	20	7	1		1000	0.31	0.14	500-600	10.2
2.1			1	35	750	0.06	0.11	500-600	0.0
2.1			1	35	800	0.06	0.11	500-600	0.0
2.1			1	35	850	0.06	0.11	500-600	3.0
2.1			1	35	900	0.06	0.11	500-600	7.2
2.1			1	35	950	0.06	0.11	500-600	10.5

assumption is reasonable as the excess oxygen is around 75% in all the experiments. The CO₂ generated during limestone decomposition can be calculated as the mass flow rate of solids is known and the percentage of decomposed limestone is determined in each experiment. This source of CO₂ has a relatively high importance in experiments where the calcination efficiency is high.

As was mentioned above, H₂O partial pressure in the system is produced during CH₄ combustion and it can be calculated assuming a complete CH₄ combustion. The calculated values are given in Table A.7.2.1. As can be seen, the H₂O partial pressure in the experiments performed varies in a small range between 0.11 and 0.16.

Calcination efficiency obtained at different temperatures using a CO₂ flow rate of 7 L/min is shown in Figure A.7.2.3 for the three particles size studied. This flow rate gives values of CO₂ partial pressures between 0.30 and 0.37. The effect of particle size can be seen as an important parameter in flash calcination process.

When the calciner was operated at 850°C, the 300-350 and 500-600 μm fractions do not decompose, and have a calcination efficiency of 0 %. However, under these experimental conditions the <100μm fraction reaches a value of 54 %. The difference between this fraction and the other two remains as the process temperature is increased. This difference indicates that in the reactor at Cranfield, flash calcination process is more suitable for particles of size less than 100 μm. When the process temperature is increased an improvement in calcination efficiency is observed in the three fractions studied. This increase is more significant between 850 and 900°C, especially for the <100 μm fraction. With a temperature of 1000°C, this fraction can reach a calcination efficiency of almost 94 %. This value is high enough to suggest that flash calcination is suitable for the production of CaO.

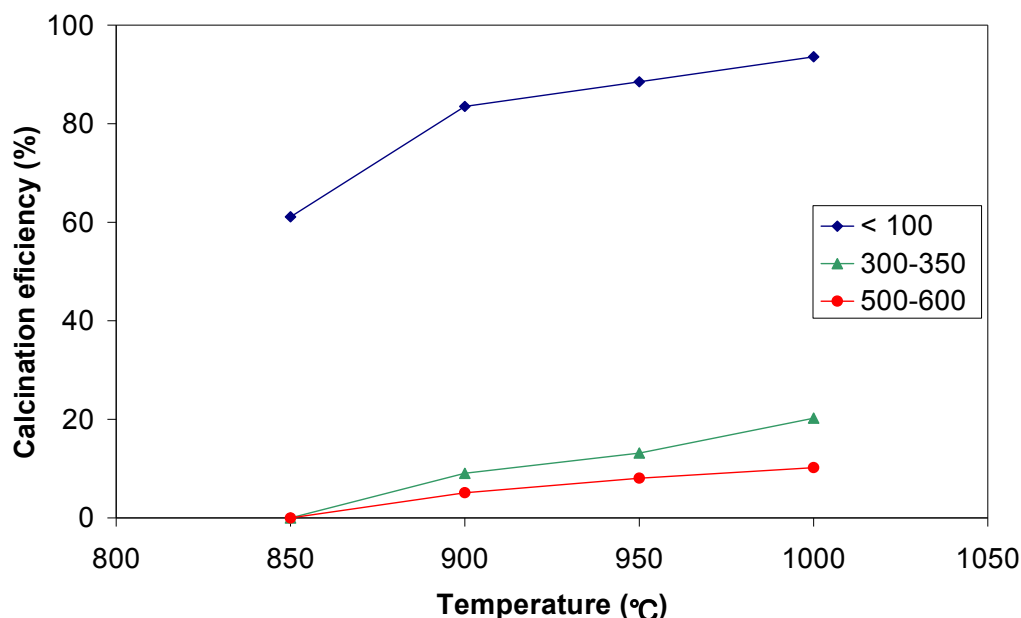


Figure A.7.2.3. Calcination efficiency of limestone at different temperatures.

The effect of CO₂ partial pressure was studied in this work by varying three sources of CO₂ in the calciner. Table A.7.2.2 shows flows of each source for the <100 μm fraction. In this table, flows are in l/min. Other fractions are not included in this work as their calcination efficiencies were too low and the CO₂ present is mainly from the added CO₂ and CH₄ combustion.

In the experiments where no CO₂ was added, limestone decomposition can generate almost 45 % of the CO₂ present in the calciner. However CO₂ is produced during limestone decomposition along the length of the reaction chamber. This fact implies that inside the calciner there will be a CO₂ partial pressure profile. Moreover CH₄ will contribute to this

profile. However, in order to discuss the results obtained, the average value of CO₂ partial pressure was calculated ignoring the partial pressure profile.

Table A.7.2.2. CO₂ sources during limestone calcination.

Temperature (°C)	Added CO ₂	CO ₂ from CH ₄ combustion	CO ₂ from limestone decomposition
850	7	2.1	1.4
900	7	2.1	1.9
950	7	2.1	2.0
1000	7	2.1	2.1
850	4	2.1	1.7
900	4	2.1	2.0
950	4	2.1	2.1
1000	4	2.1	2.1
800	0	2.1	1.6
850	0	2.1	1.8

Figure A.7.2.4 shows the calcination efficiency of the <100 μm fraction under the three CO₂ partial pressures studied in this work. As can be seen, CO₂ partial pressure has an important effect on the calcination of limestone. Average values of CO₂ partial pressure were used to represent the obtained values (0.36, 0.30 and 0.10). A reduction in calcination efficiency was observed as CO₂ partial pressure was increased. At low temperatures, especially under 900°C, calcination was strongly influenced by the CO₂ partial pressure. At 850°C, a difference of 17 % in calcination efficiency was observed between 0.31 and 0.38. This difference was smaller (3.5 %) when comparing the results obtained at 0.31 and 0.09. When temperature was increased, calcination efficiency seemed to converge to similar values under the three CO₂ partial pressure studied.

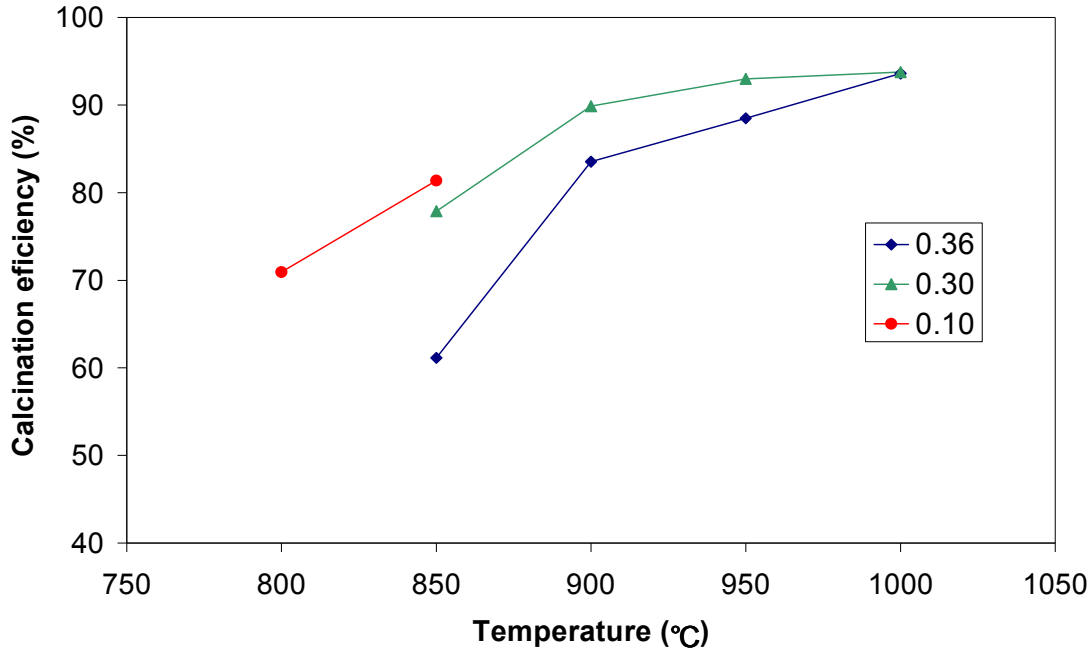
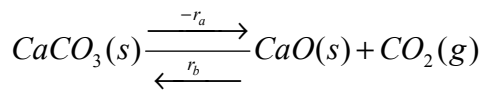


Figure A.7.2.4. Effect of CO₂ partial pressure in the calcination efficiency of 100 μm fraction.

The CO₂ partial pressure effect can be explained by looking at the thermodynamics of the system. The decomposition of limestone can be described using the following reversible reaction:



Assuming that rate of decomposition and composition are of first order and taking into account that partial pressure of solids is constant, the next equation can be obtained :

$$\frac{-r_a}{r_b} = \left(\frac{k_a p_{CaCO_3}}{k_b p_{CaO}} \right) \frac{1}{p_{CO_2}} = K_p \frac{1}{p_{CO_2}}$$

In this expression, K_p will depend exclusively on the temperature. From this equation, it can be deduced that an increase in the CO₂ partial pressure will favour the formation of CaCO₃, thus reducing the limestone decomposition

It is important to note that as temperature is increased in the calciner, the effect of CO₂ partial pressure is reduced. An industrial calciner will have to produce a stream of CO₂ of high concentration in order to be suitable in for CO₂ separation. This implies that the calcination process will have to take place under a high CO₂ partial pressure. Under these partial pressures, calcination temperature must to be high enough to ensure rapid limestone decomposition. In future experiments, higher CO₂ partial pressure will be used to study limestone decomposition under these conditions.

From the results obtained, rough guidelines for flash calcinations can be developed. The process has to use small particles size (less than 100 μm) in order to obtain high calcination

efficiencies. The calciner operation temperatures need to be high enough (more than 900-950 °C), especially when working with high values of CO₂ partial pressure.

Sintering of the oxide particles can present a problem in the performance of lime as a sorbent. As was mentioned, SEM images of fresh and calcined limestone were taken (see Figure A.7.2.5). Image 5a shows the spread of particle sizes in the <100 μm fraction. However, the calcined limestone (see Image 5b) shows higher uniformity in particle size. Moreover, it can be said that the mean particle size is smaller than in the fresh limestone. This fact can be due to the fragmentation of bigger particles during the thermal treatment. However the efficiency of the cyclone to collect the sample will also affect to the particle size distribution.

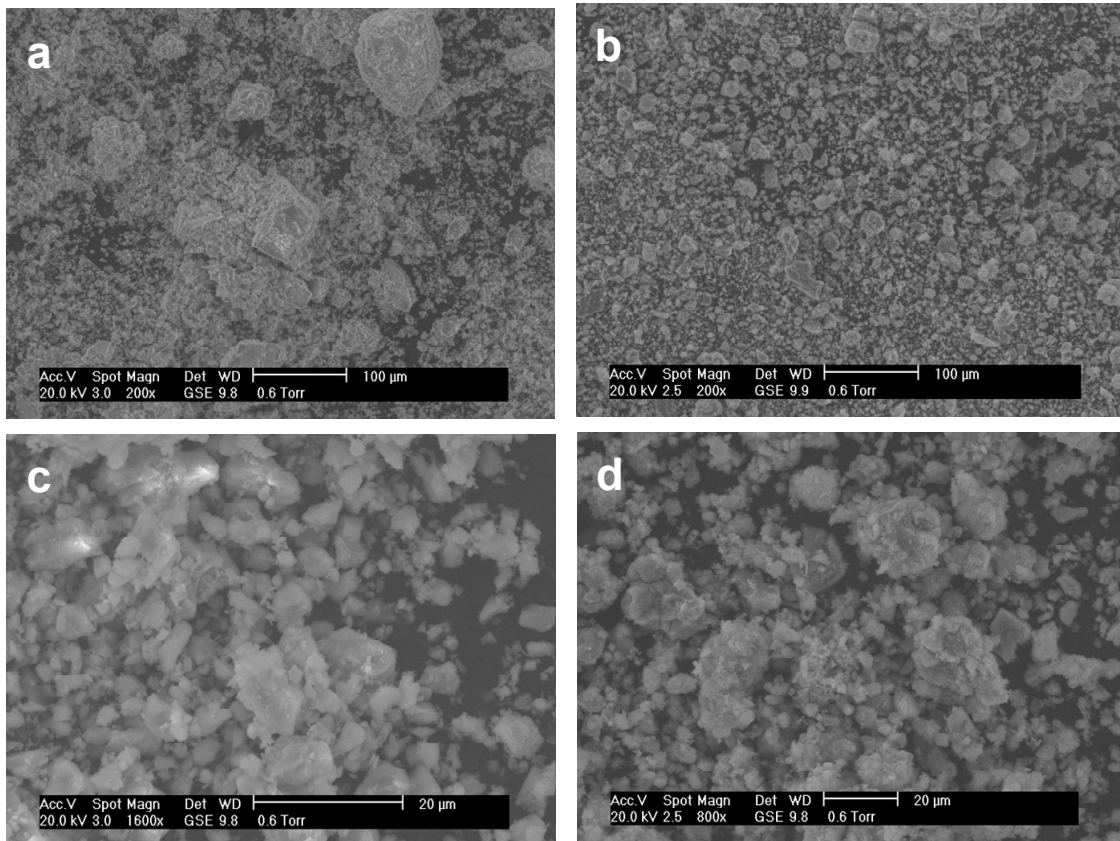


Figure A.7.2.5. SEM images of fresh limestone (a,c) and calcined limestone (b,d) of <100 μm fraction.

Images c and d show the fresh and calcined limestone in more detail. The fresh limestone is composed mainly by isolated particles. The image corresponding to the calcined material presents a similar morphology to fresh limestone, showing that under these calcination conditions the oxide does not sinter significantly.

A.8 Task 8. The development of basic reactor simulation tools.

This task included the application suitable reactor models to the key units in the LCCC system to capture CO₂: the fluidized bed carbonator and the entrained bed carbonator, where the CO₂ has to be captured by a solid stream of CaO coming from the calciner-regenerator unit. The modelling work includes the integration of suitable submodels for the gas-solid contact in the carbonators and for the sorbent performance (reactivity and maximum conversion capacity). The work under this task has mainly been carried out by CSIC. However, the key data for model validation has been supplied from sections A6 by Cranfield University, VTT and also most substantially, by the collaboration of CSIC with the CANMET Energy Technology Center, in Canada, which is active in this field from 2002.

A.8.1 Work performed at CSIC. Fluidized bed carbonator model.

Fluidized beds are the main choice for carbonator reactors to capture CO₂ with CaO (see section A9 and Abanades et al 2005). In fact, fluidized beds have already been used in practice to capture CO₂ with CaO, operating at high pressure in the Acceptor Gasification Process (Curran et al., 1967). We focus the next paragraphs on the progress understanding the fluidised bed carbonator common for most of the options considered in this project (all except in duct sorbent injection, described in section A8.2)

Supported by experiments in a pilot-scale fluidised bed reactor at CETC, we have modelled the capture of CO₂ in bubbling bed conditions by a bed of CaO. The experimental CO₂ concentration profiles measured inside the CETC's experiments were interpreted with the KL model (Kunii and Levenspiel, 1990) adapted within this project to the capture of CO₂ from a fluidised bed of CaO. In this model, the bed is assumed to be divided into two phases: a bubble and an emulsion phase. To estimate the bubble fraction, we adopt a value proportional to the extremes proposed by Kunii and Levenspiel (1990) for the bubbling regime for fine and large-sized particles:

$$\delta = \frac{u_0 - u_{mf}}{u_b + \frac{5u_{mf} - u_b \epsilon_{mf}}{4}} \quad \text{for} \quad 1 < \frac{u_b \epsilon_{mf}}{u_{mf}} < 5 \quad (\text{A.8.1.1})$$

The gas entering the bed splits between these two phases and a CO₂ exchange is allowed among them (Kunii and Levenspiel, 1990). The superficial gas velocity, u_0 , changes slightly because of the removal of CO₂ from the gas phase and, therefore, an average value is adopted in these equations. The emulsion is assumed at minimum fluidization conditions. The effective gas velocity through the gas phase, u_b^* , is defined from the gas balance in a cross section of the bed:

$$u_b^* = \frac{u_0 - (1 - \delta)u_{mf}}{\delta} \quad (\text{A.8.1.2})$$

It is assumed that no solids are contained in the bubble phase and, therefore, all solids in the bed are contained in the emulsion phase. For any time during the initiation of the experiment, the bed contains three types of solids: a fraction of active CaO reacting in the fast reaction

regime (f_a), a fraction of inactive CaO from previous carbonation-calcination cycles ($1-X_{b,N}$) and a fraction of CaCO₃ given by the carbonation conversion (X). Therefore:

$$f_a = X_{b,N} - X \quad (\text{A.8.1.3})$$

Knowing the fraction of CaO in the bed that is reacting in the fast reaction regime, f_a , allows the application of the KL model to estimate the CO₂ axial concentration profile. The KL model is formulated as a mass balance of CO₂ in the bubble and emulsion phases:

$$-u_b^* \frac{dC_{bcO_2}}{dz} = \gamma_b f_a K_r (C_{bcO_2} - C_{CO_2,eq}) + K_{be} (C_{bcO_2} - C_{eCO_2}) \quad (\text{A.8.1.4})$$

and

$$-(1-\delta)u_{mf} \frac{dC_{eCO_2}}{dz} = (1-\delta)(1-\epsilon_{mf})f_a K_r (C_{eCO_2} - C_{CO_2,eq}) - \delta K_{be} (C_{bcO_2} - C_{eCO_2}) \quad (\text{A.8.1.5})$$

The two critical parameters not yet defined in the previous equations are the reaction rate term, K_r , and the gas interchange coefficient between phases, K_{be} . Kunii and Levenspiel (1990) provide the following correlation for fluidized beds of the type used in this work (intermediate particle size):

$$K_{be} = 4.5 \frac{u_{mf}}{d_b} \quad (\text{A.8.1.6})$$

For the bubble diameter, the maximum bubble size $d_b = 0.1$ m has been adopted. Visual observation of the top surface of the bed gave evidence of “large” bubbles bursting there. Although the average value of d_b should be below this number, $d_b = 0.1$ is a conservative assumption that yields the lowest value of K_{be} . Furthermore, the sensitivity of the model to K_{be} under the conditions tested (relatively deep fluidized bed) is low, affecting only the concentration data taken from the port located 0.25m from the distributor, as will be seen below.

To define the reaction rate term K_r we assume that the carbonation rate is first order with respect to CO₂ and, including the resistance to the mass transfer of CO₂ towards the particle of CaO in the emulsion phase, we have:

$$K_r = \frac{1}{\frac{d_p}{6k_g} + \frac{1}{K_{ri}}} \quad (\text{A.8.1.7})$$

This requires the definition of the CO₂ mass transfer coefficient towards the carbonating particles, k_g , which is estimated here with the correlation of Turnbull and Davidson (1984) for the Sherwood number:

$$Sh = \frac{D_{CO_2}}{k_g d_p} = 2\epsilon_{mf} + 0.95 Re_{mf}^{0.5} Sc^{0.3} \quad (\text{A.8.1.8})$$

To define the reaction rate constant for the carbonation reaction of the particles, K_{ri} , we need to incorporate the key observations discussed in section A5. Therefore, we assume that $K_{ri} = 0$ after the particles reach the carbonation conversion limit, $X_{b,N}$, that is estimated for each experiment with equation (A.5.1.1). It is also assumed that, in the active part of the conversion curves (below $X_{b,N}$), the particle carbonates following the semi-empirical equation:

$$\frac{dX}{dt} = k_x X_{b,N} (1 - X)^{2/3} (C_{CO_2} - C_{CO_2,eq}) \quad (A.8.1.9)$$

This equation (except for the correcting term, $X_{b,N}$, to account for the decreasing fraction of active CaO as the number of cycles increases) was found by early studies reviewed by Bhatia and Perlmutter (1983). These authors also noted that equation A.8.1.9 is identical to the one obtained with the spherical grain model of Szekeley et al. (1976), consistent with our observations of the interior of the particles by SEM, if:

$$k_x = \frac{k_s S_0}{(1 - e_0)} \quad (A.8.1.10)$$

The rate constant in suitable units for the KL model can be rewritten as:

$$K_{ri} = k_s \frac{X_{b,N} S_0 \rho_{CaO}}{M_{CaO}} (1 - X)^{2/3} \quad (A.8.1.11)$$

We can adopt the reaction rate constant, k_s , as 5.95×10^{-10} m⁴/smol as measured by Bhatia and Perlmutter (1983) in conditions fully relevant for this work (temperature range between 673 and 998K and with CO₂ volume fractions between 0.1-0.42). For the surface areas of the fresh part of CaO of the calcines, values of $S_0 = 40$ m²/m³ and $e_0 = 0.5$ have been adopted for both limestones, yielding typical areas of 12 m²/g of active CaO, consistent with data from Bhatia and Perlmutter (1983) for similar calcination conditions. With all these data, the particles achieve their maximum conversion ($X_{b,N}$) in about 1 to 3 minutes. These times are in agreement with results reported by Bhatia and Perlmutter (1983), Silaban and Harrison (1995) or Shimizu et al. (1999) for the first calcination-carbonation cycle, and also agree with those obtained in section A5. Under these conditions, a fluidized bed with a sufficient amount of active CaO is a very effective CO₂ absorber, as became clear from the experimental results and in the model predictions shown below.

With the previous assumptions and correlation to estimate the different parameters in the KL model, the CO₂ concentration profiles inside the bed can be calculated and compared with the experimental results in the fluidised bed carbonator. Since the carbonation reaction is assumed to be first order, the analytical solution provided by Kunii and Levenspiel (1990) for equations (A.8.1.4) and (A.8.1.5) yields the CO₂ axial concentration profile in the fluidized bed as:

$$C_{CO_2,z} = C_{CO_2,eq} + \frac{(C_{CO_2,0} - C_{CO_2,eq})\delta}{(1 - \delta)u_o \Phi} \left[(1 - \Psi_2)(\Psi_1 \delta u_b^* + (1 - \delta)u_{mf})e^{-q_1 z} + (\Psi_1 - 1)(\Psi_2 \delta u_b^* + (1 - \delta)u_{mf})e^{-q_2 z} \right] \quad (A.8.1.12)$$

where

$$q_1, q_2 = \frac{1}{2} \frac{f_a K_r}{u_{mf}} \left[1 - \varepsilon_{mf} + \gamma_b \frac{u_{mf}}{u_b^*} \right] + \frac{1}{2} \frac{K_{be}}{u_{mf}} \left[\frac{\delta}{1 - \delta} + \frac{u_{mf}}{u_b^*} \mp \Phi \right] \quad (\text{A.8.1.13})$$

$$\Psi_1, \Psi_2 = \frac{1}{2} - \frac{1 - \delta}{2 \delta} \left[\frac{u_{mf}}{u_b^*} - \frac{f_a K_r}{K_{be}} (1 - \varepsilon_{mf} - \gamma_b \frac{u_{mf}}{u_b^*}) \mp \Phi \right] \quad (\text{A.8.1.14})$$

$$\Phi = \left[\left(\frac{f_a K_r}{K_{be}} (1 - \varepsilon_{mf} - \gamma_b \frac{u_{mf}}{u_b^*}) \right)^2 + \left(\frac{\delta}{1 - \delta} + \frac{u_{mf}}{u_b^*} \right)^2 + 2 \left(\frac{f_a K_r}{K_{be}} (1 - \varepsilon_{mf} - \gamma_b \frac{u_{mf}}{u_b^*}) \right) \left(\frac{\delta}{1 - \delta} - \frac{u_{mf}}{u_b^*} \right) \right]^{1/2} \quad (\text{A.8.1.15})$$

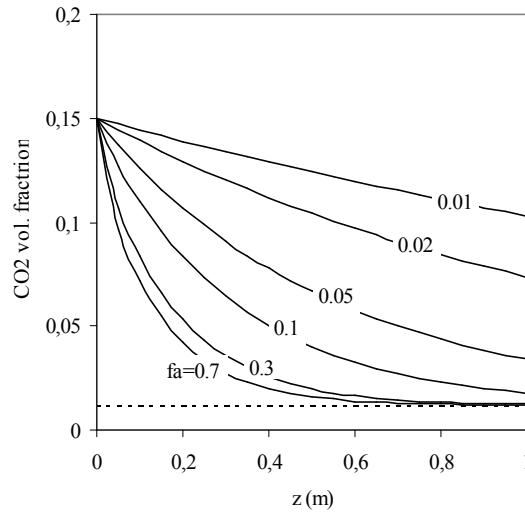


Figure A.8.1.1. Effect of the fraction of active CaO present in the bed on the axial CO₂ concentration profiles as predicted by the model under average carbonation conditions used during the experiments ($dp = 1\text{ mm}$, $u = 1\text{ m/s}$, $T = 650^\circ\text{C}$, $Wo = 5\text{ kg}$, 15 vol% CO₂ in the gas feed).

Figure A.8.1.1 presents an example of the CO₂ concentration profile in the fluidized bed carbonator calculated with equation A.8.1.11 and the auxiliary equations above, for conditions resembling those used during the experiments. As can be seen in this figure, the CO₂ concentration profiles are insensitive to values of f_a higher than 0.1. This corresponds to the early stages in the carbonation cycle during the experiments, where the emulsion phase is acting as a very effective sink for CO₂ and the overall carbonation process is controlled by the transfer of CO₂ from the bubble phase to the emulsion phase. With lower values of f_a , the concentration at the exit of the bed is appreciable and this corresponds to the beginning of the breakthrough curves.

Simulated breakthrough curves corresponding to the experimental can be estimated with the model by recalculating f_a as a function of time. This can be done by estimating the change of average carbonation conversion in the bed as:

$$X = \frac{M_{\text{CaCO}_3}}{W_0} \int_0^t Q_g (C_{\text{CO}_2,0} - C_{\text{CO}_2,\text{exit}}) dt \quad (\text{A.8.1.16})$$

The integration starts by calculating the concentration at the exit of the bed at the beginning of the experiment ($f_a = X_{b,N}$ for $t = 0$). This exercise was undertaken to produce the simulated CO₂ concentrations at the exit of the bed or at the bed heights of the gas sampling ports, that are included in Figure A.8.1.2 as continuous dotted lines. As can be seen in these figures, there is reasonable agreement with the experimental results, when considering the number of simplifications and assumptions adopted to build the fluidized bed carbonator model. It is important to emphasize that the sensitivity of these curves is low with respect to the assumptions and parameters adopted for the carbonation reaction rates at particle level, because the high reactivity of the fresh part of the CaO particles, at the conditions tested, is sufficiently large to guarantee a rapid change (both experimental and theoretical) in the CO₂ concentration at the exit of the bed in the proximity of the breakthrough conversion, $X_{b,N}$ (defined with empirical equation A.5.1.1).

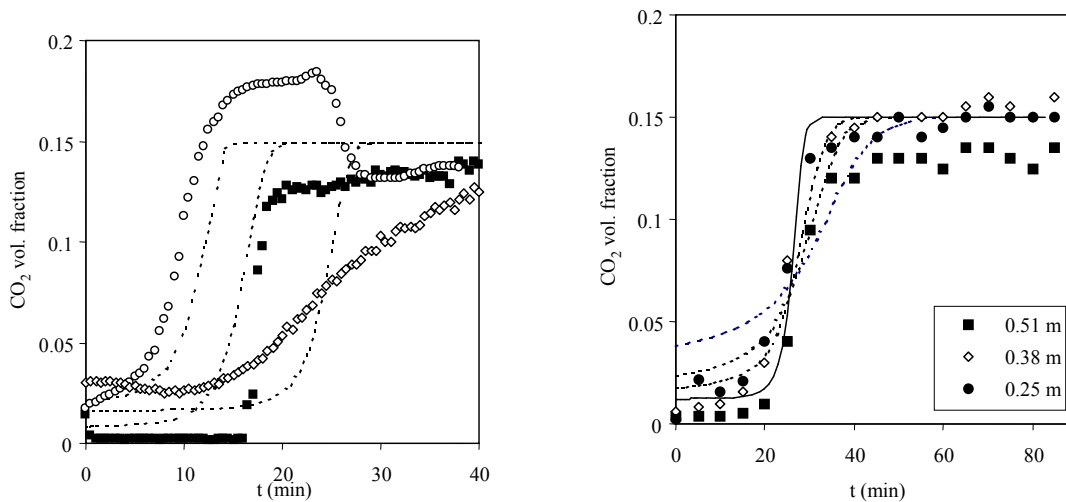


Figure A.8.1.2. Left: experimental CO₂ concentrations measured at three different bed heights during a carbonation experiment in a fluidized bed carbonator (Cadomin limestone, cycle 1, 650°C, and 15 vol% of CO₂). Right: measurements at the exit of the bed in three different carbonation cycles for Havelock limestone. Dotted lines correspond to model predictions at the exit of the bed.

The comparison between predicted and experimental CO₂ concentration data is poorer for the lower sampling ports in the fluidised bed (0.25 m above the distributor). While the model predicts significant concentration of CO₂ in the gas phase even at the beginning of the experiment (maximum f_a), all the experimental tests showed that, at the beginning of the carbonation period of each cycle, the bed was very effectively absorbing CO₂ even at this low sampling port. This discrepancy is due to the correlation adopted for the bubble-to-emulsion transport of CO₂, that seems to be too conservative for the actual bed conditions, since it does not allow more pronounced CO₂ concentration profiles even when this transport is the only resistance to progress of the carbonation reaction in the bed. It is, however, beyond the scope of this project to refine this correlation for the limited number of fluidized bed experiments conducted so far. It can also be noted that the breakthrough curves in Figure A.8.1.2 show good agreement on the expected breakthrough times but some differed from the model predictions in the shape of the CO₂ profile. As mentioned above, recarbonation in cooler parts

of the freeboard and some air leaks into the freeboard were detected in some carbonation tests. This explains why the intrinsic scattering of data seems higher in the experimental concentration of CO₂ measured at the exit of the riser than in that CO₂ concentration measured inside and just above the fluidized bed.

Finally, it is necessary to highlight that, from a practical point of view, the most interesting part of the experiments and the model simulations are those with low values of f_a . This is because, in continuous carbonation-calcination systems to separate CO₂, it will be a design objective to maximize utilization of the sorbent and minimize losses of active CaO. Therefore, the value of f_a in a continuous operation must be kept low. For low values of f_a , the sensitivity of the model to the reactivity of the sorbent arising from the calcination is much more pronounced. Under these conditions, the general bed characteristics (superficial gas velocities, bed temperature, bed heights, bubble behaviour, etc.) strongly affect performance of the fluidized bed carbonator in terms of CO₂ capture efficiency in the gas phase. Despite these remarks, and in view of the results obtained above, it has been shown that attractive operating conditions exist where a fluidized bed of free CaO is an effective absorber of CO₂ from a coal combustion flue gas at temperatures as high as 650C.

A.8.2. Work performed at Cranfield. In-duct sorbent injection modelling.

A.8.2.1. Entrained calcination model

Modelling has been carried out of the carbonation reaction in entrained flow contact mode. This model was applied to the laboratory scale entrained calciner designed at Cranfield University.

The model follows Kunni Levenspiel, with piston flow and the reaction controlled by kinetics (for small particles). Knowing the fraction of active CaO in the system, the K-L model can be applied to estimate the CO₂ concentration profile in the tube.

$$-u_{sl} \frac{dC_{CO_2}}{dz} = K_r (C_{CO_2} - C_{CO_2eq})$$

A critical parameter is the reaction rate K_r . It is assumed that the carbonation rate is first-order with respect to CO₂, and the resistance to the mass transfer of CO₂ towards the particle of CaO is included (Similar approach as in Abanades et al. 2004).

$$K_r = \frac{1}{\frac{d_p}{6k_g} + \frac{1}{K_{ri}}}$$

This requires the definition of the CO₂ mass-transfer coefficient toward the carbonating particles k_g , which is estimated through the Sherwood number. To calculate K_{ri} it is assumed that the particles convert to carbonate following the semi empirical equation:

$$\frac{dX}{dt} = k_x (1 - X)^{2/3} (C_{CO_2} - C_{CO_2eq})$$

This equation was found by early studies reviewed by Bathia and Perlmutter (1983); it has since been modified by Abanades and Alvarez (2003) to take into account the decay of maximum carbonation conversion after reusing the solids in carbonation/calcination cycles. For the purpose of these experiments fresh solids have been used in each carbonation experiment.

Converting the rate constant into different units:

$$Kri = k_s \frac{S_o \rho_{CaO}}{M_{CaO}} (1 - X)^{2/3}$$

Following the same principle as in Abanades et al. 2004, the reaction rate k_s can be taken as $5.95 \cdot 10^{-10} \text{ m}^4/\text{smol}$ as measured by Bhatia and Perlmutter (1983). For the surface area of the fresh CaO in the calcines, values of $S_o = 20 \text{ m}^2/\text{gr}$.

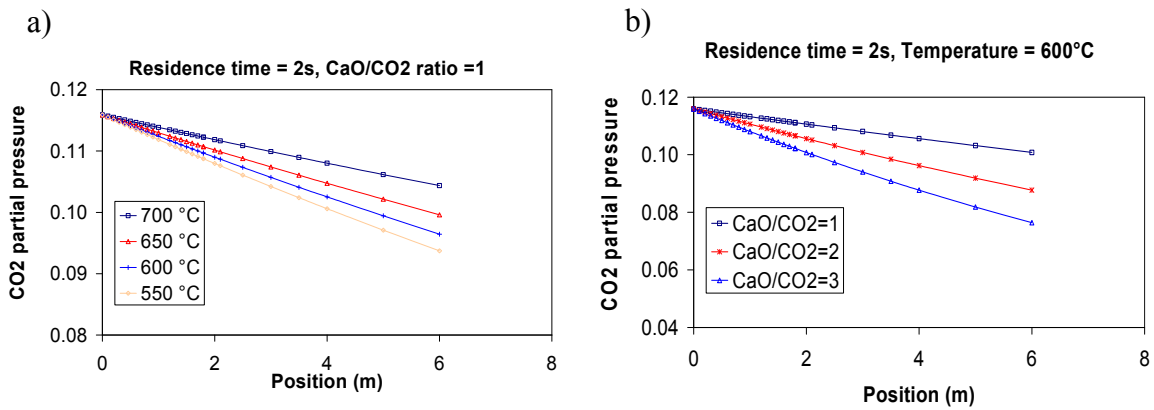


Figure A.8.2.1. Model predictions for different experimental conditions.

The applied model is able to predict CO₂ concentrations during the carbonation process. The model represents a useful tool to study the effects of different parameters on the carbonation process. In Figure A.8.2.1 the effect of the temperature and CaO/CO₂ ratio can be seen. These graphs were calculated using a gas flow of 8 L/min (20 °C, 1 atm) and lime flows of 2-4 g/min. As can be seen, the model predicts the effect of operating temperature on carbonation. As the temperature increases, the process loses efficiency and the resulting CO₂ concentrations are higher. Another important parameter in this process is the CaO/CO₂ ratio; its predicted effect can be seen in Figure A.8.2.1 (graph b). CO₂ levels are highly reduced as the CaO/CO₂ ratio increases.

The model and the values proposed for particle properties and kinetic parameters have been used to calculate CO₂ profiles along the gas path of the laboratory scale carbonation rig. These calculated values can be compared with those obtained in the experimental runs (see Task 6.2) in order to study the validity of the proposed model.

Table A.8.2.1 summarises the temperatures and flows used in the laboratory experiments. Moreover, experimental CO₂ concentrations and the predict values calculated with the model are also compiled in this table. As can be observed, the predicted CO₂ concentrations are close to the experimental ones; differences between values are less than 1 %.

Table A.8.2.1. Experimental flows and concentrations, and predicted values using the model for an entrained flow carbonation process.

T (°C)	Total Flow (l/min)	% CO ₂ (init)	% CO ₂ (after)	% CO ₂ (predicted)	Reduction (% exp.)	Reduction (% calc.)	CaO/CO ₂ (molar)	t _r (s)
626	5.28	14.22	10.35	9.46	27.2	33.5	1.30	2.81
612	4.11	8.96	6.33	5.67	29.4	36.7	1.62	3.37
599	7.77	11.59	8.96	9.43	22.7	18.6	1.08	1.97
599	8.20	11.59	9.88	9.63	14.7	16.9	1.02	1.87
587	5.09	10.81	7.25	6.60	32.9	38.9	1.77	3.05
587	6.37	9.42	5.71	6.52	39.4	30.8	1.89	2.43
587	5.98	10.04	7.10	6.24	29.3	37.8	2.16	2.59
586	8.31	11.43	8.96	9.57	21.7	16.3	0.85	1.87
581	5.46	10.19	7.41	6.61	27.3	35.1	1.47	2.89
541	7.78	12.21	9.58	9.71	21.6	20.5	0.85	2.11

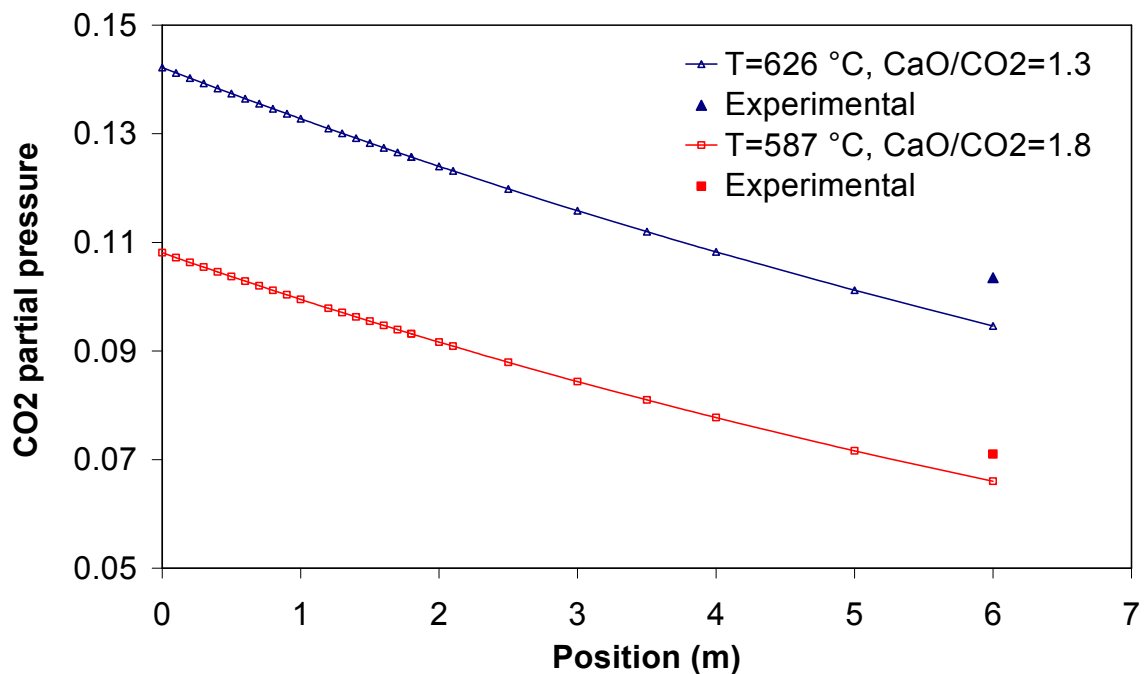
**Figure A.8.2.2.** Comparison between predicted and experimental values at a fixed residence time

Figure A.8.2.2 shows the comparison between the experimental and predicted results for a residence time of 2.8-3.1 seconds. The experimental and predicted values are in quite close agreement. The reduction of CO₂ emissions achieved at 587 °C is a 5% higher than at 626 °C. The effect of the different CaO/CO₂ ratio in these cases has to be taken into account when making the comparison. At 587 °C the ratio is higher, so the CO₂ reduction conditions are more favourable. The difference between CO₂ reduction in both conditions predicted with model is very similar to the difference obtained from the experiments.

Figure A.8.2.3 shows CO₂ concentrations of some experimental and calculated values obtained at a carbonation temperature of 587 °C, with different residence times and CaO/CO₂ ratios. The most unfavourable condition is the one plotted in red colour, as it has the lowest residence time and ratio. In these case calculated and experimental CO₂ reduction are in good agreement with a values of 16.3 and 21.7 respectively.

The other two results presented in Figure A.8.2.3 are quite close. One has a higher residence time (3.1 s) and a lower CaO/CO₂ ratio (1.8) than the other (2.6 s and 2.2 respectively). This shows that a the effect of a short residence time could be offset by increasing the loading of lime in the system.

Overall, the comparison between the experimental and model-derived results is good. Consequently, it is reasonable to use the model to investigate the effects of operating parameters.

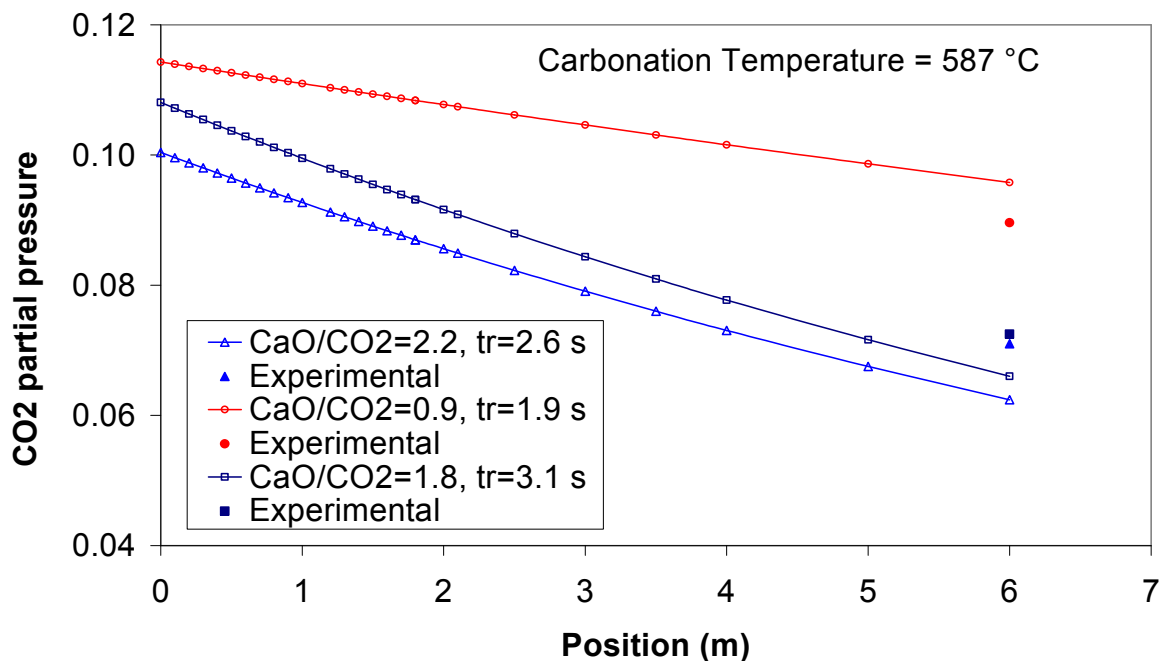


Figure A.8.2.3. Comparison between predicted and experimental values at different residence times and CaO/CO₂ ratios.

A.8.2.2. Assessment of Mass and Heat Flow balances in a Power Station with Lime Carbonation/Calcination Cycles

The option chosen as a case study in this work involves the injection of ultrafine lime in a section of the exhaust duct of an existing boiler. This approach is similar to the existing technologies for in-duct sorbent injection for SO₂ removal. The efficiencies will depend largely on the particle size and gas/particle contact times in the duct, and are expected to be

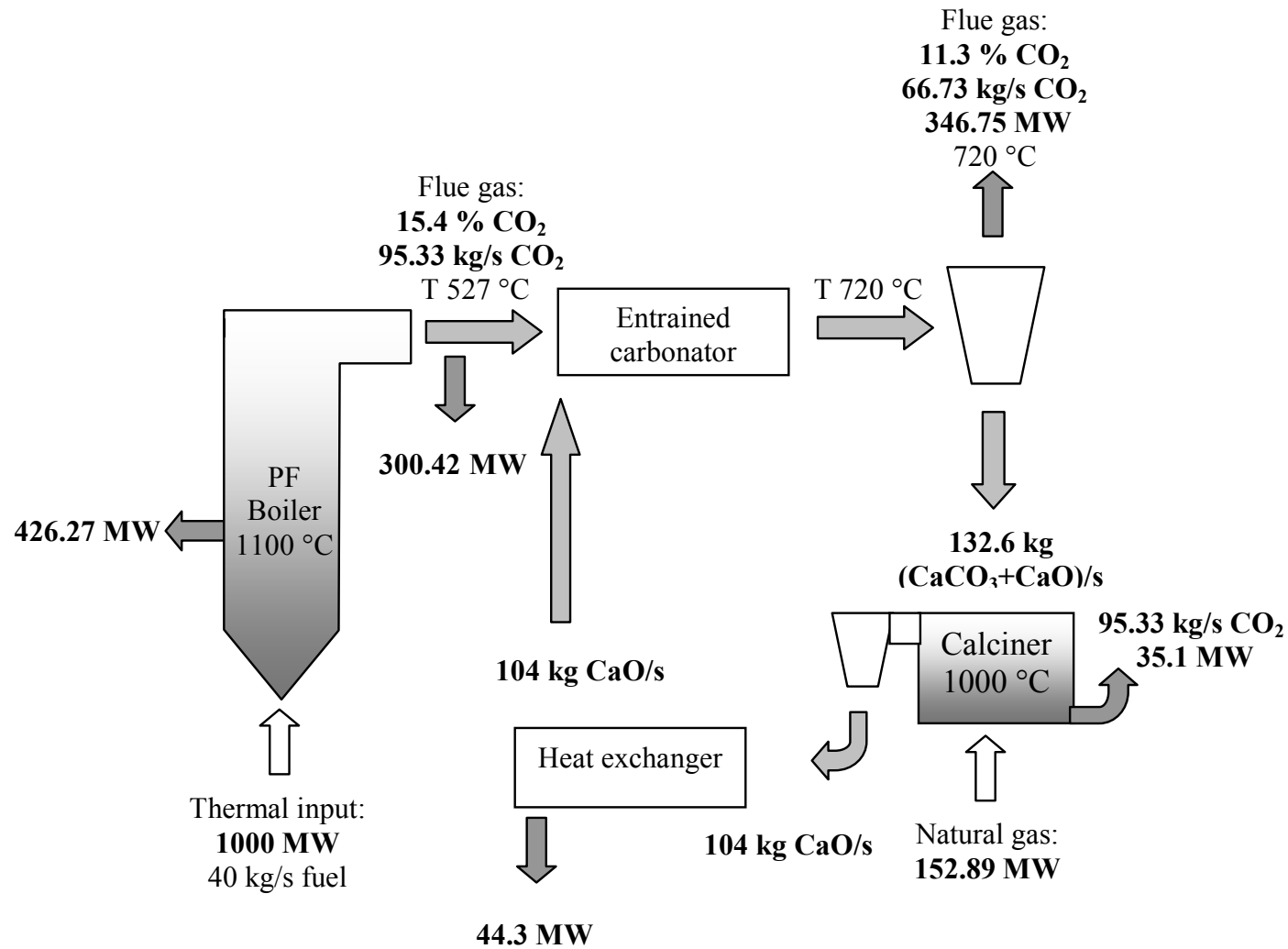


Fig. A.2.8.4. Scheme of the proposed carbonation/calcination cycle to capture CO₂ by in-duct sorbent injection.

lower than in other cycle configurations investigated in the project. However, the benefit of the entrained flow approach is the low capital costs necessary for the implementation of the carbonation stage of the cycle. Calcination can be carried out in CO₂/O₂ mixtures.

This option can be applied to any kind of boiler (pulverised fuel, fluidised bed...): the carbonation reaction takes place in entrained flow mode, in an exhaust duct of the boiler. The duct length and the volume of solids required depend on the carbonation reaction rate and the mean particle conversion achieved. Once the CO₂ content in the flue gas has been reduced, the carbonated solids are sent to the entrained flow calciner unit, where calcination can take place in a flame with an enriched O₂/CO₂ atmosphere at a temperature of around 1000 °C. The calcined solids are separated from the CO₂ stream leaving the calciner unit using a cyclone before being re-injected into the carbonator unit, after passing through a heat exchanger.

From the data obtained in the laboratory scale experiments the first model of the concept in terms of mass and heat balance in the cycle has been proposed. Figure A.8.2.4 shows the mass and heat balances for the proposed cycle for a 1000 MW thermal input boiler.

A typical coal with a lower heating value of 25 MJ/Kg was selected as fuel. The sulphur content and its effect on CO₂ capture was neglected in order to simplify this study. Excess air in the boiler was fixed at a value of 20 %. The expected gas composition at the exit of the boiler using these flows is showed in Table A.8.2.2. A mass flow of 95.3 kg/s of CO₂ exits from the boiler.

Table A.8.2.2. Gas composition at the exit of the boiler.

Gas	CO ₂	H ₂ O	O ₂	N ₂
Composition (% vol)	15.4	5.4	3.4	75.8

Carrying out a heat balance for the entrained flow calciner allows the gas temperature at the inlet to be calculated. This balance takes into account the heat generated in the calcination process and particle and gas flows through the calciner. From this balance, inlet and exit temperatures of 526 and 720 °C respectively were calculated. A lime flow of 104 kg/s in the calciner was calculated assuming a CO₂ retention efficiency of 0.3 and mean particle conversion according to the values obtained in the laboratory scale carbonation experiments describe in Task 6.2.

At the exit of the calciner, particles were removed from the flue gases. A solids mass flow of 132.6 kg/s was generated in the calciner. CO₂ concentration in flue gas will be reduced to a value of 11.3 %.

As indicated above, the calciner unit used to regenerate the limestone can be heated with a mixture of natural gas and oxygen. An approximate flow of 4 kg/s of CH₄ will be required to regenerate the limestone. In the calciner heat balance, a working temperature of 1000 °C was assumed. Products formed in the calciner will pass through a heat exchanger unit.

Table A.8.2.3 summarises the CO₂ flows and concentrations in the proposed process.

Table A.8.2.3. CO₂ flows and concentrations in the proposed lime carbonation/calcination cycle using an entrained flow carbonation approach.

	Flow (kg/s)	Concentration (%)
Exit of the boiler	95.3	15.4
Flue gases	66.7	11.3
CO ₂ captured (includes coal and CH ₄)	39.1	100

The results obtained in this case study will be used in further research to identify areas where improvements to the process may be made.

A.9 Task 9. Integration of components (CSIC and Cranfield)

This section presents an overview of the process options explored and studied in this project using lime carbonation calcinations cycles (LCCC), focusing on the “full system” ie integrating the key different units (coal combustor, carbonator and calciner) in a combustion system (for power and/or heat production) that delivers a pure stream of CO₂ suitable for storage. Figure A.9.1.1 summarizes the general scheme of a CO₂ carbonation/calcination cycle valid for all the options considered in this project. In the unit where the carbonation reaction takes place, a large molar flow of CO₂ (in the flue gas of a power plant), designated as F_{CO_2} , must contact a large molar flow of sorbent, F_R , to allow sufficiently high CO₂ capture. The remaining components of the carbonation/calcination loop, designated as F_{flue} and F_{inert} , will only be relevant to cycle heat balances, described later. The fuel split (y_{comb}) between the main combustor, where the fuel is fired with air, and the calciner, where the fuel is fired with O₂, will also be discussed below for each process case.

Hence, a mass balance on Figure csicLCCC19 provides a definition of the CO₂ capture efficiency in the carbonator as a function of the molar flows of CO₂ and sorbent entering the carbonator:

$$E_{carb} = \min\left(\frac{F_R X_{ave}}{F_{CO_2}}, E_{equil}\right) \tag{A.9.1.1}$$

For sufficiently large flows of sorbent, this capture efficiency is only limited by the maximum attainable recovery of CO₂, given by the equilibrium of CO₂ on CaO.

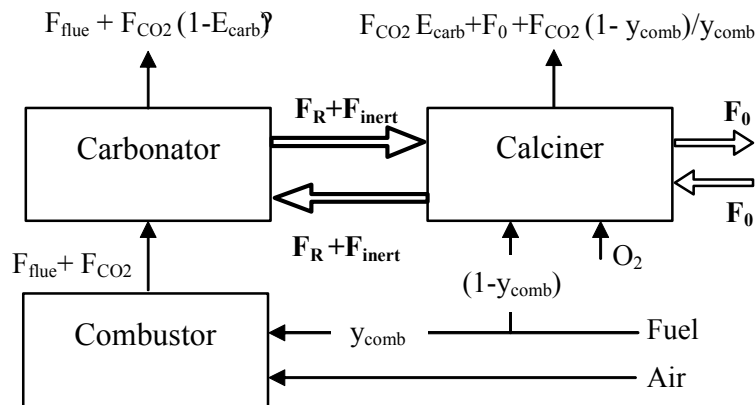


Figure A.9.1.1. General scheme and main mass flows in a CO₂ capture system using a lime carbonation/calcination cycle. LCCC.

The mass balance of Figure A.9.1.1 can be written to yield the fraction, rN , of sorbent (molecules, particles, or any other mass unit) that has gone through the sorption-desorption cycle exactly N times:

$$r_N = \frac{F_0 F_R^{N-1}}{(F_0 + F_R)^N} \quad (\text{A.9.1.2})$$

Therefore, the fraction of sorbent, S_N , that has been cycling in the sorption-desorption system at least N times is:

$$S_N = 1 - \sum_{N=1}^{\infty} r_N = \left(\frac{1}{\frac{F_0}{F_R} + 1} \right)^N \quad (\text{A.9.1.3})$$

For fluidized bed calciners (perfectly stirred reactors) the fraction of active CaO (X_{ave}) entering the carbonator to form CaCO₃ can be estimated combining the previous equation with equation A.5.1.1 (Abanades, 2002):

$$X_{ave} = \sum_{k=1}^{k=\infty} r_k X_k$$

yielding:

$$X_{ave} = \frac{f_m(1-f_w)F_0}{F_0 + F_R(1-f_m)} + f_w \quad (\text{A.9.1.4})$$

This is the design equation for the LCCC system, relating the sorbent performance parameters f_m and f_w with the sorbent flows in the systems required to achieve a given value of X_{ave} and hence E_{carb} . For the case of sorbent deactivation by CaSO₄ formation, a conservative assumption can be adopted considering the results of section A5, assuming that all sulphur present in the fuel reacts quantitatively with the active fraction of CaO:

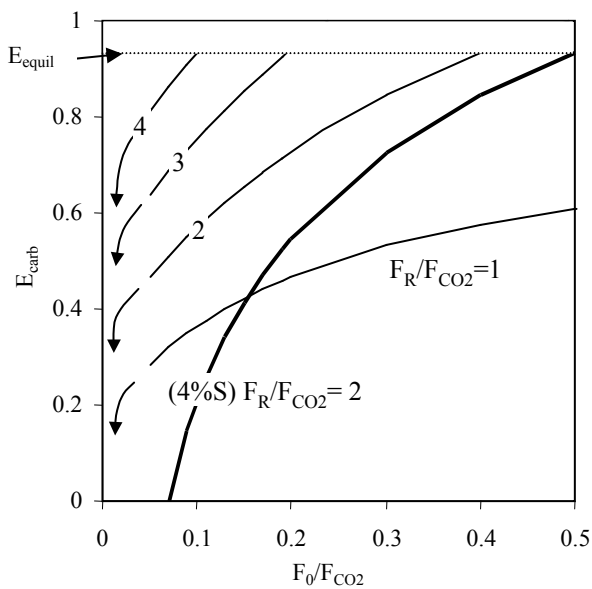
$$X_{ave} = \frac{f_m(1-f_w)F_0}{F_0 + F_R(1-f_m)} + f_w - \frac{F_{CO_2}}{F_0 r_{C/S} y_{comb}} \quad (\text{A.9.1.5})$$

where $r_{C/S}$ is the C/S mol ratio in the fuel. This equation considers the capture of all the sulfur contained in the fuel that is fed to the combustor and the calciner. If the fuel fed to the calciner for sorbent regeneration does not contain sulphur, the equation will have to be corrected deleting the term y_{comb} .

One of the last two equations can be combined with equation A.9.1.1 to estimate the attainable CO₂ capture efficiency in the carbonator for any given combination of critical sorbent flow ratios, F_{CO_2}/F_R and F_0/F_R . The critical assumption to carry out this exercise in the absence of detail reactor models of the individual units is to assume that the typical conversions of all the particles leaving the carbonator after a few minutes (1-5 minutes) of residence time will be around the value given by equation A.5.1.1. Despite the large solid circulation rates, fluidized beds can provide this order of residence times. As an example, we

note that the sorbent data available from the continuous pilot experiments carried out for the Acceptor Process (Curran et al 1967) was also well fitted with equation A.5.1.1 (see Abanades and Alvarez, 2003 and Figure A.5.1.4).

Figure A.9.1.2 illustrates the dependency of capture efficiency in the carbonator on the sorbent flow ratios. The left hand side of the figure has been left undefined since, at values of $F_0/F_{CO_2} < 0.05$, most sorbent particles in the system have experienced a number of cycles much higher than 50 and equation A.5.1.1 is valid to describe sorbent performance for $N < 50$. As seen in Figure A.9.1.2, the capture efficiency can be kept high (limited only by the equilibrium) despite the decay in sorbent activity, by increasing the fresh feed ratio (F_0/F_{CO_2}) and/or the sorbent/carbon ratio (F_R/F_{CO_2}). The problem is that these large ratios can become unacceptable in practice. This is because both F_0/F_{CO_2} and F_R/F_{CO_2} are referred to a large number (F_{CO_2} from a power plant is necessarily a very large number). Therefore, F_R/F_{CO_2} must be as close as possible to unity to minimize solid flows between units and maximize solid residence time in carbonators and calciners of any given size. The second ratio, F_0/F_{CO_2} , is the make-up flow of limestone and this has to be maintained as low as possible to minimize the operating costs associated with fresh sorbent addition to the plant and the energy requirements for its calcination. There is much scope to improve sorbent performance through reactivation, pretreatment or through the manufacture of completely synthetic CaO-based sorbents. This is an obvious subject for research in the future if these systems are to become of practical interest. However, since natural limestones are very cheap sorbents and their deactivated residue can find markets in the cement industry, higher values of F_0/F_{CO_2} may be economically feasible (see section A10). Also, as will discuss later, the deactivated CaO contains an important energy credit if used in cement manufacture.



	fuel analysis (as received, in wt %)		
	biomass	coal	pet coke
C	31	65	83
H	4	3	5
S	0	0	4
O	24	8	3
H ₂ O	40	8	5
Ash	1	16	0
Total	100	100	100
ΔH_{comb} (MJ/kg)	11.2	25	32

Table A.9.1.1. Composition of fuels used in the simulations

Figure A.9.1.2. Required flow ratios of sorbent (F_R and F_0) with respect to the flow of CO₂ (F_{CO_2}) to achieve a given CO₂ capture efficiency in the carbonator. Arrows indicate a region of uncertainty in sorbent performance (N beyond 50 cycles). The thin lines are valid for any fuel without sulphur and the thick solid line is for the case of the pet coke of Table A.9.1.1 (4% sulphur). Dotted line is the limit imposed by equilibrium at 650°C.

Further restrictions on sorbent flow ratios appear when the total heat requirements in the calciner are taken into account. In order to calcine the CaCO₃ contained in the solid stream ($F_R + F_{inert} + F_0$) of Figure A.9.1.2, we need to supply heat to bring to the calcination temperature all the solids circulating between both reactors as well as to drive the endothermic calcination of CaCO₃. The ratio between the necessary heat to calcine a mol of CaCO₃ sorbent in the stream ($F_R + F_{inert}$) and the heat input to the plant (heat generated in the combustion of a mol of CO₂) needs to be as low as possible. With highly deactivated sorbent (low X_{ave}) and/or working sorbents with high proportion of inert material, the heat requirements to bring these solids to the calcination temperature can become very important and even make the separation of CO₂ unfeasible with this approach.

Despite the previous limitations we have identified a range of technology options using natural limestones as such (as represented by equation A.5.1.1) to achieve the desired CO₂ separation with the chemical loop of Figure A.9.1.1, choosing values of F_0/F_{CO_2} and F_R/F_{CO_2} (see Table A.9.1.2) that allow good capture efficiency in the carbonator, maintaining under control the heat requirements in the calciner, as well as reasonable sorbent make-up flows.

Furthermore, any system following the scheme of Figure A.9.1.1 is capturing CO₂ not only in the carbonator but also in the calciner. Assuming 100% capture efficiency for the portion of the fuel burned with O₂ in the calciner and full calcination of the sorbent, we can define an overall CO₂ capture efficiency as:

$$E_0 = \frac{y_{comb} E_{carb} + (1 - y_{comb}) + \frac{F_0}{F_{CO_2}} y_{comb}}{1 + \frac{F_0}{F_{CO_2}} y_{comb}} \quad (\text{A.9.1.6})$$

In addition, the spent sorbent leaving the calciner (F_0) qualifies directly for a CO₂ credit as a substitute of CaCO₃ in the cement industry. If released, it eventually reacts with CO₂ in air to form CaCO₃. Therefore, higher capture efficiency can be claimed for these overall calcination/combustion systems as:

$$E_{sys} = y_{comb} E_{carb} + (1 - y_{comb}) + \frac{F_0}{F_{CO_2}} y_{comb} \quad (\text{A.9.1.7})$$

A range of process options is described below using all of these CO₂ capture efficiencies as well as the power generation efficiencies. These have focused to fluidised bed combustion system as they have been shown in previous sections to provide the highest levels of carbonation efficiencies. All simulations have been performed for a 100 MW thermal power plant delivering the CO₂ compressed at 10 MPa (suitable for storage in geological formations). The composition of the fuels considered in this study is given in Table A.9.1.1. An overall CO₂ capture efficiency, E_0 , of 90% of the carbon contained in the fuel has been assumed for all fossil fuel options. The reference combustion power plant without CO₂ capture is assumed to have 46% LHV power generation efficiency. Power losses for CO₂ compression and, where relevant, vacuum, air separation and steam generation have been estimated with ASPEN Plus (η_{1to4}) with the aid of colleagues from CANMET (Canada). More details of this collaboration can be found in Abanades et al, 2005. Table A.9.1.2 also includes the calcination heat (η_5) of the make up flow of fresh sorbent. A fraction of this heat is a

power loss in estimating power generation efficiencies (η_{pow}). However, this heat could be claimed as an energy credit if the sorbent was used in a cement plant as a feedstock substitute for CaCO₃. Although this number cannot be added directly to the power generation efficiency it is obviously an added source of efficiency for the overall power/cement production plant emerging in some of the following discussions. The energy penalty for a combined system power-cement plant is therefore very low, and unaffected by moderately large values of F_0/F_{CO_2} . Finally, table A.9.1.2 also includes in the right hand column a case where all coal is burned in a FBC with O₂ only that qualitatively agrees with the study by Shimizu *et al.* (1999).

Table A.9.1.2. Mass and heat flows for the different options. Base-case of 100 MWt using calcined limestone as CO₂ sorbent that decays in activity following equation A.5.1.1. Electricity generation efficiency is $\eta_{\text{ref}}=0.46\text{LHV}$ (also for heat outputs at $T \geq 650^\circ\text{C}$).

	A	B	C	D	E	O ₂ /CO ₂
Fuel	Coal	Coal	Coal	Biomass	Pet Coke	Coal
Fuel feed (kg/s)	4.0	4.0	4.0	Biomass	Pet Coke	4.0
y_{comb}	0.67	1	1	0.682(C)	0.66	-
Air in (Nm ³ /s)	20.3	30.3	30.3	22	21.6	-
O ₂ in (Nm ³ /s)	1.81	0	0	1.7	2.02	5.3
T combustion (°C)	850	1050	1050	700	850	850
P combustion (bar)	1	1	1	1	10	1
F_{CO_2} in kmol/s	0.145	0.216	0.216	0.157	0.143	0.216
F_{CO_2}/F_R	1/3	1/4	1/4	1/3	1/4	-
F_0/F_{CO_2}	0.1	0.15	0.15	0.1	0.3	0
Make up flow (kg limestone/kg fuel)	0.541	0.813	0.813	0.176	1.37	0
T carbonation (°C)	650	650	650	700	850	-
P carbonation (bar)	1	1	1	1	10	-
T calcination (°C)	950	850	850	950	1080	-
P calciner (bar)	1	1 (60% steam)	0.4 (vacuum)	1	10	-
X_{ave}	0.251	0.188	0.188	0.202	0.137	0
X_{sulf}	0	0	0	0	0.091	-
E_{carb}	0.753	0.752	0.752	0.607	0.549	-
E_{CO_2}	0.845	0.784	0.784	0.749	0.752	-
E_0	0.9	0.9	0.9	0.8*	0.9	-
Hcal (MW)	33	48.2	48.2	28.8	34	0
Calciner penalty, η_1	0.0317	-	-	0.0208	0.0353	0.0928
Calciner penalty, η_2	-	0.0113	-	-	-	-
Calciner penalty, η_3	-	-	0.0055	-	-	-
Compress. penalty, η_4	0.0285	0.028	0.028	0.0267	0.0125	0.0312
Makeup calcination, η_5	0.0258	0.0579	0.0579	0.028	0.0762	0
penalty (-) credit (+), η_{pow} **	0.388	0.394	0.400	0.400	0.377	0.336

* This is captured from the biomass plant (CO₂ neutral) and is therefore associated with a “negative CO₂” emission.

** This is calculated as $\eta_{\text{pow}} = 0.46 (1 - \eta_5) - \eta_1 - \eta_2 - \eta_3 - \eta_4$

The systems analysed and included in Table A.9.1.2 are indicated below:

Case A. Coal-based power plant of any type incorporating a CaO-based CO₂ absorber in the form of a circulating fluidized bed carbonator (Figure A.9.1.3). Regeneration of CaCO₃ with O₂/CO₂ mixture occurs in a fluidized bed. Shimizu *et al.* (1999) described in detail this option and simulated overall system performance. However, these authors overestimated sorbent performance by ignoring the decay in sorbent activity after only four carbonation/calcination cycles. We have, therefore, run a simulation of the process with

make-up flow of fresh limestone of 0.542 kg per kg of coal (see Table A.9.1.2). The generation efficiency is predicted to be 38.8%. The main sources of efficiency penalty are compression of CO₂ and the necessary power for O₂ generation (about 1/3 of the fuel is burned with O₂ in the calciner).

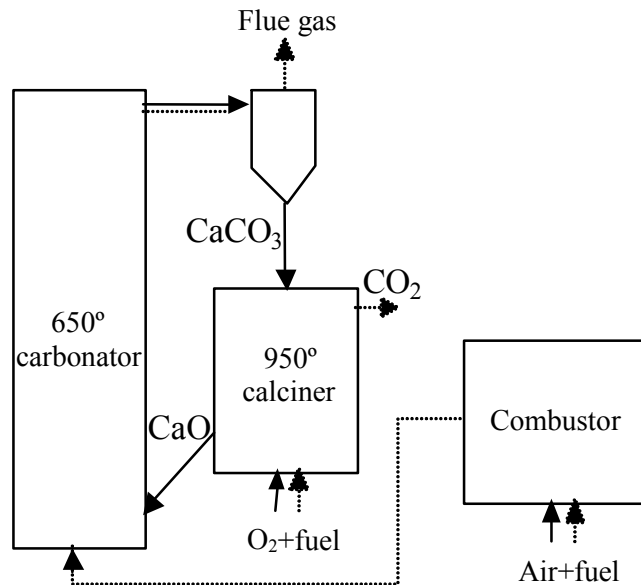


Figure A.9.1.3. Process scheme of Case A, with the carbonation/calcination cycle separated from the combustor chamber. This is an option for both existing and new power plant concepts.

Case B. Fluidized bed coal-based power plant following the scheme of Figure A.7.1.1, with a high temperature circulating fluidized bed combustor ($T = 1050^{\circ}\text{C}$) transferring heat through metallic walls to a fluidized bed calciner ($T = 850^{\circ}\text{C}$) operating at a CO₂ partial pressure of 0.4 bar obtained in the calciner by injecting steam (5.28kg/s). Solids in the calciner are fluidized with a mixture of steam and the CO₂ generated during calcination. The carbonator operates at 650°C after cooling the gases coming from the combustor. Heat requirements in the calciner are estimated to be around 48% of the energy input to the plant. Assuming an overall heat transfer coefficient between the two beds of 300 W/m²K (see section A6), an area of approximately 800 m² of metallic wall needs to be provided for transfer of the necessary heat between combustor and calciner. This area will require a special configuration of combustor and calciner cross-sections to closely integrate both units (typically 20-40 m high and almost 30 m² cross-section for the 100 Mw_t base-case, when assuming a gas velocity of around 5 m/s). These configurations require special metallic materials that have not yet been tested in practice for similar applications. It is therefore, not clear if these systems will be more feasible than the system of Case A despite their higher efficiency and the lack of air separation unit. However, it should always be possible to take

advantage, at least to some extent, of the potential for direct heat transfer from combustor to calciner as outlined in Figure A.7.1.1.

Case C. This is a system (Figure A.9.1.4) with identical process conditions to Case B except in two variations: heat transfer is attempted using a solid heat carrier and the low CO₂ partial pressure of 0.4 atm, required for lower calcination temperature in the calciner, is attempted through application of vacuum (alternatively, this could be done with steam as in case B). For the case studied, a heat carrier flow of 226 kg/s is required to transfer the heat required for calcination from the combustor to the calciner. This large circulation rate of hot solids from the combustor is still reasonable (below 10 kg/m²s) compared to standard practice in circulating fluidized bed combustors. Calcination of the sorbent will take place in contact with these hot solid stream. The heat carrier can be CaO (calcined sorbent) identical to the sorbent circulating in the carbonation/calcination loop although its activity might tend to deteriorate in the high-temperature conditions in the CFBC. However, we can also use highly sintered and dense CaO particles in the combustor/calciner loop or a completely different dense solid heat carrier (for instance Al₂O₃). In this case, the intention is to make use of the different particle density of the active sorbent particles (approximately 1500 kg/m³) and of the heat carrier (higher than 3000 kg/m³). Continuous segregation of the solids should be possible to achieve partial separation in a continuous mode. A similar segregation mechanism was used successfully to separate heavy ashes from the sorbent in the pilot plant used for the development of the Acceptor Gasification Process (Curran et al 1967). However, it has never been tested at the scale required for this application. Therefore, as in Case B, it is not yet clear if the complexities associated with the operation of the calciner of Figure csicLCCC22 will compensate for the savings arising from the lack of O₂ separation plant and the improved values of generation efficiencies (see Table A.9.1.2).

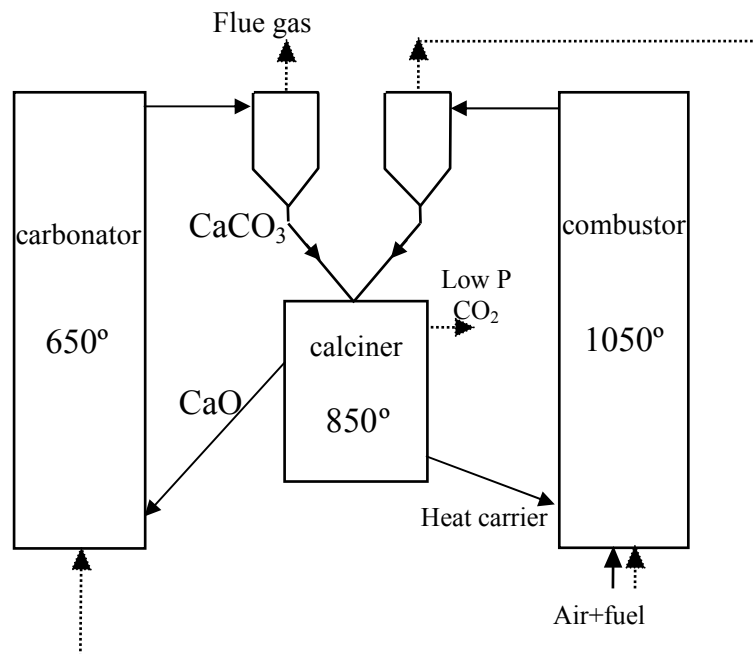


Figure A.9.1.4. Process scheme of Case C, with indirect heat transfer from the combustor to the calciner by means of a dense solid heat carrier (like sintered CaO or Al₂O₃)

Case D. *In situ* capture of CO₂ with CaO in a low temperature fluidized bed combustor. According to the CaO/CaCO₃ equilibrium, if a fuel could be burned at sufficiently low temperature (about 700°C) it would be possible to capture, *in situ*, the CO₂ generated in the combustion. Biomass is a potentially attractive fuel for this application because the synergies with coal can make it competitive in large scale (coprocessing). Furthermore, the idea of capturing CO₂ from biomass-fired systems is receiving increasing attention (Williams et al, 1996) since it can offer a route to power plants with negative emission factors (*i.e.*, a net CO₂ sink). This is because the burning of biomass without CO₂ capture is considered CO₂-neutral and, therefore, any capture and storage of CO₂ from biomass will translate into a net sink of CO₂ from the atmosphere. The scale of biomass power plants is, however, always limited and we have assumed that the plant of reference in Table A.9.1.2 is close to an existing coal power plant based. In the selected case, approximately 68% of the C content of the biomass is fed to a fluidized bed combustor operating at 700°C where a capture of around 60% of the CO₂ generated in the FBC is achieved. The unburned C is burned in the calciner. Flue gas, with a reduced amount of CO₂, and which might also contain CO, tar and unburned C, is fed to the existing power plant in a manner that these compounds are fully oxidized and the heat is recovered in the equipment of the existing boiler. As a result, the heat required for regeneration in the calciner, which accounts for 28.8% of the total heat, comes from the unburned char accompanying the carbonated sorbent leaving the carbonator. More coal from the main combustor might also be used to supply heat to the calciner. An interesting point of this Case is that it can be used as a retrofitting option to existing plants, to reduce CO₂ emissions while increasing the energy output of the plant. Therefore, it can also facilitate a strategic move from large emission factors in an existing coal combustion plants to negative emission factors in the future when/if the plant can be fully sustained by biomass. The scheme is similar to the one of Figure A.9.1.5 but with the operating conditions (atmospheric pressure) in the carbonator and calciner indicated in the previous paragraph

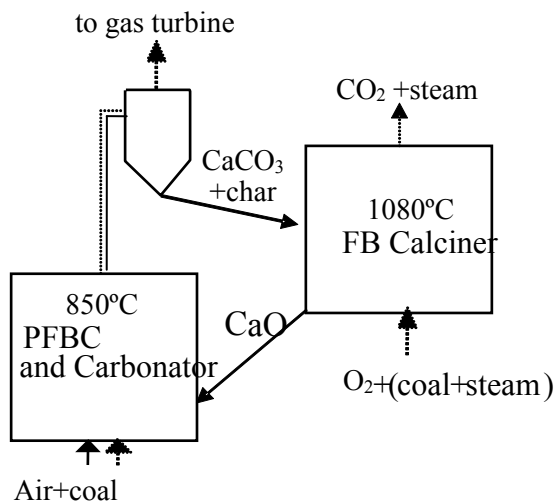


Figure A.9.1.5. Process scheme of Case E, with coal burned in high pressure fluidized bed combustor and CO₂ generated from combustion with oxygen in the fluidized bed calciner. The scheme is identical for option D (low pressure), changing the fuels and the temperatures as indicated in Table A.9.1.2.

Case E. In situ capture of CO₂ at high pressures and temperatures. This is similar scheme to Case D above, but applied to high-pressure (10 bar) and high-temperature (850°C) fluidized bed combustor and calciner. The simulation has been run for pet coke, with no ashes but high sulphur content. The details of this system have been published in collaboration with CANMET (Abanades et al 2002, Wang et al 2003) including the full ASPEN simulation sheet for pet coke cases and antracites. As in Case D, the key benefit is high levels of system integration, since combustion, CO₂ capture and SO₂ capture are all achieved in a single pressurized fluidized bed reactor. The high sulphur content in the fuel makes necessary a large supply of fresh sorbent to maintain the activity of the CO₂ capture loop, in accordance with equation A.9.1.5. This has reduced the power generation efficiency respect to other cases (37.7%LHV), but the energy and carbon credits associated with the large flow of deactivated sorbent leaving the plant (mainly CaO) should also be considered.

From the results of Table A.9.1.2, we can conclude that CO₂ capture concepts based on the carbonation/calcination cycles of CaO described above have inherent advantages, because the efficiency penalties associated with separation of CO₂ are intrinsically low. The system uses a low-cost, widely available CO₂ sorbent to compensate for its activity decay (see section A10 for details). In some cases (A and D) the individual units are commercially proven and/or there exist similar large-scale commercial processes operating in similar conditions. In the remaining cases (B,C, E) the challenge is to demonstrate novel reactor concepts that offer substantial gains in efficiency and/or avoid the air separation unit. No hazardous materials are involved in the new processes. The concepts can, in principle, be applied to CO₂ capture from the combustion of several fuel types, from fossil fuels and petroleum residues to biomass and waste. Sulfur capture is expected to be very effective in the system. However, a successful CO₂ capture system is that which can deliver CO₂ at the lowest possible cost, when all factors are properly considered in the definition of that cost. Clearly, for some of the process alternatives outlined in this work, several uncertainties need to be addressed before carrying out an economic comparison with existing CO₂ capture processes or other novel concepts currently under development.

A.10 Task 10. Economical assessment.

One of the weakest points of any LCCC system is the poor sorbent performance that translates into the need of a very large supply of fresh sorbent to keep the activity in the carbonation-calcination loop (see Figure A.9.1.1). This may translate into high operating cost associated to the purchase of this sorbent and the disposal of the deactivated residue. But it is important to put this in context with what is the situation (in terms of the same cost-component, i.e. the cost of the make up flow of sorbent) with other similar sorption-desorption systems. All CO₂ capture systems incur in additional cost respect to a similar system without capture. CO₂ capture systems are in a class by themselves because the mass flows of sorbent circulating in systems like those being developed in this project must be very large, to match (at least) the large molar flow of CO₂ (or O₂) being processed in the power plant. Figure A.9.1.1 presented a general diagram that could be also valid for many CO₂ capture systems (including CLC if O₂ is written instead of CO₂). In all cases, there is a molar flow of CO₂ (F_{CO_2}) to be captured, a sorbent flow circulating between the capture-regeneration loop (F_R) and a sorbent makeup flow (F_0). It must be emphasized that this make up flow is, to some extent, always unavoidable, due to a wide range of chemical and physical interactions of the sorbent inside the reactors and transport lines and the sorbent losses associated with gases leaving the system.

The cost of CO₂ capture is the sum of several terms encompassing the large capital costs associated to the capture plant, the new operating and maintenance (O&M) costs, the cost of additional fuel resources needed to compensate for the efficiency penalty introduced by the capture plant and the cost of CO₂ compression. Any new capture system following the scheme of Figure A.9.1.1 will have to compete in cost with existing systems which already can deliver total CO₂ capture cost below 50 Euro/tonne of CO₂ separated. Since the cost of the makeup flow of sorbent in Figure A.9.1.1 is only one component of the total capture cost, in order to keep under reasonable values the O&M cost the sorbent makeup costs cannot translate into more than few Euro per tonne of CO₂ separated. A commercially proven CO₂ capture system employing absorption with MEAs can be used to illustrate this point.

We have conducted the following analysis on commercial and pre-commercial systems with the aid of the group of Prof. Rubin (Carnegie Mellon Univ., USA) and CETC (Canada) (see Abanades et al, 2004). Rao and Rubin (2003) have shown the strict operational requirements necessary for the desulphurization unit in a power plant to keep the makeup cost of MEA reasonably low. Concentrations of SO₂ in the flue gases below 10 ppmv are necessary to minimize the sorbent makeup that otherwise deactivates rapidly due to reactions with SO₂ and other pollutants in the flue gases. If this is the case for MEA, a well-known chemical that has been used in industry for many decades, the need to keep the sorbent makeup cost per tonne of CO₂ separated very low also will be essential for any other sorption-desorption system for CO₂ capture that follows the scheme of Figure A.9.1.1. We can define the cost of sorbent per kg of CO₂ removed (COS) using the notation of Figure A.9.1.1, as follows:

$$COS = \left(\frac{F_0}{F_R} \right) \left(\frac{F_R}{F_{CO_2}} \right) \frac{bM_s}{M_{CO_2}} C_s = \left(\frac{F_0}{F_R} \right) \frac{C_s^*}{M_{CO_2}} \quad (A.10.1.1)$$

We note that the group $C_s^* = M_s C_s b (F_R / F_{CO_2})$ is a suitable variable to compare cost of different sorbents as this is the cost of the mass of sorbent required to react (or absorb) one mol of CO₂ (or O₂). Furthermore, since the ratio F_R / F_{CO_2} is equivalent to the expected average conversion of the sorbent, and this can be estimated from laboratory data, C_s^* can be readily estimated when knowing the price of the sorbent, C_s (\$/kg of sorbent). For a typical MEA-based system, (Rao Rubin, 2003) $b = 2$, $M_{MEA} = 0.061$, $C_s = \$1.25/\text{kg MEA}$, and the makeup flow is 1.5 kg MEA/tonne CO₂. The latter corresponds to values of $F_0 / F_R = 0.000152$ and $F_R / F_{CO_2} = 3.57$ (based on a lean solvent loading of 0.22 mol CO₂/mol solvent and a maximum rich loading of 0.5 mol CO₂/mol solvent, which gives $F_R / F_{CO_2} = 1/[0.5-0.22] = 3.57$). This translates into $C_s^* = 0.544$ \$/molCO₂ and a reported sorbent makeup cost for a large-scale MEA-based system of around $COS_{MEA} = \$0.0019/\text{kg CO}_2$. Although this cost represents a relatively small portion of the total capture costs (in the order of 0.01 to 0.05 \$/kgCO₂), the rationale behind the present study is that the sorbent performance in any new CO₂ capture system should be of sufficient quality to ensure that sorbent makeup costs are comparable to those being achieved today for a commercially proven technology, *i.e.*, absorption with MEA. This is assumed to be a necessary (but not sufficient) condition because we consider it unlikely that other benefits arising from a new, unproven technology could compensate for much higher values of this component of total capture cost if the overall cost of CO₂ capture is to be low. Therefore, and to be able to use a quantitative guideline in our comparisons, we suggest that for any new capture system using regenerable sorbents an acceptable level of sorbent losses in the system should be such that:

$$COS_s \leq COS_{MEA} \quad (A.10.1.2)$$

There are no reliable estimates of sorbent makeup costs for new, non-commercial systems, because there is no information on the key flow ratios in Equation A.10.1.1, and the unit cost of sorbent is also uncertain. In particular, the flow ratio F_0 / F_R can only be estimated when sufficient information is available on the performance of the sorbent at realistic process conditions and at a relevant number of sorption-desorption cycles. The unit sorbent cost is also an important variable in Equation A.10.1.1. Reasonable minimum values can be assumed for some of the sorbents listed in Table A.10.1.1, considering the price of similar solids (for example industrial active carbon-based adsorbents or synthetic catalyst based on zeolites) or the market price of the raw material (minerals and metals). A common source has been used to estimate the prices of the raw materials (US Geological Survey, 2002).

Employing the minimum unit price for the sorbents of Table A.10.1.1, we can now use the MEA system as a reference case to ascertain how much the sorbent makeup flows must decrease (or increase) to keep the sorbent makeup cost (COS_s) equal to COS_{MEA} . The results, adopting some reasonable assumptions for the degree of utilization of the sorbent (F_R / F_{CO_2}), are also listed in Table A.10.1.1 in the form of the sorbent recycle ratio F_0 / F_R .

One might argue that the ratio F_0 / F_R already gives a direct measure of the quality of the sorbent required in the system, but we have considered useful to use a relationship of this ratio more comparable with a usual variable when investigating properties of a sorbent for a multicycle operation: the number of sorption-regeneration cycles, experienced by a particle of sorbent. Therefore, using the mass balanced for Figure A.9.1.1, and equation A.9.1.3, we can define:

Table A.10.1.1. Outline of sorbent characteristics, estimated unit prices and performance criteria ($N_{1/2}$) to match the performance of a MEA-based absorption system, used as a baseline reference. The sorbent is considered the raw material in the form at which the price is given.

Sorbent	C_s (\$/kg)	M_s (kg/mol)	b	F_R/F_{CO_2}	C_s^* (\$/molCO ₂)	F_0/F_R
MEA	1.250	0.061	2	3.57	0.544	0.000152
CaCO ₃ (Crushed stone)	0.005	0.1	1	3 ⁱ	0.0015	0.0552
K ₂ O (Potash)	0.155	0.0942	1	3 ⁱ	0.044	0.00189
Na ₂ CO ₃ (Soda ash)	0.105	0.106	1	3 ⁱ	0.033	0.00248
Li ₂ CO ₃ (Lithium)	4.47	0.0739	1	3 ⁱ	0.99	0.0000835
Active carbons	0.5	0.5 ⁱⁱ	1 ⁱⁱⁱ	1 ⁱⁱⁱ	0.25	0.00075
Zeolites	1.0	0.2 ⁱⁱ	1 ⁱⁱⁱ	1 ⁱⁱⁱ	0.20	0.000375
Hydrotalcites	2.0	2.0 ⁱⁱ	1 ⁱⁱⁱ	1 ⁱⁱⁱ	4.0	0.0000207
Fe ₂ O ₃ (Iron ore)	0.026	0.160	2 ^{iv}	3	0.025	0.00332
Co (Cobalt)	33.43	0.059	2 ^{iv}	2	7.9	0.0000105
Cu (Copper)	1.812	0.1271	2 ^{iv}	2	0.46	0.00018
Ni (Nickel)	8.638	0.0587	2 ^{iv}	2	2.0	0.0000408
Mn (Manganese)	0.592	0.055	6 ^{iv}	2	0.39	0.00021

ⁱ Assuming average carbonation conversion of 1/3.

ⁱⁱ Assuming 2 mols of CO₂ adsorbed per kg of active carbon, 5 mols of CO₂ per kg of zeolite and 0.5 mols of CO₂ per kg of hydrotalcite.

ⁱⁱⁱ The definition of M_s for these sorbents already gives the mass of sorbent required to absorb one mole of CO₂

^{iv} This is per mol of O₂ transported, assuming $2Fe_2O_3 = 4FeO + O_2$, $2Me + O_2 = 2MeO$ (for Me=Co, Cu, Ni) and $6MnO + O_2 = 2Mn_3O_4$.

$$N_{1/2} = \frac{\ln 2}{\ln \left(\frac{F_0}{F_R} + 1 \right)} \quad (\text{A.10.1.3})$$

where $N_{1/2}$ is the characteristic number of cycles that indicates that 50% of the sorbent has completed the sorption-desorption cycle more than $N_{1/2}$ times.

For the case of the typical MEA-based system described earlier, $N_{1/2}$ is 4561. The meaning of this parameter for a molecule like MEA is that, on average, it cycles approximately 4500 times before it is lost from the system or encounters a poison that irreversibly deactivates it. If there are no poisons and no material losses, the molecule can, in principle, absorb and desorb CO₂ indefinitely. However, for systems using gas-solid reactions (all the remaining sorbents in Table A.10.1.1), and continuous transport of solid between reactors, the implications of high values of $N_{1/2}$ are very different. Solids reactants are known to attrite, escape from solid capture devices (cyclones, filters, *etc.*), change properties during cyclic reactions, be covered by depositions, or suffer chemical poisoning of the active part of the sorbent. All these decay processes are bound to increase and to accumulate in the particles as the number of cycles increases. As a consequence, it seems reasonable to expect that the testing of new sorbents to determine their critical properties for reactor design (reactivity, selectivity, CO₂ capture capacity, mechanical strength, *etc.*) should be carried out under conditions that can be extrapolated to, at least, the region of $N_{1/2}$ cycles. Application of this criterion to sorbents of comparable unit cost to MEA is already a major technical challenge ($N_{1/2}$ is already very high for MEA). We can illustrate this point by discussing the three main groups of solid sorbents compiled in Table A.10.1.1. Synthetic adsorbents and catalyst based on a substrate like active carbon or zeolites are common in many industrial separations. When their target is to remove a minor contaminant in a large gas flow, or to produce a high value added product, the cost of sorbent referred to one tonne of the impurity removed, or to the product produced, is allowed to be high. However, this cannot be the case in CO₂ capture systems, where the flow of the impurity is very large and the price of the product has to be very low. If CO₂ sorbents are to be developed using these substrates, their performance needs to be demonstrated after many thousands of sorption-desorption cycles. Many well established, large-scale separation processes in industry today, often used as examples to introduce a new CO₂ separation concept, could not exist if the “price” of the separated product had to be as low as a tonne of CO₂ separated from a power plant.

Natural limestones are the subject of the LCCC part of this project and have also been investigated as a regenerable sorbent for CO₂ separation in other systems. However, the sorbent cannot maintain a high capture capacity beyond 20 cycles and large quantities of limestone makeup are required for CO₂ control. This can only be acceptable because of the extremely low price of crushed limestone, and because the exhausted calcines might have some downstream value as feedstock for the cement industry. It is obvious that improved performance with synthetic or reactivated sorbents would be highly beneficial for the lime carbonation-calcination system. However, these new sorbents will have to be tested for reactivity and capture capacity at a much higher number of cycles, given the previous analysis. In general, we propose that new sorbents for CO₂ capture applications should always undergo testing to the extent suggested by Equation (A.10.1.3) in order to adequately assess the cost of sorbent makeup in any large-scale system used for CO₂ capture. While this condition is necessary for reliable economic evaluations, we note that systems using “cheap” sorbents also may face a wide range of other problems that could prevent or limit their near-term application.

ANNEX B. PUBLICATIONS AND REPORTS MADE WITHIN PROJECT**B.1. Chemical-looping combustion****Chalmers**

Abad, A., Mattisson, T., Lyngfelt, A., and Rydén, M., Chemical-Looping Combustion in a 300 W Continuously Operating Reactor System Using a Manganese-Based Oxygen Carrier. *Submitted for publication*

Johansson, E., B. Kronberger, G. Löffler, T. Mattisson, A. Lyngfelt, H. Hofbauer. A Two-Compartment Fluidized Bed for Chemical-Looping Combustion –Design and Experiments, *Seventh International Conference on Energy for a Clean Environment*, Lisbon, Portugal, 2003

Johansson, E., T. Mattisson, A. Lyngfelt and H. Thunman. *A 300 W Laboratory Reactor System for Chemical-Looping Combustion with Particle Circulation*, submitted for publication

Johansson, E., T. Mattisson, A. Lyngfelt and H. Thunman. *Combustion of Syngas and Natural Gas in a 300 W Chemical-Looping Combustor*, submitted for publication

Johansson, E., 2005, Fluidized-Bed Reactor Systems for Chemical-Looping Combustion with Inherent Separation of CO₂, PhD Thesis, Dept. of Energy and Environment, Division of Energy Conversion, Chalmers University of Technology, Göteborg, Sweden

Johansson, M., Mattisson, T. and Lyngfelt, A., "Investigation of Fe₂O₃ on MgAl₂O₄ support for chemical-looping combustion", *Industrial & Engineering Chemistry Research* 43 (2004) 6978-6987

Johansson, M., Mattisson, T. and Lyngfelt, A., 2005, "Comparison of oxygen carriers for chemical-looping combustion", *International Symposium: Moving towards zero-emission plants*, CETH/ISTFA, Leptokarya Piera, Greece. June 20-22.

Johansson, M., Mattisson, T. and Lyngfelt, A., Comparison of oxygen carriers for chemical-looping combustion. (*extended version of above paper*) *Submitted for publication*

Johansson, M., Mattisson, T. and Lyngfelt, A., Investigation of Mn₃O₄ with stabilized ZrO₂ for chemical-looping combustion. *Submitted for publication*

Kronberger, B., E. Johansson, G. Löffler, T. Mattisson, A. Lyngfelt, H. Hofbauer. A Two-Compartment Fluidized Bed Reactor for CO₂-Capture by Chemical-Looping Combustion *Chemical Engineering and Technology* 27 (2004) pp. 1318-1326.

Tobias Mattisson, Francisco Garcia-Labiano, Bernhard Kronberger, Anders Lyngfelt, Juan Adanez and Hermann Hofbauer., CO₂ capture from coal combustion using chemical-looping combustion, abstract submitted to 8th International Conference on Greenhouse Gas Control Technologies. Trondheim, Norway. June 19-23, 2006.

CSIC

L. F. de Diego, F. García-Labiano, J. Adánez, P. Gayán, A. Abad, B. M. Corbella, J. M. Palacios. *Development of Cu-based oxygen carriers for chemical-looping combustion*. Fuel 83 (2004) 1749-1757.

F. García-Labiano, L. F. de Diego, J. Adánez, A. Abad, P. Gayán. *Reduction and oxidation kinetics of a copper-based oxygen carrier prepared by impregnation for chemical-looping combustion*. Ind. Eng. Chem. Res. 43 (2004) 8168-8177.

L. F. de Diego, P. Gayán, F. García-Labiano, J. Celaya, A. Abad, J. Adánez *Impregnated CuO/Al₂O₃ oxygen carriers for chemical-looping combustion: Avoiding fluidized bed agglomeration*. Energy & Fuels 19 (2005) 1850-1856.

B. M. Corbella, L. F. de Diego, F. García-Labiano, J. Adánez, J. M. Palacios *Characterization study and five-cycle tests in a fixed-bed reactor of titania-supported nickel oxide as oxygen carriers for the chemical-looping combustion of methane*. Environmental Science & Technology 39 (2005) 5796-5803.

F. García-Labiano, J. Adánez, L. F. de Diego, P. Gayán, A. Abad. *Effect of pressure on the behavior of copper-, iron-, and nickel-based oxygen carriers for chemical-looping combustion*. Energy & Fuels (2005) in press.

A. Abad, J. Adánez, F. García-Labiano, L. F. de Diego, P. Gayán, J. Celaya *Mapping of the range of operational conditions for Cu-, Fe-, and Ni-based oxygen carriers in chemical-looping combustion*. Chemical Engineering Science (2005) submitted for publication.

A. Abad, F. García-Labiano, J. Adánez, L. F. de Diego, P. Gayán, J. Celaya. *Applicability limits of Cu-, Fe-, and Ni-based oxygen carriers in Chemical-Looping Combustion*. 8th International Conference on Greenhouse Gas Control Technologies. Trondheim, Norway. June 19-23, 2006

TUV

Kronberger, B., Löffler, G., Hofbauer, H. (2003). *Simulation of Mass and Energy Balances of a Chemical-Looping combustion System*. In Proceedings of the International Conference in Energy for a Clean Environment. Lisbon, Portugal.

Kronberger, B., Löffler, G., Hofbauer, H. (2005). *Simulation of mass and energy balances of a chemical-looping combustion system*. International Journal on Energy for a Clean Environment, Vol. 6, pp 1-14.

Johansson, E., Kronberger, B., Löffler, G., Mattisson, T., Lyngfelt, A., Hofbauer, H. (2003). *A two-compartment fluidised bed reactor for CO₂ - capture by chemical-looping combustion* In Proceedings of the International Conference in Energy for a Clean Environment. Lisbon, Portugal.

Kronberger, B., Johansson, E., Löffler, G., Mattisson, T., Lyngfelt, A., Hofbauer, H. (2004). *A Two-Compartment Fluidised Bed Reactor for CO₂ Capture by Chemical-Looping Combustion*, Chemical Engineering Technology, Volume 27, Issue 12, 1318-1326.

Kronberger, B., Wopienka, E., Löffler, G., Hofbauer, H. (2005). *Mathematical and experimental modelling of fluid dynamics of a demo-scale dual fluidised bed reactor system for chemical-looping combustion*. submitted to Powder Technology.

Kronberger, B. and Hofbauer, H. (2004). *Chemical-Looping Combustion - Ein neuartiges Kraftwerkskonzept zur CO₂ – Abtrennung, (Forschungsstatus und Entwicklungspotential)*. Proceedings (Informationsschriften). of the Expertenforum der VDI-Gesellschaft Energietechnik (GET). on Entwicklungslinien der Energietechnik, Bochum, Germany.

Kronberger, B. *Modelling Analysis of Fluidised Bed Reactor Systems for Chemical-Looping Combustion*, PhD thesis, Vienna University of Technology, 2005.

Luisser, C. (2005a). PhD thesis in progress, TU Vienna.

Aravaca, M. Master thesis in progress, Vienna University of Technology, 2005.

Navarro, P.M. Mass- and Energy Balances of a Novel Power Plant Concept, Master thesis at the Vienna University of Technology, 2002.

Wopienka, E. Hydrodynamic Investigation of a Dual Fluidised Bed Chemical Looping Combustor. Experiments and Mathematical Modelling, Master thesis at the Vienna University of Technology, 2004.

B.2. Lime Carbonation Calcination Cycles (LCCC)

The maximum capture efficiency of CO₂ using a carbonation/calcination cycle of CaO/CaCO₃. J C Abanades. *Chem. Eng. J.*, 90, 303-306 (2002)

Conversion limits in the reaction of CO₂ with lime; J C Abanades, D. Alvarez. *Energy and Fuels*, Vol 17, 2, 2003, 308-315

Clean and Efficient Use of Petroleum Coke for Combustion and Power Generation. J. Wang, E. J. Anthony, J.C. Abanades. *Fuel* 83 (2004) 1341–1348

Enhancement of CaO for CO₂ capture in FBC environment. C. Salvador, D. Lu, E.J. Anthony, J.C. Abanades. *Chem. Eng. J.* 2003, 96 (1-3) , 187-195.

Capture of CO₂ from Combustion Gases in a Fluidized Bed of CaO. J.C. Abanades , E. J. Anthony, D. Alvarez, D. Y. Lu, C.Salvador. *AIChE J* 2004 , Vol 50, No. 7, 1614-1622.

Sorbent cost and performance in CO₂ capture systems. Juan C. Abanades, Edward S. Rubin, Edward J. Anthony. *Ind. Eng. Chem. Res.* 2004, (43) 3462-3466

Fluidized bed combustion systems integrating CO₂ capture with CaO. J.C. Abanades, E. J. Anthony, J. Wang, J. E. Oakey. *Env. Sci. & Tech.* 39, 2861-2866 (2005)

Determination of the critical product layer thickness in the reaction of CaO with CO₂. D. Alvarez, J.C. Abanades, *Ind. Eng. Chem. Res* 2005, 44, 5608

Congress proceedings:

Novel combustion cycles incorporating capture of CO₂ with CaO; J.C. Abanades, John E. Oakey; Diego Alvarez; Jouni Hämäläinen, 6th Greenhouse Gas Control Technologies, Kyoto-Japan, October 2002

In-situ capture of CO₂ in a fluidized bed combustor. J.C. Abanades, E.J. Anthony, D. Alvarez, D. Lu. 17th Int. Conf. on Fluidized Bed Combustion, FL-USA, ASME. May 2003. paper10

A simulation study for fluidized bed combustion of petroleum coke with CO₂ capture. J. Wang, E.J. Anthony, J.C. Abanades 17th Int. Conf. on Fluidized Bed Combustion, FL-USA, ASME. May 2003, paper 169.

Novel CO₂ control method by means of CO₂ chemical looping. C. Salvador, D. Lu, E. J. Anthony and J. C. Abanades. 7th International Conference on Energy for a Clean Environment. 7-10 July Lisbon 2003.

Novel CO₂ control method by means of CO₂ chemical looping; C. Salvador, D. Lu, E. J. Anthony and J. C. Abanades, 7th International Conference on Energy for a Clean Environment, Lisbon Portugal, July 2003
Fecha: Julio 2003

Capture of CO₂ with CaO in a pilot fluidized bed carbonator. Experimental results and reactor model. C. Salvador, D. Lu, E. J. Anthony and J. C. Abanades; 7th Congress on Greenhouse Gas Control Technologies- GHGT-7. Vancouver, Canada, 2004

In duct sorbent injection for CO₂ capture, Gemma Grasa, Nigel Simms, John Oakey & Juan Carlos Abanades; 7th Congress on Greenhouse Gas Control Technologies- GHGT-7. Vancouver, Canada, 2004

CO₂ capture with CaO in existing power plants, Gemma Grasa, Nigel Simms, John Oakey & Juan Carlos Abanades; Gordon Research Conference on Hydrocarbon Resources. GRC Ventura-CA, EEUU, Jan 2005

ANNEX C. NOTATION**LCCC**

- A , fin cross section area (m)
 C_{CO_2} , CO₂ concentration along the tube length
 C_{CO_2eq} CO₂ concentration in equilibrium
 $C_{bCO_2,z}$, CO₂ concentration in the bubble phase at height z , mol/m³
 $C_{CO_2,0}$, CO₂ concentration in the gas entering the bed, mol/m³
 $C_{CO_2,eq}$, equilibrium CO₂ concentration over CaO, mol/m³
 $C_{CO_2,exit}$, CO₂ concentration in the gas leaving the bed, mol/m³
 $C_{CO_2,z}$, CO₂ concentration in the gas at height z , mol/m³
 $C_{eCO_2,z}$, CO₂ concentration in the emulsion phase at height z , mol/m³
 d_1 , fin thickness (m)
 d_2 , fin length (m)
 d_b , bubble diameter (m)
 D_{CO_2} , effective gas diffusivity of CO₂ in air, m²/s
 d_p , particle diameter (m)
 D_{sr} , solid dispersion coefficient (m²/s)
 e_0 , particle porosity
 E_{carb} , fraction of the CO₂ entering the carbonator that is captured as CaCO₃
 E_{equil} , fraction of CO₂ entering the carbonator that can be captured if achieving equilibrium conditions between CaO and CO₂.
 E_o , overall capture efficiency of the system, or ratio between the CO₂ captured in the calciner and the amount of CO₂ that would be released in a plant without CO₂ capture
 E_{sys} , system capture efficiency, or fraction of CO₂ leaving the calciner with respect to the total C (as fuel and as CaCO₃) entering the plant
 F_0 , make-up flow rate of fresh limestone that is equivalent to CO₂ produced from this limestone on calcination (kmol/s)
 f_a , fraction of CaO in the bed reacting in the fast reaction regime
 F_{CO_2} , flow rate of CO₂ produced by combustion (kmol/s) in the combustion chamber only (excluding the CO₂ generated by combustion in the calciner)
 F_{flue} , flow rate of all other gases, except CO₂, from the combustor (kmol/s)
 F_{inert} , flow rate of inert solids cycling in the carbonation calcination loop (kg/s).
 $f_{m,w}$, fitting constants
 $f_{m,w}$, fitting constants
 F_R , flow rate of recycled sorbent (kmol/s), excluding fresh makeup
 H_{cal} , heat required in the calciner (MW)
 h_w , overall bed heat transfer coefficient (W/m²K)
 k , fin conductivity, (W/mK)
 K_{be} , overall gas interchange coefficient between bubble and emulsion phases (1/s)
 k_g , mass transfer coefficient of CO₂ towards the particles in the emulsion phase (m/s)
 K_r , overall carbonation rate constant of particles in the emulsion phase (1/s)
 K_{ri} , carbonation reaction rate constant (1/s)
 k_s , rate constant for the carbonation reaction at the surface of CaO (m⁴/s mol)
 k_x , effective reaction rate constant

k_g	, mass transfer coefficient of CO ₂
k_s	, rate constant for the carbonation reaction at the surface of CaO m ⁴ /smol
k_x	, effective reaction rate constant
m	, $B \sqrt{\frac{h_w P}{kA}}$
M_{CaCO_3}	, molecular weight of CaCO ₃ (0.1 kg/mol)
M_{CaO}	, molecular weight of CaO (0.056 kg/mol)
N	, number of calcination/carbonation cycles
N	, number of carbonation/calcination cycles
P	, fin cross section perimeter (m)
Q_g	, total gas flow entering the bed (m ³ /s)
R	, ideal gas constant, 8.314 J/mol K
$r_{c/s}$, molar C/S ratio in the fuel
Re_{mf}	, particle Reynolds at minimum fluidization conditions
S_0	, initial surface area of CaO per unit volume of solid CaO (m ² /m ³)
Sc	, Schmidt number
Sh	, Sherwood number
T	, temperature, K
T_b	, calciner T, K
T_c	, combustor T, K
$T(l)$, temperature along fin length
u_0	, superficial gas velocity (m/s)
u_b	, bubble rise velocity (m/s)
u_b^*	, effective gas velocity in the bubble phase (m/s)
u_{mf}	, minimum fluidization velocity (m/s)
u_{sl}	, 'slip' velocity between gas and particles
W_0	, mass of limestone loaded in the bed (kg)
w_C	, carbon weight fraction in the fuel
X	, conversion of CaO to CaCO ₃
X_{ave}	, average carbon content in the carbonated sorbent that leaves the carbonator
$X_{b,N}$, carbonation conversion at the end of fast reaction period in the N th calcination/carbonation cycle
X_N	, carbonation conversion achieved after N cycles of carbonation/calcination
X_{sulf}	, average conversion of CaO to CaSO ₄
y_{comb}	, mass ratio between the fuel going to the main combustor and the total fuel into the plant
z	, height from the distributor (m)

Greek Symbols

ΔH_{comb}	, heat of combustion (LHV) of the fuel (kJ/kg)
δ	, bubble fraction in the fluidized bed
ϵ_{mf}	, bed porosity at minimum fluidization
γ_b	, volume fraction of solids in the bubble phase
ρ_{CaCO_3}	, true density of CaCO ₃ , 2710 kg/m ³

ρ_{CaO}	, true density of CaO, 3310 kg/m ³
η_1	, net penalty in power generation efficiency of the O ₂ separation
η_2	, net penalty in power generation efficiency of the steam generation for the calciner
η_3	, net penalty in power generation efficiency of the vacuum in the calciner
η_4	, net penalty in power generation efficiency of the CO ₂ compression
η_5	, heat requirements for the calcination of the CaCO ₃ in the sorbent makeup. A fraction (46%) is a net penalty in power generation. It is also an energy credit when the CaO is used in a cement plant instead of CaCO ₃ .
η_{pow}	, power generation efficiency (LHV basis).
η_{ref}	, power generation efficiency of the reference plant without CO ₂ capture, 46%LHV in this work

CLC

A	, decay constant of the riser (m ⁻¹)
Ar	, Archimedes number
a, c	, stoichiometric factor, mol of solid produced (mol of gas) ⁻¹
b	, stoichiometric factor, mol of solid reacting (mol of gas) ⁻¹
d	, parameter in eq. A.2.1.1
d _p	, particle diameter (m)
d _p *	, dimensionless particle diameter ° Ar ^{1/3}
C	, gas concentration, mol m ⁻³
C _i	, gas concentration at the inlet, mol m ⁻³
C _{eq}	, gas concentration at equilibrium conditions, mol m ⁻³
D _e	, effective diffusivity within the particles, m ² s ⁻¹
D	, diameter (m)
E	, activation energy, J mol ⁻¹
Fr	, Froude number
g	, gravity, m·s ⁻²
G _s	, specific solids circulation rate, kg m ⁻² ·s ⁻¹
H	, height, m
K _{eq}	, equilibrium constant
k	, chemical reaction rate constant, mol ¹⁻ⁿ m ³ⁿ⁻² s ⁻¹
k ₀	, preexponential factor of the chemical reaction rate constant obtained at atmospheric pressure, mol ¹⁻ⁿ m ³ⁿ⁻² s ⁻¹
k _{0,p}	, preexponential factor of the chemical reaction rate constant for pressurized conditions, mol ¹⁻ⁿ m ³ⁿ⁻² s ⁻¹
k _{H2O}	, constant to consider the effect of water in the reaction, (m ³ /mol) ³
k _x	, constant to consider the sintering
L	, layer thickness of the reacting solid for the plate-like geometry, m
m	, mass of sample, g
m _{AR}	, bed mass in air reactor, kg
m _{circ}	, circulating mass flow, kg s ⁻¹
m _{FR}	, bed mass in fuel reactor, kg
m _{ox}	, mass of the fully oxidized oxygen carrier, g or kg
m _{red}	, mass of the fully reduced oxygen carrier, g
m _{s,down}	, downward solid mass flow, kg s ⁻¹
m _{s,up}	, upwards solid mass flow, kg s ⁻¹
m	, recirculation rate, g s ⁻¹
n	, reaction order

p_0	, atmospheric pressure, Pa
PSD	, particle size distribution
P	, total pressure, atm
P_p	, partial pressure, atm
R	, gas constant, kJ/(molK)
R_0	, oxygen transport capacity of the oxygen carrier
r	, grain radius, m
r_0	, initial grain radius, m
t	, time, s
t_j	, reaction time from solid conversion 0 until the maximum variation in solid conversion, s
\bar{t}_{AR}	, mean residence time of oxygen carrier particles in the air reactor, s
\bar{t}_{FR}	, mean residence time of oxygen carrier particles in the fuel reactor, s
T	, temperature, K
TSI	, total solids inventory, kg
u	, superficial velocity, m s ⁻¹
$u_{a,s}$, solids velocity in the annulus, m s ⁻¹
$u_{c,s}$, solids velocity in the core, m s ⁻¹
u_{AR}	, fluidization velocity in the air reactor, m s ⁻¹
u_{FR}	, fluidization velocity in the fuel reactor, m s ⁻¹
u_g	, gas velocity, m s ⁻¹
u_t	, terminal velocity, m s ⁻¹
u_{mf}	, terminal velocity, m s ⁻¹
u_{RIS}	, superficial velocity in the riser, m s ⁻¹
$x_{CO_2,FR}$, molar fraction CO ₂ in the FR exit gas flow (dry basis)
X	, solid conversion
$\bar{X}_{o,AR}$, average solid oxidation conversion in the air reactor
$\bar{X}_{o,inAR}$, average solid oxidation conversion at the inlet of the air reactor
$\bar{X}_{o,inFR}$, average solid oxidation conversion at the inlet of the fuel reactor
$\bar{X}_{r,inFR}$, average solid reduction conversion at the inlet of the fuel reactor
Z	, expansion ratio

Greek letters

Δp_{FR}	, pressure drop of the fuel reactor, Pa
Δp_{RIS}	, pressure drop of the riser, Pa
Δp_{RIS}^*	, modified riser pressure drop (solids return line to top), Pa
Δp_{RIS}^*	, riser pressure drop (20mm above gas distributor to top), Pa
$\Delta H_{c,f}^0$, standard heat of combustion of the gas fuel f, kJ mol ⁻¹
ΔH_{red}	, heat of reduction, J.mol ⁻¹
ΔH_{ox}	, heat of oxidation, J.mol ⁻¹
ΔH_c	, heat of combustion, J.mol ⁻¹
ΔX_f	, variation of the fuel conversion
ΔX_s	, variation of the solid conversion

- ρ_m , molar density of the reacting material, mol m⁻³
 τ , time for complete solid conversion, s
 τ_r , time for complete solid conversion under chemical reaction control, s
 τ_d , time for complete solid conversion under diffusion control, s

ANNEX D. REFERENCES

- Abanades, J.C. and Alvarez, D.; The conversion limits in the reaction of CO₂ with lime. *Energy and Fuels*, 17(2), 308-315 (2003)
- Abanades, J.C., Anthony, E.J., Alvarez, D., and Lu, D.; In-situ capture of CO₂ in a fluidized bed combustor. 17th Int. Conf. on Fluidized Bed Combustion, FL-USA, ASME. May 2003
- Abanades, J.C., Anthony, E.J., Alvarez, D., Lu, D.Y., and Salvador, C.; Capture of CO₂ from Combustion Gases in a Fluidized Bed of CaO, *AIChE Journal*, 50 (7), 1614-1622 (2004)
- Abanades, J.C., Edward S. Rubin, Edward J. Anthony. Sorbent cost and performance in CO₂ capture systems. *Ind. Eng. Chem. Res.* 2004, (43) 3462-3466
- Abanades, J.C. , E. J. Anthony, J. Wang, J. E. Oakey Fluidized bed combustion systems integrating CO₂ capture with CaO.. *Env. Sci. & Tech.* 39, 2861-2866 (2005)
- Abanades, J.C., Grasa, G.S., (2001). Modelling the axial and lateral mixing of solids in fluidized beds. *Industrial and Engineering Chemistry Research*, 40, 5656-5665.
- Abanades, J.C., Oakey, J.E., Alvarez, D., and Hämäläinen, J.; Novel combustion cycles incorporating capture of CO₂ with CaO. *Greenhouse Gas Control Technologies. GHGT-6.* Editors: J Gale, Y. Kaya. 181-187, Pergamon, 2003
- Abanades, J.C.; The maximum capture efficiency of CO₂ using a carbonation/calcination cycle of CaO/CaCO₃. *Chem. Engng. J.*, 90, 303-306 (2002)
- Adánez, J.; Abad, A.; de Diego, L. F.; García-Labiano, F.; Gayán, P. Direct sulfidation of half-calcined Dolomite under pressurised conditions. *Ind. Eng. Chem. Res.* 2004a, 43, 4132-4139.
- Adánez, J.; de Diego, L. F.; García-Labiano, F.; Gayán, P.; Abad, A. Selection of Oxygen Carriers for Chemical-Looping Combustion. *Energy Fuels* 2004b, 18, 371-377.
- Adánez, J.; García-Labiano, F.; de Diego, L. F.; Gayán, P.; Abad, A.; Celaya, J. Development of oxygen carriers for chemical-looping combustion. In *Carbon Dioxide Capture for Storage in Deep Geologic Formations - Results from the CO₂ Capture Project.* Eds. Thomas, D., Benson, S. Volume 1, Chapter 34. Elsevier Science, London, 2005.
- Agnihotri, R.; Chauk, S.S.; Misro, S.K.; Fan, L.-S. High-Pressure Reaction Kinetics of Hydrogen Sulfide and Uncalcined Limestone Powder *Ind. Eng. Chem. Res.*, 1999, 38, 3802-3811
- Alvarez, D., JC Abanades, Pore size and shape effect on the recarbonation performance of calcium oxide submitted to repeated calcination/recarbonation cycles. *Energy and Fuels* 19, 270-278 (2005)
- Alvarez, D., JC Abanades, Determination of the critical product layer thickness in the reaction of CaO with CO₂. *Ind. Eng. Chem. Res* 2005, 44, 5608-5619

- Baker E. H.; J. Chem. Soc., 464 (1962)
- Barker R.; The Reversibility of the reaction CaCO₃, CaO + CO₂; J. Appl. Chem. Biotechnol. 1973, 23, 733-742
- Bhatia S.K. and Perlmutter D.D.; A random pore model for fluid-solid reactions: I. Isothermal, kinetic control; AIChE Journal , Vol. 26, 379 (1980)
- Bhatia, S.K. and D.D. Perlmutter, Effect of the Product Layer on the Kinetics of the CO₂-Lime Reaction, AIChE J., 29, 79 (1983).
- Bi, J. Yang, G., Kojima, T., (1995). Lateral mixing of coarse particles in fluidized beds of fine particles. IChemE, 73(A), 162-167.
- Borgwardt, R.H. (1985). Calcination kinetics and surface area of dispersed limestone particles. A.I.Ch.E. Journal, 31, 103-111.
- Capes, C.E. and Nakamura, K. (1973). Vertical Pneumatic Conveying: an Experimental Study with Particles in the Intermediate and Turbulent Flow Regimes, Can. J. Chem. Eng. 52, 31.
- Chauk, S. S.; Agnihotri, R.; Jadhav, R. A.; Misro, S. K.; Fan, L-S. Kinetics of high-pressure removal of hydrogen sulfide using calcium oxide powder. AIChE J. 2000, 46, 1157-1167.
- Cho, P. (2005) Development and Characterisation of Oxygen-Carrier Materials for Chemical-Looping Combustion PhD Thesis, Chalmers University of Technology, Göteborg
- Chong, Y.O., D.J. Nicklin, P.J. Tait. Solid Exchange Between Adjacent Fluid Beds Without Gas Mixing. Powder Technology, 47 (1986) 151-156.
- Copeland, R. J.; Alptekin, G.; Cessario, M.; Gerhanovich, Y. A Novel CO₂ Separation System. First National Conference on Carbon Sequestration, National Energy Technology Laboratory (NETL), Washington, DC, 2001.
- Copeland, R. J.; Alptekin, G.; Cesario, M.; Gershanovich, Y., Sorbent Energy Transfer System (SETS) for CO₂ Separation With High Efficiency. 27th International Conference on Coal Utilization & Fuel Systems, Clearwater, Florida March 4-7, 2002.
- Curran G P, Fink C. E., Gorin E; CO₂ Acceptor Gasification Process. Studies of Aceptor Properties. Fuel Gasification. Advances in Chemistry Series (141-165). ACS, New York 1967
- Danckwerts, P. V. Continuous flow Systems. Distribution of residence times. Chem. Eng. Sci. 1958, 2, 1-13.
- Davidson, J.; Thambimuthu, K., Technologies for Capture of Carbon Dioxide. Proceedings of the 7th International Conference on Greenhouse Gas Control Technologies, Vancouver, Canada, 5th-9th September 2004.
- de Diego, L. F.; García-Labiano, F.; Adánez, J.; Gayán, P.; Abad, A.; Corbella, B. M.; Palacios, J. M. Development of Cu-based oxygen carriers for chemical-looping combustion. Fuel 83 (2004) 1749-1757

de Diego, L. F.; Gayán, P.; García-Labiano, F.; Celaya, J.; Abad, A.; Adánez, J. Impregnated CuO/Al₂O₃ Oxygen Carriers for Chemical-Looping Combustion: Avoiding Fluidized Bed Agglomeration. *Energy & Fuels* 19 (2005) 1850-1856.

Doğu, T., The importance of pore structure in the kinetics of gas – solid non-catalytic reactions: Reaction of calcined limestone with SO₂. *Chemical Engineering Journal* 21 (1981) 213-222.

Fang, M., C. Yu, Z. Shi, Q. Wang, Z. Lou, K. Cen. Experimental research on solid circulation in a twin fluidized bed system. *Chemical Engineering Journal*, 94 (2003)

García-Labiano, F.; Abad, A.; de Diego, L.F.; Gayán, P.; Adánez, J.; Calcination of calcium-based sorbents at pressure in a broad range of CO₂ concentrations. *Chemical Engineering Science*, 2002, 57, 2381-2393.

García-Labiano, F.; Adánez, J.; Abad, A.; de Diego, L. F.; Gayán, P. Effect of Pressure on the Sulfidation of Calcined Calcium-Based Sorbents. *Energy Fuels* 2004a, 18, 761-769.

García-Labiano, F.; de Diego, L. F.; Adánez, J.; Abad, A.; Gayán, P. Reduction and Oxidation Kinetics of a Copper-Based Oxygen Carrier Prepared by Impregnation for Chemical-Looping Combustion. *Ind. Eng. Chem. Res.* 2004b, 43, 8168-8177.

García-Labiano, F.; de Diego, L. F.; Adánez, J.; Abad, A.; Gayán, P. Temperature variations in the oxygen carrier particles during their reduction and oxidation in a chemical-looping combustion system. *Chemical Engineering Science* 2005, 60, 851-862.

Geldart, D. (1985). *Elutriation, in Fluidisation, Second Edition*, J.F. Davidson, R. Clift, and D. Harrison (Eds.), Academic Press, London, UK, 383-412.

Gorin E, Synthetic CO₂ acceptor and gasification process therewith. US Patent 4,191,538 (1980)

Grasa, G., Abanades, J.C., (2001). A calibration procedure to obtain solid concentration from digital images of bulk powders. *Powder Technology* 114, (1-3), 125.

Grasa, G.; Abanades, J.C.; Oakey, J., 2004. Investigation of the solid flow between two fluidized beds connected by an orifice. *Chemical Engineering Science*, 59, 5869.

Grasa, G.; Abanades, J.C.; Narrow fluidised beds arranged to exchange heat between a combustion chamber and a CO₂ sorbent regenerator. 2005 *Chem. Engng. Sc.* (submitted)

Gupta, S.K. and Berruti, F. (2000). Evaluation of the Gas-solid Suspension Density in CFB Risers with Exit Effects, *Powder Technol.* 108, 21-31.

IPCC (2001). *Climate Change 2001 - The Scientific Basis*, Cambridge University Press.

Ishida, M.; Jin, H., A Novel Combustor Based on Chemical-Looping Reactions and its Reaction Kinetics. *Journal of Chemical Engineering of Japan* 1994, 27, 296-301.

Jerndal, E., Mattisson, T. and Lyngfelt, A., 2005, Thermal analysis of chemical-looping combustion, submitted for publication.

Jin, H.; Ishida, M. A new Advanced IGCC Power Plant with Chemical-Looping Combustion. Proc. of TAIES'97 International Conference, Beijing, 1997, p. 548-553.

Jin, H.; Okamoto, T.; Ishida, M., Development of a Novel Chemical-looping Combustion: Synthesis of a Looping Material with a Double Metal Oxide of CoO-NiO. Energy & Fuels 1998, 12, 1272-1277.

Jin, H.; Ishida, M. Reactivity study on natural-gas-fueled chemical-looping Combustion by a Fixed-Bed Reactor. Ind. Eng. Chem. Res. 2002, 41, 4004-4007.

Jin, H.; Ishida, M. A new type of coal gas fueled chemical-looping combustion. Fuel 2004, 2411-2417.

Johansson, M., (2005a) Selection of oxygen carriers for chemical-looping combustion using methane as fuel. Lic. Thesis, Chalmers University of Technology, Göteborg.

Johansson, E. (2005b) Fluidized-bed reactor systems for chemical-looping combustion with inherent separation of CO₂. PhD Thesis, Chalmers University of Technology, Göteborg

Kehlenbeck, R. Scalp of a 500kWth pilot plant with integrated circulating fluidised bed for the generation of a hydrogen rich gas from biomass steam gasification and fluid dynamic investigations of a cold model. PhD thesis at Vienna University of Technology, 2000.

Kronberger, B., E. Johansson, G. Löffler, T. Mattisson, A. Lyngfelt, H. Hofbauer. A Two-Compartment Fluidized Bed Reactor for CO₂ Capture by Chemical-Looping Combustion. Chemical Engineering Technology, 27(12) (2004) 1318-1326.

Kunni, D., Levenspiel, O., (1969). Fluidization Engineering. Wiley: New York, p. 130.

Kunii, D. and O. Levenspiel, Fluidized reactor models. 1. For bubbling beds of fine, intermediate, and large particles. 2. For the lean phase: freeboard and fast fluidization," Ind. Eng. Chem. Res., 29(7), 1226 (1990).

Kunii, D. and Levenspiel, O. (1991). Fluidisation Engineering, Second Edition, Butterworth-Heinemann, Boston.

Laursen, K., Duo, W., Lim, C. J., and Grace, J.R., Sulfation and steam reactivation characteristics of limestones of worldwide origin. Advances in Environmental Materials, Vol. II. Environmentally Preferred Materials (Tim White & Julia A. Stegeman Eds.), pp. 67-75. MRS Singapore, 2001.

Lackermeier, U. and Werther, J. (2002) Flow phenomena in the exit zone of a circulating fluidised bed Chemical Engineering and Processing 41, 771- 783.

Louge M. Y., Bricout, V., Martin-Letellier, S., On the dynamics of pressurized and atmospheric circulating fluidised bed risers. Chem. Eng. Sci, 54, 1811-1824, 1999.

Levenspiel, O., Walton, J.S., (1954). Bed-wall heat transfer in fluidised systems. Chemical Engineering Progress Symposium Services 50 (9) 1-13.

Levenspiel, O. Chemical Reaction Engineering; John Wiley and Sons: New York, 1981.

Levenspiel O. What will come after petroleum. IEC Res, 2005, 44, 5073-5078.

Lyngfelt, A.; Leckner, B., Technologies for CO₂ separation. Minisymposium on Carbon Dioxide Capture and Storage, Chalmers University of Technology and Göteborg University, Göteborg, October 22, 1999 1999, 25-35.

Lyngfelt, A.; Leckner, B.; Mattisson, T., A fluidized-bed combustion process with inherent CO₂ separation; application of chemical-looping combustion. Chemical Engineering Science 2001, 56, 3101-3113.

Lyngfelt, A.; Thunman, H., Construction and 100 h of operational experience of a 10-kW chemical looping combustor. The CO₂ Capture and storage Project (CCP) for Carbon Dioxide Storage in Deep Geologic Formations For Climate Change Mitigation, Volume 1 - Capture and Separation of Carbon Dioxide From Combustion Sources. Ed.: Thomas, D. Elsevier Science, London 2004.

Lyngfelt, A.; Kronberger, B.; Adánez, J.; Morin, J.-X.; Hurst, P., The GRACE project. Development of oxygen carrier particles for chemical-looping combustion. Design and operation of a 10 kW chemical-looping combustor. 7th International Conference on Greenhouse Gas Control Technologies, Vancouver, Canada, 5th-9th September 2004.

Mattisson, T.; Lyngfelt, A.; Cho, P., Possibility of Using Iron oxide as an Oxygen Carrier for Combustion of Methane with removal of CO₂ - Application of Chemical-Looping Combustion. 5th International Conference on Greenhouse Gas Control Technologies 13-16 August, Cairns, Australia, 2000

Mattisson, T.; Lyngfelt, A., Capture of CO₂ using chemical-looping combustion. in Scandinavian-Nordic Section of Combustion Institute. 2001. Göteborg 2001.

Mess, D., A.F. Sarofim and J.P. Longwell, Product Layer Diffusion during the Reaction of Calcium Oxide with Carbon Dioxide, Energy & Fuels, 13(5), 999 (1999).

Paterson N. , Elphick S., Dugwell D. R., and Kandiyoti R. ; Calcium-Based Liquid Phase Formation in Pressurized Gasifier Environments, Energy & Fuels; 2001; 15(4); 894-902.

Pugsley, T.S. and Berruti, F. (1995). A Core-Annulus Solids Interchange Model for Circulating Fluidised Bed and FCC Risers, in Fluidisation VIII, 379-388.

Pugsley, T.S., Berruti, F., Godfroy, L., Chaouki, J., Patience, G.S. (1994). A Predictive Model for the Gas-Solid Flow Structure in Circulating Fluidised Bed Risers, in Circulating Fluidised Bed Technology IV, A.A. Avidan (Ed.), AIChE, New York, USA, 41-48.

Qiu, K.; Anthony, E.J.; Jia, L. Oxidation of sulfided limestone under the conditions of pressurized fluidized bed combustion. Fuel, 2001, 80(4), 549-558.

Ranade, P.V., and Harrison, D.P., The grain model applied to porous solids with varying structural properties. Chemical Engineering Science 34 (1979) 427-432.

- Rao, A.B.; Rubin, E.S. A Technical, Economic and Environmental Assessment of Amine-Based CO₂ Capture Technology for Power Plant Greenhouse Gas Control. *Environ. Sci. Technol.*, 2002, 36, 4467.
- Ryu, H.-J.; Bae, D.-H.; Lee, S.-Y.; Jin, G.-T. Conceptual Design of a 50 kWth CLC plant. *Theor. Appl. Chem. Eng.* 2002, 8, 3798-3792. (article in korean)
- Ryu, H.-J.; Jin, G.-T.; Bae, D.-H.; Yi, C.-K., Continuous Operation of a 50kWth Chemical-Looping Combustor: Long-Term Operation with Ni- and Co-Based Oxygen Carrier Particles. Presented at the 5th China-Korea Joint Workshop on Clean Energy Technology, October 25-28, Qingdao University, China, 2004, 221-230.
- Saastamoinen, J., Richard, J.-R., Simultaneous drying and pyrolysis of solid fuel particles. *Combustion and Flame*, 106 (1996) 288-300.
- Schlichthaerle, P. and Werther, J. (1999). Axial Pressure Profiles and Solids Concentration Distributions in the CFB Bottom Zone, *Chem. Eng. Sci.* 54, 5485-5493.
- Shen, L. ; Zhang, M. ; Xu, Y., (1995). Solids mixing in fluidised beds. *Powder Technology* 84, 207-212.
- Shi, Y.; Fan, L.T., (1984). Lateral Mixing of Solids in Batch Gas-Solids Fluidized Beds. *Ind. Eng. Chem. Process Des. Dev.* 23, 337-341.
- Shimizu T., HIRAMA T., Hosoda H., Kitano K., Inagaki M. and Tejima K.; A Twin Fluid-Bed Reactor for removal of CO₂ From combustion processes *Trans IChemE*, Vol 77 part A, 62 (1999).
- Shimizu, T., Peglow, M., Yamagiwa, K., and Tanaka, M., Comparison among attrition-reaction models of SO₂ capture by uncalcined limestone under pressurized fluidized bed combustion conditions. *Chem. Eng. Sci.* 58 (2003) 3053-3057.
- Silaban A., Narcida M. ad Harrison P; Charactertics of the reversible reaction between CO₂(g) and calcined dolomite; *Chem. Eng. Comm.* 1996. Vol 146. 149-162
- Takematsu, T., Maude, Ch. Coal Gasification for IGCC power Generation. IEA Coal Research: London, 1991.
- Wang, J., Anthony, E.J., and Abanades, J.C.; Clean and Efficient Use of Petroleum Coke for Combustion and Power Generation. *Fuel*, 83, 1341–1348 (2004)
- Wang, J., Anthony, E.J., On the decay behaviour of the CO₂ absorption capacity of CaO-based sorbents. *Ind. Eng. Chem. Res.* 44 (2005) 627-629.
- Werther, J., Bellgardt, D., Groenenwald, H., Hillgardt, K., (1987). Influence of immersed heat exchange surfaces on fluid mechanics and solids mixing in fluidized beds. *Proc. 9th Int. Conf. Fluidized Bed Combustion*; Mustonen, J.P., Ed.; ASME: New York, 152.
- Westphalen, D., Glicksman, L., (1995). Lateral solids mixing measurements in circulating fluidized beds. *Powder Technolgy*, 82, 153-167.

Williams, R.H. ; Fuel Decarbonization for Fuel Cell Applications and Sequestration of the Separated CO₂, PU/CCES Report No. 295, Center for Energy and Environmental Studies, Princeton University, January 1996.

Wolf, J.; Anheden, M.; Yan, J. Performance Analysis of Combined Cycles with Chemical Looping Combustion for CO₂ Capture Requirements for the Oxidation and Reduction Reactors. International Pittsburg Coal Conference, Newcastle, New South Wales, Australia, Dec 3-7, 2001.

Wolf, J.; Anheden, M.; Yan, J. Comparison of nickel- and iron-based oxygen carriers in chemical looping combustion for CO₂ capture in power generation. *Fuel* 2005, 84, 993-1006.

Zenz, F.A. and Weil, N.A. (1958). A Theoretical-Empirical Approach to the Mechanism of Particle Entrainment from Fluidised Beds, *AIChE J.* 4, 472-479.